Quantum transport in quantum dots with spin-effects, electron-vibration interaction and superconductivity

Dissertation
submitted for the degree of a

Doctor rerum naturalium
(Doctor of Natural Science)

presented by

Pascal Stadler

at the

Faculty of Science
Department of Physics

Date of the oral examination: October 11th, 2016
First referee: Prof. Dr. Wolfgang Belzig
Second referee: Prof. Dr. Guido Burkard

Preface

The dissertation was written under the supervision of Prof. Wolfgang Belzig in the Quantum Transport Group at the University Konstanz. All results presented in the dissertation were obtained after many discussion with Prof. Wolfgang Belzig.

During the time of the dissertation, I additionally collaborated with Dr. Cecilia Holmqvist and Dr. Gianluca Rastelli. Chapter 3 contains published work which was done jointly with Dr. Cecilia Holmqvist. The work presented in chapters 4, 5 and 6 were done in close collaboration and under the supervision of Dr. Gianluca Rastelli. The results of chapter 4 are published and the work in chapter 5 is submitted. These chapters contain many input from numerous discussion with Dr. Gianluca Rastelli who in many cases also gave the direction on which problem to focus on.

Zusammenfassung in deutscher Sprache

Supraleitende, ferromagnetische und normalleitende Heterostrukturen finden in der Festkörperphysik vielfältige Anwendungen in der Elektronik und haben eine wichtige Bedeutung in der Grundlagenforschung. Die faszinierenden Eigenschaften solcher Strukturen kommen durch Quanteneffekte zustande und werden für neue Technologien in der Mikroelektronik, Quanteninformationsverarbeitung und Sensorik eingesetzt.

Zu den grundlegenden Heterostrukturen in der Tieftemperaturelektronik gehören Josephson-Kontakte. Ein Josephson-Kontakt besteht aus zwei Supraleitern, die durch ein normalleitendes Material getrennt sind. Der inhärente quantenmechanische Effekt ist der sogenannte Josephson-Effekt, der einen dissipationslosen Ladungstransport durch den Kontakt beschreibt. Die Transporteigenschaften sind dabei durch den normalleitenden Bereich zwischen den beiden Supraleitern bestimmt. Interessante Effekte treten auf, wenn der normalleitende Bereich mit magnetischen Eigenschaften kombiniert wird. In dieser Arbeit werden wir die Steuerung des Josephson-Stroms durch einen molekularen Magneten untersuchen, der an den Josephson-Kontakt gekoppelt ist.

Weitere quantenmechanische Effekte treten in Heterostrukturen auf, in denen elektronischer Transport mit mechanischen Schwingungen wechselwirkt. Eine interessante Art solcher nanoelektromechanischen Systeme sind freihängende Kohlenstoffnanoröhrchen, mit denen grundlegende Forschungsfragen wie zum Beispiel den Übergang von der Quanten- zur klassischen Physik analysiert werden können. Die mechanische Biegeschwingung freihängender Kohlenstoffnanoröhrchen – makroskopische Objekte bestehend aus Millionen von Atomen – kann in den Grundzustand gekühlt werden um die resultierende Nullpunktsbewegung zu messen oder verschränkte mechanische Zustände zu erzeugen. Um das Quantenregime mit freihängenden Kohlenstoffnanoröhrchen zu erreichen, sind Temperaturen unterhalb des mK-Bereichs erforderlich. Ein Ziel dieser Arbeit ist es zu zeigen, dass die Biegeschwingung durch die Wechselwirkung zwischen elektronischem Transport und der Auslenkung des Kohlenstoffnanoröhrchen in den quantenmechanischen Grundzustand gekühlt werden kann.

Die Arbeit ist wie folgt gegliedert. Kapitel 2 befasst sich mit den theoretischen Methoden, mit denen wir die physikalischen Eigenschaften in den Kapiteln 3 bis 6 berechnen werden. Da der Transport durch verschiedenartige Kontakte und die Phononenbesetzung außerhalb des thermodynamischen Gleichgewichts berechnet werden soll, werden die Nichtgleichgewichts-Green-Funktionen und deren Relationen zu physikalischen Observablen eingeführt. Um supraleitende Kontakte zu beschreiben, diskutieren wir die BCS Theorie und die Green-Funktionen eines Supraleiters. Darüber hinaus werden die grundlegenden Transportprozesse erläutert, die in normalleitenden-supraleitenden und Josephson-Kontakten auftreten.

In Kapitel 3 untersuchen wir den Josephson-Strom durch einen Quantenpunkt, der

mit einem molekularen Magneten über die Austauschwechselwirkung gekoppelt ist. Die Transporteigenschaften werden dabei mit Nichtgleichgewichts-Green-Funktionen berechnet. Wir werden zeigen, dass der Josephson-Strom durch den molekularen Magneten beeinflußt wird und mit einem Magnetfeld oder einer Vorspannung umgekehrt werden kann.

Die Nichtgleichgewichts-Phononendynamik und den Quantentransport in freihängenden Kohlenstoffnanoröhrchen untersuchen wir in den Kapiteln 4 und 5. Zur Berechnung dieser Eigenschaften verwenden wir die Methode der Nichtgleichgewichts-Green-Funktionen und behandeln dabei die Elektron-Phonon-Wechselwirkung mit Hilfe der Störungstheorie.

In Kapitel 4 betrachten wir einen Quantenpunkt der an zwei ferromagnetische Kontakte gekoppelt ist. Das freistehende Kohlenstoffnanoröhrchen wird durch einen harmonischen Resonator beschrieben. Der Spin der Elektronen wechselwirkt mit der Auslenkung des Resonators sowohl über die Spin-Bahn Kopplung der Kohlenstoffnanorörchen als auch über ein angelegtes magnetisches Gradientenfeld. Spinpolarisierte Ströme führen dann zu einer Änderung der Phononenbesetzung der Biegeschwingung. Die Zu- oder Abnahme der Phononenbesetzung hängt dabei von der durch ein Magnetfeld induzierten Zeeman-Aufspaltung der Energieniveaus des Quantenpunkts ab. Wenn die Zeeman-Aufspaltung der Frequenz des Resonators entspricht oder im Bereich der Frequenz des Resonators liegt, kann die Phononenbesetzung stark reduziert werden, so daß eine Kühlung des Resonators in den quantenmechanischen Grundzustande erfolgt. Durch Änderung der angelegten Spannung oder der Magnetisierung der Kontakte, erhöht sich die Besetzung der Schwingungsmode über ihren Wert im Gleichgewicht und führt zur einer Instabilität des Resonators. Die Instabilität ist auf die Störungstheorie zur führenden Ordnung in der Kopplungsstärke zurückzuführen. Wir werden sowohl das Kühlen in den Grundzustand also auch die Energiezufuhr in den Resonator in Kapitel 4 diskutieren.

Die Ergebnisse aus Kapitel 4 werden zeigen, dass elektronischer Transport die Schwingungszustände eines freihängenden Kohlenstoffnanoröhrchens steuern kann. Die Kühlung in den quantenmechanischen Grundzustand begründet sich dabei auf der Resonanzbedingung zwischen den Zeeman-aufgespaltenen Spinniveaus des Quantenpunkts. In Kapitel 5 untersuchen wir eine Heterostruktur in der ein Resonator ohne Erfüllung der Resonanzbedingung gekühlt und zudem mehrere Moden gleichzeitig in den quantenmechanischen Grundzustand gebracht werden können. Diese Heterostruktur besteht aus einen Quantenpunkt, der an ein normalleitendes Metall und an einen Supraleiter gekoppelt ist. Im Unterschied zu Kapitel 4 wird die Kopplung zwischen der elektrischen Ladung und der Auslenkung der Biegeschwingung betrachtet um die Phononenbesetzung des Resonators zu beeinflussen. In einem normalleitend-supraleitenden Kontakt findet Transport unterhalb der Energielücke des Supraleiters durch Andreev Reflexion statt. Durch die Wechselwirkung der Ladung des Quantenpunkts mit dem Resonator treten inelastische Andreev Reflexionen mit einer Emission oder Aborption eines Phonons auf. Die inelastischen Andreev Reflexionen finden auf zwei Pfaden statt, die miteinander interferieren. Diese Interferenz ermöglicht das Steuern der Phononenbesetzung für einzelne und mehrere Moden des Resonators.

In Kapitel 6 untersuchen wir das frequenzabhängige Stromrauschen in einem Quan-

tenpunkt, der an zwei metallische Kontakte gekoppelt ist und über die Elektron-Phonon-Wechselwirkung mit einem Resonator gekoppelt ist. Die Ergebnisse werden durch die Analogie des Quantenrauschens mit Emissionen und Absorptionen von Photonen erklärt.

Die Dissertation schließt mit einer Zusammenfassung und einem Ausblick in Kapitel 7 ab.

Contents

1 Abstract and Motivation

In condensed matter physics, superconducting, ferromagnetic and normal conducting heterostructures have various applications as basic building blocks in electronics and play an important role in fundamental research. The underlying reasons are various kinds of quantum effects appearing in such systems and the accompanied possibility to create novel technologies for microelectronics, quantum information science and sensors.

Superconducting heterostructures, as for instance Josephson junctions, belong to the most basic elements used in low temperature electronics. A Josephson junction consists of two superconducting leads separated by a normal conducting region. The amazing quantum mechanical effect in this junction is the Josephson effect and describes the dissipationless supercurrent carried by the Andreev bound states which are formed inside the normal region. The transport properties of such a system strongly depend on the region between the superconductors and can be manipulated by proper engineering the non-superconducting region. In the first part of the dissertation, we investigate the control of the Josephson current by attaching a molecular magnet within the junction.

The second part of the dissertation addresses the transport through heterostructures in which the electronics interacts with mechanical vibrations. A particular interesting kind of these nanoelectromechanical systems (NEMS) are suspended carbon nanotube quantum dots (CNTQDs). The extraordinary properties of CNTQDs allow in principle to test fundamental research questions as for instance the crossover from quantum to classical physics. The interest in suspended CNTQDs also arises from the possibility to put macroscopic objects made off millions of atoms to the ground state and observe the remaining zero-point motion or to generate entangled mechanical states. To reach the quantum regime with CNTQDs, the resonator must be cooled to temperatures below the mK-range which constitutes a major challenge with standard cryogenic techniques in CNTQDs. Therefore active cooling is required to obtain a very low occupation of the vibrational modes. In this dissertation, we employ the electron-phonon interaction to cool the mechanical motion of a suspended CNTQD to the ground state by purely electronic transport.

The content of the dissertation is as follows. In chapter 2 we introduce the theoretical tools, which we need to derive the physical properties in chapters 3-6. Since we are interested in transport and the nonequilbrium phonon occupation through different junctions, we review the nonequilibrium Green's function formalism and the relation of nonequilibrium Green's function to the physical observables in chapter 2. A part of the dissertation concerns superconducting junctions and we will discuss the BCS theory and the Green's functions for a superconductor. Chapter 2 also includes a discussion of the basic transport processes appearing in a normal-superconducting

contact and a brief introduction to nanoelectromechanical systems.

In chapter 3, we study the Josephson current through a quantum dot coupled to a molecular magnet via the exchange interaction. The coupling between the quantum dot and the molecular magnet allows to control the Josephson current by applying a magnetic field. To calculate the transport properties in the junction, we use the Keldysh Green's function technique. The main result is that the Josephson current can be reversed by manipulating external parameters as the gate voltage or the magnetic field.

The nonequilibrium phonon dynamics and the quantum transport in suspended CNTQDs is studied in chapters 4 and 5. To calculate these properties we use the nonequilibrium Green's function technique. The coupling between the electrons and the vibration is treated to the leading order in the coupling strength.

In Chapter 4, we consider a quantum dot in contact with two ferromagnetic leads. The vibration of the suspended CNTQD is modeled as a harmonic resonator. In this system, the spin of the quantum dot is coupled to the vibration of the nanotube. The spin-vibration interaction allows to control the vibrational states of the flexural mode by spin-polarized current. The enhancement and suppression of the equilibrium occupation of the nanotube's vibration strongly depends on the Zeeman splitting induced by a small magnetic field applied on the quantum dot. When the Zeeman splitting matches or is close to the frequency of the resonator, the occupation can be strongly reduced such that the resonator is cooled close to the ground state. By changing the bias voltage or the magnetization of the leads, the vibrational mode can be strongly "heated" and approaches an instability. We will study both ground-state cooling and "heating" in chapter 4. Additionally we discuss the characteristic features due to the nonequilibrium resonator in the current of the system.

The result of chapter 4 shows that using electronic transport and the spin-vibration interaction is a promising route to control the vibrational states of a CNTQD. However, the ground-state cooling relies on the resonance condition between the two spin-level on the quantum dot. In chapter 5, we discuss a hybrid device consisting of a normal metal and a superconductor. Similar to chapter 4, we use the nonequilibrium Green's function technique to determine the phonon occupation and the current. In contrast to chapter 4, here we discuss the coupling between the charge and the vibration to control the occupation of the resonator. In a normal-superconducting junction, Andreev reflections give rise to transport for voltages below the superconducting gap. The interaction between the dot's charge and the resonator leads to inelastic Andreev reflections with the emission or absorption of one phonon. Remarkably, such processes can occur through two different paths which can interfere. This interference plays the key role to achieve ground-state cooling in the normal-superconducting junction. The interference allows to cool the resonator without any resonance condition and to put several mode simultaneously to the ground state.

In chapter 6, we first study the current noise in a quantum dot coupled to two normal leads and in a normal-superconducting contact. Then, we derive the frequency-dependent noise in a quantum dot coupled to two normal contacts in the presence of electron-vibration interaction and discuss the features of the resonator in the current noise. The results of the frequency-dependent noise will be explained in analogy with

the emission and absorption of photons.

The dissertation ends with a conclusion and an outlook in chapter 7.

2 Introduction

2.1 Many-particle Green's functions

Condensed matter theory aims to derive physical observables from a microscopic description of the physical system. Since in condensed matter many electrons and phonons interact among each others, the underlying microscopic model is manifested in the many-body Schrödinger equation,

$$i\hbar\frac{\partial}{\partial t}\Psi(\mathbf{x}_1,\mathbf{x}_2,\ldots,\mathbf{x}_N,t)=\mathcal{H}\Psi(\mathbf{x}_1,\mathbf{x}_2,\ldots,\mathbf{x}_N,t)\,, \tag{2.1}$$

with the many-body wave function $\Psi(\mathbf{x}_1,\mathbf{x}_2,\ldots,\mathbf{x}_N,t)$ and the many-body Hamiltonian $\mathcal{H}$ describing electrons, ions and interactions in a solid. If we are able to calculate the wave function, we have all the information of the system. However, due to the huge number of degrees of freedom, a wave function treatment is not feasible. Many-particle Green's functions are a powerful method to calculate observables of many-body Hamiltonians. In particular, the many-body Green's functions allow a perturbative approach to the problem using Feynman diagrams [1]. Usually a small parameter allows a controlled perturbation expansion to a finite order. However, some problems require a non-perturbative treatment.

To solve a many-body problem using many-body Green's functions, we express the observables in terms of Green's functions and then determine the Green's functions corresponding to the observables. In general, the observables depend on different kinds of Green's functions. Many-body systems at equilibrium and finite temperature are characterized by the Matsubara Green's function [2]. At finite temperature and out of equilibrium, the Keldysh Green's function technique is utilized to calculate the properties of the many-body system [3, 4]. In this thesis, we are concerned with the Keldysh Green's function technique.

2.1.1 Contour-ordered Green's function

This section focuses on the derivation of the contour-ordered Green's function which is particularly useful for perturbation expansion.

We consider a system at finite temperature described by the Hamiltonian $\mathcal{H} = H + H'(t)$ with a time-dependent perturbation $H'(t)$ switched on at time $t = t_0$. Prior to the time t_0, the system is characterized by the Hamiltonian $H = H_0 + H_i$ with a term

$$H_0=\int d\mathbf{x}\,\psi^\dagger(\mathbf{x},t)\left[\frac{1}{2m}\left(-i\hbar\frac{\partial}{\partial\mathbf{x}}\right)^2-\mu\right]\psi(\mathbf{x},t)\,, \tag{2.2}$$

the chemical potential μ and the field operator $\psi(\mathbf{x},t)$ represented in the Heisenberg

picture. Interactions not quadratic in the field operators are included into H_i, i.e. the electron-electron or electron-phonon interaction.

We first assume that we want to calculate an expectation value of an observable O which is determined by $\langle O\rangle = \mathrm{Tr}\,\rho(t)O$ with the density matrix $\rho(t)$. After the perturbation is switched on at $t = t_0$, we aim at calculating the time dependence of the density matrix. Since the system is in equilibrium at $t < t_0$, we can shift the time dependence of the density matrix to the operator O by an unitary transformation $\rho(t) = U(t,t_0)\rho(H)U^\dagger(t,t_0)$ with the evolution operators

$$U(t,t_0) = \mathcal{T}\exp\left(-i\int_{t_0}^{t} dt'\mathcal{H}(t')\right), \tag{2.3}$$

$$U^\dagger(t,t_0) = \tilde{\mathcal{T}}\exp\left(i\int_{t_0}^{t} dt'\mathcal{H}(t')\right), \tag{2.4}$$

and the time-ordering operator $\mathcal{T}$ which orders the operators on the real time axis in a sequence with later times to the left. Similarly, the anti-time ordering operator $\tilde{\mathcal{T}}$ orders the operators with later times to the right. At $t \leq t_0$, the system is in equilibrium and the density matrix is calculated by $\rho(H) = e^{-\beta H}/\mathrm{Tr}\,e^{-\beta H}$ with $\beta = 1/k_BT$ and the trace calculated over the multi-particle state space of the corresponding system. The expectation value of an observable then is $\langle O\rangle = \mathrm{Tr}\,\rho(H)O_{\mathcal{H}}(t)$ with the $O_{\mathcal{H}}(t) = U^\dagger(t,t_0)O(t_0)U(t,t_0)$ in the Heisenberg picture.

Similar to the observables, we define the greater Green's function as

$$G^{>}(\mathbf{x},t,\mathbf{x}',t') = -i\langle\psi(\mathbf{x},t)\psi^\dagger(\mathbf{x}',t')\rangle\,, \tag{2.5}$$

with the statistical average containing the density matrix $\rho(H)$ and the field operators in the Heisenberg picture with the evolution operators in Eqs. (2.3) and (2.4). Keldysh was able to show that the time-ordering and anti-time ordering operators in the density matrix $\rho(H)$, as well as an imaginary time due to the Boltzmann factor, can be written in terms of one contour ordering operator [5, 6]. To accomplish the transformation of the greater Green's function from the real time to the contour time, we first write the field operators to the interaction picture and second rewrite the Boltzmann factor in the density matrix.

The transformation of the field operators in Eq. (2.5) to the interaction picture with the perturbation $H_i'(t) = H_i + H'(t)$ is given by

$$\psi(\mathbf{x},t) = V^\dagger(t,t_0)\psi_{H_0}(\mathbf{x},t)V(t,t_0)\,, \tag{2.6}$$

$$V(t,t_0) = \mathcal{T}\exp\left(-i\int_{t_0}^{t} H'_{i\,H_0}(t')dt'\right), \tag{2.7}$$

with $\psi_{H_0}(\mathbf{x},t) = U^\dagger_{H_0}(t,t_0)\psi(\mathbf{x},t_0)U_{H_0}(t,t_0)$ and similar for the perturbation $H'_{i\,H_0}(t) = U^\dagger_{H_0}(t,t_0)H_i'(t)U_{H_0}(t,t_0)$. Since H_0 is time-independent, the evolution operator in the interaction picture is $U_{H_0}(t,t_0) = e^{-iH_0(t-t_0)}$. Instead of transforming the field operators to the interaction picture, we can use the evolution operator in the Schrödinger picture and write

$$\psi(\mathbf{x},t) = U^\dagger(t,t_0)U_{H_0}(t,t_0)\psi_{H_0}(\mathbf{x},t)U^\dagger_{H_0}(t,t_0)U(t,t_0)\,, \tag{2.8}$$

with the evolution operator $U(t,t_0)$ and $U^\dagger(t,t_0)$ of Eqs. (2.3) and (2.4). Comparing Eq. (2.6) and (2.8), we obtain the relation

$$V(t,t_0) = U^\dagger_{H_0}(t,t_0)U(t,t_0)\,. \tag{2.9}$$

This relation can now be used to rewrite the Boltzmann factor of the greater Green's function. The density matrix is calculate at times prior to t_0 when the Hamiltonian $\mathcal{H}$ is time-independent. The relation Eq. (2.9) then reduces to $V_{H_i}(t,t_0) = U^\dagger_{H_0}(t,t_0)U_H(t,t_0) = e^{iH_0(t-t_0)}e^{-iH(t-t_0)}$ with

$$V_{H_i}(t,t_0) = \mathcal{T}\exp\left(-\frac{i}{\hbar}\int_{t_0}^{t} dt' H^i_{H_0}(t')\right). \tag{2.10}$$

The Boltzmann factor in the statistical average can be expressed in terms of the evolution operators as $e^{-\beta H} = U_H(t_0 - i\beta, t_0) = e^{-\beta H_0}V_{H_i}(t_0 - i\beta, t_0)$. Then, using the relation Eq. (2.6) for the field operators, the greater Green's function in Eq. (2.5) can be written as

$$\begin{aligned} G^>(\mathbf{x}_1,t_1,\mathbf{x}_2,t_2) = -i\frac{1}{Z}\langle(e^{-\beta H_0}V_{H^i}(t_0-i\beta,t_0)V^\dagger(t_2,t_0) \\ \psi^\dagger_{H_0}(\mathbf{x}_2,t_2)V(t_2,t_1)\psi_{H_0}(\mathbf{x}_1,t_1)V(t_1,t_0)\rangle\,. \end{aligned} \tag{2.11}$$

Here, we used the property $V(t_2,t_1) = V(t_2,t_0)V^\dagger(t_1,t_0)$ of the evolution operator. From Eq. (2.11) we can see that all the time- and anti-time ordering operators of the evolution operators can be brought under one contour ordering operator. The contour is shown in Fig. 2.1 and stretches from t_0 to t_1, goes further from t_1 to t_2, rewinds back from t_2 to t_0 and stretches on the imaginary axis from t_0 to $t_0 - i\beta$. The two field operators are ordered along the contour to the position given by the time arguments in Eq. (2.11). More general, we define the contour-ordered Green's function [3]

$$G(\mathbf{x},\tau_1,\mathbf{x}',\tau_2) = -i\left\langle \mathcal{T}_c\left(e^{-\frac{i}{\hbar}\int_{\tau_0}^{\tau} H'_{iH_0}(\tau')d\tau'}\psi_{H_0}(\mathbf{x},\tau_1)\psi_{H_0}(\mathbf{x}',\tau_2)\right)\right\rangle_0 . \tag{2.12}$$

Assuming τ_1 on the lower branch and τ_2 on the upper branch, we obtain the greater Green's function in Eq. (2.11).

The contour-ordered Green's function is suitable in way that perturbation expansion can be applied and the Green's function can be calculate to arbitrary order in the perturbation $H'_i = H_i + H'$ by expanding the exponential function. The essential point in Eq. (2.12) is that the statistical average is calculated with respect to the unperturbed Hamiltonian. The expansion of the exponential function in Eq. (2.12) will generate higher-order correlation functions which are in general difficult to calculate. These higher-order correlation functions can be decomposed into Green's functions with two operators by Wick's theorem [7] which only can be applied if the statistical average is calculated with respect to the quadratic Hamiltonian. The result of Wick's theorem is that a n-particle Green's functions can be decomposed into Green's

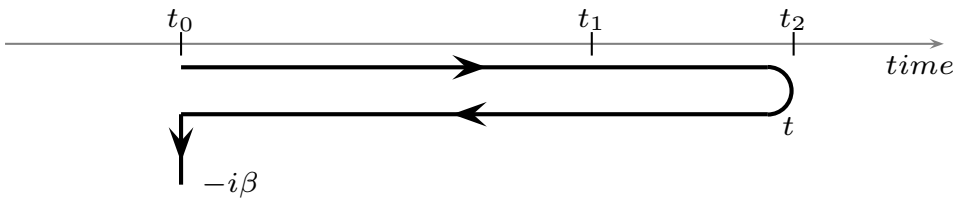

Figure 2.1: The contour-ordering operator $\mathcal{T}_c$ orders the field operators in Eq. (2.12) according to their time arguments on the contour.

functions with two operators as [4]

$$G^{(n)}(1,\dots n;1',\dots,n') = (-1)^n \sum_p (-1)^p \langle \mathcal{T}\psi(1)\psi^\dagger(1')\rangle_0 \dots \langle \mathcal{T}\psi(n)\psi^\dagger(n')\rangle_0 \,, \quad (2.13)$$

with $1 = (\mathbf{x}_1, t_1)$, the summation over all permutations of $1,...,n;n',...,1'$ and the field operators represented in the interaction picture.

After applying Wick's theorem, the goal is to find a closed equation for Eq. (2.12) and to capture the effect of the interaction in a self-energy $\Sigma(1,1')$ such that the contour-ordered Green's function is

$$G(1,1') = G_0(1,1') + \int d\mathbf{x}_3 \oint \tau_3 \int d\mathbf{x}_2 \oint d\tau_2 \, G_0(1,2)\Sigma(2,3)G(3,1') \,, \quad (2.14)$$

with the unperturbed Green's function $G_0(1,1')$. Equation (2.14) is known as the Dyson equation. The self-energy is the sum of all irreducible diagrams to all order in the perturbation. In Fourier space, the Dyson equation is an algebraic equation and can be solved by matrix inversion.

2.1.2 Keldysh Green's function

The contour-ordered Green's function in Eq. (2.12) is useful for diagrammatic expansion which can be applied in the same way as for the time-ordered Green's function [4]. However, after the expansion, the contour-ordered Green's function must be transformed from the contour time to the real times t and t'.

This transformation is accomplished in the following way. We label to upper and lower branch of the contour in Fig. 2.1 with the index 1 and 2, and replace the contour integration by $\oint d\tau \to \int_{-\infty}^{\infty} dt_1 - \int_{-\infty}^{\infty} dt_2$ with the time t_1 and t_2 on the upper and lower contour. The explicit form of the contour-ordered Green's function can be written as a 2×2-matrix in Keldysh space and has the structure

$$\check{G}(1,1') = \begin{pmatrix} G_{11}(1,1') & G_{12}(1,1') \\ G_{21}(1,1') & G_{22}(1,1') \end{pmatrix} = \begin{pmatrix} G(1,1') & G^<(1,1') \\ G^>(1,1') & \tilde{G}(1,1') \end{pmatrix} , \quad (2.15)$$

with the time-ordered, the anti-time ordered and the lesser Green's function defined

as

$$G(\mathbf{x},t,\mathbf{x}',t') = -i\langle \mathcal{T}\psi(\mathbf{x},t)\psi^\dagger(\mathbf{x}',t')\rangle\,, \tag{2.16}$$

$$\tilde{G}(\mathbf{x},t,\mathbf{x}',t') = -i\langle \tilde{\mathcal{T}}\psi(\mathbf{x},t)\psi^\dagger(\mathbf{x}',t')\rangle\,, \tag{2.17}$$

$$G^<(\mathbf{x},t,\mathbf{x}',t') = i\langle \psi^\dagger(\mathbf{x}',t'),\psi(\mathbf{x},t)\rangle\,. \tag{2.18}$$

The elements of the matrix Green's function are not independent. After a Larkin-Ovchinnikov rotation [8] $\check{G} \to L\tau_3\check{G}L^\dagger$ with $L = (1-i\tau_2)/\sqrt{2}$ and the Pauli matrix τ_2, the Green's function can be written as

$$\check{G}(\mathbf{x},t,\mathbf{x}',t') = \begin{pmatrix} G^R(\mathbf{x},t,\mathbf{x}',t') & G^K(\mathbf{x},t,\mathbf{x}',t') \\ 0 & G^A(\mathbf{x},t,\mathbf{x}',t') \end{pmatrix}, \tag{2.19}$$

with the retarded, advanced and Keldysh Green's functions defined as

$$G^R(\mathbf{x},t,\mathbf{x}',t') = -i\theta(t-t')\langle\{\psi(\mathbf{x},t),\psi^\dagger(\mathbf{x}',t')\}\rangle\,, \tag{2.20}$$

$$G^A(\mathbf{x},t,\mathbf{x}',t') = i\theta(t'-t)\langle\{\psi(\mathbf{x},t),\psi^\dagger(\mathbf{x}',t')\}\rangle\,, \tag{2.21}$$

$$G^K(\mathbf{x},t,\mathbf{x}',t') = -i\langle[\psi(\mathbf{x},t),\psi^\dagger(\mathbf{x}',t')]\rangle\,. \tag{2.22}$$

Here, we introduced the commutator $\{\cdot\,,\cdot\}$ and anticommutator $[\cdot\,,\cdot]$. The Larkin-Ovchinnikov rotation is very useful, since the information about the occupation of the states is now included in the retarded and the advanced Green's functions. As an example, the density of state is related to the Fourier transform of the retarded Green's function by [4]

$$N(\mathbf{x},\varepsilon) = -\frac{1}{\pi}\mathrm{Im}\,G^R(\mathbf{x},\varepsilon)\,. \tag{2.23}$$

The Keldysh Green's function contains the information about the distribution of the states and is for instance import to calculate transport properties. It is related to the current by [4]

$$j(\mathbf{x},t) = \frac{e\hbar}{2m}\left(\frac{\partial}{\partial\mathbf{x}} - \frac{\partial}{\partial\mathbf{x}'}\right) G^K(\mathbf{x},t,\mathbf{x}',t)|_{\mathbf{x}'=\mathbf{x}}\,. \tag{2.24}$$

A summary of all Green's functions and their relations is given in the appendices A.1 and A.2.

2.2 Superconductivity and BCS theory

The BCS theory was developed by Bardeen, Cooper and Schrieffer in 1957 to describe phonon-mediated superconductivity in the weak coupling regime of the electron-phonon interaction [9]. The essential idea was presented by Cooper [10] who considered a pair of electrons above a noninteracting Fermi sea. Cooper showed that an arbitrary weak attractive interaction between the electrons leads to an instability of the Fermi sea. In a superconductor, this attractive interaction is originated by the electron-phonon coupling and can overcome the screened Coulomb repulsion of the electrons. Since the Fermi sea is not stable against the formation of Cooper pairs, the new ground-state proposed in the BCS theory [9] consists of coherent superpositions

of Cooper pairs with opposite momenta and spins. The attractive interaction induces a gap Δ in the excitation spectrum of a superconductor. Cooper pairs are correlated over the coherence length ξ_0. At zero temperature the coherence length is given by $\xi_0 = \hbar v_F/\Delta_0$ with the Fermi velocity v_F and the gap Δ_0 at zero temperature.

2.2.1 BCS Hamiltonian

The BCS theory of superconductivity relies on the assumption that the attractive interaction between the electrons can be described by a mean-field theory. The BCS Hamiltonian has the form

$$H_{\mathrm{BCS}} = \int d\mathbf{x} \sum_{\sigma} \left[\psi_\sigma^\dagger(\mathbf{x}) h(\mathbf{x}) \psi_\sigma(\mathbf{x})\right] - \Delta^*(\mathbf{x})\psi_\uparrow(\mathbf{x})\psi_\downarrow(\mathbf{x}) - \Delta(\mathbf{x})\psi_\downarrow^\dagger(\mathbf{x})\psi_\uparrow^\dagger(\mathbf{x})\,, \quad (2.25)$$

with $h(\mathbf{x}) = \left(-i\hbar\partial_{\mathbf{x}}\right)^2/2m - \mu$, the chemical potential μ and the complex order parameter

$$\Delta(\mathbf{x}) = \lambda\langle\psi_\uparrow(\mathbf{x})\psi_\downarrow(\mathbf{x})\rangle\,. \quad (2.26)$$

The strength of the attractive interaction is denoted by λ. Since the BCS-ground state is not an eigenstate of the number operator, particle conservation is violated and the average of the field operators in Eq. (2.26) is finite. In general, the order parameter depends on temperature and coordinates and must be determined self-consistently. The temperature dependence of the order parameter enters through the statistical average in Eq. (2.26).

The BCS Hamiltonian Eq. (2.25) can be written in a quadratic form by introducing field operators in Nambu space [11]. These field operators are defined as

$$\Psi(\mathbf{x}) \equiv \left(\psi_\uparrow(\mathbf{x}), \psi_\downarrow^\dagger(\mathbf{x})\right)^T \qquad \Psi^\dagger(\mathbf{x}) \equiv \left(\psi_\uparrow^\dagger(\mathbf{x}), \psi_\downarrow(\mathbf{x})\right) \quad (2.27)$$

and obey the usual fermionic commutation relations. Using the definitions of the field operators in Nambu space, the BCS Hamiltonian becomes

$$H_{\mathrm{BCS}} = \int d\mathbf{x}\, \Psi^\dagger(\mathbf{x}) \begin{pmatrix} h(\mathbf{x},t) & \Delta(\mathbf{x}) \\ \Delta^*(\mathbf{x}) & -h^*(\mathbf{x}) \end{pmatrix} \Psi(\mathbf{x})\,. \quad (2.28)$$

Equation (2.28) is called the Bogoliubov-de Gennes Hamiltonian. To calculate the excitation spectrum of a bulk superconductor, we transform the field operators to momentum space [12]. The excitation spectrum is then determined by setting the determinant of the matrix in Eq. (2.28) to zero. The solutions are $E_k = \pm\sqrt{\xi_k^2 + |\Delta|^2}$ with $\xi_k = \hbar^2k^2/2m - \mu$. The minimal energy to excite the system is therefore given by $|\Delta|$. A calculation of the density of states gives $N(\varepsilon)/N_0 = |\varepsilon|/\sqrt{\varepsilon^2 - |\Delta|^2}$ with the density of states N_0 in the normal state.

2.2.2 Gorkov equation

In a similar way to the BCS Hamiltonian in Nambu space, we define the contour-ordered Green's function in Nambu space as

$$\hat{G}(\mathbf{x},t,\mathbf{x}',t') = -i\langle\mathcal{T}\,\Psi(\mathbf{x},t)\Psi^\dagger(\mathbf{x}',t')\rangle = \begin{pmatrix} G(\mathbf{x},t,\mathbf{x}',t') & F(\mathbf{x},t,\mathbf{x}',t') \\ \tilde{F}(\mathbf{x},t,\mathbf{x}',t') & \tilde{G}(\mathbf{x},t,\mathbf{x}',t') \end{pmatrix}, \quad (2.29)$$

with the field operators represented in the Heisenberg picture and the anomalous Green's function $\tilde{F}(\mathbf{x}_1, t_1, \mathbf{x}_2, t_2) = F^\dagger(\mathbf{x}_2, t_2, \mathbf{x}_1, t_1)$ describing the coherence of quasiparticle in the superconducting state. The order parameter is related to the anomalous Green's function by $\Delta(\mathbf{x}) = -i\lambda \lim_{\mathbf{x}'\to\mathbf{x}} F(\mathbf{x}', \mathbf{x})$. Using the Heisenberg equation of motion and the BCS Hamiltonian, the superconductor can be described by the Gorkov equation,

$$\begin{pmatrix} i\hbar\partial_t - h(\mathbf{x}, t) & \Delta(\mathbf{x}, t) \\ \Delta^*(\mathbf{x}, t) & -i\hbar\partial_t - h^*(\mathbf{x}, t) \end{pmatrix} \hat{G}(\mathbf{x}, t, \mathbf{x}', t') = \hbar\delta(\mathbf{x} - \mathbf{x}')\delta(t - t')\,. \tag{2.30}$$

The Gorkov equation must be solved self-consistently with the pairing potential $\Delta(\mathbf{x}, t)$ depending on the anomalous Green's function.

2.2.3 Quasiclassical approximation

The quasiclassical approximation accounts for the various length scales in a superconductor. As discussed in Sec. 2.2.1, the density of states has a gap of 2Δ around the Fermi energy. The excitation energies of the quasiparticles are inside a tiny shell around the Fermi energy E_F which results in a pronounced peak at k_F in the Fourier transformed Green's function. In spatial space the peak of the Green's functions in momentum space leads to a strongly oscillating behavior as a function of the relative coordinate $\mathbf{x}-\mathbf{x}'$ on the scale of the Fermi wavelength and an envelope function decaying on a length scale of the coherence length. The quasiclassical approximation aims to integrate out the fast oscillations of the Green's functions and keeps the direction of $\mathbf{k}$. Since the Green's functions oscillate as a function of the relative coordinate, it is useful to transform the Green's functions to the Wigner representation with the center of mass coordinates $\mathbf{R}$ and T [3, 4]. The quasiclassical Green's functions are therefore defined as

$$\hat{g}(\mathbf{R}, T, \mathbf{k}_F, E) = \frac{i}{\pi} \int d\xi_{\mathbf{k}} \hat{G}(\mathbf{R}, T, \mathbf{k}, E) \quad \text{with} \quad d\xi_{\mathbf{k}} = \hbar v_F\, d(k - k_F) \tag{2.31}$$

with a normalization condition $g(\mathbf{R}, T, \mathbf{k}_F, E)^2 = 1$ and the Fermi velocity $v_F = \hbar k_F/m$. The observables then have to be expressed in terms of the quasiclassical Green's functions [6].

2.3 Mesoscopic superconductivity

Interesting phenomena appear when superconducting materials are brought into contact with other materials as for instance normal metals. In this section, we discuss the underlying processes giving rise to transport in normal-superconducting nanocontacts and Josephson junctions. It is instructive to use the scattering formalism to describe the transport processes. This chapter is intended to provide the basics of the chapters 3 and 5, in which we use the Green's function technique to determine the properties in similar types of junctions.

2.3.1 Andreev reflection

Andreev reflection describes the scattering of electrons (holes) as holes (electrons) at the interface of a normal metal and a superconductor [13]. For energies of the incoming electron smaller than the superconducting gap, no states are available in the superconductor. The only possibility for an electron to enter the superconductor is to form a Cooper pair and condensate in the superconductor. This implies that an other electron is removed from the normal metal forming a hole excitation.

To gain insight into the microscopic process of Andreev reflection, we study an one dimensional junction consisting of a normal metal attached to a superconductor. The order parameter $\Delta(x)$ is assumed to be a step-like function with $\Delta(x) = \Delta$ in the superconducting and $\Delta(x) = 0$ in the normal region. The excitation energies of the normal metal and the superconductor are calculated by the Bogoliubov-de Gennes Hamiltonian (2.28). Using the fact that the excitation energies of quasiparticles are much smaller than the Fermi energy E_F, the excitation spectrum in the normal metal is $E_k^n = |\xi_k|$ with $\xi_k = \hbar v_F(k - k_F)$ and the Fermi velocity v_F. A similar calculation for the superconducting region gives the excitation spectrum $E_k^s = \sqrt{\xi_k^2 + \Delta^2}$. In the expression of the excitation energies, we take account of the convention that the

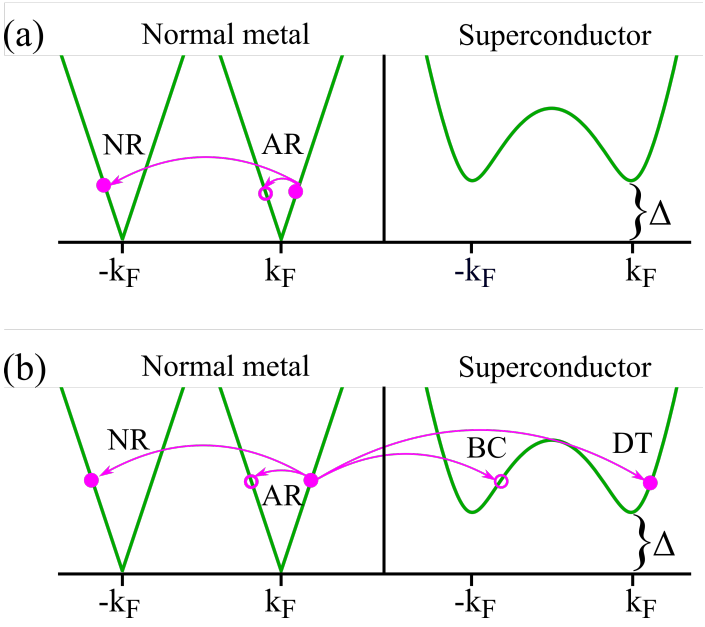

Figure 2.2: Sketch of processes appearing in a normal-superconducting contact. An electron-like excitation is incoming in the normal metal. (a) Below the gap Δ, the quasiparticle can be Andreev reflected (AR) or normal reflected (NR). (b) Above the gap, direct tunneling (DT) and branch crossing (BC) appear in addition to AR and NR. Electron-like particles are sketches as filled circles, hole-like particles as empty circles.

group velocity $v = \hbar^{-1}(\partial E_k^{n,s}/\partial k)$ is positive for electron excitations and negative for hole excitations. In the normal metal, we speak of a electron (hole) excitation for $|k| > |k_F|$ ($|k| < |k_F|$). Since superconductivity mixes electron and hole states we have electron-like excitations for $|k| > |k_F|$ and hole-like excitations for $|k| < |k_F|$. The excitation spectrum of the normal metal and the superconductor is shown in Fig. 2.2 (green lines).

We now consider transport processes in the contact. We can distinguish between processes above and below the superconducting gap. An electron-like excitation incoming at energy $E_k < \Delta$ can not penetrate into the superconductor since no states are available. However, the electron-like excitation can be Andreev reflected (AR) or normal reflected (NR). Energy is conserved in both AR and NR. Momentum is conserved in AR but not in NR. In spin-dependent transport, spin is conserved for both AR and NR. If an electron excitation is incoming with energies $E_k > \Delta$, it can be Andreev or normal reflected, and can be scattered to the superconductor by direct tunneling (DT) or branch crossing (BC). The possible processes above the gap are shown in Fig. 2.2(b).

A full description of the processes requires the solution of the Bogoliubov-de Gennes Hamiltonian. In Ref. [14], the interface between the normal metal and the superconductor was modeled by a δ-function potential. All possible amplitudes are then obtained by matching the wave function and their derivatives at the interface. An alternative approach uses the scattering formalism to calculate the transmissions [12].

Due to Andreev reflection, superconducting correlation can penetrate into the normal region. This phenomena is known as proximity effect and is characterized by a non-vanishing anomalous Green's function $F(\mathbf{x}, t, \mathbf{x}', t')$ in Eq. (2.29) [6].

2.3.2 Andreev bound states

In this section, we consider a contact with two superconductors separated by a nanostructure. To gain insight into the underlying processes, we use the scattering approach to determine the transport process resulting in a dissipationless current known as Josephson current [15]. In Chapter 3, we will study the transport through a quantum dot embedded between the superconductors and coupled to a molecular magnet with the Green's function technique.

The order parameter of the superconductors differ by their phases and are given by $\Delta_\alpha = |\Delta| e^{i\phi_\alpha}$ with $\alpha = (l, r)$, $\phi_l = -\phi/2$ and $\phi_r = \phi/2$. For simplicity, we consider only energies $|E_k| < |\Delta|$ (we omit the index k in the following) such that quasiparticles are only Andreev or normal reflected at the superconductor. The Andreev reflection processes are sketched in Fig. 2.3. Each Andreev reflection is associated with a phase shift which differs for electrons and holes. An Andreev reflected electron and hole acquire a phase shift of $\varphi_{eh}^\alpha = -\arccos[E/\Delta] + \phi_\alpha$ and $\varphi_{he}^\alpha = -\arccos[E/\Delta] - \phi_\alpha$, respectively [12, 16]. If the phase difference is a multiple of 2π, quasiparticle bound states are formed within the superconducting gap known as Andreev bound states.

To determine the energy of Andreev bound states, we use the scattering matrix connecting the incoming states $\mathbf{a}_\nu$ with the outgoing states $\mathbf{b}_\nu$ with $\nu = (e, h)$ for electrons and holes, respectively. The states $\mathbf{a}_\nu$ and $\mathbf{b}_\nu$ denote a vector collecting the

amplitudes of the left and right side of the nanostructure. These states are defined as $\mathbf{a}_\nu = \left(a_\nu^l \; a_\nu^r\right)^t$ and $\mathbf{b}_\nu = \left(b_\nu^l \; b_\nu^r\right)^t$ [16]. A sketch of the amplitudes is shown in Fig. 2.3.

The incoming and outgoing states are connected by two kinds of scattering matrices. Incoming electrons are connected with outgoing electrons by the scattering matrix $s(E)$ via $\mathbf{b}_e = s(E)\mathbf{a}_e$. Similarly, incoming holes and outgoing holes are connected by $\mathbf{b}_h = s^\dagger(-E)\mathbf{a}_h$. Due to Andreev reflection, the electrons and holes are connected by the scattering matrices $s_{eh}(E)$ and $s_{he}(E)$ with $\mathbf{b}_e = s_{eh}\mathbf{a}_h$ and $\mathbf{b}_h = s_{he}\mathbf{a}_e$.

The expressions for the scattering matrices are [16]

$$s(E) = \begin{pmatrix} r(E) & t(E) \\ t(E) & r(E) \end{pmatrix} \qquad s_{eh}(E) = e^{-i\chi(E)} \begin{pmatrix} e^{-i\phi/2} & 0 \\ 0 & e^{i\phi/2} \end{pmatrix} = e^{-i\chi(E)} r_A \tag{2.32}$$

with reflection and transmission amplitudes, $r(E)$ and $t(E)$, $\chi(E) = \arccos\left[E/\Delta\right]$ and $s_{he}(E) = s_{eh}^*(E)$. Since normal reflection and Andreev reflection couples the incoming and outgoing states, the energies of the Andreev bound state are determined from the equation [16]

$$\det\left[1 - e^{-2i\chi(E_A)} s^\dagger(-E_A) r_A^* s(E_A) r_A\right] = 0\,. \tag{2.33}$$

In general, Eq. (2.33) has to be solved numerically. In the limit of short junction, the scattering matrices are independent of energy and we use the approximation $\chi(E) = \chi(0)$. The Andreev bound states can then be determined by Eq. (2.33) and are given by

$$E_A^\pm = \pm\Delta\sqrt{1 - T\sin(\phi/2)^2}, \tag{2.34}$$

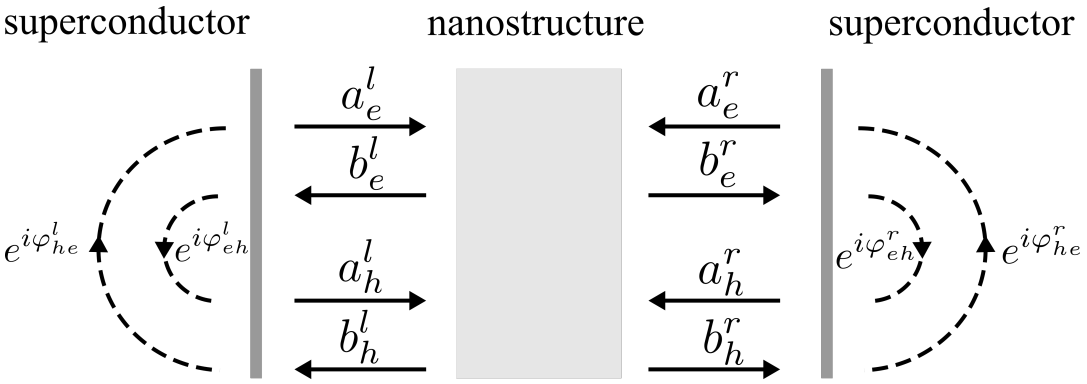

Figure 2.3: Schematic sketch of the scattering amplitudes and phase shifts in a Josephson contact with a nanostructure between the superconductors. The incoming and outgoing amplitude on the nanostructure are denoted with a and b respectively. The normal scattering matrix connects the incoming and outgoing amplitudes of electrons (upper two left and right horizontal arrows). In the process of Andreev reflection, the electron (hole) acquires a phase shift of ϕ_{eh}^α depending on the left ($\alpha = l$) or right ($\alpha = r$) superconductor.

with the transmission coefficient $T = |t|^2$. For a non-ideal contact, a gap of width $E_g = 2\Delta\sqrt{1-T}$ opens at $\phi = \pi$. The backscattering of electrons leads to an avoided crossing of the Andreev bound states. Independently of the transmission, the Andreev bound states reach the gap edge $E_A = \Delta$ at $\phi \to 0$ and $\phi \to 2\pi$. The current carried by the Andreev bound states is calculated by

$$I(\phi) = -\frac{2e}{\hbar} \sum_{s=\pm} \frac{\partial E_A^s}{\partial \phi} \tanh(\beta E_A^s/2). \tag{2.35}$$

with $\beta = 1/k_B T$. The last term im Eq. (2.35) contains the occupation of the Andreev bound states.

2.4 Noise

The measurement of fluctuations in macroscopic observables provides information about the microscopic dynamics not accessible by the measurement of averaged quantities. This is the case for the averaged current and the noise in nanocontacts. In these contacts, different sources contribute to fluctuations. At non-zero temperature, thermal noise causes the occupation number to fluctuate. Shot noise is a further fundamental source of fluctuations and appears due to the discreteness of the charge and a finite probability of transmission at the interface. This kind of noise occurs in systems driven out-of equilibrium. In a stationary system, we define the non-symmetrized noise as [12]

$$S(\omega) = 2 \int_{-\infty}^{\infty} d(t-t') e^{i\omega(t-t')} \langle \hat{I}(t) \hat{I}(t') \rangle \,, \tag{2.36}$$

with the current operator $\hat{I}(t)$. Since operators in general do not commute, we have that $S(\omega) \neq S(-\omega)$. In the following, we discuss the thermal and shot noise and study in Sec. 2.4.1 as an example the noise in a two terminal contact. The description of the thermal noise and the shot noise follows the Refs. [12] and [17].

Thermal noise

In a conductor the available states are filled with electrons and a state at energy ε is either occupied ($n_\varepsilon = 1$) or empty ($n_\varepsilon = 0$). The statistical average of the occupation at temperature T is determined by the Fermi function $f(\varepsilon) = \langle n_\varepsilon \rangle = 1/[1+\exp(\varepsilon/k_B T)]$ such that the probability of an occupied state at energy ε is given by $f(\varepsilon)$. Fluctuations around this value can be calculated by $\langle \Delta n_\varepsilon \rangle = \langle (n_\varepsilon - \langle n_\varepsilon \rangle)^2 \rangle = \langle n_\varepsilon^2 \rangle - \langle n_\varepsilon \rangle^2$. Taking into account that the states are either occupied or empty, the fluctuations can be simplified to $\langle \Delta n_\varepsilon \rangle = f(\varepsilon)(1 - f(\varepsilon))$. Hence, the thermal fluctuations are given by the probability that a state is occupied $f(\varepsilon)$ multiplied with the probability that the state is empty $1 - f(\varepsilon)$. At zero temperature the fluctuations of the occupation vanish and the fluctuations reduce to the Boltzmann distribution at large temperature ($k_B T \gg \varepsilon$).

Shot noise

The shot noise (partition noise) is a fundamental source of noise and appears due to the discreteness of the charge in systems driven out of equilibrium ($eV \neq 0$) and a finite transmission between, for instance, a two terminal contact. To explain the origin of shot noise, we consider a two terminal contact with one channel and a scattering region in between. We want to calculate the probability P_N that out of $N_{\Delta t}$ attempts in the time interval Δt, N electrons are transferred through the scattering region. An electron incoming at the scattering region can be either transmitted with probability T or reflected with probability $1-T$. Under the assumption that the tunneling events are independent, the probability that N electrons tunnel through the contact and $N_{\rm at}-N$ are reflected, is given by $T^N(1-T)^{N_{\rm at}-N}$. Since there are $\binom{N_{\rm at}}{N}$ different combinations of the N transmission and $N_{\rm at}-N$ reflections, the total probability that N electrons are transfered through the contact is [12]

$$P_N = \binom{N_{\rm at}}{N} T^N (1-T)^{N_{\rm at}-N} \qquad (0 \leq N \leq N_{\rm at})\,, \tag{2.37}$$

which is known as the binomial distribution. From this distribution, we can calculate the average of the transmitted electrons $\langle N\rangle$ and the variance $\langle \Delta N^2\rangle$ which are given by $\langle N\rangle = N_{\rm at}T$ and $\langle \Delta N^2\rangle = \langle N\rangle(1-T)$, respectively. The transmitted electrons give rise to a current which is $I = Ne/t$ with the charge e of the electrons. The noise at zero frequency in Eq. (2.36) is then calculated by

$$S(0) = 2e\langle I\rangle(1-T)\,. \tag{2.38}$$

If the number of electrons tunneling through the contact goes to infinity and the probability for transmission goes to zero ($T \ll 1$), the binomial distribution reduces to the Poission distribution. At small transmission, the time interval of two electrons tunneling through the scattering region becomes large, and hence the Poission distribution describes the transfer of uncorrelated electrons. In this limit, the zero-frequency noise is given by $S(0) = 2e\langle I\rangle$ which is known as the Schottky formula. Deviation from the Schottky value of noise are manifested in the Fano factor

$$F = \frac{S(0)}{2e\langle I\rangle}\,, \tag{2.39}$$

defined as the ratio between the zero-frequency noise and the Schottky value. If $F > 1$, the noise is called superpoissonian, if $F < 1$ subpoissonian.

2.4.1 Noise in a two terminal contact

In this section, we consider as an example a two terminal contact and discuss the zero-frequency and the frequency-dependent noise. The contact consist of a number of energy-independent channels T_i. A derivation of the noise by using the scattering formalism is given in Refs. [12] and [17]. The discussion in this section is useful to understand the results in chapter 6 in which we study the current noise in normal and superconducting contacts by the Green's function technique.

Zero-frequency noise

The zero-frequency noise in a two terminal contact is given by [17]

$$S(0) = \frac{4e^2}{h} \int d\varepsilon \sum_i \{T_i \left(f_l(\varepsilon)(1-f_l(\varepsilon)) + f_r(\varepsilon)(1-f_r(\varepsilon))\right) + T_i(1-T_i)(f_l(\varepsilon)-f_r(\varepsilon))^2\}\,, \quad (2.40)$$

with the Fermi functions of the left and right lead $f_\alpha(\varepsilon) = 1/[1+\exp((\varepsilon-\mu_\alpha)/k_BT)]$ and the chemical potential μ_α ($\alpha = (l,r)$). At equilibrium ($V = 0$), the Fermi function on the left and right lead are equal ($f_l(\varepsilon) = f_r(\varepsilon)$) and the noise reduces to the thermal noise $S(0) = (8e^2/h)k_BT\sum_i T_i$. Via the fluctuation-dissipation theorem, the thermal equilibrium noise is directly related to the conductance $G = (2e^2/h)\sum T_i$ of the system by $S(0) = 4Gk_BT$. Hence, the measurement of the thermal noise will give the same information as the measurement of the conductance. In the opposite limit of zero temperature ($T = 0$), the noise is given by the shot noise

$$S(0) = (4e^2/h)\sum_i T_i(1-T_i)eV\,. \quad (2.41)$$

In the limit of small transmission, $T_i \ll 1$, we obtain the Schottky formula [18], $S(0) = 2e\langle I\rangle$. The Fano factor is determined by

$$F = \frac{\sum_i T_i(1-T_i)}{\sum_i T_i}\,. \quad (2.42)$$

For fully open $T_i = 1$ or closed channels $T_i = 0$, the shot noise in Eq. (2.41) and the Fano factor vanishes.

Frequency-dependent noise

The frequency-dependent noise and the shot noise are similar expression except that the energies in the Fermi function are shifted by $\pm\omega$. A calculation of the frequency-dependent noise for a two terminal contact gives the result [17]

$$S(\omega) = \frac{4e^2}{h} \int d\varepsilon \sum_i \{T_i \left(f_l(\varepsilon)(1-f_l(\varepsilon-\omega)) + f_r(\varepsilon)(1-f_r(\varepsilon-\omega))\right) + T_i(1-T_i)\left(f_l(\varepsilon)-f_r(\varepsilon)\right)\left(f_l(\varepsilon-\omega)-f_r(\varepsilon-\omega)\right)\}\,. \quad (2.43)$$

At zero temperature the noise can be written as ($eV > 0$)

$$S(\omega) = 2G \begin{cases} -2\hbar\omega & \hbar\omega < -eV \\ (eV-\omega) - (1-F)(eV+\omega) & -eV < \omega < 0 \\ F(eV-\omega) & 0 < \omega < eV \\ 0 & eV < \omega\,, \end{cases} \quad (2.44)$$

with the conductance at zero temperature $G = (2e^2/h)\sum_i T_i$ and the Fano factor F given by Eq. (2.39). The frequency-dependent noise for one channel and different

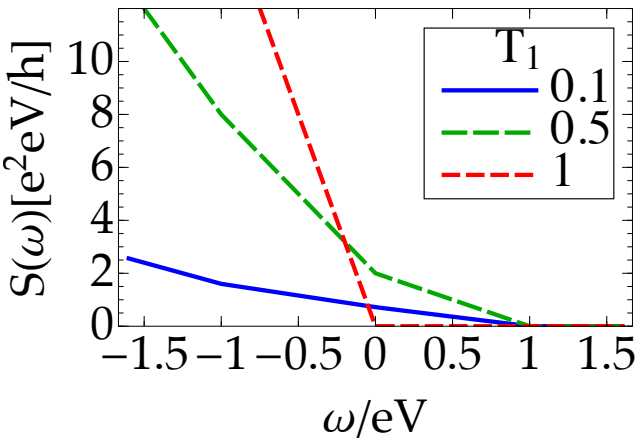

Figure 2.4: Frequency-dependent noise $S(\omega)$ at zero temperature and a single channel with Fano factor F.

transmissions is shown in Fig. 2.4. The frequency-dependent noise can be understood in terms of photon-assisted tunneling in which the current noise at frequency ω is due to emission and absorption of photons at the same frequency. Negative frequencies corresponds to the absorption of photons by the nanostructure whereas at positive frequency, the nanostructure emits photons. Since at zero temperature, the system is in the ground-state, the threshold for emission is set by the applied voltage (see Fig. 2.4). In this sense, the frequency-dependent noise gives a measure for excitations in the nanostructure.

2.5 Nanoelectromechanical systems with carbon nanotubes

NEMS describe a wide variety of suspended nano resonators. In particular, suspended carbon nanotubes have extraordinary properties combining the stiffness and low mass of graphene [19]. The low mass of the resonator makes them ideal for mass [20] and force [21] sensing. Reducing the size as well the frequency of the nanomechanical oscillators have the distinct advantages to increase the sensitivity as nanoscale detectors, the quality factor Q and the amplitude of the zero-point fluctuations.

In Sec. 2.5.1, we briefly study the Euler-Bernoulli theory of beams applied to these resonators [22, 23]. Ground-state cooling of mechanical motion is discussed in Sec. 2.5.2.

2.5.1 Euler-Bernoulli theory of beams

The vibrational modes of a suspended beam can be determined by the Euler-Bernoulli equation. This equation can be applied for microscopic and macroscopic beams with a length l much larger than the width and height. The solution of the Euler-Bernoulli equation with the proper boundary conditions gives a set of eigenmodes and corre-

sponding eigenfrequencies ω_n. We can model the suspended carbon nanotube by cylindrical beam and assume that the nanotube is clamped at both of its ends. Since the mode spectrum is sufficiently sparse [24], we are concerned only with the flexural mode with frequencies in the $\simeq$ MHz range.

We consider now a beam with length l and apply a force to it [23, 25]. The force pulls on the beam and causes a deformation (strain) of the beam. Because of the strain, internal forces induce a stress acting against the strain. The ability of a beam to be deformed when a force is applied, is expressed in terms of Young's modules E which is the ratio between the stress and strain. The suspended beam can additionally be under tension due to the clamping at the contacts.

The Hamiltonian for the mechanical flexural motion in one plane reads [22]

$$H_{vib} = \int_0^l dz \left[\frac{\hat{\pi}^2(z)}{2\rho} + \frac{EI}{2}\left(\frac{d^2\hat{u}(z)}{dz^2}\right)^2 - \frac{T}{2}\left(\frac{d\hat{u}(z)}{dz}\right)^2 \right] \tag{2.45}$$

$$= \sum_n \hbar\omega_n \hat{b}_n^\dagger \hat{b}_n \,, \tag{2.46}$$

with the operator $\hat{u}(z)$ corresponding to the local transversal displacement and $\hat{\pi}(z)$ to the conjugate operator such that $[\hat{u}(z), \hat{\pi}(z)] = i\hbar\delta(z-z')$. For a cylindrical beam, the polar moment of inertia is $I = \pi r^4/4$ with the radius r of the nanotube and T is the uniform tension on the beam. The second form of Hamiltonian Eq. (2.45) is obtained via a canonical transformation in which the local displacement reads $\hat{u}(z) = \sum_n f_n(z) u_n(\hat{b}_n + \hat{b}_n^\dagger)$ and $\hat{\pi}(z) = i\sum_n f_n(z) m\omega_n u_n(\hat{b}_n^\dagger - \hat{b}_n)$, with the waveform $f_n(z)$, $u_n = \sqrt{\hbar/(2m\omega_n)}$ and the nanotube's mass m. The waveform satisfy the normalization condition $(1/l)\int_0^l dz f_n(z) f_{n'}(z) = \delta_{nn'}$.

For sufficiently strong tension $T \gg Er^4/l^2$, one can neglect the second term in the first line of Eq. (2.45) corresponding to the elastic energy for the length-variation of an infinitesimal element caused by the local bending. Then, Eq. (2.45) reduces to a wave equation and the wave-form functions $\{f_n(z)\}$ are the orthonormal set solutions of the standard wave equation for an elastic string with eigenfrequencies $\omega_n = (n+1)\,\pi\sqrt{T/(\rho l^2)}$ and $f_n(z) = \sqrt{2}\sin[\pi(n+1)z/l]$ for integers $n \geq 0$.

2.5.2 Ground-state cooling of mechanical motion

Cooling a nanomechanical resonator close to the ground-state is a major challenge due to the low temperatures required to reach low occupations of the vibrational modes. If we succeed to refrigerate the mechanical motion to temperatures much smaller than the frequency of the resonator, $k_B T \ll \hbar\omega$, the resonator is in the quantum ground-state. Ground-state cooling of mechanical motion has been demonstrated in optomechanical systems, in which the nanomechanical motion is coupled to photons in optical cavities [26–28]. The coupling allows to put the resonator to the ground-state and observe superposition of quantum-mechanical states [29, 30]. Alternatively to the interaction of photons and the mechanical motion, the electron-phonon coupling can be exploited to cool nanomechanical resonators. This coupling mechanism has the advantage that the vibrational states of the resonator can be manipulated by applying a current.

In the ground-state, the resonator exhibits zero-point fluctuations with amplitude

$$x_{\mathrm{zpm}} = \sqrt{\frac{\hbar}{2m\omega}}\,, \tag{2.47}$$

with mass m and frequency ω of the resonator. An advantage of carbon nanomechancial resonators is the relatively large zero-point fluctuation ($\simeq 10$ pm). Additionally, carbon nanomechanical resonators offer the additional advantage of high quality factors which can be larger than 10^6 [31]. However, due to the frequencies in the $\simeq$ MHz range, it is very challenging to cool the mechanical motion to the ground state by conventional cooling techniques. Hence, on top of the conventional cooling, active cooling must be exploited to cool the resonator to the ground state if one aims to reach the quantum regime.

3 Josephson current through a quantum dot coupled to a molecular magnet

3.1 Abstract

We theoretically study the electronic transport of a magnetically tunable nano-scale junction consisting of a quantum dot connected to two superconducting leads and coupled to the spin of a molecular magnet. The exchange interaction between the molecular magnet and the quantum dot modifies the Andreev states due to a spin-dependent renormalization of the quantum dot's energy level and the induction of spin flips. A magnetic field applied to the central region of the quantum dot and the molecular magnet further tunes the Josephson current and starts a precession of the molecular magnet's spin.

We use the nonequilibrium Green's function approach to evaluate the transport properties of the junction. Our calculations reveal that the energy level of the dot, the magnetic field, and the exchange interaction between the molecular magnet and the electrons occupying the energy level of the quantum dot can trigger transitions from a 0 to a π state of the Josephson junction. The redistribution of the occupied states induced by the magnetic field strongly modifies the current-phase relation. The critical current exhibits sharp features as a function of either the energy level of the dot, the magnetic field, or the exchange interaction.

3.2 Introduction

Molecular spintronics combines the two fields of molecular electronics and spintronics [32]. In spintronics, the electron spin is used as the degree of freedom in which information is encoded [33]. Molecular electronics investigates the electrical and thermal properties of molecules and aims to build devices composed of single molecules or ensembles of molecules. In molecular spintronics, the spin of molecules is used to manipulate the spin and charge transport. In particular, molecular magnets are interesting as basic building blocks for electronic devices [32, 34, 35] and for quantum computing [36, 37]. These molecules have a permanent magnetization due to their anisotropy barrier as well as long coherence times [38] that facilitate further quantum-mechanical phenomena such as interference [39, 40] and quantum tunneling of the magnetization.

Experimentally, the transport properties of different kinds of junctions containing magnetic molecules have been extensively studied in three terminal devices [41–47]. Current measurements through molecular magnets allows one to identify the magnetic states and directly observe the magnetic anisotropy and the orientation of the

easy axis [47]. These magnetic states of the molecule have been proposed to enable quantum computing [36]. An alternative way to probe the properties of molecular magnets is to deposit the molecules on carbon nanotubes [48] or graphene layers [49]. The presence of the magnetic molecule modifies the transport through the junction and oppositely, the tunneling electrons modify the magnetization of the molecule and can reverse the magnetization [49].

Other experiments used superconducting electrodes with the advantage that the heat losses in these devices disappear. The proximity-induced superconductivity and the accompanied Andreev reflections modify the transport properties through the molecule [50, 51]. As discussed in Sec. 2.3.2, in a junction consisting of two superconducting leads coupled over a non-superconducting region, the Andreev-reflected electron- and hole-like quasiparticles at the left and right interfaces form Andreev levels which carry the Josephson current. Josephson junctions offer the possibility for applications in superconducting electronics, as well as quantum information and computing [52, 53]. The Andreev levels of a Josephson junction can in principle be used as a two-level qubit [54, 55]. In Ref. [56], an Andreev-level qubit with spin-orbit coupling was discussed as a building block to perform quantum computations using the spin degree of freedom in order to manipulate the Andreev states. The manipulation of the Josephson current by adding quasiparticles to the Andreev states and the resulting suppression of the Josephson current were measured in Ref. [57]. An alternative way to manipulate the Andreev states of a quantum point contact in the presence of a magnetic scatterer was studied in Ref. [58].

The presence of a molecular magnet in a Josephson junction offers a further possibility to tune the current and manipulate the Andreev states. These states are experimentally accessible and have been observed in Refs. [59] and [60]. By comparison of the energy of the Andreev states with the experimental data it is also possible to extract information about the parameters affecting the current in the constriction.

Besides the spectroscopy of the Andreev states, the measurement of the Josephson current reveals detailed information about the internal structure of the junction. Direct measurement of the current-phase relation in superconducting atomic contacts have been performed in Ref. [61]. The shape of the current-phase relation strongly depends on the details of the contact between the electrodes and is important for applications in superconducting devices. The state of the system can change from a 0 to a π state in which the current changes sign. This transition to the π state was proposed in Ref. [62] as a result of tunneling through magnetic impurities. Experimentally, this transition was measured in a junction consisting of two superconducting leads coupled over a quantum dot in the Coulomb blockade regime which was occupied with a odd number of electrons [63]. The singlet wave function of the Cooper pairs experiences a phase shift of π due to coherent cotunneling processes, leading to the reversal of the supercurrent. The 0 to π transition has been studied in many other kinds of Josephson junctions, such as ferromagnetic heterostructures [64, 65], and theoretically analyzed in magnetic junctions associated with a molecular magnet in Refs. [66–74].

In this chapter, we study the Josephson current through a quantum dot which is coupled to a molecular magnet. We focus on the limit of low temperature, $T \ll \Delta$

with the superconducting energy gap Δ, and on the regime of small Coulomb interactions compared to the superconducting gap and the coupling of the quantum dot to the leads. The magnetic moment of the molecular magnet is assumed to be large enough to allow for a classical treatment of the molecular magnet's magnetization. Furthermore, we assume that the molecule has an isotropic magnetization and may, for instance, be a fullerene molecule doped with a magnetic impurity [50, 75]. The spin of the magnetic molecule then interacts with the electrons occupying the quantum dot via the exchange interaction. In Refs. [66] and [67], the Josephson current through an isotropic magnetic molecule was studied in the Kondo regime and in the regime of negligible Coulomb interaction, respectively. In comparison to the work in Ref. [66], in this chapter a magnetic field is applied to the central region consisting of the quantum dot and the molecular magnet, whose magnetization then precesses with the Larmor frequency, ω_L. The magnetic field and a gate voltage applied to the quantum dot introduce additional parameters for manipulating the Andreev states and tuning the current through the junction. We mainly focus on the dependence of the Josephson current on the energy level of the dot and the magnetic field. The manipulation of the Andreev states by the molecular magnet is studied and the parameter range enabling the junction to be in a 0 or π state can be determined by the critical current.

Different methods have been studied to include electronic interactions on the quantum dot [76–82]. Here, we consider the regime in which electronic interactions U are small compared to the superconducting gap Δ and the coupling Γ of the quantum dot to the leads [83, 84]. The lowest-order perturbation expansion in U splits the energy level of the quantum dot and leads to a renormalization of the induced superconducting correlations [77]. In a simplified way, the effect of electronic interactions can therefore be absorbed in an effective level splitting and effective superconducting correlations. This treatment of the electronic interactions is not sufficient to completely describe the physics associated with electronic interaction on the quantum dot and is only valid in the regime $U < \Gamma$. Experimentally, the situation is comparable with Ref. [59], where the quantum dot is realized by a carbon nanotube that additionally favors the coupling of a molecular magnet [48].

The outline of the chapter is as follows. In Sec. 4.3, we introduce the model Hamiltonian of the junction and describe the different couplings including the effect of the molecular magnet. The following Sec. 3.4 concerns with the method and approximations used to determine the transport properties of the junction. The results, starting with the density of states of the quantum dot and the Andreev states, are presented in Sec. 3.5. This section also includes a discussion about the current-phase relation and the critical current. We conclude with a summary of the results in Sec. 3.6.

3.3 Model

The junction, which is depicted in Fig. 3.1(a), consists of two superconducting leads coupled to a quantum dot in the presence of a molecular magnet. A magnetic field

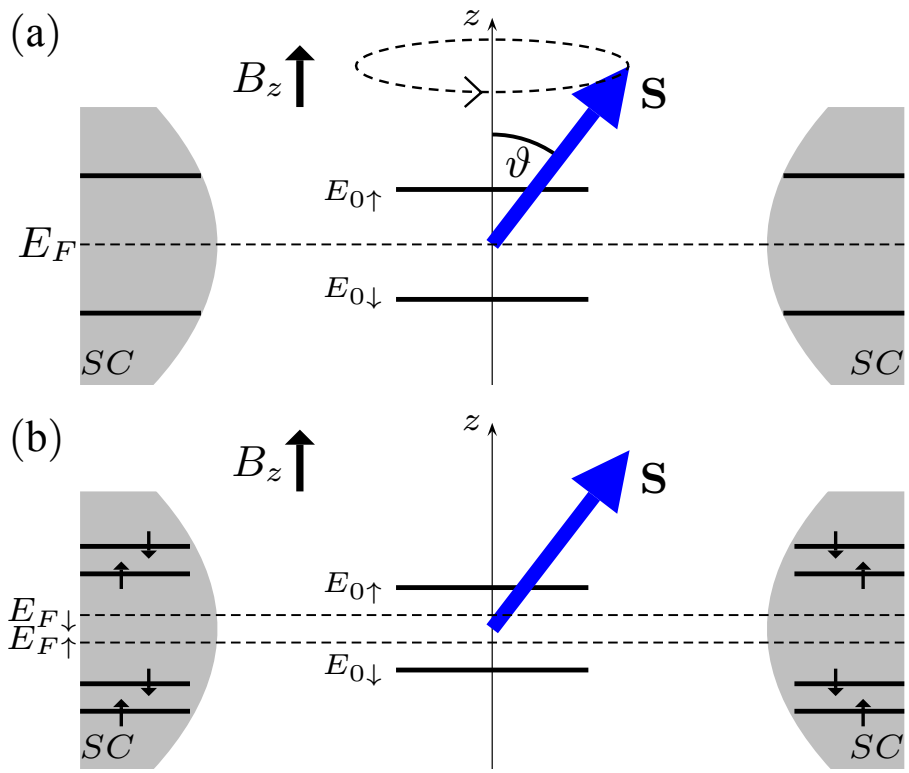

Figure 3.1: Junction with two superconducting leads and a quantum dot coupled to the spin **S** of a molecular magnet. In the laboratory frame, panel (a), the magnetic field forming an angle of ϑ with the spin, starts a precession of the spin and splits the energy level of the quantum dot into $E_{0\uparrow}$ and $E_{0\downarrow}$. In the frame of the rotating spin panel (b), the Fermi energies of the spin-up (spin-down) electrons and the quasiparticle states in the leads are shifted by $-(+)\omega_L/2$. The transformation cancels the Zeeman splitting of the quantum-dot energy level induced by the magnetic field and the finite splitting is only due to the exchange interaction.

applied along the z axis induces a Zeeman splitting of the quantum dot's energy level as well as a precession of the spin of the molecular magnet. The Hamiltonian of the junction is written as

$$\hat{H}(t) = \sum_{\alpha=L,R} \left(\hat{H}_\alpha + \hat{H}_{T\alpha}\right) + \hat{H}_D + \hat{H}_S(t) + \hat{H}_{SD}(t)\,, \tag{3.1}$$

where the index α corresponds to the left (L) or right (R) side of the junction.

The left and right superconducting leads are described by the BCS Hamiltonian $\hat{H}_\alpha = \sum_{k_\alpha\sigma} \xi_{k_\alpha} \hat{c}^\dagger_{k_\alpha\sigma}\hat{c}_{k_\alpha\sigma} + \Delta_\alpha \hat{c}^\dagger_{k_\alpha\uparrow}\hat{c}^\dagger_{-k_\alpha\downarrow} + \Delta^\dagger_\alpha \hat{c}_{-k_\alpha\downarrow}\hat{c}_{k_\alpha\uparrow}$ with $\sigma = (\uparrow,\downarrow) = \pm 1$ and the dispersion $\xi_k = \hbar^2k^2/(2m) - \mu$. The order parameter is given by $\Delta_\alpha = |\Delta_\alpha| e^{i\varphi_\alpha}$ and for symmetry reasons we assume that $\varphi_{R,L} = \pm\varphi/2$. In general, the temperature and magnetic field dependence of the order parameter must be taken into account in a self-consistent way. Since we restrict our discussion to the limit $T \ll |\Delta|$, we neglect the temperature dependence and for simplicity we assume that the applied magnetic

field does not fundamentally affect the superconducting leads. The electrons in the leads with momentum k and spin σ are created and annihilated by the operators $\hat{c}^\dagger_{k\sigma}$ and $\hat{c}_{k\sigma}$. The Hamiltonian describing the tunneling between the dot and the superconducting leads is written as $\hat{H}_{T\alpha} = \sum_{k_\alpha\sigma} \hat{d}^\dagger_\sigma V_{d_\sigma,k_\alpha} \hat{c}_{k_\alpha\sigma} + \hat{c}^\dagger_{k_\alpha\sigma} V^\dagger_{d_\sigma,k_\alpha} \hat{d}_\sigma$. The hopping V_{d_σ,k_α} describes the coupling between the dot and the leads and is assumed to be independent of energy. The operators acting on the dot correspond to $\hat{d}^\dagger_\sigma$ and $\hat{d}_\sigma$. The Hamiltonian of the dot $\hat{H}_D$ and the Zeeman energy are written as $\hat{H}_D = \sum_\sigma (E_0 + \sigma\mu_B B_z)\hat{d}^\dagger_\sigma \hat{d}_\sigma$ and $H_S(t) = -\boldsymbol{\mu}_M(t)\mathbf{B}$, with the magnetic field $\boldsymbol{B} = (0, 0, B_z)$ and the magnetic moment of the molecular magnet $\boldsymbol{\mu}_M(t)$. The magnetic moment is related to the spin of the molecular magnet via $\boldsymbol{\mu}_M(t) = -\gamma\mathbf{S}(t)$ with the gyromagnetic ratio $\gamma = g_M e/(2m)$. The Landé factor of the molecular magnet is denoted by g_M and has in principle to be determined by comparison with experiments. In the following, we assume that the Landé factor of the molecular magnet equals that of free electrons and $g_M = 2$ [85]. Due to the magnetic field, the magnetization of the molecular magnet precesses with the Larmor frequency. We assume that the motion of the spin is undamped which can be achieved by dc and rf fields [86, 87]. The equation of motion is then given by $\partial\mathbf{S}/\partial t = -\gamma\mathbf{S}\times\mathbf{B}$. The solution of this equation is $\mathbf{S}(t) = S\left(\cos(\omega_L t)\sin(\vartheta)\mathbf{e}_x + \sin(\omega_L t)\sin(\vartheta)\mathbf{e}_y + \cos(\vartheta)\mathbf{e}_z\right)$, with the magnitude of the spin $|\mathbf{S}| = S$ and the Larmor frequency $\omega_L = \gamma B_z$. The exchange interaction between the molecular magnet and the quantum dot is described by

$$\hat{H}_{SD}(t) = \frac{1}{2}\sum_{\sigma\sigma'} V_s \hat{d}^\dagger_\sigma (\mathbf{S}(t)\boldsymbol{\sigma})_{\sigma\sigma'} \hat{d}_{\sigma'}\,, \tag{3.2}$$

with the coupling V_s between the spin and the quantum dot and the Pauli matrices $\boldsymbol{\sigma} = (\sigma_x, \sigma_y, \sigma_z)$. The exchange interaction occurs due to the Pauli principle and the electrostatic interaction between the electrons on the quantum dot and the molecular magnet. Eq. (3.2) can be transformed into

$$\hat{H}_{SD}(t) = \sum_\sigma \sigma v_s \cos(\vartheta)\hat{d}^\dagger_\sigma \hat{d}_\sigma + v_s \sin(\vartheta) e^{-i\omega_L t}\hat{d}^\dagger_\uparrow \hat{d}_\downarrow + v_s \sin(\vartheta) e^{i\omega_L t}\hat{d}^\dagger_\downarrow \hat{d}_\uparrow\,, \tag{3.3}$$

with $v_s = SV_s/2$. The first term induces a spin-dependent shift of the energy levels of the dot while the second and third terms account for the spin flip of the electrons occupying the dot. Since the magnetic field enters in the Hamiltonian of the dot and the exchange interaction, we can rewrite the Hamiltonian of the dot in terms of the Larmor frequency of the molecular magnet as $\hat{H}_D = \sum_\sigma \left(E_0 + \sigma\frac{\hbar\omega_L}{2}\right)\hat{d}^\dagger_\sigma \hat{d}_\sigma$.

3.4 Approach

The transport properties of the system are described by a nonequilibrium Green's function approach [88–90]. In order to simplify the evaluation of the Green's functions, we perform a unitary transformation to the rotating frame of the molecular magnet's spin, since in this frame the Hamiltonian is time independent. The state vector transforms according to $|\tilde{\Psi}\rangle = U^\dagger|\tilde{\Psi}\rangle$ and the Hamiltonian in the rotating frame can

be written as $\bar{H} = U^\dagger H U + i\hbar(\partial_t U^\dagger)U$ with the unitary transformation operator

$$U(t) = \exp\left[-i\frac{\omega_L}{2}t\sum_{\alpha k_\alpha}\left(\hat{c}^\dagger_{k_\alpha\uparrow}\hat{c}_{k_\alpha\uparrow} - \hat{c}^\dagger_{k_\alpha\downarrow}\hat{c}_{k_\alpha\downarrow} + \hat{d}^\dagger_\uparrow\hat{d}_\uparrow - \hat{d}^\dagger_\downarrow\hat{d}_\downarrow\right)\right]. \tag{3.4}$$

In the rotating frame, the Hamilton operator (3.1) is given by

$$\bar{H} = \sum_\alpha(\bar{H}_\alpha + \bar{H}_{T\alpha}) + \bar{H}_D + \bar{H}_S + \bar{H}_{SD}\,. \tag{3.5}$$

The transformation results in a spin-dependent shift of the quasiparticles' energies in the leads and the quantum dot. The Hamiltonian of the leads reduces to

$$\bar{H}_\alpha = \sum_{k_\alpha\sigma}(\xi_{k_\alpha\sigma} - \sigma\frac{\hbar\omega_L}{2})\hat{c}^\dagger_{k_\alpha\sigma}\hat{c}_{k_\alpha\sigma} + \Delta\hat{c}^\dagger_{k_\alpha\uparrow}\hat{c}^\dagger_{-k_\alpha\downarrow} + \Delta^\dagger\hat{c}_{-k_\alpha\downarrow}\hat{c}_{k_\alpha\uparrow}\,. \tag{3.6}$$

Due to the spin-dependent energy shift, the Zeeman energy in the Hamiltonian of the dot is canceled by the transformation such that the Hamiltonian of the dot is given by $\bar{H}_D = \sum_\sigma E_0\hat{d}^\dagger_\sigma\hat{d}_\sigma$. The spin is fixed in the rotating frame and the exchange Hamiltonian is written as

$$\bar{H}_{SD} = \sum_\sigma \sigma v_s\cos(\vartheta)\hat{d}^\dagger_\sigma\hat{d}_\sigma + v_s\sin(\vartheta)\hat{d}^\dagger_\uparrow\hat{d}_\downarrow + v_s\sin(\vartheta)\hat{d}^\dagger_\downarrow\hat{d}_\uparrow\,. \tag{3.7}$$

The remaining terms of the Hamiltonian (3.1) are not affected by the transformation (3.4). Figure 3.1 (b) depicts the system in the frame of the rotating spin. The splitting of the spin-up and spin-down energy levels of the quantum dot appears because of the exchange interaction. According to the first term in Eq. (3.7) the energy shift of the spin-up (spin-down) quasiparticles in the rotating frame is given by $+(-)v_s\cos(\vartheta)$.

In order to evaluate the Green's functions of the system, we divide the structure into three subsystems, which are the left lead (L), the right lead (R), and the quantum dot (D) [91]. The spin dependence and the superconducting state are taken into account by writing the Green's functions in Nambu-spin space. Since the system is out of equilibrium, we additionally write the Green's functions in Keldysh space. In Keldysh-Nambu-spin space, the Green's functions have the structure

$$\check{G}_{\beta\beta'}(t,t') = \begin{pmatrix}\hat{G}^R_{\beta\beta'} & \hat{G}^K_{\beta\beta'}\\ 0 & \hat{G}^A_{\beta\beta'}\end{pmatrix}(t,t'). \tag{3.8}$$

The symbols $\check{}$ and $\hat{}$ denote a matrix in Keldysh-Nambu-spin and Nambu-spin space, respectively. The labels R, A, and K indicate the retarded, advanced, and Keldysh elements of the Green's function $\check{G}_{\beta\beta'}(t,t')$. The indices β and β' refer to operators in one of the three subsystems; e.g., the retarded Green's function $\hat{G}^R_{LD}$ is given by $\hat{G}^R_{LD}(t,t') = -i\theta(t-t')\langle\{\psi_L(t),\psi^\dagger_D(t')\}\rangle$, where we have introduced the operators of the quantum dot and the leads in Nambu-spin space as $\psi_D = (d_\uparrow\ d_\downarrow\ d^\dagger_\uparrow\ d^\dagger_\downarrow)^T$ and $\psi_\alpha = (c_{\alpha\uparrow}\ c_{\alpha\downarrow}\ c^\dagger_{-\alpha\uparrow}\ c^\dagger_{-\alpha\downarrow})^T$ with the index α referring to the momentum k_α in the left or right lead. The elements of the matrix in (3.8) are related by $G^< = (1/2)\left(G^K - G^R + G^A\right)$ with the lesser Green's function defined by $G^<_{DL}(t,t') = i\langle\psi^\dagger_L(t')\psi_D(t)\rangle$.

Taking into account all k states of the leads, we define the matrices $\mathbf{G}_{\beta\beta'}$ and $\mathbf{V}_{\beta\beta'}$ as $(\mathbf{G}_{\beta\beta'})_{ij} = \hat{G}_{\beta_i,\beta'_j}$ and $(\mathbf{V}_{\beta\beta'})_{ij} = \hat{V}_{\beta_i,\beta'_j}$ with the diagonal matrices

$$\hat{V}_{\alpha,d} = \begin{pmatrix} V_{d_\uparrow} & 0 & 0 & 0 \\ 0 & V_{d_\downarrow,\alpha} & 0 & 0 \\ 0 & 0 & -V_{d_\uparrow,-\alpha} & 0 \\ 0 & 0 & 0 & -V_{d_\downarrow,-\alpha} \end{pmatrix}$$

in Nambu-spin space. The indices i and j indicate all k states in the leads. The matrices (3.8) of all subsystems are then combined in an enlarged Hilbert space into one matrix defined by $\tilde{\mathbf{G}}$. The full and the unperturbed Green's function are written as

$$\tilde{\mathbf{G}} = \begin{pmatrix} \check{\mathbf{G}}_{LL} & \check{\mathbf{G}}_{LD} & \check{\mathbf{G}}_{LR} \\ \check{\mathbf{G}}_{DL} & \check{\mathbf{G}}_{DD} & \check{\mathbf{G}}_{DR} \\ \check{\mathbf{G}}_{RL} & \check{\mathbf{G}}_{RD} & \check{\mathbf{G}}_{RR} \end{pmatrix}$$

and

$$\tilde{\mathbf{G}}_0 = \begin{pmatrix} \check{\mathbf{G}}_{0L} & 0 & 0 \\ 0 & \check{\mathbf{G}}_{0D} & 0 \\ 0 & 0 & \check{\mathbf{G}}_{0R} \end{pmatrix}.$$

The coupling of the quantum dot to the leads and to the molecular magnet is given by

$$\tilde{\mathbf{V}} = \begin{pmatrix} 0 & \check{\mathbf{V}}_{LD} & 0 \\ \check{\mathbf{V}}_{DL} & \check{\mathbf{V}}_{DD} & \check{\mathbf{V}}_{DR} \\ 0 & \check{\mathbf{V}}_{RD} & 0 \end{pmatrix},$$

with $\hat{V}_{DD} = v_s\left(\hat{\sigma}_z \cos(\vartheta) + \hat{\sigma}_x \sin(\vartheta)\right)$, is treated as a perturbation. The elements containing the coupling between the quantum dot and the leads are diagonal in Keldysh space and are in Nambu space given by $\hat{V}_{\alpha,d}$.

Fourier-transforming the Dyson equation to energy space, we obtain

$$\tilde{\mathbf{G}} = \tilde{\mathbf{G}}_0 + \tilde{\mathbf{G}}_0 \tilde{\mathbf{V}} \tilde{\mathbf{G}}\,, \tag{3.9}$$

and can calculate the retarded and advanced Green's functions of the dot as

$$\hat{G}^{R/A}_{DD} = \left(1 - \hat{G}^{R/A}_{0D}\left(\hat{\Sigma}^{R/A} + \hat{V}_{DD}\right)\right)^{-1} \hat{G}^{R/A}_{0D}\,, \tag{3.10}$$

where the self-energy is defined as $\hat{\Sigma} = \hat{V}_{DL}\hat{g}_{LL}\hat{V}_{LD} + \hat{V}_{DR}\hat{g}_{RR}\hat{V}_{RD} = \hat{\Sigma}_L + \hat{\Sigma}_R$. These self-energies are obtained by summation over all quasiparticle states in the left and right leads, respectively. This summation can be replaced by the integral $\sum_{k_\alpha} \to \frac{1}{(2\pi)^3}\int d^3k_\alpha \to N_0 \int d\xi_\alpha \int \frac{d\Omega_{k_\alpha}}{4\pi}$ with the normal density of states at the Fermi energy, N_0. The integration over the quasiparticle energies in the superconductor leads to the so-called quasiclassical Green's function [see Sec. 2.2.3] which read [90, 92]

$$\hat{g}^{R/A}_\alpha = \frac{-\pi}{\sqrt{|\Delta|^2 - (E^{R/A})^2}} \begin{pmatrix} E^{R/A} & \Delta_\alpha i\sigma_y \\ i\sigma_y \Delta^*_\alpha & -E^{R/A} \end{pmatrix},$$

together with the normalization condition $\left(\hat{g}_\alpha^{R/A}\right)^2 = -\pi^2\hat{1}$. In the wide-band limit, the retarded and advanced self-energies are approximated by $\hat{\Sigma}_\alpha^{R/A} = N_\alpha|\hat{V}|^2\hat{g}_\alpha^{R/A}$ with the energy $E^{R/A}$ defined as $E^{R/A} = E \pm i\eta$ and an infinitesimal small real part $\eta \to 0$. In the rotating frame, the self-energies are given by (setting $\tilde{\omega} = \hbar\omega_L/2$)

$$\hat{\Sigma}_\alpha^R = -\Gamma_\alpha \begin{pmatrix} \frac{E^R+\tilde{\omega}}{\sqrt{|\Delta|^2-(E^R+\tilde{\omega})^2}} & 0 & 0 & \frac{-\Delta_\alpha}{\sqrt{|\Delta|^2-(E^R+\tilde{\omega})^2}} \\ 0 & \frac{E^R-\tilde{\omega}}{\sqrt{|\Delta|^2-(E^R-\tilde{\omega})^2}} & \frac{\Delta_\alpha}{\sqrt{|\Delta|^2-(E^R-\tilde{\omega})^2}} & 0 \\ 0 & \frac{-\Delta_\alpha^\dagger}{\sqrt{|\Delta|^2-(E^R-\tilde{\omega})^2}} & \frac{-(E^R-\tilde{\omega})}{\sqrt{|\Delta|^2-(E^R-\tilde{\omega})^2}} & 0 \\ \frac{\Delta_\alpha^\dagger}{\sqrt{|\Delta|^2-(E^R+\tilde{\omega})^2}} & 0 & 0 & \frac{-(E^R+\tilde{\omega})}{\sqrt{|\Delta|^2-(E^R+\tilde{\omega})^2}} \end{pmatrix}, \tag{3.11}$$

with the tunneling rates defined by $\Gamma_\alpha = \pi N_0 V_{D\alpha}^2$. The electron and hole part of the spin-up and spin-down unperturbed Green's function of the dot in Nambu-spin space is given by $(\hat{G}_{0D}^R)^{-1}_{11/22} = E^R - E_0$ and $(\hat{G}_{0D}^R)^{-1}_{33/44} = -(E^R + E_0)$. The unperturbed Green's function and the self-energy enable us to evaluate the full Green's function of the dot (3.10).

The average charge current operator in the Nambu-spin space from the left lead to the quantum dot is obtained by using the Heisenberg equation of motion

$$\hat{J}_L = -i\frac{e}{\hbar}\left\langle\left[\hat{\tilde{H}}, \hat{\tilde{N}}_L\right]\right\rangle = -i\frac{e}{\hbar}\left\langle\left[\hat{\tilde{H}}_T, \hat{\tilde{N}}_L\right]\right\rangle, \tag{3.12}$$

with the Hamilton operator $\hat{\tilde{H}}$ in the rotating frame, the number operator $\hat{\tilde{N}}_L = \frac{1}{2}\sum_{k_L}\psi_{k_L}^\dagger\hat{\sigma}_0\psi_{k_L}$ and the tunneling operator $\hat{\tilde{H}}_{T\alpha} = \frac{1}{2}\sum_{k_\alpha}\psi_{k_\alpha}^\dagger\hat{V}_{d,k_\alpha}\psi_d + \psi_d^\dagger\hat{V}_{d,k_\alpha}^\dagger\psi_{k_\alpha}$. The Josephson current (3.12) can then be written in terms of the lesser Green's function as [93]

$$J_L = \frac{e}{2\hbar}\int\frac{dE}{2\pi}\,\mathrm{Tr}\left(\hat{\sigma}_0\left(\mathbf{G}_{DL}^<\mathbf{V}_{LD} - \mathbf{V}_{DL}\mathbf{G}_{LD}^<\right)\right). \tag{3.13}$$

By using the Dyson equation (3.9) in the enlarged Hilbert space, we calculate the elements $\mathbf{G}_{DL}^<$ and $\mathbf{G}_{LD}^<$ with the help of the relation $G^< = (1/2)\left(G^K - G^R + G^A\right)$. The results are [94]

$$\mathbf{G}_{DL}^< = \mathbf{G}_{DD}^<\mathbf{V}_{DL}\mathbf{g}_{LL}^A + \mathbf{G}_{DD}^R\mathbf{V}_{DL}\mathbf{g}_{LL}^<, \tag{3.14}$$

$$\mathbf{G}_{LD}^< = \mathbf{g}_{LL}^<\mathbf{V}_{LD}\mathbf{G}_{DD}^A + \mathbf{g}_{LL}^R\mathbf{V}_{LD}\mathbf{G}_{DD}^<. \tag{3.15}$$

The Josephson current then simplifies to

$$J_L = \frac{e}{\hbar}\int\frac{dE}{2\pi}\,\mathrm{Re}\left[\mathrm{Tr}\,\hat{\sigma}_0\left(\hat{G}_{DD}^R\hat{\Sigma}_L^< + \hat{G}_{DD}^<\hat{\Sigma}_L^A\right)\right]. \tag{3.16}$$

The Green's function $\hat{G}_{DD}^<$ is obtained from the Keldysh equation by $\hat{G}_{DD}^< = \hat{G}_{DD}^R\hat{\Sigma}^<\hat{G}_{DD}^A$ with $\hat{\Sigma}^< = \hat{\Sigma}^R\hat{F} - \hat{F}\hat{\Sigma}^A$. Due to the transformation to the rotating frame, the effective Fermi energy in Nambu-spin space is shifted and $\hat{F}$ is given by

$$\hat{F} = \begin{pmatrix} f(E+\tilde{\omega}) & 0 & 0 & 0 \\ 0 & f(E-\tilde{\omega}) & 0 & 0 \\ 0 & 0 & f(E-\tilde{\omega}) & 0 \\ 0 & 0 & 0 & f(E+\tilde{\omega}) \end{pmatrix} \tag{3.17}$$

with the Fermi function $f(E) = 1/(1 + \exp(E/k_BT))$.

3.5 Results

The charge transport properties of the junction can now be investigated. In principle, the current is given by two contributions. The first is the current carried by Andreev states whose energies lie within the superconducting gap. The second contribution is carried by continuum states outside the superconducting gap. Before we consider the transport properties in the junction, it is instructive to discuss first the density of states of the quantum dot and the behavior of the Andreev levels for different parameters.

3.5.1 Density of states of the quantum dot

The density of state of the quantum is calculated by (see Eq. (2.23))

$$N(E) = -\frac{1}{\pi}\mathrm{Im}\,\mathrm{Tr}\,\sigma_0\hat{G}_D^R(E)\,. \tag{3.18}$$

Figure 3.2 shows the spin-resolved density of states of the quantum dot at $\varphi = \pi/2$, $E_0 = 0$ and a symmetric coupling to the leads with $\Gamma = \Gamma_L = \Gamma_R = 0.1\Delta$. For clarity, we choose a small coupling to the leads to prevent an overlap of the Andreev states with the continuum states. In panel (a), we consider a static magnetization of the molecular magnet in the z direction ($\omega_L = 0, \vartheta = 0$). The exchange interaction between the molecular magnet and the quantum dot lifts the spin degeneracy and shifts the energy level of the quantum dot in the rotating frame by $\pm v_s$ for spin-up and spin-down electrons, respectively. Therefore, the spin-up energy level, which is broadened by Γ, is closer to the upper superconducting gap edge increasing the density of the spin-up continuum states for $E > \Delta$ whereas the density of the spin-down continuum states is decreased. The exchange interaction also lifts the spin degeneracy of the Andreev states and shifts the states E_I and E_{II} (E_{III} and E_{IV}) of the spin-up (spin-down) quasiparticles to higher (lower) energies. For the parameters in panel (a), the exchange coupling pushes both spin-up (spin-down) states above (below) $E = 0$.

In panel (b), a magnetic field is applied in addition to the exchange coupling of the molecular magnet and the quantum dot. The magnetic field shifts the continuum states by $-(+)\omega_L/2$ for spin-up (spin-down) electrons due to the transformation in the rotating frame and also slightly pushes the Andreev states towards $|E| \to 0$ compared to panel (a). If the magnetization points in an arbitrary direction ($\vartheta \neq 0$), the electrons can undergo spin flips into sidebands separated by the energy ω_L according to the Hamiltonian (3.1). In the frame of the rotating spin, the transformation compensates the exchange of energy and the electrons are scattered into states at the same energy. In panel (c), $\vartheta = \pi/4$ and the Andreev states as well as the continuum states can be occupied with spin-up and spin-down electrons, respectively. In panel (d), $\vartheta = \pi/2$, the magnetization is precessing in the xy plane and the density of the scattered states increases.

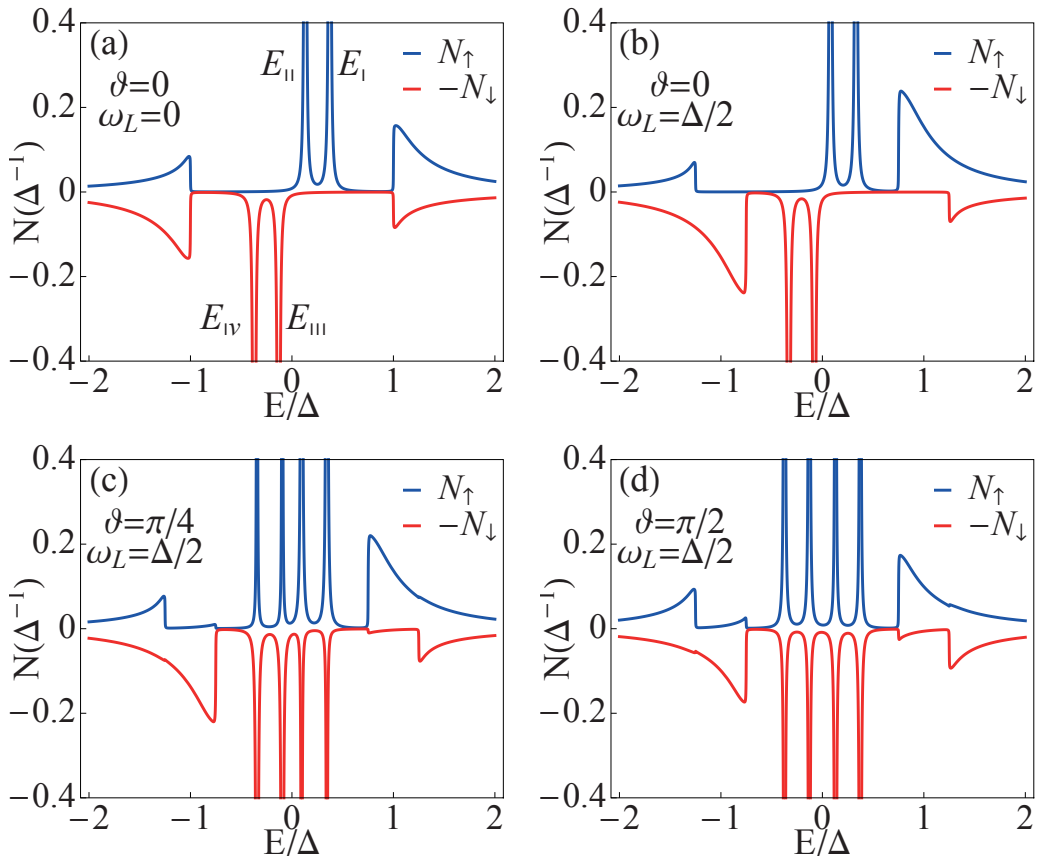

Figure 3.2: Spin-resolved density of states of the quantum dot. In (a) and (b), $v_s = 0.3\Delta$ and $\vartheta = 0$. In (b) a magnetic field of $\omega_L = \Delta/2$ is applied, shifting the continuum states of the spin-up (spin-down) electrons by $\pm\omega_L/2$. In (c) and (d), $\vartheta \neq 0$ and an electron on the quantum dot can change its spin direction such that the states of the spin-up and spin-down electrons are mixed. In (d), the magnetization is precessing in the plane ($\vartheta = \pi/2$). The other parameters in (a)-(d) are $\varphi = \pi/2$, $\Gamma = 0.1\Delta$, $E_0 = 0$, and $\eta = 10^{-3}\Delta$.

The complete parameter dependence of the Andreev states in the central region are obtained by the poles of the Green's function in Eq. (3.10) which are given by

$$\mathcal{A}_+\mathcal{A}_- - \mathcal{B} = 0\,. \tag{3.19}$$

Using the notation $\tilde{\omega} = \omega_L/2$, the elements are

$$\mathcal{A}_\pm = \left((E \mp v_s\cos\vartheta)\sqrt{\Delta^2 - (E \pm \tilde{\omega})^2} + 2\Gamma(E \pm \tilde{\omega})\right)^2 - 4\Gamma^2\Delta^2\cos^2(\varphi/2) - E_0^2\left(\Delta^2 - (E \pm \tilde{\omega})^2\right)\,,$$

and

$$\mathcal{B} = v_s^2 \sin^2\vartheta \sqrt{(\Delta^2-(E-\tilde{\omega})^2)(\Delta^2-(E+\tilde{\omega})^2)}$$
$$\Big[8\Gamma^2\left(\Delta^2\cos^2(\varphi/2)+\left(E^2-\tilde{\omega}^2\right)\right)+\sqrt{\Delta^2-(E-\tilde{\omega})^2}\sqrt{\Delta^2-(E+\tilde{\omega})^2}\left(-v_s^2\sin^2\vartheta\right.$$
$$\left.+2\left(E^2+E_0^2-v_s^2\cos^2\vartheta\right)\right)+4\Gamma\Big((E+\tilde{\omega})(E+v_s\cos\vartheta)\sqrt{\Delta^2-(E-\tilde{\omega})^2}$$
$$+(E-\tilde{\omega})(E-v_s\cos\vartheta)\sqrt{\Delta^2-(E+\tilde{\omega})^2}\Big)\Big].$$

The pole equation (3.19) reduces to that of Ref. [95], if the quantum dot does not interact with the molecular magnet and no magnetic field is applied ($v_s = \tilde{\omega} = 0$). In this case $\mathcal{A}_+$ is equal to $\mathcal{A}_-$ and $\mathcal{B} = 0$. If no magnetic field is applied, the ϑ dependence of the Andreev states vanishes since no spin-quantization axis is preferred. In this limit, the equation of the Andreev states agrees with the result in Ref. [66]. If $\vartheta = \pi/2$, the spin precesses in the xy plane and the equation of the Andreev states is symmetric with respect to $\omega_L \to -\omega_L$. Additionally, the Andreev states are symmetric under the transformation $E_0 \to -E_0$.

In the limit $E \ll \Delta$, the equation of the Andreev states can be explicitly solved with the result

$$E_{I,II} \approx \frac{1}{v}\left(\pm\sqrt{\frac{\left(2\Gamma\Delta\cos(\varphi/2)\right)^2}{\Delta^2-\tilde{\omega}^2}+E_0^2}\right.$$
$$\left.+\sqrt{\left(v_s\cos(\vartheta)-\frac{\Gamma\omega}{\sqrt{\Delta^2-\tilde{\omega}^2}}\right)^2+v_s^2\sin^2(\vartheta)}\right) \tag{3.20}$$

and

$$E_{III,IV} \approx \frac{1}{v}\left(\pm\sqrt{\frac{\left(2\Gamma\Delta\cos(\varphi/2)\right)^2}{\Delta^2-\tilde{\omega}^2}+E_0^2}\right.$$
$$\left.-\sqrt{\left(v_s\cos(\vartheta)-\frac{\Gamma\omega}{\sqrt{\Delta^2-\tilde{\omega}^2}}\right)^2+v_s^2\sin^2(\vartheta)}\right) \tag{3.21}$$

with $v = \sqrt{|\Delta|^2-\tilde{\omega}^2}/\left(\sqrt{|\Delta|^2-\tilde{\omega}^2}+2\Gamma\right)$. In general, however, the Andreev states must be calculated numerically from Eq. (3.19) and are shown in Fig. 3.3. In panel (a), the spin degeneracy is lifted due to the exchange interaction between the quantum dot and the molecular magnet. The spin-up (spin-down) electrons are shifted to higher (lower) energies. Since the Andreev states lie well inside the energy gap, we can use Eqs. (3.20) and (3.21) to find expressions for the splitting of the Andreev states. The displacement of the Andreev states in panel (a) due to the exchange interaction is given by $\pm v_s/(\Delta+2\Gamma)$. The exchange interaction shifts the Andreev states across the Fermi energy, which from Eq. (3.17) is located at $E = 0$ at $T = 0$. Therefore, the

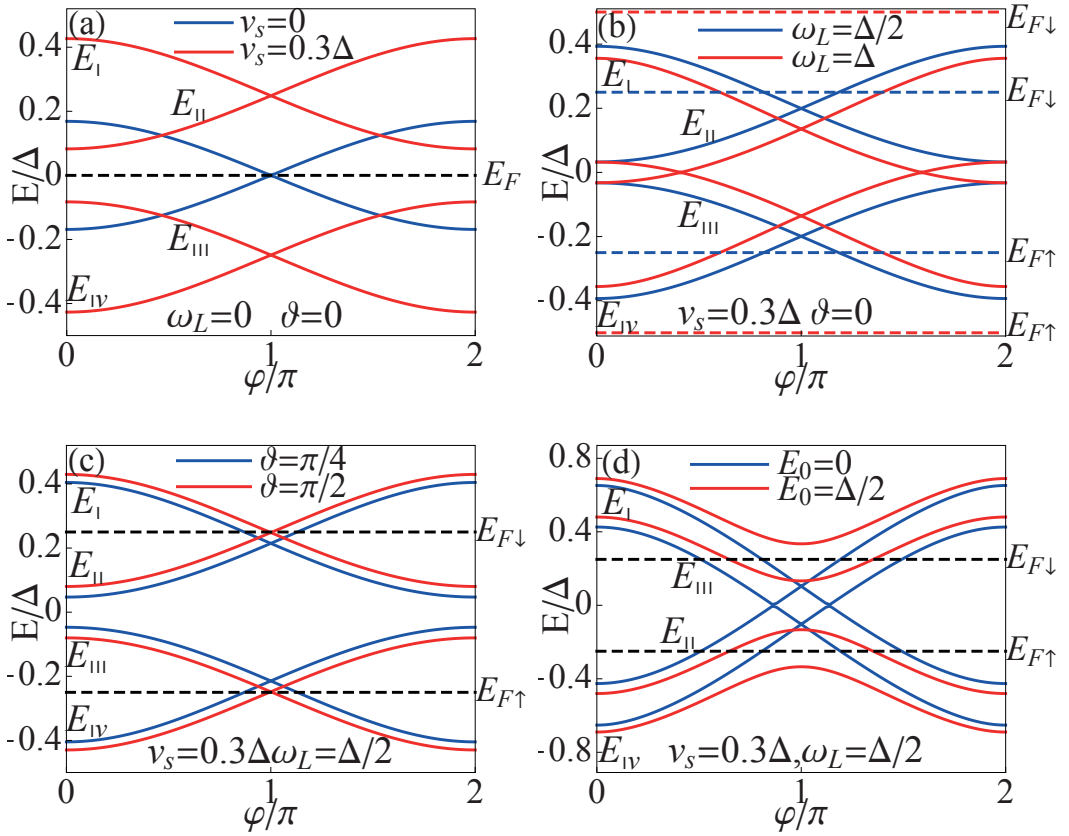

Figure 3.3: Phase dependence of the Andreev states. In (a)-(c), $\Gamma = \Delta/10$ and $E_0 = 0$. In (a), the exchange coupling v_s splits the Andreev state into spin-up and spin-down states. The effect of a finite ϑ is shown in (c). Panel (d) shows the Andreev states for $\Gamma = \Delta/2$, $\vartheta = \pi/4$, and a position of the energy level on the dot of $E_0 = 0$ and $E_0 = \Delta/2$. The dashed lines indicate the effective Fermi energies of the spin-up and spin-down quasiparticles at zero temperature.

current is expected to be strongly modified in panel (a) if the coupling v_s is increased. An applied magnetic field counteracts the shift of the Andreev states induced by the exchange interaction, v_s. The combined shift of the Andreev states due to v_s and ω_L is given by $\pm(1/v)(v_s - \Gamma\tilde{\omega}/(\sqrt{\Delta^2-\tilde{\omega}^2}))$. The effective Fermi energies in panel (b) at $T = 0$ and $\omega_L = \Delta/2$ are located at the energies $-(+)\omega_L/2$ for spin-up (spin-down) electrons. In this case, both spin-up Andreev states are shifted above the effective Fermi energy $E_{F\uparrow}$, whereas both spin-down Andreev states are below the effective Fermi energy $E_{F\downarrow}$. The effect of ϑ on the Andreev states is shown in panel (c). Now, all Andreev states below $E_{F\downarrow}$ ($E_{F\uparrow}$) are occupied with spin-down (up) electrons similarly to the situation of the density of states in Figs. 3.2(c) and (d). In Fig. 3.2(d), $\Gamma = \Delta/2$ and the shift of the Andreev states due to Γ is larger than the splitting due to v_s such that at $\varphi = 0$ the states E_{II} and E_{IV} are below the effective Fermi energy $E_{F\downarrow}$ and the states E_I and E_{III} are above the effective Fermi energy $E_{F\uparrow}$.

3.5.2 Current-phase relations

The Andreev states discussed in the last section carry the Josephson current $I_n(\varphi)$. The contribution to the current of each Andreev state $E_n(\varphi)$ is proportional to the derivative of the Andreev state with respect to the phase multiplied with the Fermi function at the energy of the Andreev state [96],

$$I_n(\varphi) = \frac{e}{\hbar} f(E_n(\varphi)) \frac{dE_n(\varphi)}{d\varphi} \,. \tag{3.22}$$

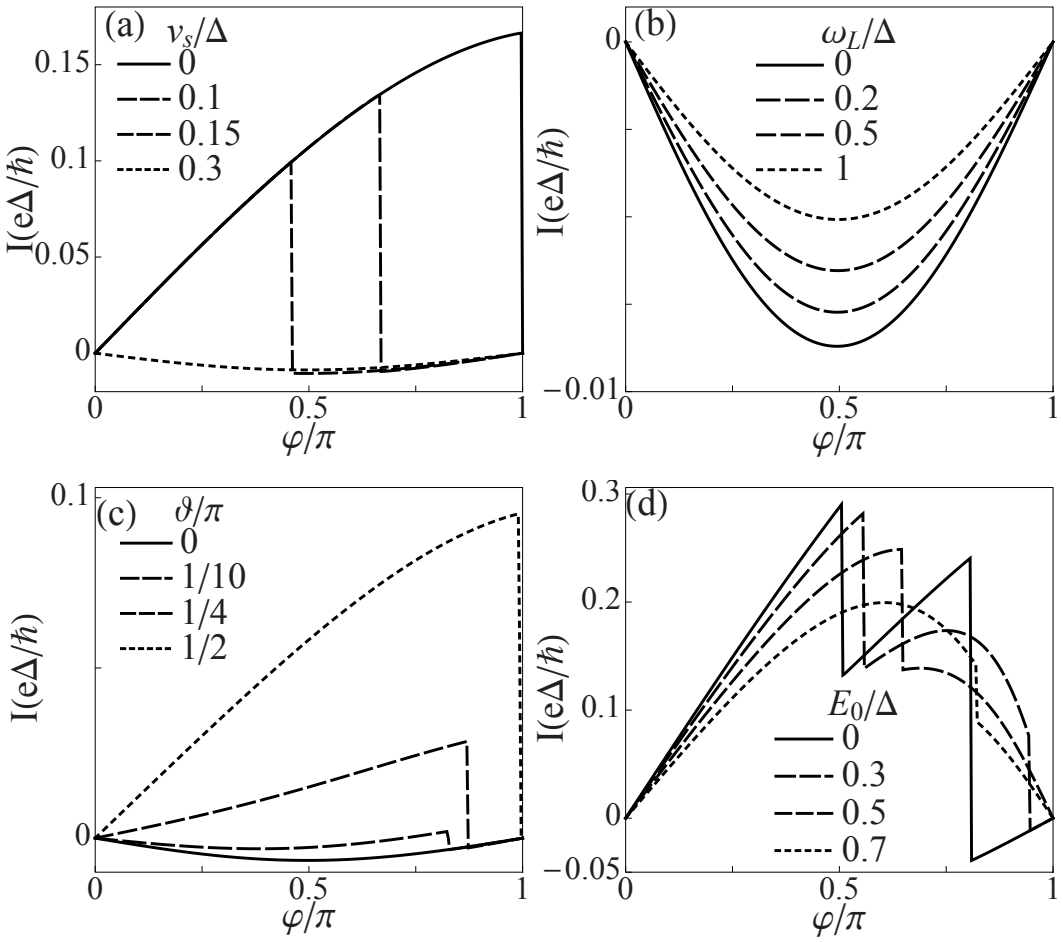

Figure 3.4: Current-phase relations for $\Gamma = \Delta/10$ and $E_0 = 0$ [(a)-(c))]. In (a) $\omega_L = 0$, $\vartheta = 0$, and v_s varies from 0 to 0.3Δ. The values correspond to the Andreev states of Fig. 3.3(a), where the current is strongly suppressed due to the shift of the Andreev states across the Fermi energy. In (b), $v_s = 0.3\Delta$, $\vartheta = 0$ and ω_L varies from 0 to Δ. In (c), $v_s = 0.3\Delta$, $\omega_L = \Delta/2$ and ϑ varies from 0 to $\pi/2$. In (d), $v_s = 0.3\Delta$, $\omega_L = \Delta/2$, $\vartheta = \pi/4$, $\Gamma = \Delta/2$ and E_0 is varied. The temperature is set to $k_B T = 10^{-4}\Delta$ and $\eta = 10^{-4}\Delta$.

The Josephson current is then given by the summation over all Andreev states n.

In the following, we discuss the current-phase relation obtained by Eq. (3.16) in the low temperature limit $k_BT = 10^{-4}\Delta$. Eq. (3.16) contains the contribution to the current from Andreev (Eq. (3.22)) as well as the continuum states. Figure 3.4 (a) shows the current-phase relation of a static spin in the z direction ($\vartheta = 0$) and zero magnetic field ($\omega_L = 0$) and four different values of v_s. The Andreev states corresponding to the values of $v_s = 0$ and $v_s = 0.3\Delta$ are depicted in Fig. 3.3(a). At $v_s = 0$, the spin-degenerate Andreev state below the Fermi energy E_F carries a positive current for $\varphi < \pi$ according to relation (3.22). If the exchange coupling is increased to $v_s = 0.3\Delta$, the contributions from the currents of both current-carrying Andreev states E_{III} and E_{IV} in Fig. 3.3 (a) cancel whereas the Andreev states E_I and E_{II} are completely unoccupied above the Fermi energy. In this case, the current is strongly suppressed since in total the Andreev states do not contribute to the current and the current is carried by the continuum states giving rise to a π state of the junction. Between $v_s = 0$ and the complete shift of the E_{III} state below the Fermi energy, the current-phase relation sharply decreases at phases where the E_{III} level intersects the Fermi energy. These phases are determined from Eq. (3.19) to $\varphi = 2\arccos(v_s/2\Gamma)$. At phases larger than $2\arccos(v_s/2\Gamma)$, a negative current appears due to the continuum states since the Andreev-state contributions to the current cancel.

Figure 3.4(b) shows the current-phase relation for the same parameters as in panel (a) at $v_s = 0.3\Delta$ and $\vartheta = 0$, but the magnetic field is increased from $\omega_L = 0$ to $\omega_L = \Delta$. The Andreev states corresponding to the current-phase relation at $\omega_L = \Delta/2$ and $\omega_L = \Delta$ are depicted in Fig. 3.3(b). For the parameters chosen in Fig. 3.4(b), the spin-up (spin-down) Andreev states do not cross the corresponding effective Fermi energy $E_{F\uparrow}$ ($E_{F\downarrow}$) and no sharp change of the current is observed. The Andreev states E_I and E_{II} [Fig. 3.3(b)], which carry spin-up electrons, are for all values of ω_L in Fig. 3.4(b) above the effective Fermi energy $E_{F\uparrow}$ and therefore do not contribute to the current. The Andreev states E_{III} and E_{IV} carrying spin-down electrons are both below the effective Fermi energy $E_{F\downarrow}$ and do not contribute either due to current cancellation of the E_{III} and E_{IV} states. Therefore, only the continuum states give rise to a current such that the junction is in the π state.

In Fig. 3.4(c), the current-phase relation is shown for the same parameters as in panel (b) at $\omega_L = \Delta/2$ but the angle ϑ increases from 0 to $\pi/2$. Since the electrons on the quantum dot can undergo spin flips at finite ϑ, the Andreev states in the rotating frame are degenerate and we have to take into account four spin-degenerate Andreev states following from the density of states in Fig. 3.2(c) and 3.2(d). The Andreev states corresponding to the current-phase relation in Fig. 3.4(c) at $\vartheta = \pi/4$ and $\vartheta = \pi/2$ are shown in Fig. 3.3(c). At $\vartheta = 0$, the current is the same as in panel (b) at $\omega_L = \Delta/2$ where E_I and E_{II} are empty while E_{III} and E_{IV} are occupied with spin-down electrons and therefore the Andreev states do not contribute to the current. If ϑ is increased, spin-down (spin-up) electrons are scattered into E_I and E_{II} (E_{III} and E_{IV}) states. The particles scattered into the E_{II} and E_{IV} states are below the corresponding effective Fermi energy $E_{F\downarrow}$ and $E_{F\uparrow}$, respectively. These

two states give a positive contribution and therefore a finite ϑ increases the current. The sharp step for phases close to π of the current-phase relation appears because an

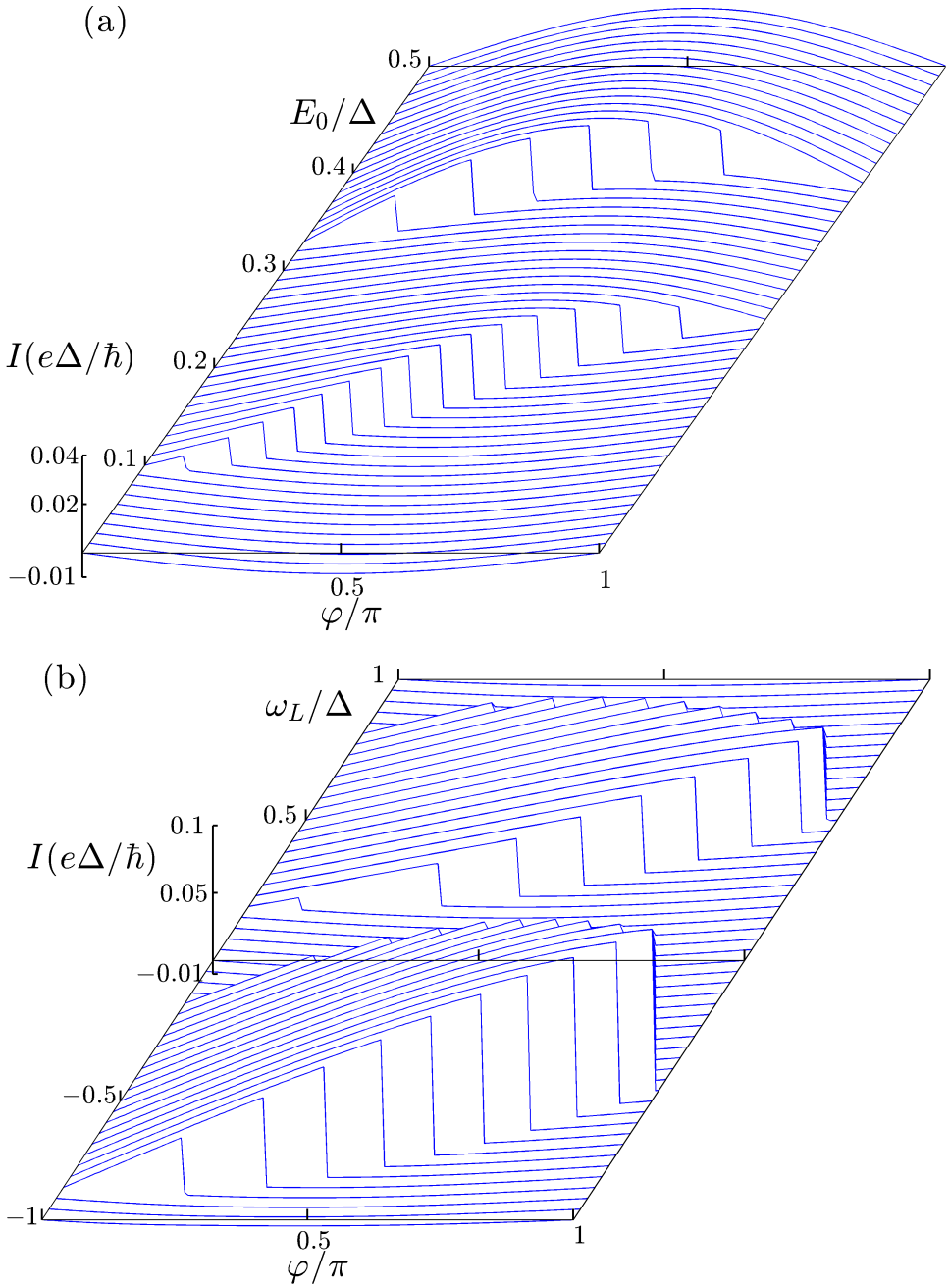

Figure 3.5: Current-phase relation for $v_s = 0.1\Delta$, $\vartheta = \pi/4$, $\omega_L = \Delta/2$ (a). By changing E_0, the state changes from a 0 to a π state. In (b), $E_0 = 0$, $v_s = 0.3\Delta$, and $\vartheta = 0.4\pi$. The magnetic field changes from $\omega_L = -\Delta$ to $\omega_L = \Delta$. In both panels $\Gamma = \Gamma_L = \Gamma_R = 0.1\Delta$, $k_BT = 10^{-4}\Delta$ and, $\eta = 10^{-4}\Delta$.

Andreev state crosses the Fermi energy, similarly as in panel (a). For $\Gamma = \Delta/2$, the current-carrying Andreev states cross the Fermi energy twice thus leading to the two steps in the current-phase relation as shown in panel (d). A finite E_0 opens a gap of the Andreev states at $\varphi = \pi$.

So far we have discussed the current-phase relations of the Andreev states shown in Fig. 3.3. We now consider how the 0 to π transition and the reverse process are driven by E_0 or ω_L. The current-phase relation as a function of E_0 is shown in Fig. 3.5 (a). The state changes from a π junction at $E_0 = 0$ to a 0 junction at $E_0 = \Delta$. The current increases stepwise as a function of φ, but the position of this stepwise increase changes as a function of E_0. This behavior appears twice, since the spin degeneracy of the Andreev states is lifted due to the exchange interaction. Since the current is symmetric under the transformation $E_0 \to -E_0$, the same transition is driven by decreasing E_0 from $E_0 = 0$ to $E_0 = -\Delta$. In panel (b) of Fig. 3.5, the current-phase relation is evaluated as a function of ω_L. If the magnetic field is increased from $\omega_L = -\Delta$ to $\omega_L = 0$, the junction is driven from a π to 0 and back to a π state. Since the Andreev states are symmetric under the transformation $\omega_L \to -\omega_L$ if $\vartheta = 0.5\pi$ (Sec. 3.5.1), the Josephson current shows a similar behavior if ϑ approaches 0.5π.

3.5.3 Critical current

As we discussed in the previous section, different parameters can drive the junction from a 0 to a π state or vice versa. In order to further investigate the transport properties, we consider the critical current, which is experimentally more easily accessible than the current-phase relation.

Figure 3.6 shows the critical current as a function of the energy level at $\omega_L =$

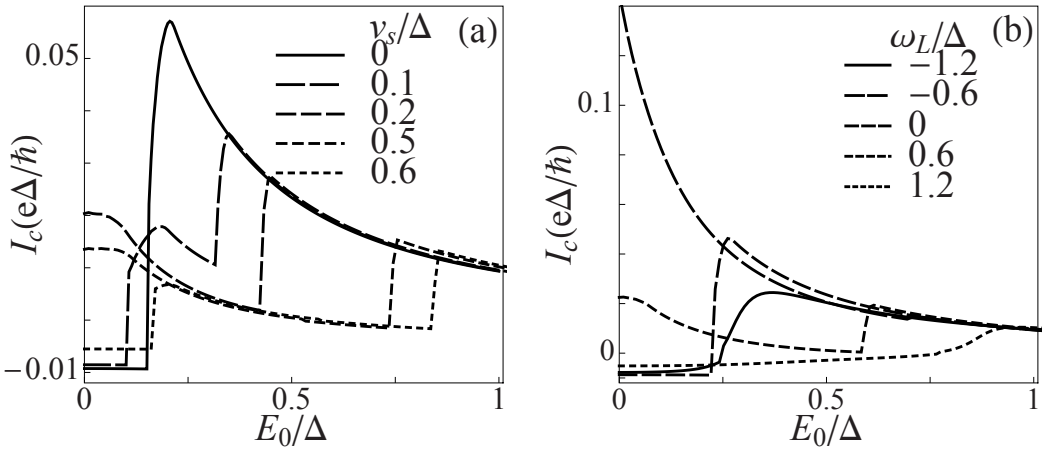

Figure 3.6: Critical current as a function of E_0. The parameters in (a) correspond to Fig. 3.3(c) for different exchange couplings at $\vartheta = \pi/4$ and $\omega_L = \Delta/2$. In (b), $v_s = 0.3\Delta$ and $\vartheta = \pi/4$. In both panels $\Gamma = \Delta/10$ and $k_BT = 10^{-4}\Delta$.

$\Delta/2$ and different couplings v_s in panel (a). For small E_0, the state of the junction undergoes a π to 0 transition by increasing v_s and finally goes back to the π state. If the junction is in a π state at E_0, a transition is driven to the 0 state by increasing E_0 for all values of the exchange coupling shown in panel (a). The critical current at $v_s = 0.1\Delta$ in the range of $E_0 = 0$ to $E_0 = \Delta/2$ corresponds to the maximal current of each current phase relations shown in Fig. 3.5 (a). The sharp increase of the critical current occurs due to the shift of Andreev states across the Fermi energy within a small parameter range of E_0. In panel (b), $v_s = 0.3\Delta$ and the critical current is depicted for different values of ω_L. Again, by increasing E_0, the junction undergoes a π to 0 transition at $\omega_L = 0$ and $\omega_L = \pm 1.2\Delta$. In addition, the junction also exhibits multiple transitions for $E_0 \simeq \Delta/2$ as ω_L is increased.

Contour plots of the critical current are depicted in Fig. 3.7. In all panels, we assume a symmetric coupling between the quantum dot and the leads and calculate

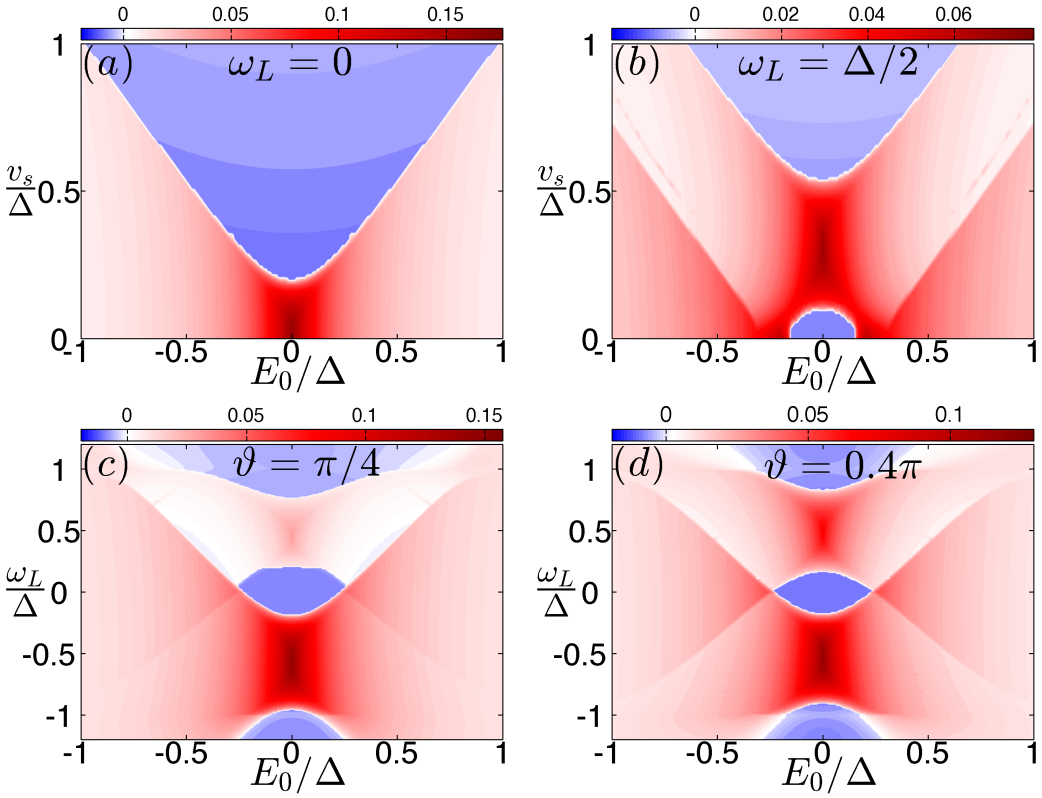

Figure 3.7: Critical current I_c in units of $e\Delta/\hbar$ as a function of E_0 and v_s at $\vartheta = \pi/4$ [(a) and (b)]. In (a) $\omega_L = 0$ and in (b) $\omega_L = \Delta/2$. In (c) and (d), the critical current is shown as a function of E_0 and ω_L at $v_s = 0.3\Delta$. The angle ϑ varies from $\vartheta = \pi/4$ in (c) to $\vartheta = 0.4\pi$ in (d). The other parameters are $\Gamma = \Gamma_L = \Gamma_R = 0.1\Delta$ and $k_B T = 10^{-4}\Delta$.

the critical current in the low-temperature limit. In (a) and (b), the critical current is plotted as a function of E_0 and v_s at $\vartheta = \pi/4$ and the magnetic field is set to $\omega_L = 0$ in (a) and $\Delta/2$ in (b). In panel (a), the junction exhibits a 0 to π transition due to an increase of the exchange coupling, v_s. In this case, the contribution to the current of the Andreev states does not depend on ϑ since the magnetic field is zero. The Andreev states intersect the Fermi function at $v_s = \pm\sqrt{4\Gamma^2 \cos(\varphi_{\max}/2)^2 + E_0^2}$, with the phase $\varphi_{\max}$ corresponding to the phase at the critical current. At these values of the exchange coupling, the junction exhibits the transition. If $v_s \geq 2\Gamma|\cos(\varphi_{max}/2)|$, the junctions also exhibits π to 0 transitions as a result of increasing E_0. In panel (b), the magnetic field is set to $\omega_L = \Delta/2$ and the Andreev states are degenerate due to the spin-flip scattering. The parameters in this panel correspond to the critical current shown in Fig. 3.6(a). Transitions are driven by either increasing E_0 or v_s. Due to the redistribution of the occupied states at finite ω_L, the critical current exhibits an additional step which is due to a shift of the Andreev states across the Fermi energy. In panels (c) and (d), the critical current is shown as a function of E_0 and ω_L at $v_s = 0.3\Delta$ and ϑ changes from $\vartheta = \pi/4$ to $\vartheta = 0.4\pi$. Due to the spin-flip term, the critical current shows a mirror structure around $\omega_L = 0$ with different intensities for $\omega_L \to -\omega_L$. As discussed in Sec. 3.5.1, the Andreev states are symmetric with respect to $\omega_L \to -\omega_L$ at $\vartheta = 0.5\pi$. Therefore, the critical current shows a symmetric behavior as a function of ω_L since ϑ is close to 0.5π. For small E_0, the junctions exhibits multiple transitions as a function of the magnetic field.

3.6 Conclusions

We have studied the electronic transport in the low-temperature limit of a Josephson junction consisting of two superconducting leads and a quantum dot connected to a molecular magnet. The effect of electronic interactions is taken into account in an effective way and can be extended to a more realistic description of the quantum dot. The exchange interaction lifts the spin degeneracy of the energy level of the dot as well as of the Andreev states.

The current-phase relation shows a strong modification when an Andreev state intersects the Fermi energy and the Josephson junction can be driven into the π state by the exchange interaction [Fig. 3.4(a)]. A magnetic field applied to the central region induces a Zeeman energy of the electrons on the quantum dot and a precession of the molecular magnet's magnetization. As a result, an electron on the dot can undergo spin-flip scattering and the occupation of the Andreev states is redistributed by the magnetic field. The redistribution depends on the orientation between the magnetic field and the magnetization of the molecular magnet and can lead to an increase in the current-phase relation [Fig. 3.4(c)] when the electron-like quasiparticles are scattered into states below the Fermi energy carrying the current in positive direction. The results in Figs. 3.4(a) and (c) are in particular interesting to extract the exchange interaction or the orientation of the molecular magnet's magnetization from a measurement of the current-phase relation.

Figures 3.4(b,d) and 3.5 shows the dependence of the current-phase relation on the magnetic field and gate voltage. Experimentally, the Josephson current can be

controlled by these parameters. For instance, Fig. 3.5(b) shows that a magnetic field can tune the state of the Josephson junction from a 0 to π-state.

The critical current in Fig. 3.7 shows the possibility to observe multiple transitions as a function of a gate voltage which changes the energy level of the dot. Multiple transitions are also obtained if the magnetic field is swept around zero. However, in a more realistic system the dependence of the superconducting gap on the magnetic field must be taken into account in a self-consistent way.

In principle, the results of the chapter can be used in two ways. First, the measurement of the physical magnitudes of either the energy of Andreev levels, the current-phase relation, or the critical current allows one to reveal the internal structure of the Josephson junction. Different parameters are possible to extract from measurements such as the strength of the exchange interaction. Second, the presence of the molecular magnet offers the possibility to manipulate the current through the junction by changing the parameters such as the energy level of the dot or the magnetic field. This manipulation strongly affects the Andreev states which allows possible application in quantum computation [56, 58].

4 Control of vibrational states by spin-polarized current

4.1 Abstract

We study spin-dependent transport in a suspended carbon nanotube quantum dot in contact with two ferromagnetic leads and with the dot's spin coupled to the flexural mechanical modes. The spin-vibration interaction induces spin-flip processes between the two energy levels of the dot. This interaction arises from the spin-orbit coupling or a magnetic field gradient. The inelastic vibration-assisted spin flips give rise to a mechanical damping and, for an applied bias voltage, to a steady nonequilibrium occupation of the harmonic oscillator.

We analyze the nonequilibrium occupation as function of the energy-level separation of the dot and the magnetic polarization of the leads. The main results is that a spin-polarized current at finite bias voltage causes either active cooling or energy pumping of the mechanical modes. In the cooling regime, maximal cooling is achieved at resonant transport when the energy splitting between two dot levels of opposite spin equals the vibrational frequency ω. Even for weak electron-resonator coupling and moderate polarizations ($p \simeq 0.5$) we can achieve ground-state cooling with a high temperature of the leads, for instance, of $T \sim 10 - 50\omega$. In the opposite regime of energy pumping, we find that within our approximation, the system approaches a regime of mechanical instability. Furthermore, owing to the sensitivity of the electron transport to the spin orientation, we find signatures of the nanomechanical motion in the current-voltage characteristic. Hence, the vibrational state can be read out in transport measurements.

4.2 Introduction

Advances in the fabrication of NEMS [97, 98] have opened the possibility to measure extremely small forces and masses [99, 100]. As the displacements of mechanical vibrations are conveniently registered by electron transport measurements, NEMS may prove also useful technologically as ultra-sensitive detectors of charge [101] and spin [102].

Moreover, high-frequency NEMS devices operating at cryogenic temperatures can themselves approach the quantum regime and pave the way for testing quantum mechanics in solid objects formed by a macroscopic number of atoms [103–105]. In fact, recent experiments already cooled a mechanical mode to its quantum ground state in different types of nanomechanical oscillators [26, 27, 106].

Furthermore, a common and promising strategy to enter the quantum mechanical

regime consists in interfacing the mechanical degree of freedom with an elemental quantum object, i.e., a quantum two-level system such as superconducting Josephson qubits [107], single Andreev levels [108, 109] or single spins [110, 111]. A successful accomplishment of this strategy was reported for a nanomechanical dilatation oscillator coupled to a phase-qubit [28]. This experiment and others motivate the interest in hybrid quantum nano systems containing nanomechanical oscillators approaching the quantum regime [112, 113].

Concerning spin-oscillator systems, a variety of nanomechanical devices have been proposed. For instance, in magnetic resonance force microscopy experiments, a mechanical cantilever with a ferromagnetic tip can detect single spins in solid samples [102, 114–116]. Alternatively, the spin can be exploited for sensing the mechanical motion as for instance in experiments with nitrogen vacancy centers [117, 118]. The interplay between mechanical motion and spin transport has been analyzed in nanomechanical torsion oscillators [119–122] in which a change of the angular momentum (spin flip) of the itinerant electron creates a mechanical torque similar to the Einstein-de Haas effect. In another recent experiment [123], the magnetization reversal of a single-molecule magnet attached to a suspended carbon nanotube (CNT) [124] was probed by electrical transport measurements.

Suspended CNTQDs [125–135] have been discussed as a suitable playground for the realization of a coherent quantum spin-vibration system. The spin of discrete electron levels on the dot can couple to the flexural vibration via an extrinsic mechanism under a magnetic field [136] or via the intrinsic spin-orbit interaction [137–141]. Similar mechanisms were discussed in double dot systems [142, 143]. Remarkably, CNTQDs play also a crucial role in spintronics. Indeed, spin-current injection has been experimentally reported in CNTs in a spin-valve geometry with gate-field control [144–147].

To conclude the state of this field, we emphasize that the interplay between nanomechanical effects and spin-dependent transport can lead to interesting phenomena as mechanical self-excitations [148], shuttle mechanism controlled by external magnetic field [149], phonon lasing [150] or cooling of mechanical vibrations [151–153].

Motivated by the growing interest in combining nanomechanics with spintronics, we discuss in this chapter the effects of the spin-vibration interaction when a suspended CNTQD is sandwiched between two ferromagnets and a bias-voltage is applied (see Fig. 4.1). We consider a model with a single mechanical (flexural) mode of frequency ω. We show that spin-polarized electrons tunneling through the CNTQD can exchange energy with the oscillator by flipping the spin. Such vibration-assisted spin-flip processes give rise to a mechanical damping of the oscillator and to inelastic transport through the CNTQD. Concurrently, when electric current flows through the CNTQD, the oscillator is also driven towards a steady, non-thermally equilibrated regime in which the average energy stored into the oscillator is larger ("heating") or smaller (cooling) than the thermal energy. This corresponds to a phonon occupation different from the thermal Bose distribution at the lattice temperature.

When the oscillator is heated, the damping coefficient can also vanish at a threshold voltage and then becomes negative at higher voltages. We obtain this result in the

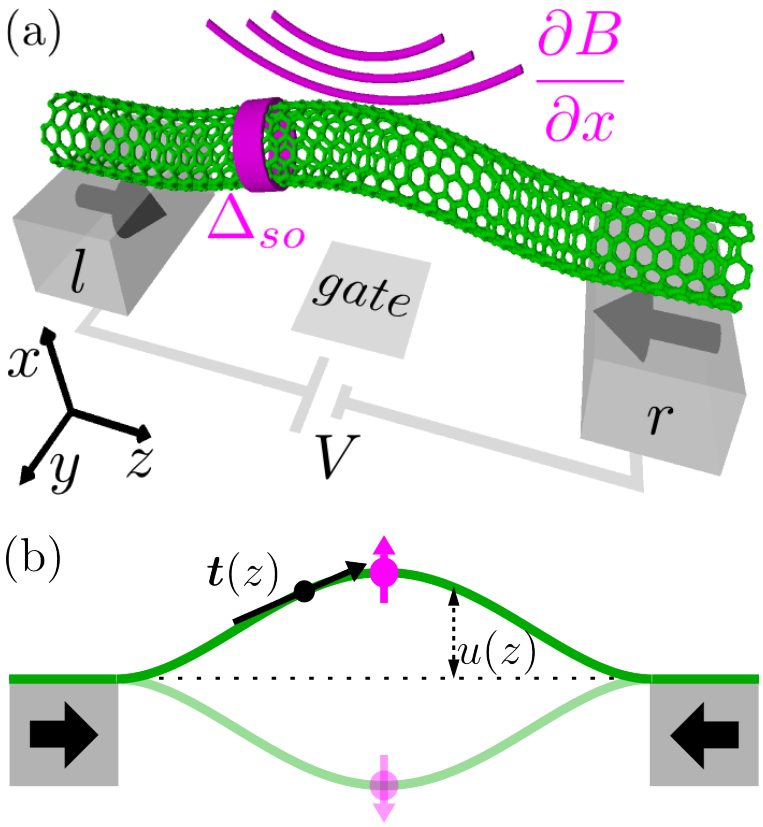

Figure 4.1: Schematic views of a carbon nanotube quantum dot suspended between two ferromagnetic leads. (a) The spin-vibration interaction can be either induced by the intrinsic spin-orbit coupling Δ_{SO} or by a magnetic gradient $\partial B/\partial x$. (b) Due to the spin-vibration interaction, the dot spin's component $\hat{\sigma}_x$ parallel to the mechanical displacement u couples to the flexural mode. The local tangent vector is denoted by $\boldsymbol{t}$.

perturbation expansion for the spin-vibration coupling and neglecting anharmonic effects and feedback action of the resonator on the current. Such effects will eventually remove the mechanical instability. However, our results point out a special regime of parameters in which we expect interesting effects as, for instance, vibrational lasing.

Finally, we find remarkable features in the current-voltage characteristic which are directly related to the non-thermal phonon occupation of the oscillator. Hence, transport measurements offer the possibility for monitoring the oscillator's state directly by varying the voltage polarity and/or the relative alignment of the magnetizations in the leads (parallel or antiparallel).

The chapter is structured as follows. In Sec. 4.3, we introduce the model Hamiltonian and derive the formulas for the mechanical damping, the steady-state nonequilibrium phonon occupation, and the current using the Keldysh nonequilibrium Green's functions technique. We calculate such quantities to the leading order in the spin-

vibration coupling strength. In Secs. 4.4-4.6, we discuss the damping and the nonequilibrium phonon occupation obtained by applying a bias voltage. We investigate the active cooling of the mechanical oscillator in different regimes in Sec. 4.5. In Sec. 4.6, we discuss the pumping of the resonator and the instability. The effects of the spin-vibration interaction on the current is considered Sec. 4.7. Finally, we draw our conclusions in Sec. 4.8.

4.3 Model

4.3.1 Microscopic derivation of the Hamiltonian

The nanomechanical spin valve that we consider consists of a suspended CNTQD in contact with ferromagnetic leads [Fig. 4.1(a)]. In this section, we introduce the model Hamiltonian of a suspended CNTQD and derive the spin-vibration interaction induced by the spin-orbit coupling or by the application of a magnetic gradient.

Carbon nanotube quantum dot

In a confining potential and for vanishing magnetic field and spin-orbit interaction, the localized electronic levels of a CNTQD are, at least, fourfold degenerate owing to the spin and circumferential orbital degrees of freedom [19]. We denote the corresponding states as $|\tau,\sigma\rangle$ with $\tau = \pm$ and $\sigma = \pm$ referring to the orbital and spin states, respectively. We choose the spin quantization axis along the z direction. The effective low-energy Hamiltonian for a single dot shell is given by [138, 139, 141]

$$\hat{H}_{\mathrm{CNT}} = \frac{\Delta_{\mathrm{SO}}}{2}\hat{\tau}_3\mathbf{t}(z)\cdot\hat{\boldsymbol{\sigma}} - \mu_{orb}\hat{\tau}_3\mathbf{B}\cdot\mathbf{t}(z) + \mu_B\mathbf{B}\cdot\hat{\boldsymbol{\sigma}} + \Delta_{KK'}\hat{\tau}_1\,, \tag{4.1}$$

with the orbital magnetic moment μ_{orb}, the Bohr magneton μ_B, the intrinsic spin-orbit coupling Δ_{SO}, the coupling $\Delta_{KK'}$ between different orbital states due to disorder, and the magnetic field $\boldsymbol{B}$. The Pauli matrices in spin (orbital) space are denoted as $\hat{\boldsymbol{\sigma}} = (\hat{\sigma}_x, \hat{\sigma}_y, \hat{\sigma}_z)$ ($\hat{\boldsymbol{\tau}} = [(\hat{\tau}_1, \hat{\tau}_2, \hat{\tau}_3)]$ and the local tangent vector at each point of the tube is written as $\mathbf{t}(z)$ whose direction varies with the position z [Fig. 4.1(b)]. The validity of the Hamiltonian (4.1) is based on the energy scale separation between the high-energy spacing associated to the gap due to the longitudinal and the circumferential quantization and the small coupling energies appearing in Eq. (4.1) [138, 139]. Moreover, since typically $\Delta_{KK'} \ll (\Delta_{SO}, \mu_{orb}B, \mu_B B)$, we neglect the coupling between different orbitals in the following as we discuss the transport far away from the regime in which the energy crossing between different orbital states occurs.

Spin-vibration interaction

The deflection associated with the flexural mode leads to a coupling of the spin on the quantum dot with the vibration which is either mediated by the spin-orbit coupling or by a magnetic gradient. The electronic model and the coupling induced by the spin-orbit coupling were studied in Refs. [141], [142] and [143]. Here, we additionally derive the coupling between the deflection and the spin due to a magnetic gradient.

Such a coupling was also analyzed in Ref. [153]. It arises from the relative motion of the suspended nanotube in a magnetic gradient in addition to a homogeneous magnetic field [154].

We depict in Fig. 4.1 the choice of the coordinate axes and assume in the following that the nanotube oscillates in the $x-z$ plane. The deflection $\hat{u}(z)$ can be written as a linear combination of the oscillation amplitudes of the eigenmodes, $\hat{u}(z) = \sum_n f_n(z) u_n (\hat{b}_n + \hat{b}_n^\dagger)$, with the waveform $f_n(z)$, the zero-point amplitude $u_n = [\hbar/(m\omega_n)]^{1/2}$, and the bosonic annihilation (creation) operators $\hat{b}$ ($\hat{b}^\dagger$) for a single mode with frequency ω_n. For a suspended elastic rod of length L, mass line density ρ, and with sufficient strong tension T, the eigenfrequency is $\omega_n = (n+1)\,\pi\sqrt{T/(\rho L^2)}$ and the waveform is given by $f_n(z) = \sqrt{2}\sin[\pi(n+1)z/L]$ for integers $n \geq 0$.

Assuming that the deflections are sufficiently small, we approximate the variation of the tangent vector as $\delta\mathbf{t}(z) \simeq [d\hat{u}(z)/dz, 0, 0]$. Additionally, the magnetic field along the nanotube changes by $\delta\mathbf{B} = (\partial\mathbf{B}/\partial x)\hat{u}(z)$ due to the magnetic gradient. Thus we expand $\mathbf{B}\cdot\mathbf{t}(z) \simeq B_z + \mathbf{B}\cdot\delta\mathbf{t}(z) + \delta\mathbf{B}\cdot\mathbf{z}$ in which we neglect $\delta\mathbf{t}(z)\cdot\delta\mathbf{B}$ corresponding to higher-order terms in $\hat{u}$ ($\mathbf{z}$ denotes the unit vector in the z direction). In the following, we assume a leading magnetic gradient dB_x/dx perpendicular to the nanotube z axis and neglect the variation of the y and z components of the magnetic field along the x axis $dB_{y,z}/dx = 0$. Furthermore, we assume a vanishing magnetic field in the x direction $B_x = 0$. With these assumptions and inserting the expansion of $\boldsymbol{B}$ and $\boldsymbol{t}(z)$ into Eq. (4.1) we obtain [141, 151]

$$\hat{H}_{cnt} = \hat{H}_{cnt}^{(0)} + \hat{H}_{SV,1} + \hat{H}_{SV,2}\,, \tag{4.2}$$

with

$$\hat{H}_{cnt}^{(0)} = \frac{\Delta_{SO}}{2}\hat{\tau}_3\hat{\sigma}_z - \mu_{orb}B_z\hat{\tau}_3 + \mu_B B_z\hat{\sigma}_z \tag{4.3}$$

$$\hat{H}_{SV,1} = \mu_B\frac{\partial B_x}{\partial x}\sum_n \langle f_n(z)\rangle\, u_n\left(\hat{b}_n + \hat{b}_n^\dagger\right)\hat{\sigma}_x \tag{4.4}$$

$$\hat{H}_{SV,2} = \frac{\Delta_{SO}}{2}\sum_n \langle f_n'(z)\rangle u_n\left(\hat{b}_n + \hat{b}_n^\dagger\right)\hat{\tau}_3\hat{\sigma}_x\,, \tag{4.5}$$

in which the waveform f_n is averaged over the electronic orbital in the dot (we also assumed that the variation of the magnetic gradient along the nanotube axis is negligible). For a quantum dot with symmetric orbital electronic density, the averages $\langle f_n(z)\rangle$ ($\langle f_n'(z)\rangle$) vanish for all odd (even) harmonics. To give a simple estimation, we consider a uniform distribution of the electronic charge on the dot. We obtain $\langle f_0(z)\rangle = 2\sqrt{2}/\pi$ for the first even mode (the fundamental mode) and $\langle df_1(z)/dz\rangle = 2\sqrt{2}/L$ for the first odd mode. In this way, the coupling constant

$$\lambda_n \simeq \mu_B(\partial B_x/\partial x)u_n\langle f_n(z)\rangle \tag{4.6}$$

in $\hat{H}_{SV,1}$ can be estimated as $\lambda_0 = 0.5$ MHz for the fundamental mode with $\partial B_x/\partial x = 5\cdot 10^6$ T/m [116]. The coupling constant

$$\lambda_n \simeq (\Delta_{SO}/2)u_n\langle df_n(z)/dz\rangle \tag{4.7}$$

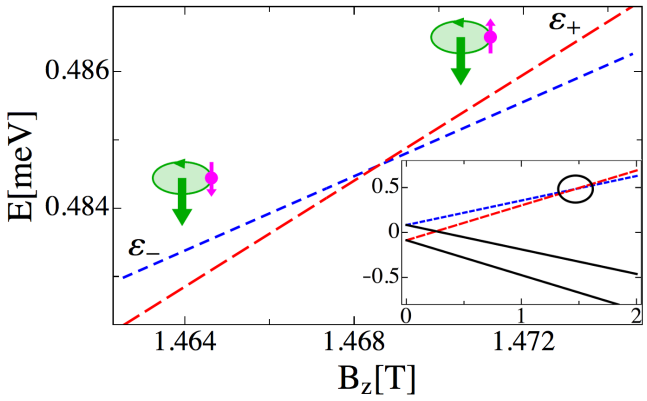

Figure 4.2: Spectrum of the Hamiltonian for a defect-free carbon nanotube quantum dot as a function of magnetic field along the nanotube axis as given by the Hamiltonian Eq. (4.3). The inset shows the full spectrum. The circle in the inset points out the crossing point between the two levels reported in the main panel. We focus on the electron transport in which only two levels of energies ε_+ and ε_- are involved. They have the same orbital state and opposite spin. The sketches illustrate the direction of the orbital (large green arrow) and spin (small magenta arrow) magnetic moments along the z-axis. The parameters are $\Delta_{SO} = 170$ μeV and $\mu_{orb} = 330$ μeV/T from Ref. [155].

in $\hat{H}_{SV,2}$ is estimated as $\lambda_1 \sim 2.5$ MHz for the first odd mode with $\Delta_{SO} \simeq 400$ μ eV [141].

Single mode model with two spin levels

We now consider the suspended CNTQD embedded between ferromagnetic leads. The leads are described by the Stoner model in which one assumes a spin asymmetry in the density of states for the spin-up and -down bands $\rho_{\alpha\sigma} = \rho_\alpha(1 + \sigma p_\alpha)$ with the degree of spin polarization in lead α defined as $p_\alpha = (\rho_{\alpha+} - \rho_{\alpha-})/(\rho_{\alpha+} + \rho_{\alpha-})$. The effect of the ferromagnets is captured by the spin-dependent tunneling rates $\Gamma^\sigma_\alpha = \pi|t_{\alpha\sigma}|^2\rho_{\alpha\sigma}$. The Hamiltonian of the whole system is given by

$$\hat{H} = \hat{H}_l + \hat{H}_t + \hat{H}_d\,, \tag{4.8}$$

with the Hamiltonian of the leads ($\alpha = L, R$) $\hat{H}_l = \sum_{\alpha\sigma k}(\varepsilon_{k\sigma} - \mu)\hat{c}^\dagger_{\alpha k\sigma}\hat{c}_{\alpha k\sigma}$, the chemical potential μ_α of the leads and the tunneling Hamiltonian $\hat{H}_t = \sum_{\alpha\sigma k}(t_{\alpha\sigma}\hat{c}^\dagger_{\alpha k\sigma}\hat{d}_\sigma + h.c.)$. The operators $\hat{c}^\dagger_{\alpha k\sigma}$ ($\hat{c}_{\alpha k\sigma}$) and $\hat{d}^\dagger$ ($\hat{d}$) are the creation (annihilation) operators for the corresponding electronic states in the ferromagnetic leads and for the dot states. To discuss the effects of the spin-vibration interaction, we start by discussing the part of the spectrum of the CNTQD given by the Hamiltonian (4.3), i.e., the situation in which only two spin channels for the same orbital level are involved in the transport, as shown in Fig. 4.2. This regime occurs when the orbital energy splitting is the largest energy scale in Eq. (4.3).

From Eqs. (4.4) and (4.5), the model Hamiltonian for the two spin states of the same orbital and the spin-vibration interaction with a single mechanical mode of frequency ω is finally described by

$$\hat{H}_d = \sum_\sigma \varepsilon_\sigma \hat{d}_\sigma^\dagger \hat{d}_\sigma + \lambda \hat{\sigma}_x \left(\hat{b}^\dagger + \hat{b}\right) + \hbar\omega \hat{b}^\dagger \hat{b}\,, \tag{4.9}$$

with the energy levels $\varepsilon_\sigma = \varepsilon_0 + \sigma\varepsilon_z/2$ and the splitting between the two spin states given by ε_z. The $x-$component of the local spin operator in the dot $\hat{\sigma}_x = \hat{d}_+^\dagger \hat{d}_- + \hat{d}_-^\dagger \hat{d}_+$ is chosen to be perpendicular to the quantization axis for the spin transport. The index n in the bosonic operators is omitted since we assume that only a single vibrational mode is relevant.

The Hamiltonian Eq. (4.9) is similar to the well-known Anderson-Holstein model widely discussed in literature [156–171] in which the quantum oscillator is linearly coupled to the dot charge $\hat{n} = \hat{d}^\dagger \hat{d}$ of a spinless level, according to the Hamiltonian $\hat{H}_{int} = \lambda(\hat{b}^\dagger + \hat{b})\hat{n}$. We recover such a model if the operator $\hat{\sigma}_x$ is replaced with $\hat{\sigma}_z$, i.e., when the spin-vibration interaction is parallel to the magnetization axis of the two leads so that the transport occurs through two spin channels separately.

The Hamiltonian Eq. (4.9) is also similar to the phenomenological model discussed in Refs. [172] and [173] for an electron-vibration interaction invoking different dot levels [174]. However, these previous works assumed mainly the case of non-ferromagnetic leads, whereas we will focus on the effects of spin-polarized tunneling on the vibration.

4.3.2 Phonon Green's function

Electrons tunneling inelastically on and off the CNTQD yield a damping of the vibration with a rate γ and a frequency renormalization $\Delta\omega$. Moreover, an electron current flowing through the CNTQD drive the oscillator to a non-thermal state with phonon occupation $n \neq n_B(\omega)$ [$n_B(\omega)$ is the Bose distribution] if the intrinsic coupling of the oscillator to the external thermal bath is sufficiently small. To address these effects, we use the Keldysh nonequilibrium Green's functions technique.

We start with the Dyson equation for the phonon Green's function in Keldysh space defined as

$$\check{D}(\varepsilon) = \check{d}(\varepsilon) + \check{d}(\varepsilon)\left[\check{\Pi}(\varepsilon) + \check{\Sigma}_0(\varepsilon)\right]\check{D}(\varepsilon)\,, \tag{4.10}$$

in which the retarded, advanced and Keldysh Green's functions are defined as

$$D^R(t,t') = -i\theta(t-t')\langle[\hat{A}(t), \hat{A}(t')]\rangle \tag{4.11}$$

$$D^A(t,t') = i\theta(t'-t)\langle[\hat{A}(t), \hat{A}(t')]\rangle \tag{4.12}$$

$$D^K(t,t') = -i\langle\{\hat{A}(t'), \hat{A}(t)\}\rangle\,. \tag{4.13}$$

with $\hat{A}(t) = \hat{b}^\dagger(t) + \hat{b}(t)$ and the commutator (anti-commutator) [,] ({ , }). We used the triangular Larkin-Ovchinnikov representation

$$\check{D}(t) = \begin{pmatrix} D^R(t) & D^K(t) \\ 0 & D^A(t) \end{pmatrix}\,, \tag{4.14}$$

The bare phonon Green's functions in Eq. (4.10) are given by (using η as an infinitesimal small real part)

$$d^{R,A}(\varepsilon) = 2\hbar\omega/[(\varepsilon \pm i\eta)^2 + (\hbar\omega)^2], \tag{4.15}$$

$$d^{K}(\varepsilon) = -2\pi i\,[\delta(\varepsilon - \hbar\omega) + \delta(\varepsilon + \hbar\omega)]\coth[\hbar\omega/(2T)]\,. \tag{4.16}$$

In Eq. (4.10), $\check{\Pi}(\varepsilon)$ corresponds to the phonon self energy (polarization diagram) associated to the spin-vibration interaction between the oscillator and the electrons [see Fig. 4.3(a)]. To the leading order in the coupling strength of the spin-vibration interaction, the three components of the phonon self-energies are given by:

$$\Pi^{R/A}(\varepsilon) = -i\frac{\lambda^2}{2}\sum_\sigma \left[G^K_{-\sigma}(\varepsilon')\circ G^{A/R}_\sigma(\varepsilon'-\varepsilon) + G^{R/A}_{-\sigma}(\varepsilon')\circ G^K_\sigma(\varepsilon'-\varepsilon)\right], \tag{4.17}$$

$$\begin{aligned}\Pi^{K}(\varepsilon) = -i\frac{\lambda^2}{2}\sum_\sigma \Big[&G^K_{-\sigma}(\varepsilon')\circ G^K_\sigma(\varepsilon'-\varepsilon)\\ &+G^R_{-\sigma}(\varepsilon')\circ G^A_\sigma(\varepsilon'-\varepsilon) + G^A_{-\sigma}(\varepsilon')\circ G^R_\sigma(\varepsilon'-\varepsilon)\Big]\,.\end{aligned} \tag{4.18}$$

The symbol $\circ$ denotes the convolution product

$$a(x)\circ b(x-y) = \int_{-\infty}^{\infty}(dx/2\pi)a(x)b(x-y)\,. \tag{4.19}$$

Note that the interaction vertex due to the spin-vibration couples only spins of opposite direction [see Fig. 4.3(a)]. The electron Green's functions of the dot appearing in Eqs. (4.17) and (4.18) are those associated to the Hamiltonian with vanishing spin-vibration interaction. They correspond to the exactly solvable problem of two dot levels coupled to the leads and they are given by

$$G^{R,A}_\sigma(\varepsilon) = (\varepsilon - \varepsilon_\sigma \pm i\Gamma^\sigma_l \pm i\Gamma^\sigma_r)^{-1}\,, \tag{4.20}$$

$$\begin{aligned}G^K_\sigma(\varepsilon) &= -2iG^R_\sigma(\varepsilon)\{\Gamma^\sigma_l[1-2f_l(\varepsilon)] + \Gamma^\sigma_r[1-2f_r(\varepsilon)]\}G^A_\sigma(\varepsilon)\\ &= -2i\frac{\Gamma^\sigma_l(1-2f_l(\varepsilon)) + \Gamma^\sigma_r(1-2f_r(\varepsilon))}{(\varepsilon-\varepsilon_\sigma)^2 + (\Gamma^\sigma_l+\Gamma^\sigma_r)^2}\,.\end{aligned} \tag{4.21}$$

with $\alpha = l, r$, the Fermi functions $f_\alpha(\varepsilon) = \{1+\exp[(\varepsilon-\mu_\alpha)/k_BT]\}^{-1}$ and the lead chemical potentials μ_α. We also employed the wide band approximation by neglecting the energy dependence of the coupling rates $\Gamma^\sigma_{r/l}$.

To take into account the intrinsic damping of the oscillator, we additionally include a self-energy $\check{\Sigma}_0(\varepsilon)$ in the phonon Dyson equation Eq. (4.10). Such a self-energy can be calculated by assuming that the environment is formed by a bath of independent harmonic oscillators (Caldeira-Leggett model) with a low-frequency linear dispersion for the spectral function.

Finally, we can approximate $\Sigma^R_0(\varepsilon) \simeq \Sigma^R_0(\omega)$ for $Q \gg 1$ in the Dyson equation (4.24) (see appendix B.1 for further details). From this phenomenological model, one obtains the expressions

$$\text{Im}\,\Sigma^R_0(\varepsilon) = -\varepsilon/Q\,, \tag{4.22}$$

$$\Sigma^K_0(\varepsilon) = -2i\varepsilon\coth(\varepsilon)/Q\,, \tag{4.23}$$

in which the coefficient Q corresponds to the quality factor of the oscillator.

The phonon Green's function is obtained by solving the Dyson equation (4.10),

$$\begin{aligned} D^R(\varepsilon) &= \frac{2\hbar\omega}{\varepsilon^2 - (\hbar\omega)^2 - 2\hbar\omega[\Pi^R(\varepsilon) + \Sigma_0^R(\varepsilon)]} \\ &\simeq \frac{1}{\varepsilon - \tilde{\omega} + i\gamma_{tot}} - \frac{1}{\varepsilon + \tilde{\omega} + i\gamma_{tot}}\,, \end{aligned} \tag{4.24}$$

$$\begin{aligned} D^K(\varepsilon) &= D^R(\varepsilon)[\Pi^K(\varepsilon) + \Sigma_0^K(\varepsilon)]D^A(\varepsilon) \\ &\simeq [\Pi^K(\varepsilon) + \Sigma_0^K(\varepsilon)] \sum_{s=\pm} \frac{1}{(\varepsilon + s\hbar\tilde{\omega})^2 + \gamma_{tot}^2}\,. \end{aligned} \tag{4.25}$$

We introduced the renormalized frequency $\tilde{\omega} = \omega + \Delta\omega$ with $\Delta\omega = \mathrm{Re}[\Pi^R(\omega) + \Sigma_0^R(\omega)]$ [175]. In the following, we set $\tilde{\omega} \to \omega$. In the approximations in Eqs. (4.24) and (4.25) we expanded the self-energies and the retarded phonon Green's functions around $\varepsilon \simeq \omega$. Furthermore, we also introduced the total mechanical damping coefficient as

$$\gamma_{tot}(\omega) = -\mathrm{Im}[\Pi^R(\omega) + \Sigma_0^R(\omega)]\,, \tag{4.26}$$

calculated at the frequency of the resonator.

4.3.3 Mechanical damping

The total mechanical damping can be also written as $\gamma_{tot} = \gamma_0 + \gamma$ with the intrinsic damping coefficient $\gamma_0 = -\mathrm{Im}\,\Sigma_0^R(\omega) = \omega/Q$ of the oscillator and the damping $\gamma = -\mathrm{Im}\,\Pi^R(\omega)$ associated to the interaction with the electrons.

We assumed the underdamped regime for the mechanical oscillator $\gamma, \gamma_0 \ll \omega$ which justifies the approximation of the self energy $\check{\Pi}(\varepsilon)$ to the leading order in the spin-vibration coupling strength. After some algebra, the explicit form for the damping coefficient reads as

$$\gamma = \sum_{\alpha,\beta=l,r} \sum_{s=\pm} s\,\gamma_{\alpha\beta}^s\,, \tag{4.27}$$

$$\gamma_{\alpha\beta}^s = \frac{\lambda^2}{2} \int \frac{d\varepsilon}{2\pi} T_{\alpha\beta}^s(\varepsilon,\omega) f_\alpha(\varepsilon)\,[1 - f_\beta(\varepsilon + s\omega)]\,, \tag{4.28}$$

with the functions

$$T_{\alpha\beta}^s(\varepsilon,\omega) = 4 \sum_\sigma \Gamma_\alpha^\sigma \Gamma_\beta^{-\sigma} |G_\sigma^R(\varepsilon)|^2 |G_{-\sigma}^R(\varepsilon + s\omega)|^2. \tag{4.29}$$

The coefficients $\gamma_{\alpha\beta}^s$ correspond to the rates for vibration-assisted inelastic processes in which a spin flip occurs for one electron tunneling from lead α to lead β accompanied by the absorption ($s = +$) or emission ($s = -$) of a vibrational energy quantum ω. Equation (4.27) also shows that the damping γ is given by a sum of positive and negative terms associated to the processes of emission and absorption of energy, respectively.

From this observation we can anticipate that, contrary to the intrinsic damping induced by the environment for which we assume $\gamma_0 > 0$, the oscillator can approach

a regime in which $\gamma < 0$ for certain parameter ranges when the phonon emission processes overcome the phonon absorption processes. In other words, the system reaches a threshold at which the total damping coefficient vanishes $\gamma_{tot} = 0$. Beyond this point, one obtains the result $\gamma_{tot} < 0$ pointing out a mechanical instability region. In the following discussion, we will distinguish between the single level and the resonant regime.

Single level regime

In the high-temperature regime $T \gg \Gamma_\alpha^\sigma$ and for high-energy separation $T \ll \varepsilon_z$, one can use an analytic approximation for the rates $\gamma_{\alpha\beta}^s$, which is in excellent agreement with the full results of Eq. (4.28). The Lorentzian functions appearing in Eq. (4.29) can be treated separately as δ functions in the integral of Eq. (4.28) and we can cast each rate as the sum of two spin-resolved rates $\gamma_{\alpha\beta}^s \simeq \sum_\sigma \gamma_{\alpha\beta}^{s\sigma}$, for the tunneling through the dot level with spin $\sigma = \pm$. The latter rates read as

$$\gamma_{\alpha\beta}^{s\sigma} = \frac{\lambda^2}{\Gamma_l^\sigma + \Gamma_r^\sigma} \Big\{ \Gamma_\alpha^\sigma \Gamma_\beta^{-\sigma} T_+^{s\sigma} f_\alpha(\varepsilon_\sigma) \left[1 - f_\beta(\varepsilon_\sigma + s\omega)\right] + \Gamma_\alpha^{-\sigma} \Gamma_\beta^\sigma T_-^{s\sigma} f_\alpha(\varepsilon_\sigma - s\omega) \left[1 - f_\beta(\varepsilon_\sigma)\right] \Big\} \quad (4.30)$$

with $T_\pm^{s\sigma} = 1/\left[(\Gamma_l^{-\sigma} + \Gamma_r^{-\sigma})^2 + (\sigma\varepsilon_z \pm s\omega)^2\right]$.

4.3.4 Phonon occupation

Applying a bias voltage, the electron current drives the oscillator towards a nonequilibrium steady state with an occupation

$$\langle \hat{b}^\dagger \hat{b} \rangle = \bar{n} = \left[(i/8\pi) \int d\varepsilon D^K(\varepsilon)\right] - 1/2\,. \quad (4.31)$$

In the limit $\gamma_{tot} \ll (\omega, \Gamma_l, \Gamma_r, T, eV)$ and separating the contributions of the intrinsic damping and of the spin-vibration interaction, the occupation can be written as

$$\bar{n} = \frac{\gamma_0 n_B(\omega) + \gamma n}{\gamma_0 + \gamma}. \quad (4.32)$$

Hence, the steady-state phonon occupation is the result of the competition between the interaction of the mechanical oscillator with the thermal bath and the interaction with the tunneling electrons. Using Eqs. (4.18), (4.20), (4.21), and (4.25), the expression for the electronic contribution to the average occupation induced by the spin-vibration interaction reads as

$$n = \frac{1}{\gamma} \sum_{\alpha\beta s} s\gamma_{\alpha\beta}^s n_B[\omega + s(\mu_\alpha - \mu_\beta)]\,. \quad (4.33)$$

With the notation $\delta\gamma_{\alpha\beta} = \gamma_{\alpha\beta}^+ - \gamma_{\alpha\beta}^-$, Eq. (4.32) can be written as

$$\bar{n} = \left[\gamma_0 + \delta\gamma_{ll} + \delta\gamma_{rr} + \delta\gamma_{lr} + \delta\gamma_{rl}\right]^{-1} \left[(\gamma_0 + \delta\gamma_{ll} + \delta\gamma_{rr}) n_B(\omega) + (\gamma_{lr}^+ - \gamma_{rl}^-) n_B(\omega + eV) + (\gamma_{rl}^+ - \gamma_{lr}^-) n_B(\omega - eV)\right] \quad (4.34)$$

The inelastic spin-flip processes involving only a single lead with rates $\delta\gamma_{rr}$ and $\delta\gamma_{ll}$ correspond to electrons tunneling on the dot, flipping the spin by exchanging a vibrational energy quantum, and then coming back to the initial lead. Since the two leads have the same temperature as the external thermal bath, such processes drive the phonon occupation towards the equilibrium occupation $n_B(\omega)$, as it is shown in Eq. (4.34).

4.3.5 Lowest order perturbation theory for the current

The transport properties through the system are calculated using the same technique, viz., the Keldysh-Green's functions. To understand the effect of the spin-vibration interaction, in this work we calculate the correction to the current to the first leading order in the spin-vibration coupling [4, 94, 160, 165, 176]. The current through the left contact can be expressed as ($e > 0$)

$$I_l = -e\langle\frac{d\hat{N}_l}{dt}\rangle = \frac{2e}{h}\,\mathrm{Re}\left[\sum_{k\sigma} t_{l\sigma}\int_{-\infty}^{+\infty} d\varepsilon\; \mathcal{G}^{<}_{d\sigma,lk\sigma}(\varepsilon)\right], \tag{4.35}$$

with the standard quantum statistical average $\langle\dots\rangle$ and the Fourier transform $\mathcal{G}^{<}_{d\sigma,lk\sigma}(\varepsilon)$ of the lesser Green's function $\mathcal{G}^{<}_{d\sigma,lk\sigma}(t,t') = i\langle\hat{c}_{lk\sigma}(t')\hat{d}^{\dagger}_{\sigma}(t)\rangle$ [177, 178]. The corresponding Green's function on the Keldysh contour is defined as $\mathcal{G}_{d\sigma,lk\sigma}(\tau,\tau') = -i\langle T_c\hat{c}_{lk\sigma}(\tau)\hat{d}^{\dagger}_{\sigma}(\tau')\rangle$ with the time-ordering operator T_c along the Keldysh contour. As shown in chapter 2, we transform from the contour variable τ to the real time and use the Larkin-Ovchinnikov rotation to introduce the triangular matrix representation $\check{\mathcal{G}}$ such that $\check{\mathcal{G}}$ has the three components $\mathcal{G}^{R,A,K}$. From standard diagrammatics we obtain the Dyson equation $\check{\mathcal{G}}_{d\sigma,l\sigma} = \check{\mathcal{G}}_{d\sigma,d\sigma}\check{t}^{*}_{l\sigma}\check{g}_{lk\sigma}$ where $\check{g}_{lk\sigma}$ denotes the Keldysh Green's function for vanishing tunneling and spin-vibration interaction. Inserting the lesser element $\mathcal{G}^{<}_{d\sigma,lk\sigma} = (\mathcal{G}^{K}_{d\sigma,lk\sigma} - \mathcal{G}^{R}_{d\sigma,lk\sigma} - \mathcal{G}^{A}_{d\sigma,lk\sigma})/2$ of $\check{\mathcal{G}}_{d\sigma,lk\sigma}$ in the current (4.35) one obtains

$$I_l = \frac{e}{h}\sum_{\sigma}\Gamma^{\sigma}_{l}\,\mathrm{Im}\int d\varepsilon\{2[1-2f_l(\varepsilon)]\mathcal{G}^{R}_{d\sigma,d\sigma}(\varepsilon) - \mathcal{G}^{K}_{d\sigma,d\sigma}(\varepsilon)\}. \tag{4.36}$$

The problem then reduces to the calculation of the dot-dot Green's functions $\mathcal{G}^{K,R,A}_{\sigma\sigma}$ (neglecting the index dd). We expand the Green's function on the Keldysh contour $\mathcal{G}_{\sigma\sigma}(\tau,\tau') = -i\langle T_c\hat{d}_{\sigma}(\tau)\hat{d}^{\dagger}_{\sigma}(\tau')\rangle$ to the order λ^2 treating the spin-vibration interaction as the perturbation. Finally, we transform the contour variable to the real time and use the Larkin-Ovchinnikov transformation to represent the perturbation expansion in frequency space as

$$\check{\mathcal{G}}_{\sigma\sigma}(\varepsilon) = \check{G}_{\sigma}(\varepsilon) + \check{G}_{\sigma}(\varepsilon)\check{\Sigma}_{-\sigma-\sigma}(\varepsilon)\check{G}_{\sigma}(\varepsilon)\,. \tag{4.37}$$

The corrections to the current are obtained by inserting the retarded and the Keldysh element of the perturbative expansion (4.37) into Eq. (4.36).

The elements of the self energies $\check{\Sigma}_{\sigma\sigma}$ due to the spin-vibration interaction in

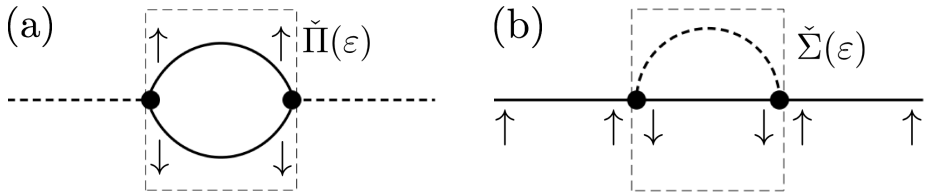

Figure 4.3: Leading-order diagrams corresponding to the perturbation expansion of the phonon Green's function $\check{D}(\varepsilon)$ (a) and the electronic Green's function $\check{\mathcal{G}}(\varepsilon)$ (b). The plane lines indicate the electronic Green's function $\check{G}(\varepsilon)$ for vanishing spin-vibration interaction. The dashed lines represent the bare phonon Green's functions. The filled circle is the vertex for the spin-vibration interaction with coupling constant λ which couples electronic Green's functions of opposite spin with a phonon Green's function.

Eq. (4.37) are denoted as $\Sigma^{R,A,K}_{\sigma\sigma}$ and they are given by

$$\Sigma^{R,A}_{\sigma\sigma}(\varepsilon)=i\frac{\lambda^2}{2}[D^{R,A}(\varepsilon')\circ G^K_\sigma(\varepsilon-\varepsilon')+D^K(\varepsilon')\circ G^{R,A}_\sigma(\varepsilon-\varepsilon')], \tag{4.38}$$

$$\Sigma^{K}_{\sigma\sigma}(\varepsilon)=i\frac{\lambda^2}{2}\sum_{\zeta=R,A,K} D^\zeta(\varepsilon')\circ G^\zeta_\sigma(\varepsilon-\varepsilon') \tag{4.39}$$

with the phonon Green's functions $D^{R,A,K}$ of Eqs. (4.24) and (4.25).

If we compare our model with the Anderson-Holstein model, we observe that for the spin-vibration interaction here discussed, the tadpole diagram vanishes as the interaction vertex connects electron Green's functions with opposite spin [see Fig. 4.3(b)]. Hence, the expression in Eqs. (4.38) and (4.39) for the rainbow diagram represents the only finite contribution to the self-energy to the leading order. On the other hand, the self-energy itself $\check{\Sigma}_{\sigma\sigma}$ is similar to the analytic expression for the Anderson-Holstein model [4, 160, 165] except the spin dependence due to the spin-dependent interaction (see appendix B.2 for further details).

4.4 Damping of the oscillator and phonon occupation

An applied voltage drives the oscillator to a nonequilibrium state with phonon occupation $\bar{n}$. This non thermal occupation strongly depends on the configuration of the lateral ferromagnets (parallel or antiparallel magnetization configuration). In Sec. 4.5, we discuss the active quantum ground-state cooling in the antiparallel magnetization configuration. In the following Sec. 4.6, we focus on the strong heating of the oscillator which is the precursor of a mechanical instability. Such a regime is equivalent to a region in which phonon lasing was recently discussed for another spin-valve system [150]. The results of the phonon occupation for a single polarized lead and for the parallel magnetization configuration are reported in Secs. 4.5.3 and 4.6.2, respectively.

4.5 Active cooling to the ground-state

To gain insight into the problem, we start with the case of fully polarized ferromagnets although efficient cooling is achieved even for small polarizations. A simple picture of the basic cooling process is shown in Fig. 4.4 for the case of fully polarized leads in the antiparallel magnetization configuration. We consider the resonant regime, in which the energy separation of the spin-up and spin-down level corresponds to the frequency of the resonator. Voltage is applied in a way that transport appears from the left to the right lead. An electron tunnels from the left lead to the spin-down level. Then it extracts energy from the resonator and thereby lowers the phonon occupation of the resonator. After the interaction of the electron with the resonator the spin-up electron tunnels to the right lead.

4.5.1 Fully polarized ferromagnetic leads

For $p = 1$, the diagonal rates in Eq. (4.33) vanish $\gamma^s_{ll} = \gamma^s_{rr} = 0$, as the electron cannot come back to its original lead after a spin flip. Moreover, in the high-voltage limit $eV \gg T$ ($e > 0$), we can safely neglect the processes $\gamma^s_{rl} \simeq 0$ being $V > 0$ as electrons tunneling from the right lead are Pauli blocked. Accordingly, the total damping reduces to the sum of only two processes $\gamma \simeq \gamma^+_{lr} - \gamma^-_{lr}$ and the expression of n simplifies to the average distribution resulting from these two competing processes

$$n \simeq \frac{\gamma^+_{lr} n_B(\omega + eV) - \gamma^-_{lr} n_B(\omega - eV)}{\gamma^+_{lr} - \gamma^-_{lr}} \simeq \frac{\gamma^-_{lr}}{\gamma^+_{lr} - \gamma^-_{lr}} \,. \tag{4.40}$$

The second step in Eq. (4.40) holds for $eV \gg \omega$, when the nonequilibrium phonon occupation is completely ruled by the ratio $\gamma^+_{lr}/\gamma^-_{lr}$. Although in the region of stability defined by $\gamma^+_{lr} > \gamma^-_{lr}$ the total damping is always positive, n can show heating or cooling: for $\gamma^+_{lr} \gtrsim \gamma^-_{lr}$ the mechanical oscillator is almost undamped and it is actively

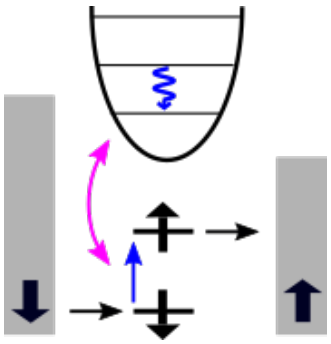

Figure 4.4: Schematic sketch of basic processes for active cooling. An spin-down electron from the left lead tunnels to the spin-down level of the quantum dot. It flips the spin and tunnels to the spin-up level and thereby extracts energy from the resonator and lowers the phonon occupation.

heated to $n \gtrsim n_B(\omega)$ whereas for $\gamma_{lr}^{+} \gg \gamma_{lr}^{-}$ the dominant emission processes yield an efficient cooling of the oscillator, viz. $n \ll n_B(\omega)$.

Single spin-level regime

We now discuss the result for the fully polarized case in Fig. 4.5. Since $\Gamma_l^{+} = \Gamma_r^{-} = 0$ one of two terms appearing in Eq. (4.30) vanishes for each spin channel. For symmetric contacts $\Gamma_l^{-} = \Gamma_r^{+} = \Gamma$ and setting $T^s = \lambda^2\Gamma/[\Gamma^2 + (\omega - s\varepsilon_z)^2]$, the single spin-channel rates read [see Eq. (4.30)]

$$\gamma_{lr}^{s\sigma} = T^s \, f_l(\varepsilon_\sigma - s\omega\delta_{\sigma+}) \, [1 - f_r(\varepsilon_\sigma + s\omega\delta_{\sigma-})] \; . \tag{4.41}$$

In Fig. 4.5(a) we show an example of the case $\varepsilon_z \gg \omega$ for an asymmetric voltage bias for which only the spin-down level is involved in transport. In this limit $T^{+} \simeq T^{-}$ and the difference between the absorption rate γ_{lr}^{+} and emission rate γ_{lr}^{-} is mainly given by the product the Fermi functions in Eq. (4.41). The system is expected to switch from cooling to heating when we move from the regime $\gamma_{lr}^{+} \gg \gamma_{lr}^{-}$ to the regime $\gamma_{lr}^{+} \gtrsim \gamma_{lr}^{-}$. In a simple picture, the switch is expected close to the line $\mu_r = \varepsilon_-$. For $\mu_r > \varepsilon_-$ (cooling region) the emission processes are suppressed due to the occupation of the low energy level in the right lead [left inset Fig.4.5(a)]. For $\mu_r < \varepsilon_-$ (heating region) emission processes are relevant and they compete with the absorption ones [right inset Fig.4.5(a)]. At finite temperature, the thermal broadening of the Fermi functions causes a smooth transition between the two regimes so that the crossing line corresponding to $n = n_B$ occurs at $\varepsilon_- = \mu_r + 8T^2/\varepsilon_z$ to leading order in T/ε_z and for $T \gg \omega$. Note that, in this discussion, the left lead plays only the role of a source for injecting one electron with spin up in the dot level. Hence cooling is achieved even for a normal left contact ($p_l = 0$) as discussed in Sec. 4.5.3.

Resonant regime

The minimum of the phonon occupation as a function of voltage decreases with the ratio ε_z/ω. The optimal cooling is achieved at $\varepsilon_z = \omega$. At this point and in the limit $eV \gg (T, \omega, \varepsilon_0)$, $f_l \simeq 1$ and $f_r \simeq 0$ and the phonon occupation of Eq. (4.33) becomes $n \simeq (\Gamma/\omega)^2$. Further decreasing the ratio ε_z/ω does not improve the cooling.

The strong cooling obtained for the resonant regime can be explained as follows. The absorption processes for each spin channel are now the same and we have $\gamma_{lr}^{++} = \gamma_{lr}^{+-}$ as the virtual levels $\varepsilon_- + \omega$ and $\varepsilon_+ - \omega$, which are involved in the spin-flip tunneling for cooling, coincide, respectively, to the real dot spin levels ε_+ and ε_-. This yields a strong enhancement of the (transmission) function T^{+} (phonon absorption) as compared to T^{-} (phonon emission) in Eq. (4.41), namely $T^{+} \gg T^{-}$, which explains the strong cooling effect. As a consequence, n has a weak dependence on the alignment of the average level position ε_0 and the lead chemical potential μ_α. In Fig.4.5(b) we show the resonant case with a finite intrinsic damping $\gamma_0/\omega = 10^{-5}$ to illustrate the behavior of $\bar{n}$.

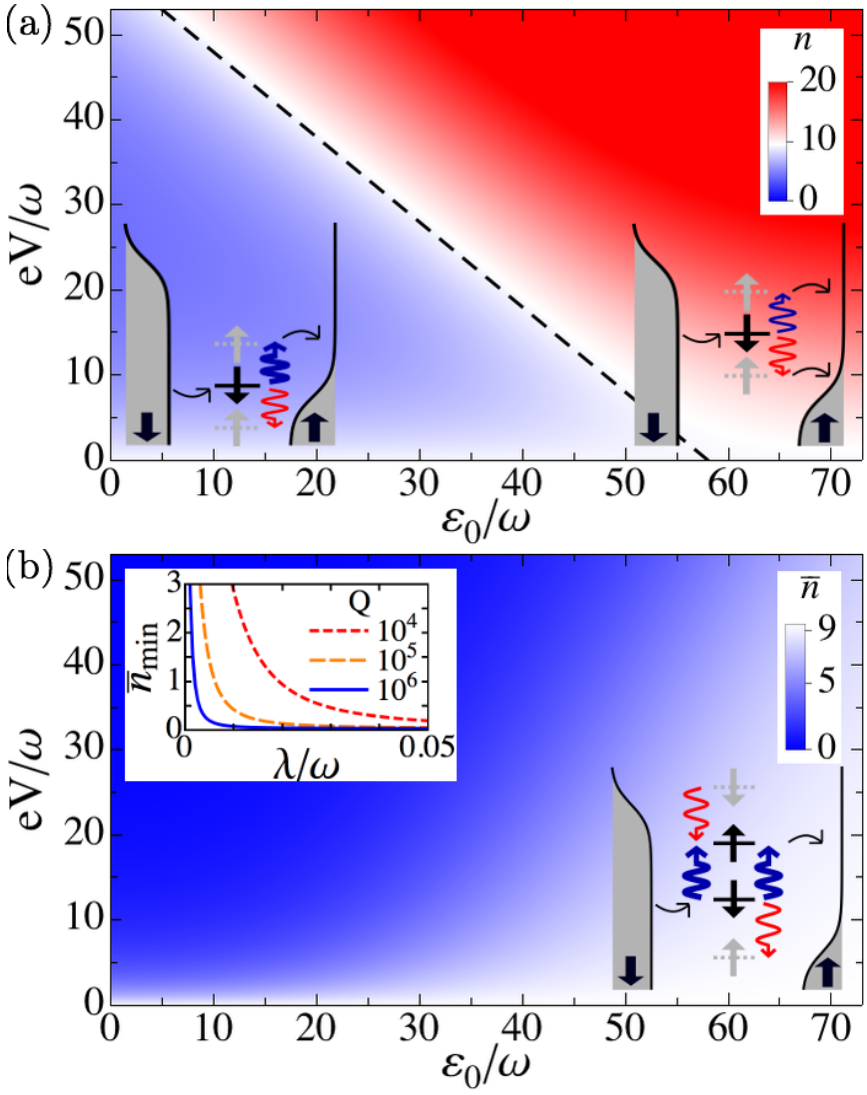

Figure 4.5: Phonon occupation as function of the bias voltage V and ε_0. The parameters are $p = 1$ (fully polarized), $\Gamma_l^- = \Gamma_r^+ = 0.2\omega$, and $T = 10\omega$. White corresponds to $n_B(\omega)$. (a) Vanishing external damping $\gamma_0 = 0$, $\varepsilon_z = 10T$, $\mu_r = \varepsilon_0 - eV$, and $\mu_l = \varepsilon_0$. The black dashed line indicates the transition from cooling to heating (see text). Inset: schematic behavior of the relevant spin-flip processes in the region of cooling (left) and heating (right). (b) Resonant regime $\varepsilon_z = \omega$ with $\gamma_0 = 10^{-5}\omega$, $\lambda/\omega = 0.01$, and $\mu_{l,r} = \varepsilon_0 \pm eV/2$. Inset, left: the minimum occupation $\bar{n}_{\min}$ as a function of the spin-vibration coupling constant λ for different quality factors. Inset, right: schematic behavior of the energy levels and of the inelastic resonant spin-flip tunneling.

4.5.2 Effects of finite polarization

We discuss now the effects of finite polarization. For symmetrically applied voltage, the results for the minimal value $\bar{n}_{min}$ as a function of the energy separation for different polarizations are shown in Fig. 4.6(a). Even in this case, at arbitrary fixed polarization, optimal cooling is again achieved for the resonant regime $\omega = \varepsilon_z$. A finite polarization always decreases the minimum occupation as $\bar{n}_{min}$ increases as a function of p independent of the ratio ε_z/ω [Fig. 4.6(b)].

To discuss this behavior we consider the analytic high-voltage approximation for the phonon occupation given by

$$n \simeq \frac{\gamma_{lr}^{-} + n_B(\omega)\,(\gamma_{ll} + \gamma_{rr})}{\gamma_{lr}^{+} - \gamma_{lr}^{-} + \gamma_{ll} + \gamma_{rr}}, \tag{4.42}$$

where we set the short notation $\gamma_{\alpha\alpha} = \gamma_{\alpha\alpha}^{+} - \gamma_{\alpha\alpha}^{-}$. From Eq. (4.43) we observe that the diagonal lead processes $\gamma_{\alpha\alpha}$, which are not present for $p = 1$, have the effect

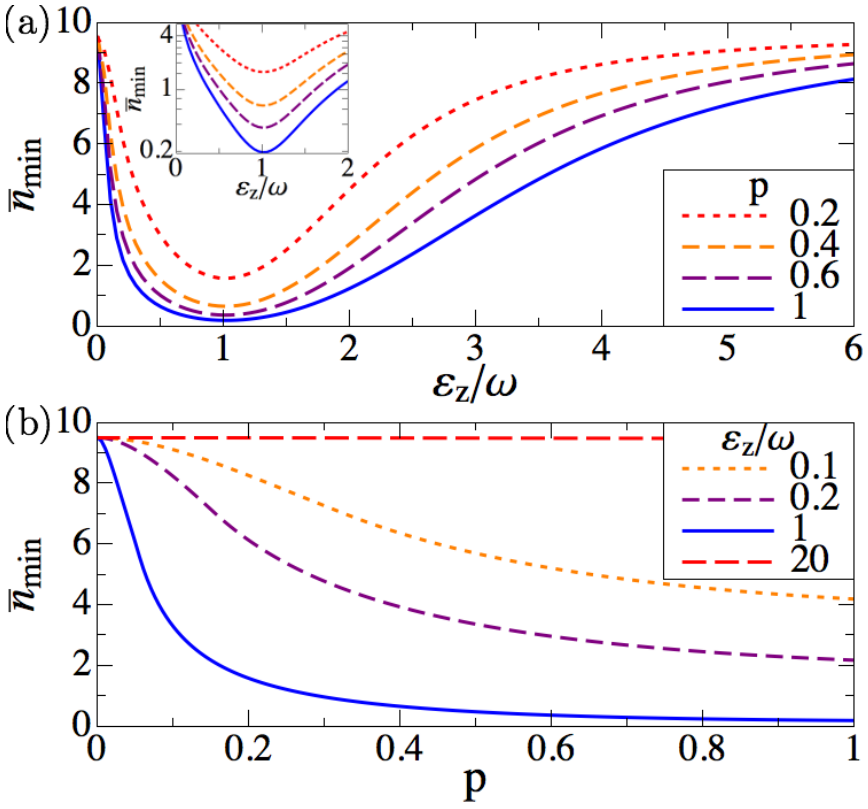

Figure 4.6: Minimum of the phonon occupation $\bar{n}_{min}$ for an intrinsic damping of $Q = 10^4$ and $\lambda/\omega = 0.05$. The temperature is $T = 10\omega$ and $\Gamma_l = \Gamma_r = 0.2\omega$. (a) Minimal occupation as function of ε_z/ω for different polarizations. The inset (log scale for y axis) shows that maximal cooling is achieved at $\varepsilon_z = \omega$. (b) Minimal phonon occupation as a function of polarization for different energy separations.

of thermalizing the oscillator. As an example, assuming a strong asymmetry of the leads, as for instance $\Gamma_l \simeq 0$ ($\Gamma_r \simeq 0$), we have $\gamma_{lr}^{\pm} = 0$: the dot is contacted only with one left (right) lead and the oscillator is always at the thermal equilibrium. Such processes compete with the cooling processes γ_{lr}^{+} leading to an increase of the minimum phonon occupation.

Clearly, taking into account the intrinsic damping of the mechanical oscillator also increases the minimum phonon occupation. Remarkably, a phonon occupation of $\bar{n}_{min} \simeq 0.5$ is still achieved for $Q \simeq 10^4$, $\lambda/\omega = 0.05$, and polarizations $p > 0.48$ [Fig.4.6(b)]. The minimal phonon occupation reduces to $\bar{n}_{min} = 0.2$ at $p = 1$. An occupation of $\bar{n}_{min} \simeq 0.5$ is also obtained for $Q \simeq 10^5$ and $p > 0.3$ ($\bar{n}_{min} = 0.05$ at $p = 1$).

Motivated by a recent experiment that reported large spin-orbit interaction coupling Δ_{SO} [179], one can also consider coupling constants of order $\lambda/\omega = 0.2$ which implies a strong reduction of the polarization required for cooling. As an example, $\bar{n}_{min} \simeq 0.5$ for $Q \simeq 10^4$ and $p > 0.3$. Therefore, we conclude that even for modest polarizations, which appears feasible in promising experiments with CNTQDs [147, 180, 181], quantum ground-state cooling is achievable.

4.5.3 Single polarized lead

In the previous section, we discussed the phonon occupation for fully polarized ferromagnetic leads. A finite polarization reduces the vibration-assisted spin-flip rates γ_{lr}^{s} and γ_{rl}^{s} in comparison to those rates at fully polarized ferromagnets. Additionally, as shown in Eq. (4.34), we have to consider the vibration-assisted spin-flip processes involving a single lead, with rates γ_{ll}^{s} and γ_{rr}^{s}, which drive the oscillator to thermal equilibrium.

In this section, we show that active cooling can be achieved even for a single polarized lead. We assume a polarized left lead ($-1 \leq p_l < 0$) and a normal right lead ($p_r = 0$). In Fig. 4.7, we show the result for the minimum of the phonon occupation $\bar{n}_{min}$ on the surface (ε_0, eV) as a function of the energy separation ε_z. We remark that, for a single polarized lead, ground-state cooling is achieved with $\bar{n}_{min} \ll 1$ at resonance $\varepsilon_z = \omega$. The reason for the strong cooling can be understood by considering the phonon occupation Eq. (4.34) which in the high-voltage approximation $eV \gg (T, \omega)$ can be written as

$$\bar{n} \simeq \frac{(\gamma_0 + \delta\gamma_{ll} + \delta\gamma_{rr}) n_B(\omega) + \gamma_{lr}^{-}}{\gamma_0 + \delta\gamma_{ll} + \delta\gamma_{rr} + \delta\gamma_{lr}}. \tag{4.43}$$

At $p_l = -1$ the rates $\delta\gamma_{ll}$ are zero and only the spin-flip processes at the right lead with a rate $\delta\gamma_{rr}$ are active to drive the oscillator towards thermal equilibrium. However, such processes give a relevant contribution to the damping γ only if one of the two spin levels is aligned or close to the right chemical potential μ_r. Therefore, if we have, for instance, $\varepsilon_{\pm} \gg \mu_r$, these processes are strongly suppressed and ground-state cooling can still be achieved at resonance. In a simple picture, the left lead acts essentially as a source of spin-polarized electrons with the same spin orientation of the lower energy-level in the dot. However, at finite polarization of the left lead, $-1 < p_l < 0$,

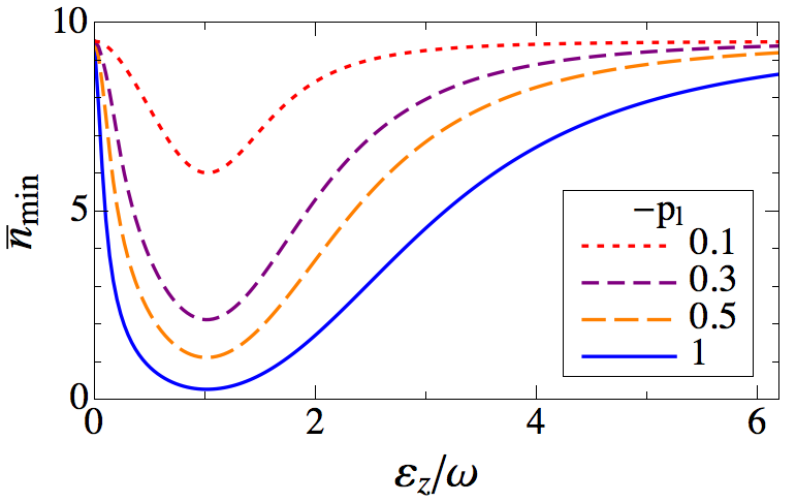

Figure 4.7: Minimal phonon occupation on the surface (ε_0, eV) for a polarized left lead with $-1 \leq p_l < 0$ and a normal right lead as a function of ε_z/ω. The parameters are $\Gamma_l = \Gamma_r = 0.2\omega$, $T = 10\omega$, $Q = 10^4$ and $\lambda = 0.05\omega$. The minimum of $\bar{n}_{min}$ is approached at resonance $\varepsilon_z = \omega$ with $\bar{n}_{min} \simeq 0.2$ for a fully polarized left lead $p_l = -1$.

the spin-flip processes at the left lead are unavoidable ($\delta\gamma_{ll} \neq 0$) so that cooling is reduced.

Concerning the state of the oscillator, the configuration $-1 \leq p_l < 0$ and $p_r = 0$ discussed so far is equivalent to the configuration $p_l = 0$ and $0 < p_r \leq 1$. Since the left lead is a normal metal, both the spin-up and spin-down level can be occupied by an electron tunneling from the left to the dot's levels at voltages $eV > 0$. Assuming for simplicity the resonant case $\varepsilon_z = \omega$ and $p_r = 1$, the right lead then selects only spin-up electrons. The process of an absorption of a vibrational energy quantum, where the spin-down electrons flips the spin and tunnels to the right lead, occurs in resonance and thus leads again to active cooling of the oscillator.

4.6 Strong heating and mechanical instability

For strong enough driving, the system can approach a mechanical instability when the total damping rate vanishes $\gamma_{tot} = 0$. To gain an insight into the problem, we consider the state of the mechanical oscillator for fully polarized ferromagnets ($p_r = -p_l = p = 1$). This assumption simplifies the discussion as the single lead spin-flip processes vanish ($\delta\gamma_{ll} = \delta\gamma_{rr} = 0$).

A simple picture of the process of energy pumping is shown in Fig. 4.8. Contrary to the active cooling processes in Fig. 4.4 transport occurs from the right to the left lead. A spin-up electron from the right lead tunnels to the spin-up level of the quantum dot. The it flips the spin and thereby give an energy quantum of ω to the resonator

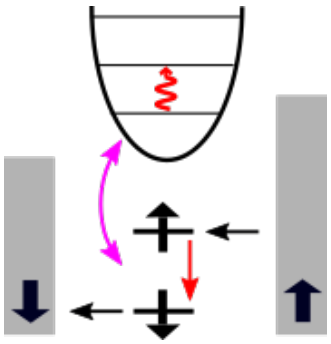

Figure 4.8: Schematic sketch of basic processes for energy pumping. An spin-up electron from the right lead tunnels to the spin-up level of the quantum dot. It flips the spin and tunnels to the spin-down level and thereby pumps energy to the resonator and increases the phonon occupation.

and increase the phonon occupation.

4.6.1 Fully polarized ferromagnetic leads

In the limit of fully polarized leads, the expression for the phonon occupation Eq. (4.33) reads as

$$n_{(p=1)}=\frac{(\gamma_{lr}^{+}-\gamma_{rl}^{-})n_B(\omega+eV)+(\gamma_{rl}^{+}-\gamma_{lr}^{-})n_B(\omega-eV)}{\delta\gamma_{lr}+\delta\gamma_{rl}}. \tag{4.44}$$

The formula for the mechanical damping Eq. (4.27) reduces to $\gamma=\delta\gamma_{lr}+\delta\gamma_{rl}$ and the total sign of the damping coefficient is now determined by the competition between the absorption and emission processes. Furthermore, we can consider the high-voltage approximation $|eV|\gg(T,\omega)$ in which, for instance, electrons tunneling from the right to the left lead are Pauli blocked for positive applied voltage and we can neglect the corresponding rate $\gamma_{rl}^{s}\ll\gamma_{lr}^{s}$. The mechanical damping reduces to $\gamma\simeq\delta\gamma_{lr}$ for $eV>0$ and $\gamma\simeq\delta\gamma_{rl}$ for $eV<0$. Similarly, the phonon occupation reads as

$$n_{(p=1)} \simeq n_{(p=1)}^{(+)}=\left(\gamma_{lr}^{+}/\gamma_{lr}^{-}-1\right)^{-1} \quad (eV>0) \tag{4.45}$$

$$n_{(p=1)} \simeq n_{(p=1)}^{(-)}=\left(\gamma_{rl}^{+}/\gamma_{rl}^{-}-1\right)^{-1} \quad (eV<0)\,. \tag{4.46}$$

Equations (4.45) and (4.46) show that the phonon occupation is determined by the ratio between the absorption and emission rates. In particular, strong heating ($n\gg1$) is expected if the mechanical damping coefficient vanishes $\delta\gamma_{\alpha\beta}\to0^{+}$.

To understand the behavior of these rates, it is useful, as a first step, to approximate the rates for relatively large energy separation ε_z such that mainly either the spin-up or spin-down level is involved in transport. For this reason, we first discuss the phonon occupation for $\varepsilon_z\gg\omega$ without intrinsic damping ($\gamma_0=0$) and, second, we focus on the resonant case $\varepsilon_z=\omega$ including also the intrinsic damping ($\gamma_0>0$).

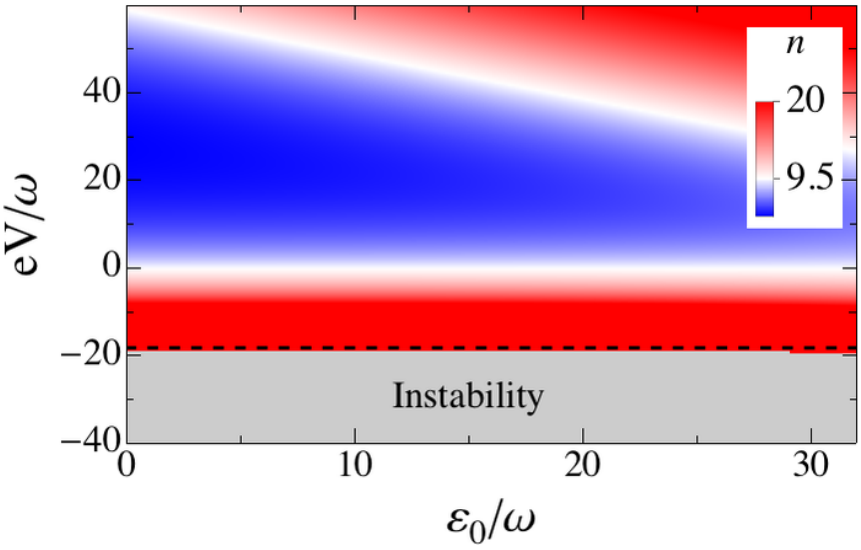

Figure 4.9: Phonon occupation n as function of the bias voltage eV and gate voltage ε_0. The parameters are $p_l = -1$ and $p_r = 1$, $\Gamma_l = \Gamma_r = 0.2\omega$, and $T = 10\omega$. White color corresponds to $n_B(\omega) \approx 9.5$. Here we assume a vanishing external damping $\gamma_0 = 0$, a large spin splitting $\varepsilon_z = 10T = 100\omega$, and the chemical potential fixed to $\mu_r = \varepsilon_0 - eV$ and $\mu_l = \varepsilon_0$. The instability regions (in gray) correspond to $\gamma < 0$ and the dashed (black) line correspond to the analytical formula for the threshold $\gamma = 0$ (see text).

Single spin-level regime

The phonon occupation for $\varepsilon_z = 10T$ and vanishing external damping is reported in Fig. 4.5(a). We observe that for $eV > 0$ the oscillator can be cooled or heated, whereas for $eV < 0$ the oscillator is strongly heated by increasing the bias voltage. The region $eV > 0$ was discussed in Sec. 4.5 and hereafter we focus on $eV < 0$. Beyond a certain threshold $-eV \gtrsim 20\omega$ the system approaches a mechanical unstable region. This threshold is given by a vanishing damping $\gamma = 0$. Approaching the threshold $\gamma = 0$ from the stable region $\gamma > 0$, we have that the oscillator is strongly overheated with $n \gg n_B(\omega)$ since the mechanical oscillator is almost undamped for $\gamma \gtrsim 0$ and it can store a large amount of energy.

As we explained, for $p = 1$ the rates $\gamma^{s\sigma}_{\alpha\alpha}$ vanish, as the electron cannot return to its original lead after a spin-flip. Additionally, since $\Gamma^+_l = \Gamma^-_r = 0$, one of the two terms appearing in Eq. (4.30) is zero for the spin-resolved rates $\gamma^{s\sigma}_{lr}$ and $\gamma^{s\sigma}_{rl}$. Assuming symmetric contacts $\Gamma^-_l = \Gamma^+_r = \Gamma$ and setting $T^s_\pm = \lambda^2\Gamma/[\Gamma^2 + (s\omega \pm \varepsilon_z)^2]$, the spin-resolved rates reduce to

$$\gamma^{s\sigma}_{lr} = T^s_- f_l(\varepsilon_\sigma - s\omega\delta_{\sigma+})\left[1 - f_r(\varepsilon_\sigma + s\omega\delta_{\sigma-})\right] , \tag{4.47}$$

$$\gamma^{s\sigma}_{rl} = T^s_+ f_r(\varepsilon_\sigma - s\omega\delta_{\sigma-})\left[1 - f_l(\varepsilon_\sigma + s\omega\delta_{\sigma+})\right] . \tag{4.48}$$

The processes associated to the rates $\gamma^{s\sigma}_{lr}$ in Eq. (4.47) are shown in Figs. 4.10(a)-

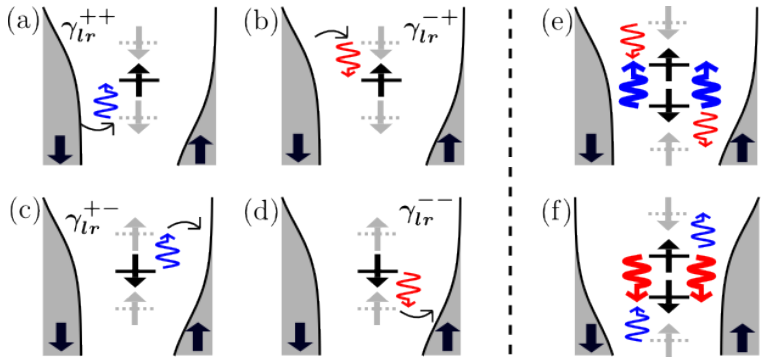

Figure 4.10: Schematic picture of the energy levels, Fermi functions, and the spin-flip processes with rate $\gamma_{lr}^{s\sigma}$ for fully polarized ferromagnets. In (a)-(d), a single level contributes to the inelastic transport which is characterized by the absorption (upwards blue arrows) or the emission (downward red arrows) of a vibrational energy quantum. In (e) and (f), the resonant condition $\varepsilon_z = \omega$ is fulfilled. When the transport is mainly determined by the process shown in (e), optimal ground-state cooling of the oscillator is achieved. On the contrary, when the transport is dominated by the process shown in (f), a strong heating occurs which is the precursor of a mechanical instability (see also Fig. 4.11).

4.10(d) for $eV > 0$.

The behavior of the phonon occupation in Fig. 4.9 can be now understood by considering the rates in Eqs. (4.47) and (4.48). For instance, in Fig. 4.5(a), we chose the chemical potentials as $\mu_l = \varepsilon_0$ and $\mu_r = \varepsilon_0 - eV$ such that for $eV < 0$ mainly the spin-up level contributes to transport. In the high-voltage approximation $|eV| \gg (T, \omega)$, we have $\gamma_{lr}^{s\sigma} \ll \gamma_{rl}^{s\sigma}$. The damping coefficient can then be approximated by the difference of two rates as $\gamma = \gamma_{rl}^{++} - \gamma_{rl}^{-+}$. The electrons tunnel from the right lead to the dot and finally to the left accompanied by a spin-flip. Further approximating the Fermi functions in the rates $\gamma_{rl}^{\sigma+}$ by $f_r \simeq 1$ and $f_l = 0$, we obtain that the damping scales as $\gamma \sim T_+^+ - T_+^-$. In other words, the instability of the oscillator is related to the different magnitude of the transmissions. When the transmission for emission processes (heating) is larger than the transmission for absorption ones (cooling), i.e., $T_+^- \gtrsim T_+^+$, one obtains that the damping coefficient is negative.

Equations (4.47) and (4.48) allow us to discuss the onset of the instability. To determine the threshold $\gamma = 0$ quantitatively, we cannot use the high voltage approximation since the instability occurs at relatively small voltages. In the limit of $\varepsilon_z \gg \omega$, the damping reduces to $\gamma = \gamma_{rl}^{++} - \gamma_{rl}^{-+} + \gamma_{lr}^{++} - \gamma_{lr}^{-+}$. Then, setting $\gamma = 0$, we obtain the equation for the onset of instability for vanishing intrinsic damping ($\gamma_0 = 0$). To leading order in T/ε_z the result reads as $eV = -T \ln[1 + (\omega + \varepsilon_z/2)/T]$ pointing out that the critical line does not depend on the level position $\mu - \varepsilon_0$ as shown in Fig. 4.5(a).

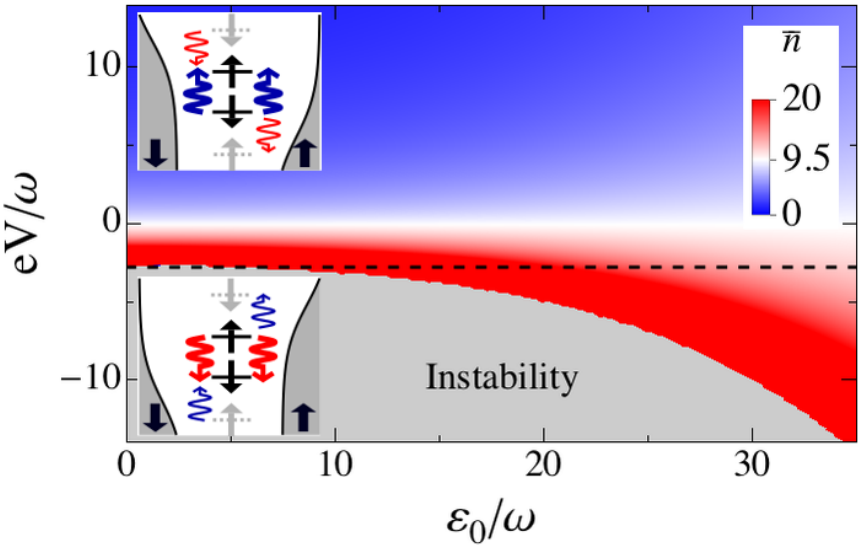

Figure 4.11: Phonon occupation $\bar{n}$ as function of the bias voltage eV and gate voltage ε_0 for fully polarized leads and the resonant regime. We consider the resonant regime $\varepsilon_z = \omega$ with $\gamma_0 = 10^{-5}\omega$, $\lambda/\omega = 0.01$, and $\mu_{l,r} = \varepsilon_0 \pm eV/2$. The other parameters are $p_l = -1$ and $p_r = 1$, $\Gamma_l = \Gamma_r = 0.2\omega$, and $T = 10\omega$. White color corresponds to $n_B(\omega) \approx 9.5$. The instability region (in gray) corresponds to $\gamma_{tot} < 0$ and the black dashed line shows the analytic formula for the threshold $\gamma_{tot} = 0$ (see text). The upper and lower sketches indicate the schematic behavior of the energy levels and the inelastic vibration assisted spin-flip processes which lead to cooling for $eV > 0$ and heating for $eV < 0$, respectively. Absorption (emission) of a vibrational energy quantum occurring in resonance is shown as blue (red) bold wiggled arrows.

Resonant regime

So far, we considered a large energy splitting $\varepsilon_z \gg \omega$ without intrinsic damping. In Fig. 4.11, we show the phonon occupation at resonance $\varepsilon_z = \omega$, an intrinsic quality factor damping $Q = 10^5$, a spin-vibration coupling of $\lambda = 0.01\omega$ and symmetrically applied voltage $\mu_{l,r} = \varepsilon_0 \pm eV/2$.

In the resonant case, the virtual levels at energy $\varepsilon_+ - \omega$ and $\varepsilon_- + \omega$ coincide, respectively, with the real dot spin levels ε_- and ε_+ (Fig. 4.10 (e) and (f)). This yields a strong enhancement of the vibration assisted emission or absorption processes. For $eV > 0$, strong cooling $\bar{n} \ll n_B(\omega)$ is achieved as discussed in Ref. [151]. By reversing the voltage $eV < 0$, we pass to the regime of strong heating and the oscillator becomes unstable. This result depends on our choice for the energy of the two levels in the dot ($\varepsilon_+ > \varepsilon_-$ for spin up and down) and for the orientation of the left and right ferromagnets. Changing exclusively the two levels or reversing exclusively the magnetization of the leads, the phonon occupation is still given by Fig. 4.5(b) replacing $V \to -V$.

Since now both levels are involved in transport, we have to analyze Eq. (4.28) for the rates to discuss the instability. In the high-voltage approximation, we have again that $\gamma \simeq \delta\gamma_{lr}$ for $eV > 0$ and $\gamma \simeq \delta\gamma_{rl}$ for $eV < 0$. In the first case, we have $\delta\gamma_{lr} > 0$, such that the system remains stable. In the second case, we found $\delta\gamma_{rl} < 0$ for sufficient large voltages so that the damping rate γ becomes negative.

As shown in Fig. 4.5(b), the system becomes unstable even for relatively low bias voltages. To evaluate the threshold $\gamma_{tot} = 0$, we consider the high-temperature limit $T \gg (eV, \varepsilon_0, \varepsilon_z)$. Then, we expand the Fermi functions in Eq. (4.28) to lowest order in ε/T and perform the integration in Eq. (4.28). As a result we obtain the line for which the total damping rate vanishes,

$$eV = -\left[\frac{4\Gamma^2 + \omega^2}{\omega} + 16\,\gamma_0\,T\,\Gamma\frac{4\Gamma^2 + \omega^2}{\lambda^2\omega^2}\right], \tag{4.49}$$

with $\Gamma_l = \Gamma_r = \Gamma$. This line in plotted in Fig. 4.5(b) and agrees with the onset of the instability for $\varepsilon_0 \lesssim T \approx 10\omega$. Notice that increasing the intrinsic damping γ_0 reduces the region of instability by shifting the critical voltage to higher values. As shown Fig. 4.5(a), for larger ε_0, the approximation $T \gg \varepsilon_0$ gradually breaks down and becomes less accurate. In this regime, the instability line strongly depends on the intrinsic damping.

4.6.2 Parallel magnetization configuration

We briefly summarize the result obtained in the parallel magnetization configuration. For fully polarized leads $p_r = p_l = \pm 1$, all the vibration-assisted inelastic spin flip rates in Eq. (4.28) vanish since these rates are proportional to the products $\Gamma^+_\alpha\Gamma^-_\beta = 0$. An electron can neither tunnel from one lead to the other lead nor to the initial lead accompanied by an inelastic spin flip and, according to Eq. (4.32), the oscillator remains at equilibrium $\bar{n} = n_B(\omega)$.

At finite but equal polarization $p_r = p_l \neq \pm 1$, it is instructive to compare the majority and minority charge carriers involved in an inelastic tunneling event in the parallel and antiparallel configuration. In both parallel and antiparallel configurations, the processes associated to the rates $\gamma^s_{\alpha\alpha}$ connect the majority spin carriers with the minority carriers of the same lead. The processes associated to the rates γ^s_{lr} and γ^s_{rl} in the antiparallel configuration connect the majority carriers from one lead with the majority carriers of the opposite lead. However, in the parallel configuration, the rates γ^s_{lr} and γ^s_{rl} connect the majority spin carriers with the minority carriers leading to a suppression of these rates. In the parallel configuration, we found that an applied voltage increases the phonon occupation $\bar{n} > n_B(\omega)$ and neither active cooling neither mechanically instability occur.

4.7 Current

In this section, we investigate the influence of the spin-vibration interaction and the resulting nonequilibrium phonon occupation on the current through the quantum dot.

To this end, we calculate the corrections to the current to the leading order in the spin-vibration coupling and for two different cases.

The general expansion for the current is derived in Sec. 4.7.1. In Sec. 4.7.2, we assume that the oscillator is strongly coupled to the external bath such that $\gamma_0 \gg \gamma$. Then, the time for thermal relaxation is much smaller than the time associated to the inelastic spin-flip processes to set the oscillator in an unequilibrated state. The oscillator is mainly in an equilibrated state and its phonon occupation can be described by the Bose distribution function. This regime is referred as the regime of thermal or equilibrated vibration.

In Sec. 4.7.3, we consider the regime $\gamma_0 \ll \gamma$. Then, as we discussed in the previous section, the oscillator is driven by the current itself towards a nonequilibrium phonon occupation. This regime is referred as the regime of nonequilibrated vibration.

4.7.1 General expansion for the current

The current is obtained by inserting the Keldysh and retarded elements of the expansion (4.37) in the expression for the current (4.36). The result can be written as an elastic current I_0 in the absence of the spin-vibration coupling, an elastic and an inelastic correction I_{ec} and I_{in},

$$I = I_0 + I_{ec}\left[\check{\Sigma}\right] + I_{in}\left[\check{\Sigma}\right]. \tag{4.50}$$

The result for the elastic current corresponds to the well-known formula

$$I_0 = \frac{e}{h}\int d\varepsilon \sum_\sigma 4\Gamma_l^\sigma \Gamma_r^\sigma |G_\sigma^R(\varepsilon)|^2 \left(f_l(\varepsilon) - f_r(\varepsilon)\right), \tag{4.51}$$

with the Green's function given by the Eqs. (4.20) and (4.21). Both I_{ec} and I_{in} are proportional to λ^2 and they are functional of the electron self energies $\check{\Sigma}$ appearing in Eqs. (4.38) and (4.39) which are related to the phonon Green's function $\check{D}$.

4.7.2 Current with equilibrated vibration

Assuming $\gamma_0 \gg \gamma$, we approximate $\gamma_{tot} \simeq \gamma_0$ in Eq. (4.24) for the retarded/advanced component of the phonon Green's function. Correspondingly, we neglect Π^K (related to the spin-vibration interaction) as $|\Pi^K| \ll |\Sigma_0^K|$ in Eq. (4.25) for the Keldysh component of the phonon Green's function. Inserting the resulting phonon Green's function in the electronic self-energies in Eqs. (4.38) and (4.39), we calculate the currents I_{ec} and I_{in} in Eq. (4.50). In the remaining part of this section, we discuss separately the elastic corrections to the linear conductance and the inelastic corrections to the differential conductance. Thereby, we mainly focus on the characteristic features of the ferromagnetic leads and the spin-vibration interaction in the transport.

Elastic correction with equilibrated vibration

The elastic correction of our model Hamiltonian can be written as

$$I_{ec} = \frac{e}{h}\int d\varepsilon \sum_{\sigma} 8\Gamma_l^{\sigma}\Gamma_r^{\sigma}|G_{\sigma}^{R}(\varepsilon)|^2 \\ \mathrm{Re}[G_{\sigma}^{R}(\varepsilon)\Sigma_{-\sigma-\sigma}^{R}(\varepsilon)][f_l(\varepsilon)-f_r(\varepsilon)]\,. \tag{4.52}$$

We focus the discussion on the linear conductance at $T = 0$. In this case, the retarded self-energy $\Sigma_{\sigma\sigma}^{R}$ inside the integral of Eq. (4.52) can be calculated analytically in the limit $\gamma_0 \ll (\omega, \Gamma_l, \Gamma_r, eV)$ and the explicit expression is given in Appendix B.2. The correction to the linear conductance $G = dI_{ec}/dV|_{V=0}$ reduces to ($\varepsilon_s = \varepsilon + s\omega$)

$$\frac{G_{ec}}{G_0\lambda^2} = \sum_{s\sigma} \frac{2\Gamma^{-\sigma}\Gamma_l^{\sigma}\Gamma_r^{\sigma}\varepsilon_{\sigma}}{(\Gamma^{\sigma 2}+\varepsilon_{\sigma}^2)^2[\Gamma^{-\sigma 2}+(\varepsilon_{-\sigma}+s\omega)^2]} \left(\frac{\varepsilon_{-\sigma}+s\omega}{\Gamma^{-\sigma}} \right. \\ \left. \left(1+\frac{2s}{\pi}\tan^{-1}\left(\frac{\varepsilon_{-\sigma}}{\Gamma^{-\sigma}}\right)\right) - \frac{s}{\pi}\ln\left(\frac{\omega^2}{\varepsilon_{-\sigma}^2+\Gamma^{-\sigma 2}}\right)\right), \tag{4.53}$$

with $G_0 = 2e^2/h$, $\Gamma^{\sigma} = \Gamma_l^{\sigma} + \Gamma_r^{\sigma}$ and $\mu_l = \mu_r = 0$. In Figs. 4.12(a) and (b), we show the correction to the elastic conductance for the parallel ($p_r = p_l = 0.8$) and antiparallel ($p_r = -p_l = 0.8$) configuration with $\Gamma_l = \Gamma_r = \Gamma$.

In the parallel configuration, we observe that the correction at $G_{ec}(\varepsilon_0)$ differs from the corrections at $G_{ec}(-\varepsilon_0)$ whereas we find that $G_{ec}(\varepsilon_0) = G_{ec}(-\varepsilon_0)$ in the parallel configuration. Such a behavior is explained by the polarization of the ferromagnetic leads. In the parallel configuration, the spin-up level is coupled stronger to the leads than the spin-down level. The different couplings lead to sharp features in the correction to the conductance close to the spin-down level, whereas close to the spin-up

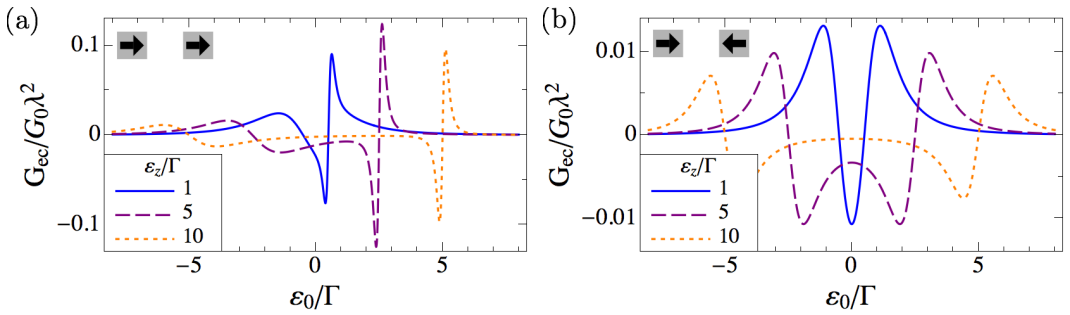

Figure 4.12: Elastic correction to the linear conductance at $T = 0$, symmetric coupling $\Gamma_l = \Gamma_r = \Gamma$, $\omega = 5\Gamma$, and zero chemical potentials. (a) Parallel magnetization configuration ($p_r = p_l = 0.8$). (b) Antiparallel configuration ($p_r = -p_l = 0.8$). The different magnetization configurations in (a) and (b) lead to $G_{ec}(\varepsilon_0) \neq G_{ec}(-\varepsilon_0)$ in (a) whereas the correction is symmetric $G_{ec}(\varepsilon_0) = G_{ec}(-\varepsilon_0)$ in (b). In the range $\varepsilon_+\varepsilon_- < 0$ the correction to the conductance is negative (see text).

level the correction is broadened. On the contrary, for the antiparallel configuration, there are always electrons of the majority and minority spin involved when an electron tunnels from the left to the right lead. This gives rise to the symmetric behavior $G_{ec}(\varepsilon_0) = G_{ec}(-\varepsilon_0)$.

We notice that the elastic correction to the conductance in Fig. 4.12 can be either positive or negative as varying ε_0 both for the parallel and antiparallel configurations. Such a behavior is different from the results obtained in the Anderson-Holstein model for a spinless dot level in which the sign of the conductance corrections does not change to the first leading order in the electron-vibration coupling [165].

The negative correction to the conductance occurs due to interference effects [see Fig. 4.13]. At finite polarization, an electron with spin σ can pass the quantum dot through two different paths. The first path corresponds the elastic tunneling of an electron with spin-up (-down) through the spin-up (-down) level without interacting with the oscillator. The second path is associated to the spin-vibration interaction. For instance, an electron of spin σ can also tunnel elastically from one lead to the other lead by flipping its spin and virtually exciting the oscillator. The latter is excited by an emission (absorption) of a vibrational energy quantum followed by an absorption (emission) of a vibrational energy quantum so that the electron ends up at the same energy of its initial state [see Fig. 4.3(b)].

In the range $\varepsilon_+\varepsilon_- < 0$, the spin-up level is above the Fermi energy and particle-like processes contribute to the correction whereas the spin-down level is below the Fermi energy and hole-like processes dominate. The transmission amplitude of the electronlike and holelike paths differ by a phase of π leading to the negative correction to the conductance in the range $\varepsilon_+\varepsilon_- < 0$ in similar way to the interference between the paths of two levels [182, 183].

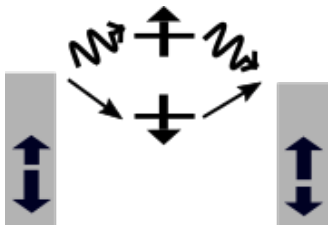

Figure 4.13: Interference of two possible paths leading to a negative correction to the conductance in Fig. 4.12. A small voltage is applied to the left lead such that transport occurs from left to right. At finite polarization, a spin-down electron can tunnel elastically from the left to the right lead and passes through the spin-down level of the quantum dot. Alternatively, the electron can tunnel through the spin-up level by virtually exciting the resonator. In this processes the electron flips the spin twice such that for both paths the initial and the final state are the equal.

Inelastic current with equilibrated vibration

In the limit $\gamma_0 \ll (\omega, \Gamma_l, \Gamma_r, T, eV)$, the inelastic current can be written in terms of the rates $\gamma^s_{\alpha\beta}$ of Eq. (4.28) as

$$I_{in} = \frac{2e}{\hbar}\left[(n_B(\omega)+1)\left(\gamma^-_{lr}-\gamma^-_{rl}\right)+n_B(\omega)\left(\gamma^+_{lr}-\gamma^+_{rl}\right)\right]. \tag{4.54}$$

Transport is possible via the emission and the absorption of vibrational energy quanta. At zero temperature, $n_B(\omega)=0$, and the threshold voltage for having an emission of a vibrational energy quantum is $eV=\omega$. Note that, as we calculated the inelastic current to the leading order in the coupling, only single-phonon processes are taken into account in Eq. (4.54).

The differential conductance $G_{in} = dI_{in}/dV$ at zero temperature can be written as

$$\frac{G_{in}}{G_0\lambda^2} = \sum_{\sigma\alpha}\Gamma^{\sigma}_{\alpha}\Gamma^{-\sigma}_{-\alpha}|G^R_{\sigma}(\mu_\alpha)G^R_{-\sigma}(\mu_\alpha-\alpha\omega)|^2\theta(\mu_l-\mu_r-\omega), \tag{4.55}$$

with $(\alpha,\beta)=(l,r)=\pm$ and the retarded Green's function given by Eq. (4.20). Figures 4.14 (a) and (b) show the inelastic differential conductance at zero temperature in the parallel and antiparallel configurations, respectively. The voltage is applied symmetrically $\mu_l = eV/2$ and $\mu_r = -eV/2$, the energy level on the dot is set to $\varepsilon_0 = 2\omega$, and the polarization is $p = p_r = p_l = 0.4$ for the parallel configuration and $p = p_r = -p_l = 0.4$ for the antiparallel configuration. In Fig. 4.14, the inelastic processes can occur at the voltages $eV/2 = \varepsilon_\pm$ and $eV/2 = \varepsilon_\pm + \omega$. To illustrate the behavior of these inelastic peaks, we discuss in details the antiparallel case shown in Fig. 4.14(b) for $\varepsilon_z = 1.5\omega$. The first peak appears due to the resonance of the left Fermi level with the spin-down level on the quantum dot ($eV/2 = \varepsilon_-$). In this case, a spin-down electron is transferred to the quantum dot followed by a spin flip and an emission of a vibrational energy quantum when it moves to the right barrier [see

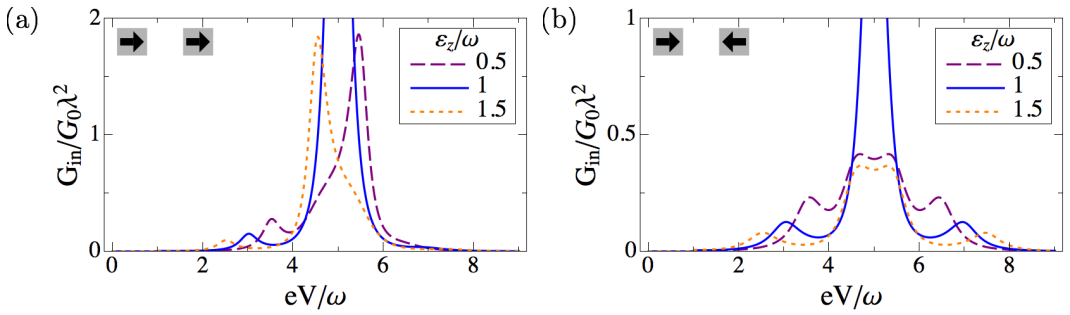

Figure 4.14: Inelastic contribution to differential conductance at zero temperature and $\varepsilon_0 = 2\omega$, $\Gamma_l = \Gamma_r = 0.2\omega$, and symmetrically applied voltage. In (a), the polarization of the ferromagnetic leads are aligned parallel $p_l = p_r = 0.4$. In (b), we show the antiparallel configuration with $p_r = -p_l = 0.4$. The peaks of the inelastic differential conductance appear at voltages $eV/2 = \varepsilon_\pm$ and $eV/2 = \varepsilon_\pm + \omega$ (see text).

the schematic picture in Fig. 4.10(d)]. At higher voltage, a second peak appears at $eV/2 = \varepsilon_- + \omega$. In this case, a spin-up electron tunneling from the left lead can enter the dot spin-down level by emitting a vibrational energy quantum. Similar processes occur at higher voltage when the Fermi energy in the left lead is in resonance with the spin-up level of the quantum dot $eV/2 = \varepsilon_+$ or at the voltage $eV/2 = \varepsilon_+ + \omega$, the latter case reported in Fig. 4.10(b).

At resonance $\varepsilon_z = \omega$, two peaks merge into a single peak and the differential conductance is strongly increased compared to the case out of resonance. Following similar arguments reported in Sec. 4.6, this is due to the virtual level $\varepsilon_- + \omega$ coinciding with the real dot level ε_+.

4.7.3 Current with unequilibrated vibration

As a next step, we discuss the current for the case of unequilibrated vibration for antiparallel ferromagnetic leads. We found clear signatures of the nonequilibrium phonon occupation in terms of a suppression (enhancement) of the current when the phonon occupation of the oscillator decreases (increases) compared to thermal vibration.

For the regime of unequilibrated vibration, we use the full phonon Green's functions (4.24) and (4.25) to calculate the electron self-energies (4.38) and (4.39) and, hence, the current Eq. (4.50) in the limit $\gamma_{tot} \ll (\omega, \Gamma_l, \Gamma_r, T, eV)$. The results are similar to the previous case for the equilibrated vibration. For instance, the inelastic correction I_{in} is similar to (4.54) in which we have to replace the thermal phonon occupation $n_B(\omega)$ with the nonequilibrium occupation $\bar{n}$ as given by Eq. (4.32). For oscillators with very high quality factor, we have that $\bar{n}$ is essentially n, as given by Eq. (4.32). A similar approach was used in other nanomechanical systems [176]. We consider such an approach reasonable for weak spin-vibration coupling and low current through the dot.

At the same time, it is also useful to discuss qualitatively the behavior of the system to understand the possible features appearing in the current-voltage characteristic associated to a strongly cooled or heated oscillator. A more refined self-consistent approach, as discussed in Ref. [108], is beyond the aim of this work.

We start with the discussion of fully polarized leads in the antiparallel configuration $p_r = -p_l = 1$. Notice that, in this case, the elastic contributions to the current vanish: $I_0 = 0$ [Eq. (4.51)] and $I_{ec} = 0$ [Eq. (4.52)], since the electrons have to change their spin when tunneling from one lead to another. This can happen only through inelastic phonon-assisted spin-flip processes. Therefore, the total current Eq. (4.50) reduces to the inelastic current I_{in} given by Eq. (4.54) with $n_B(\omega)$ replaced by $\bar{n}$. At resonance $\varepsilon_z = \omega$, such inelastic processes can cool the oscillator, $\bar{n} \ll n_B(\omega)$, for positive voltage $eV > 0$ [see Fig. 4.10(e)], whereas they can heat the oscillator, $\bar{n} \gg n_B(\omega)$, for negative voltage $eV < 0$ [see Fig. 4.10(f)].

In Fig. 4.15(a) and (b), we compare the current at resonance for equilibrated $[\gamma_0 \gg \gamma, \bar{n} \simeq n_B(\omega)]$ and unequilibrated vibration $[\gamma_0 \ll \gamma, \bar{n} \simeq n]$ for fully polarized antiparallel ferromagnets at finite temperature $T = 10\omega$. Essentially, the nonequilibrium phonon occupation corresponding to the current of Fig. 4.15(b) is shown in

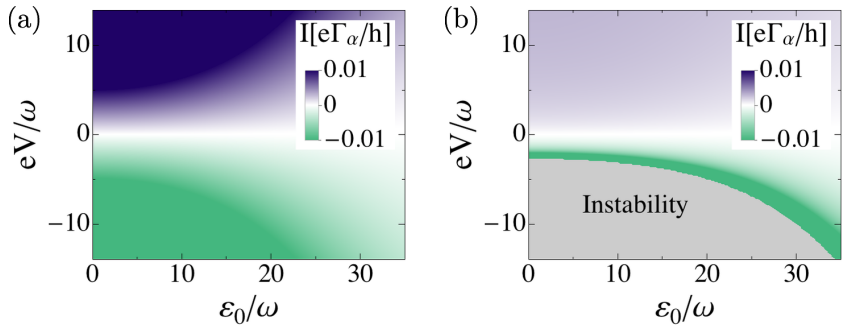

Figure 4.15: Inelastic current for fully polarized antiparallel ferromagnets ($p_r = -p_l = 1$) at resonance $\varepsilon_z = \omega$, $T = 10\omega$, and $\Gamma = 0.2\omega$. (a) Equilibrated vibration with $\bar{n} = n_B(\omega)$. (b) Unequilibrated vibration with a coupling constant $\lambda = 0.01\omega$ and an intrinsic damping of $\gamma_0 = 10^{-5}\omega$. The nonequilibrium phonon occupation $\bar{n}$ corresponding to the inelastic current in (b) is shown in Fig. 4.11. For $eV > 0$, the oscillator is strongly cooled $\bar{n} \ll n_B(\omega)$, leading to a suppression of the inelastic current in (b) compared to the case of equilibrated vibration in (a).

Fig. 4.11. For $eV > 0$, the current in Fig. 4.15(b) is strongly suppressed compared to the case of equilibrated vibration. In this case, the oscillator is cooled close to its quantum ground state ($\bar{n} \ll 1$) so that electrons can tunnel only through phonon-emission characterized by the rate γ_{lr}^{-} [see Eq. (4.54)]. Since in the cooling regime the relation $\gamma_{lr}^{-} \ll \gamma_{lr}^{+}$ holds, the current flowing through the dot results extremely low. In other words, increasing the current implies cooling the oscillator more efficiently which turns out in a reduction of the current itself. By contrast, for $eV < 0$, the current strongly decreases with the voltage for unequilibrated vibration before the regime of instability is reached at some threshold voltage.

In Figs. 4.16 (a) and (b), we show the inelastic current for equilibrated and unequilibrated vibration and different energy separation ε_z. The parameters are the same as in Fig. 4.15 but the current is shown as a function of voltage at $\varepsilon_0 = 0$. In Fig. 4.16(a), the vibration-assisted spin-flip rates give the largest contribution to the current at resonance $\varepsilon_z = \omega$. In Fig. 4.16 (b), we find that the current for $eV > 0$ is strongly suppressed compared to the current in Fig. 4.16(a). For $eV < 0$, the current sharply decreases since the oscillator approaches the mechanical instability. Out of resonance, the current decreases at larger negative voltages compared to the resonant case. The differences between equilibrated and unequilibrated vibration are also visible in the differential conductance dI_{in}/dV shown in Figs. 4.16 (c) and (d).

As last point, we analyzed the effects of a finite polarization in the current-voltage characteristic. We calculated the full current as given by Eq. (4.50) including the leading elastic term I_0 [Eq. (4.51)] and the elastic correction I_{ec} [Eq. (4.52)]. In Figs. 4.17 (a) and (b), we compare the current for equilibrated and unequilibrated vibrations at $p_r = -p_l = 0.5$. Here, we set $\lambda = 0.2\omega$ ($\omega = 2\pi \cdot 100$ MHz) for large spin-orbit coupling estimated by recently reported measurement for the spin-orbit

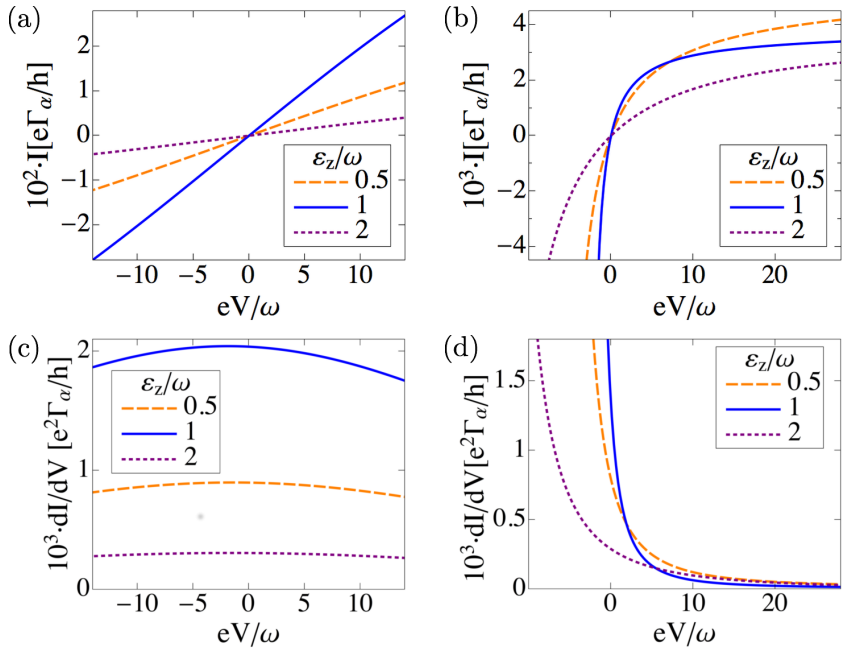

Figure 4.16: Current for equilibrated (a) and unequilibrated vibration (b) for fully antiparallel polarized ferromagnets $p_r = -p_l = 1$, $T = 10\omega$, $\varepsilon_0 = 0$, $\Gamma = 0.2\omega$, $\lambda = 0.01\omega$, and $\gamma_0 = 10^{-5}\omega$. For $eV > 0$, the current in (b) is suppressed compared to the current in (a). At negative voltages in (b), the oscillator approaches the mechanical instability and sharply decreases. In (c) and (d), we show the differential conductance dI_{in}/dV corresponding to (a) and (b), respectively.

coupling Δ_{SO} in carbon nanotubes [179]. We can still observe the strong suppression of the current at $eV > 0$ compared to equilibrated vibration in Fig. 4.17 (a) as well as the sharp decrease of the current when the oscillator approaches the mechanical instability. At positive voltages in Fig. 4.17(b), the current is dominated by the elastic current I_0, since the oscillator is strongly cooled. The sharp decrease at negative voltages occurs due to the corrections to the current. Note the different scales of the current in Fig. 4.17 and 4.16. The differential conductances corresponding to the current in Fig. 4.17 (a) and (b), are shown in Fig. 4.17 (c) and (d), respectively.

Summarizing this section we note that the current follows the nonequilibrium phonon occupation in some regime. Since the current strongly depends on the polarization and alignment of the ferromagnets, transport measurements with tunable nano-ferromagnetic contacts can provide a feasible way to detect the spin-vibration interaction in suspended CNTQDs.

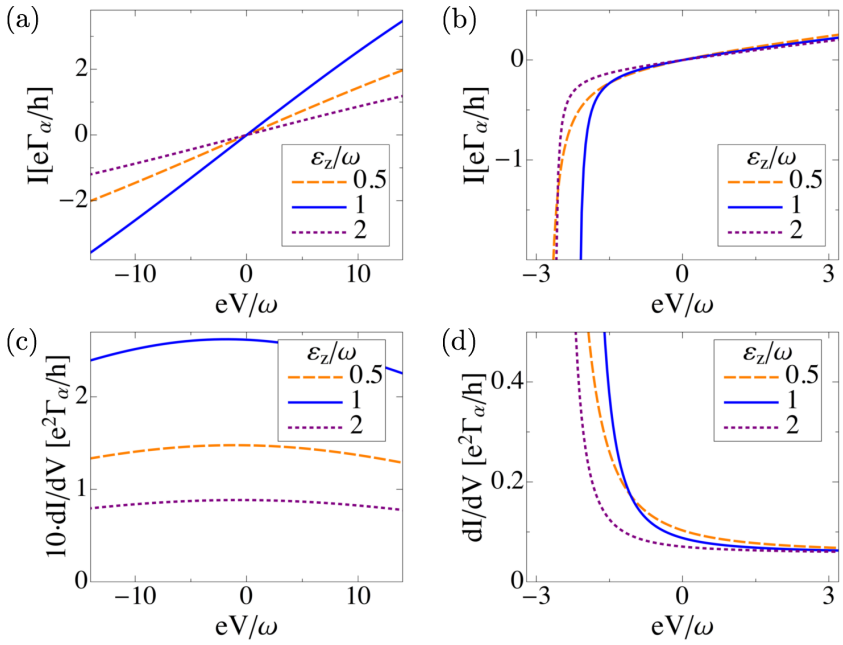

Figure 4.17: Current and differential conductance for equilibrated [(a) and (c)] and unequilibrated vibration [(b) and (d)] at polarization $p_r = -p_l = 0.5$, $T = 10\omega$, $\varepsilon_0 = 0$, $\Gamma = 0.2\omega$, $\lambda = 0.2\omega$, and $\gamma_0 = 10^{-5}\omega$. In (b) the current at $eV < 0$ decreases since the oscillator approaches the mechanical instability and the phonon occupation strongly increases. At $eV > 0$, the current is suppressed compared to the current in (a) since $\bar{n} < n_B(\omega)$. In (c) and (d), we show the differential conductance dI/dV corresponding to (a) and (b), respectively.

4.8 Summary

For a suspended CNTQD in a spin-valve geometry, we studied the spin-dependent current through two spin levels and the steady-state phonon occupation for a vibrational flexural mode in presence of a spin-vibration interaction. Such a spin-vibration interaction can have the origin in the spin-orbit coupling or a magnetic gradient.

We have shown that even weakly spin-polarized currents allow the control of the phonon occupation $\bar{n}$ in a way that a flexural mode can be cooled [$\bar{n} \ll n_B(\omega)$] or heated [$\bar{n} \gg n_B(\omega)$] or even driven towards a mechanical instability regime in which the mechanical damping becomes negative. Such a control can be achieved by manipulating several parameters of the system. In particular, it can be obtained using electrical fields, viz. varying the bias-voltage polarity or the gate voltage, or using magnetic fields, viz. by changing the orientation of the magnetic polarization of the ferromagnetic contacts or tuning the energy separation of the dot's spin levels.

The current shows characteristic features of the nonequilibrium phonon occupation and directly can be exploited to demonstrate the presence of the spin-vibration interaction and the non-thermal phonon occupation of the oscillator.

5 Ground-state cooling by noise-interference in Andreev reflection

We study the ground-state cooling of a mechanical oscillator linearly coupled to the charge of a quantum dot inserted between a normal metal and a superconducting contact. Such a system can be realized e.g. by a suspended carbon nanotube quantum dot with capacitive coupling to a gate. Applying a bias-voltage, inelastic Andreev reflections and inelastic quasiparticle tunneling will drive the resonator to a nonequilibrium state.

We analyze the junction in the regime of a small coupling between the quantum dot and the resonator. As main result of this chapter we obtain that the vibration-assisted reflections can occur through two distinct interference paths. The interference determines the ratio between the rates for absorption and emission processes of vibrational energy quanta. We show that ground-state cooling of the mechanical oscillator can be achieved in a wide parameter range and due to the interference even for many oscillator's modes simultaneously.

The chapter is organized as follows. In Sec. 5.1, we give a brief introduction to the topic. The subgap transport regime in which inelastic vibration-assisted Andreev reflections drive the phonon occupation to a nonequilibrium state is discussed in Sec. 5.2. In Sec. 5.3, we briefly consider the effect of the quasiparticles above the gap on the damping and the phonon occupation. Finally, we draw our conclusions in Sec. 5.4.

5.1 Introduction

Nanoelectromechanical and optomechanical systems promise to manipulate mechanical motion in the quantum regime using, respectively, electrons [134, 184] or photons [30], for the realization of fundamental tests of quantum mechanics in a hitherto unaccessible parameter regime. This goal requires that the mechanical oscillator to be in or near its quantum ground state, viz. $T \ll \omega$, with the mechanical frequency ω. Ground-state cooling, i.e. the average vibrational quanta $n \ll 1$, has been achieved in some nanomechanical devices, for instance, by direct cooling of an oscillator of GHz frequency using standard dilution refrigeration [28]. In another example, ground-state cooling was obtained using the so-called sideband method [185, 186] in which the resonator is coupled to a superconducting microwave electromagnetic cavity acting as an effective low-temperature bath of $T \lesssim 1\text{mK}$ [27].

Reducing the size as well the frequency of nanomechanical oscillators have the distinct advantages to increase the sensitivity as nanoscale detectors, the quality factor Q and the amplitude of the zero-point fluctuations. For this reason, suspended carbon

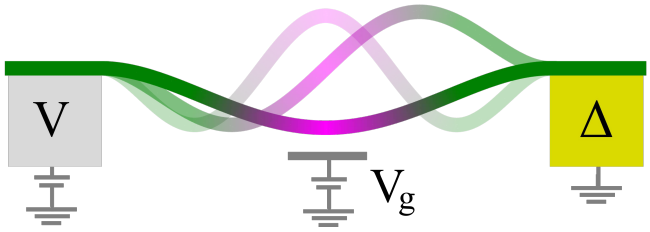

Figure 5.1: Sketch of a suspended carbon nanotube quantum dot between a normal and superconducting lead of gap Δ with a capacitive coupling between the dot's charge and the flexural mechanical modes. Applying a voltage V, inelastic vibration-assisted Andreev reflections (ARs) can cool one or several mechanical modes towards the quantum ground state.

nanotube quantum dots are considered good candidates: (i) their mechanical modes can reach elevated high quality factors $Q \sim 10^6$ without detriment of the electron transport properties [31, 125] and (ii) recent experiments also showed unprecedented control of the tunability of both electron transport and electromechanical coupling [135]. For such systems, approaching the quantum regime is still an open challenge due to the low-frequency spectrum of the flexural modes ($f \leq 100$MHz) which corresponds to demanding temperatures for electronic circuits.

Several and interesting theoretical proposals have been analyzed for achieving cooling or ground-state cooling by using electron transport [109, 168, 172, 174, 187–197], exploiting the interaction between the oscillator with a given quantum conductor. Most of them are closely related to the mechanism of the side-band cooling employed in opto-mechanical devices and, in a scattering picture, are based on an enhanced phonon absorption between two levels of energy difference ΔE. This enhancement is caused by a resonance in the density of states in the electronic system. As consequence, cooling is obtained in a limited range of the system parameters which satisfy a particular resonant condition for the oscillator's frequency $\omega = \Delta E$. We remark that cooling by pure electron transport has been experimentally achieved so far using a superconducting single electron transistor [198–200].

5.2 Subgap regime

In this chapter, we analyze a novel approach for the ground-state cooling of a CNTQD suspended between a normal metal and a superconducting lead, see Fig. 5.1. Focusing on the subgap transport regime - defined by $|eV| \ll \Delta$, with the bias-voltage V and the superconducting gap Δ - we found ground-state cooling without the fulfilling of any resonant condition and in a wide range of the transport parameters, in particular the gate voltage. We show that this result can be used for cooling many mechanical modes simultaneously. This effect results from the interference of the inelastic Andreev reflections (ARs). An example of an inelastic AR is shown in Fig. 5.2 with an incoming electron and the absorption of a phonon with frequency ω before the AR.

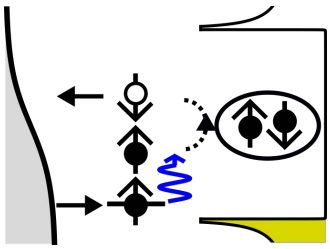

Figure 5.2: Example of inelastic vibration-assisted ARs allowing for the absorption of energy from the resonator (blue arrow).

A microscopic picture of this mechanism is the following. A discussed in Sec. 2.3.1, in a process of an elastic AR, an incident electron from the normal contact at energy less than Δ forms a Cooper pair in the superconductor with the reflection of a hole in the normal lead. Due to the interaction of the electrons and holes with the mechanical oscillator, ARs can be inelastic with the emission or absorption of a vibrational energy quantum. For an electron-vibration interaction smaller than the frequency of the resonator, one can consider such vibration-assisted AR involving only one phonon. Remarkably, a single vibration-assisted AR has two possible paths associated with the energy exchange with the resonator before or after an AR. An example of the two possible paths for an inelastic AR with one phonon absorption is shown in Fig. 5.3(a). The two paths can interfere in the total inelastic transmission amplitude. More precisely, the inelastic AR is related to the sum of two amplitudes $|A_s + B_s|^2$ with $s = +$ for absorption and $s = -$ for emission of one phonon and the amplitudes A, B for the two paths (phonon exchange After or Before an AR). Then, by varying the dot's energy level, one can tune the emission or absorption rates in a way that, for instance, phonon emission is greatly suppressed and the resonator is cooled, namely $|A_+ + B_+|^2 \gg |A_- + B_-|^2$ is fulfilled although the moduli of all the amplitudes are of the same order of magnitude. The interference is the dominant cooling process in the regime of a large coupling Γ_s to the superconductor, $\Gamma_s \gg \omega$. In the opposite regime $\Gamma_s \ll \omega$, cooling appears due to the resonance of both transmission amplitudes (see Fig. 5.3(a)). In this case $|A_+|^2 \gg |A_+|^2$ and $|B_+|^2 \gg |B_+|^2$. The latter regime allows for cooling of single modes by varying the gate voltage.

5.2.1 Model

For a quantum dot between a superconducting lead and a normal lead, we consider the Hamiltonian

$$\hat{H} = \hat{H}_n + \hat{H}_t + \hat{H}_{dS}\,. \tag{5.1}$$

The part of the normal lead and its tunnel coupling with the quantum dot reads

$$\hat{H}_n = \sum_{k\sigma} (\varepsilon_k - \mu - eV)\hat{c}^\dagger_{k\sigma}\hat{c}_{k\sigma} \tag{5.2}$$

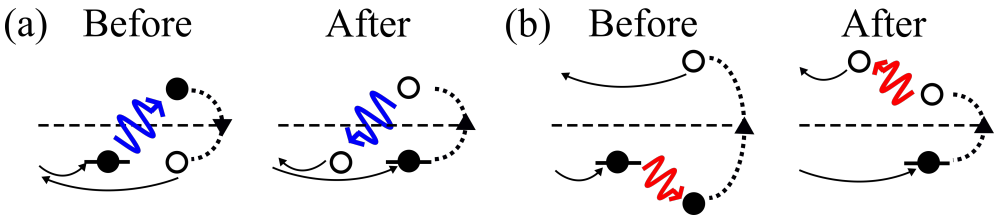

Figure 5.3: Schematic view of the inelastic ARs for an incoming electron from the normal lead with the dot's energy below the Fermi level ($\varepsilon_0 < 0$) of the right superconductor (dashed line). Two possible paths are associated to the phonon absorption or phonon emission *after* or *before* an AR. In (a), the electron absorbs a vibrational energy quantum (blue arrow). In (b), the electron emits a vibrational energy quantum (red arrow). The filled and empty circles represent electron and holes, respectively.

and

$$\hat{H}_t = \sum_{k\sigma} (t\hat{d}_\sigma^\dagger \hat{c}_{k\sigma} + \text{H.c.})\,. \tag{5.3}$$

Hereafter we consider all energies with respect to the chemical potential μ and we omit it. The operators $\hat{c}_{k,\sigma}$ and $\hat{d}_\sigma$ are the annihilation operators for the electronic states k and spin σ in the normal lead and in the dot. We set $\Gamma_n = \pi\rho_n|t_n|^2$ with the density of states ρ_n of the normal lead. Elastic as well as inelastic tunneling of quasiparticles above the gap can be neglected deep in the subgap regime $eV \ll \Delta$ as their contribution is exponentially small in Δ/T with the temperature of the leads $T \ll \Delta$ (see Sec. 5.3). Then, the physics of the problem is captured by the effective Hamiltonian for the dot (see appendix C.1)

$$H_{dS} = \sum_\sigma \varepsilon_0 \hat{d}_\sigma^\dagger \hat{d}_\sigma - \Gamma_s(\hat{d}_\uparrow^\dagger \hat{d}_\downarrow^\dagger + \hat{d}_\downarrow \hat{d}_\uparrow)\,, \tag{5.4}$$

with the intra-dot pairing term and the coupling strength Γ_s between the dot and the superconducting lead. The eigenstates of the dot coupled to the superconductor correspond to Andreev bounds states formed by coherent superposition of electron and hole and with energies $\pm E_A = \pm\sqrt{\varepsilon_0^2 + \Gamma_s^2}$. Note that the coupling Γ_s to the superconductor does not produce any broadening.

In a suspended CNTQD, the electrostatic force between the dot and the gate depends on the mechanical displacement leading to a capacitive coupling between the flexural modes and the dot's charge [125]. An effective Holstein interaction [159] can be derived by expanding the electrostatic energy in terms of the tube's transversal displacement and the average dot's charge [201]. This yields

$$H_m = \sum_k [\omega_k \hat{b}_k^\dagger \hat{b}_k + \lambda_k(\hat{b}_k + \hat{b}_k^\dagger)\hat{n}_d]\,, \tag{5.5}$$

with the bosonic annihilation operators $\hat{b}_k$ for the flexural modes $\{k\}$ with frequency ω_k and the fluctuating part of the charge $\hat{n}_d$. We assume a low-frequency spectrum $\omega_k = k\omega$ with $k = 1, 2, 3\ldots$ (i.e. under sufficiently high-tension). Assuming weak coupling, one can neglect the effects of the resonator on the electron system in first

approximation. Then we can analyze, separately for each mechanical mode, the electromechanical damping γ and the nonequilibrium phonon occupation number n due to the interaction with the dot's charge. We will first focus on the damping and the phonon occupation for a single mode.

5.2.2 Damping for a single mode

We found that the electromechanical damping is determined by inelastic, vibration-assisted ARs and normal reflections (NRs). Detailed calculations are reported in appendix C.2. For the damping rate we obtain the result $\gamma = \gamma_{\rm AR} + \gamma_{\rm NR}$ in which, for instance, the damping associated to the ARs reads

$$\gamma_{\rm AR} = \gamma^{+}_{eh} + \gamma^{+}_{he} - \gamma^{-}_{eh} - \gamma^{-}_{he}\,. \tag{5.6}$$

The individual rates γ^{s}_{eh} and γ^{s}_{he} in Eq. (5.6) correspond to inelastic reflections with the absorption $s = +$ or emission $s = -$ of one phonon for an incoming electron from the normal lead reflected as hole (eh) or vice versa (he). As example, we report

$$\gamma^{\pm}_{eh} = \frac{\lambda^2\Gamma_n^2}{2}\int\frac{d\varepsilon}{2\pi}\, f_e(\varepsilon)[1 - f_h(\varepsilon \pm \omega)]\, |A_{\pm}(\varepsilon) + B_{\pm}(\varepsilon)|^2\,, \tag{5.7}$$

with the charge vibration coupling constant λ, the Fermi function for electrons $f_e(\varepsilon) = [1 + \exp\left((\varepsilon - eV)/T\right)]^{-1}$ and the Fermi function for holes $f_h(\varepsilon) = 1 - f_e(-\varepsilon)$. The last term inside the integral in Eq. (5.7) represents the transmission for inelastic ARs of an incoming electron and is given by the coherent sum of two amplitudes which are $A_{\pm}(\varepsilon) = G_e(\varepsilon)F^*(\varepsilon \pm \omega)$ and $B_{\pm}(\varepsilon) = -F(\varepsilon)G^*_h(\varepsilon \pm \omega)$. $G_{e,h}(\varepsilon)$ are the conventional dot's Green functions for electrons and holes and, qualitatively, are related to the particle's tunneling. $F(\varepsilon)$ is the anomalous dot's Green function corresponding to the amplitude of elastic ARs without charge vibration interaction. These amplitudes are associated to the two possible paths in which the phonon is emitted or absorbed before $(B_{\pm})$ or after $(A_{\pm})$ a single AR.

To calculate these Green's functions, we introduce the Nambu space as discussed in Sec. 2.2. A detailed calculation is given in appendix C.1. The retarded Green's function is defined as

$$\hat{G}^R(\varepsilon) = \begin{pmatrix} G_e(\varepsilon) & F(\varepsilon) \\ F(\varepsilon) & G_h(\varepsilon) \end{pmatrix}, \tag{5.8}$$

and, as a result using the Hamiltonian Eq. (5.1), we obtain for the elements

$$G_\nu(\varepsilon) = g_\nu(\varepsilon)/[1 - \Gamma_s^2 g_+(\varepsilon)g_-(\varepsilon)]\,, \tag{5.9}$$

$$F(\varepsilon) = \Gamma_s[(g_+(\varepsilon)g_-(\varepsilon))^{-1} - \Gamma_s^2]^{-1} \tag{5.10}$$

with $g_\nu(\varepsilon) = [\varepsilon - \nu\varepsilon_0 + i\Gamma_n]^{-1}$ and $\nu = (e, h) = (\pm)$.

Hereafter, to be definite, we consider $eV > 0$ and the high-voltage limit, namely $eV \gg T, \omega, E_A$. In this case the rate of the reflections for incoming holes are negligible compared to the one associated to electrons (vice versa for $eV < 0$) and we approximate $\gamma_{\rm AR} \simeq \gamma^{+}_{eh} - \gamma^{-}_{eh}$. Moreover, we can approximate $f_e \simeq 1$ and $f_h \simeq 0$ in Eq. (5.7). Hence, the behavior of the rates for the inelastic ARs are ruled completely by the transmission function $|A_{\pm}(\varepsilon) + B_{\pm}(\varepsilon)|$.

5.2.3 Phonon occupation due to inelastic Andreev reflections

We first analyze the contribution of inelastic ARs to the phonon occupation assuming that NRs are negligible. In this case we have the result

$$n \simeq n_{\mathrm{AR}} = \frac{1}{\kappa - 1}\,, \tag{5.11}$$

with

$$\kappa = \frac{\gamma^{+}_{+-}}{\gamma^{-}_{+-}} \simeq \frac{(\varepsilon_0 - \omega/2)^2 + \Gamma_n^2}{(\varepsilon_0 + \omega/2)^2 + \Gamma_n^2}\,, \tag{5.12}$$

valid for $\kappa > 1$. Thus, n_{AR} is the outcome of the competition between emission and absorption processes for inelastic ARs: for $\kappa \gg 1$, the resonator can be cooled to the ground state with $n_{\mathrm{AR}} \ll 1$, whereas the phonon occupation is increased for $\kappa \geq 1$ such that $n_{\mathrm{AR}} \gg 1$. Eventually the resonator is unstable for $\kappa < 1$ [197]. The different regimes can be reached only by tuning the dot's energy level ε_0 (i.e. the gate voltage): $n_{\mathrm{AR}} > 1$ and the instability occurs always for $\varepsilon_0 > 0$ whereas $n_{\mathrm{AR}} < 1$ is achieved as long as $\varepsilon_0 < 0$. In particular, the lowest phonon occupation is given by

$$n_{\mathrm{opt}} = (\Gamma_n/\omega)^2\,, \tag{5.13}$$

corresponding to ground-state cooling for $\Gamma_n \ll \omega$ [135].

Although the result in Eq. (5.11) is independent of Γ_s, it is interesting to analyze the behavior of the individual rates as a function of ω as shown in Fig. 5.4. We focus on the cooling regime, viz. $\varepsilon_0 < 0$, in which the absorption rate dominates over the emission one $\gamma^{+}_{eh} \gg \gamma^{-}_{eh}$. Cooling occurs either in the limit $\Gamma_s \ll |\varepsilon_0|$ when γ^{+}_{eh} has a peak as shown Fig. 5.4(a), or in the limit $\Gamma_s \gg |\varepsilon_0|$ when γ^{-}_{eh} has a broadened depletion with a dip as shown in Fig. 5.4(b). The peak in Fig. 5.4(a) results from a resonance in the system: the reflected hole is injected at the same energy of the incoming electron $\varepsilon_0 = -\omega/2$ in case of phonon absorption. This energy alignment holds independently whether the absorption occurs after or before an AR, see Fig. 5.3(a), and enhances the phonon absorption amplitudes. Such an alignment does not occur for ARs with phonon emission, see Fig. 5.3(b). By contrast, the dip of the emission rate in Fig. 5.4(b) occurs by the fact that the two paths with phonon emission in Fig. 5.3(b) have a destructive interference, viz. $|A_{-}(\varepsilon) + B_{-}(\varepsilon)| \simeq 0$. Increasing the frequency, the two rates becomes comparable $\gamma^{+}_{eh} \sim \gamma^{-}_{eh}$ and both rates show a peak at $\omega \simeq 2\Gamma_S$, Fig. 5.4(b), corresponding to the energy separation between the two Andreev levels ($E_A \simeq \Gamma_s$). The suppression of the emission rate for inelastic AR opens the possibility to achieve ground-state cooling for many mechanical modes. For $|\varepsilon_0| \leq \omega \leq \Gamma_S$, we notice that γ^{-}_{eh} is two orders of magnitude smaller than γ^{+}_{eh} (see Fig. 5.4(b)) and this range sets approximatively the cooling spectral band of the inelastic AR.

Cooling of a mechanical resonator by interference was also discussed in [202] but using a dissipative optomechanical coupling. Notice also that this mechanism of cooling is different from the method based on the quasiparticle transport proposed in [203] and experimentally demonstrated in suspended nanowires [204, 205] in which an electron tunnels from the normal lead to the superconducting lead above the gap

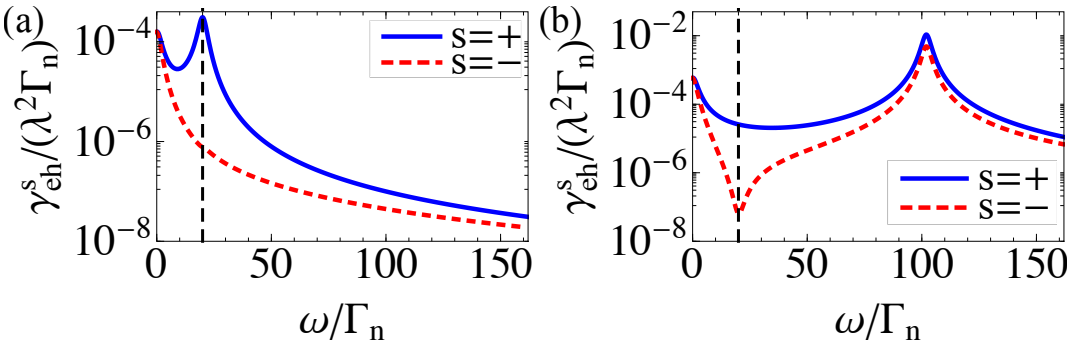

Figure 5.4: The rates $\gamma^{\pm}_{eh}$ for inelastic ARs for $\varepsilon_0 = -10\Gamma_n$ (s=+ absorption, s=- emission). The vertical dashed line is $\omega = 2|\varepsilon_0|$. (a) Weak coupling regime between dot and superconductor with $\Gamma_s = 0.1|\varepsilon_0|$. (b) Strong coupling regime with $\Gamma_s = 5|\varepsilon_0|$.

by absorbing phonons. Via a similar mechanism, we obtained cooling even for the voltage close to Δ as we discuss in Sec. 5.3. Interplay of inelastic quasiparticles and Andreev scattering on heating has been discussed in [206] although subgap ground-state cooling was not studied.

5.2.4 General results and effects of normal reflections

At a more formal level, the electromechanical damping γ and the steady nonequilibrium phonon occupation n are determined by the spectrum of the non-symmetrized noise of the electron occupation on the dot

$$S(\varepsilon) = \int dt\, e^{i\varepsilon t} \langle \hat{n}_d(t)\hat{n}_d \rangle \,, \tag{5.14}$$

where the quantum statistical average is taken over the electron system [207]. Hence, the rates are associated to the elemental processes forming the quantum noise. The damping and the occupation are related to the non-symmetrized noise by [207]

$$\gamma = \lambda^2 (S(\omega) - S(-\omega))/2 \tag{5.15}$$

and

$$n = S(-\omega)/(S(\omega) - S(-\omega)) \,. \tag{5.16}$$

The derivation of the noise $S(\varepsilon)$, the damping γ, and the phonon occupation n is given in appendix C.2. For the phonon occupation, we obtain the general result

$$\bar{n} = \frac{\gamma_{\rm AR}\, n_{\rm AR} + (\gamma_{\rm NR} + \gamma_0)\, n_B(\omega)}{\gamma_{\rm AR} + \gamma_{\rm NR} + \gamma_0} \,, \tag{5.17}$$

in which we have also taken into account an intrinsic damping $\gamma_0 = \omega/Q$. The Bose function is given by $n_B(\omega) = [\exp(\omega/T) - 1]^{-1}$. Notice that the NRs, involving only

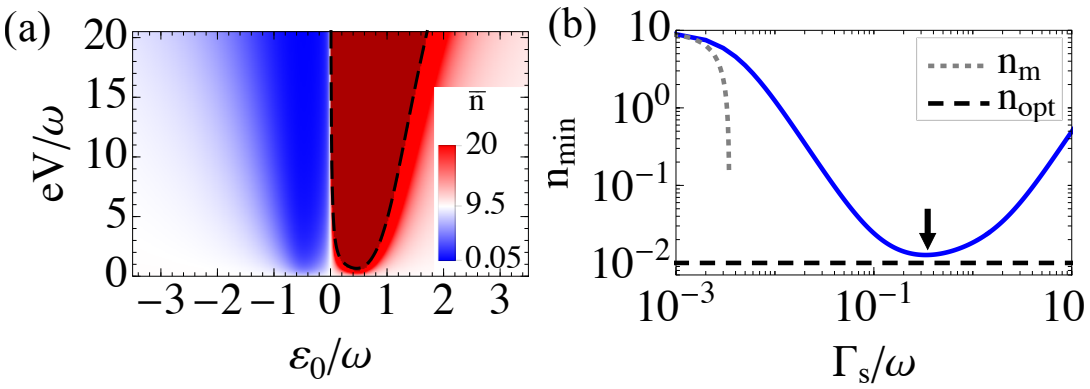

Figure 5.5: (a) Phonon occupation as function of the bias voltage V and ε_0 for $\Gamma_s = 0.35\omega$. White color corresponds to $n_B(\omega)$. The dark red region limited by the dashed line corresponds to the instability region $\gamma_{\rm AR}+\gamma_{\rm NR}+\gamma_0 < 0$. (b) Minimal phonon occupation as a function of Γ_s for $\varepsilon_0 = -\omega/2$. The dotted line (gray) is the analytic approximation valid at $\Gamma_s \ll |\varepsilon_0|$: $n_m = n_B(\omega)(1-2\pi\Gamma_s^2(10\Gamma_n^2+\omega^2)/\left[\Gamma_n\gamma_{\rm NR}(\Gamma_n^2\omega^2/4)\right])$. The lowest phonon occupation is $n_{\rm opt} = (\Gamma_n/\omega)^2$. Parameters: $\Gamma_n = 0.1\omega$, $T = 10\omega$, $\gamma_0/\omega = 10^{-6}$ and $\lambda = 0.1\omega$ [201].

the single normal lead at the bath's temperature, can drive the phonon occupation only at thermal equilibrium. The general expression for $n_{\rm AR}$ reads

$$n_{\rm AR} = \sum_{s=\pm} s\left[\gamma_{eh}^{s} n_B\left(\omega + s\,2eV\right) + \gamma_{he}^{s} n_B\left(\omega - s\,2eV\right)\right]/\gamma_{\rm AR}\,. \tag{5.18}$$

An example of the result for $\bar{n}$ is shown in Fig. 5.5(a) for some realistic parameters. We note that, restoring the NRs in the phonon occupation, increases the minimum occupation. However, we obtain in Fig. 5.5(a) $n_{\rm min} \simeq 0.05$, i.e. ground-state cooling is still feasible. Finally, by setting the level $\varepsilon_0 > 0$ the situation is reverted: the emission rates of the inelastic ARs dominates over the absorption ones $\gamma_{eh}^{-} \gg \gamma_{eh}^{+}$ leading to an increase of the phonon occupation and to a mechanical instability [197].

When we takes into account NRs the minimal occupation becomes a function of Γ_s and there is an optimal value for the coupling with the superconducting lead that maximizes the cooling. An example of results is shown in Fig. 5.5(b). Setting $\varepsilon_0 = -\omega/2$ and $eV \gg (\omega, T)$, we have

$$n_{\rm min} \approx \frac{\gamma_{eh}^{+} n_{\rm opt} + \gamma_{\rm NR} n_B}{\gamma_{eh}^{+} + \gamma_{\rm NR}}\,, \tag{5.19}$$

valid for $\gamma_0 \ll \gamma_{\rm NR}$ and $n_{\rm opt} \ll 1$. In the limit $\Gamma_s \to 0$, we have $\gamma_{eh}^{+} \to 0$, NRs dominates over ARs and the oscillator is close at thermal equilibrium, see Fig. 5.5(b). Increasing Γ_s, the resonator starts to be cooled due to inelastic ARs and the phonon occupation approaches the optimal value $n_{\rm opt}$. As the AR rates γ_{eh}^{+} vanish at large Γ_s (i.e. when the Andreev levels move away from the Fermi level), $n_{\rm min}$ shows a non-monotonic behavior.

5.2.5 Results for several mechanical modes

As previously discussed the interference effect in vibration-assisted ARs allows ground-state cooling of mechanical modes with different frequency simultaneously. We illustrate this possibility in this section. We limit the calculations by considering a finite number of modes as we have a natural cut-off given by the temperature: high-frequency modes with $\omega \geq T$ are close to the ground state. As example, for $T = 10\omega$ we set $N = 7$ modes, and we have a phonon occupation $n_{k=8} \simeq 0.81$ for the highest frequency mode. In Fig. 5.6, we show the result for the average mechanical energy defined as $E_{\rm tot} = \sum_{k=1}^{7} k\omega n_k$. The nonequilibrium value n_k for each modes is calculated by Eq. (5.17).

In Fig. 5.6(a) we consider the regime of small dot's coupling with the superconductor ($\Gamma_s \ll \omega_k$), namely the regime of cooling by resonance. In this case, by matching the resonance condition at $2|\varepsilon_0| = \omega_k = k\omega$, one can address cooling of each individual mode, as for instance $k = 1$ or $k = 6$, whereas the rest of the modes are approximatively at thermal equilibrium. In Fig. 5.6(b) we consider the regime of strong dot's coupling with the superconductor ($\Gamma_s \gg \omega_k$), namely the regime of cooling by interference. In this case, several modes of the resonator can be cooled close the ground state at given optimal point for ε_0. Notice that the nonequilibrium distribution of the modes does not correspond to the Bose function $n_B^*(\omega_k)$ with an common effective temperature T^*, e.g. example of the fitting result is the dashed line in inset of Fig. 5.6(b). The reason is that for a certain mode k, the minimal phonon occupation is $n_{k,\rm opt} = (\Gamma_n/\omega_k)^2$ for $\varepsilon_0 = -\omega_k/2$ such that the nonequilibrium distribution corresponds to the interplay of an algebraic decay and the Bose function.

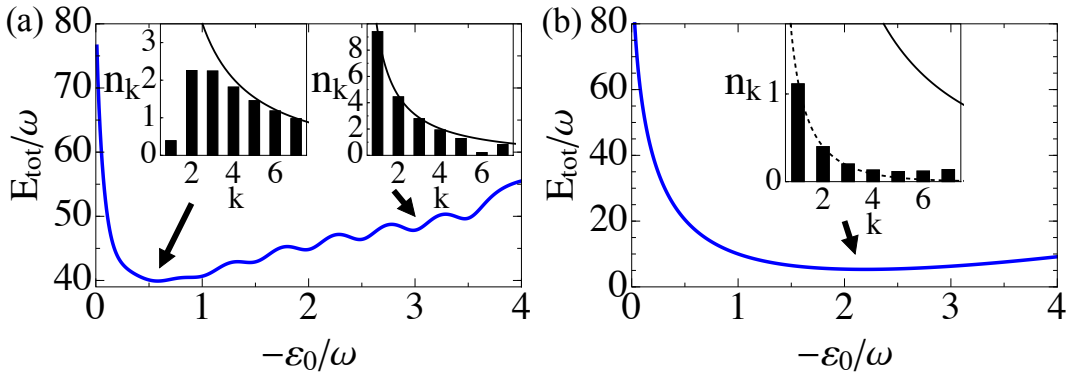

Figure 5.6: The total mechanical energy with $k = 7$ modes (see text) as a function of ε_0 at $eV = 16\omega$ for $\Gamma_s = 0.1\omega$ (a) and $\Gamma_s = 5\omega$ (b). The insets show the occupation of modes k at specific points of ε_0 indicated by the arrows. The solid black line shows the thermal distribution. The parameters are $\Gamma_n = 0.1\omega$, $T = 10\omega$.

5.2.6 Dc-current measurement

In this section, we discuss the effect of the nonequilibrium phonon occupation on the current. To lowest order in the electron-vibration coupling, the current can be expressed as $I = I_0 + I_{\rm ec} + I_{\rm in}$, with the elastic current I_0, the elastic correction $I_{\rm ec}$ and the inelastic current $I_{\rm in}$.

Fig. 5.7 shows the current at $eV = 5\omega$ as a function of ε_0. Beyond a peak at $\varepsilon_0 = 0$, two vibrational side-peaks appear at $\varepsilon_0 = \pm\omega/2$ associated to inelastic ARs with emission or absorption of one phonon. Similar vibrational sidebands have been observed for molecular vibrational modes but under the condition $T \ll \omega$ (for instance, in suspended CNTQDs, see Refs. [128, 129, 208]) and in other non suspended devices due to other bosonic modes of the environment [209]. Here, these peaks are visible in the subgap transport even for the temperature of the leads $T \gg \omega$. Analytic expressions for the I_0 and $I_{\rm ec}$ are given in appendix C.4, here we focus on the inelastic term. As shown in Fig. 5.7, around the region $\varepsilon_0 = \pm\omega/2$ the main contribution to the current is given by the inelastic component, which reads

$$I_{\rm in} = e\left[(\bar{n}+1)\left(\gamma^{-}_{+-} - \gamma^{-}_{-+}\right) + \bar{n}\left(\gamma^{+}_{+-} - \gamma^{+}_{-+}\right)\right], \tag{5.20}$$

to the leading order in Γ_n. For $\gamma_0 \gg \gamma$, $\bar{n} \simeq n_B(\omega)$, the side-peaks are approximately symmetric. In the opposite case $\gamma_0 \ll \gamma$, $\bar{n} \simeq n$ and the two peaks are strongly asymmetric such that width of the peaks associated to the phonon absorption (emission) is reduced (enhanced).

We employ the inelastic side-peaks in the current as a function of gate voltage to extract information about the phonon occupation. The peaks at $\varepsilon_0 < 0$ and $\varepsilon_0 > 0$ correspond to absorption (emission) of one vibrational phonon, respectively. As shown in Fig. 5.7, the elastic current is negligible at $\varepsilon_0 = \pm\omega/2$ in the limit $\Gamma_n \ll \omega$. In this case the current can be approximated by the inelastic current. In the high-voltage limit $eV \gg (T, \omega, E_A)$, we have the expression $I_{\rm in} = (\bar{n}+1)\gamma^{-}_{+-} + \bar{n}\gamma^{+}_{+-}$ to the leading order in Γ_n. We can integrate the peaks due to inelastic absorption and emission separately and can write

$$\begin{aligned}\Delta I_{\rm l} &\simeq \int_{-\frac{\omega}{2}-\frac{\Gamma_n}{2}}^{-\frac{\omega}{2}+\frac{\Gamma_n}{2}} d\varepsilon_0\; I_{\rm in}(\varepsilon_0) \\ &\simeq (\bar{n}_l+1)\int_{-\frac{\omega}{2}-\frac{\Gamma_n}{2}}^{-\frac{\omega}{2}+\frac{\Gamma_n}{2}} d\varepsilon_0\,\gamma^{-}_{+-} + \bar{n}_l\int_{-\frac{\omega}{2}-\frac{\Gamma_n}{2}}^{-\frac{\omega}{2}+\frac{\Gamma_n}{2}} d\varepsilon_0\,\gamma^{+}_{+-} = \zeta(2\bar{n}_l+1)\,,\end{aligned} \tag{5.21}$$

$$\begin{aligned}\Delta I_{\rm r} &\simeq \int_{\frac{\omega}{2}-\frac{\Gamma_n}{2}}^{\frac{\omega}{2}+\frac{\Gamma_n}{2}} d\varepsilon_0\; I_{\rm in}(\varepsilon_0) \\ &\simeq (\bar{n}_r+1)\int_{\frac{\omega}{2}-\frac{\Gamma_n}{2}}^{\frac{\omega}{2}+\frac{\Gamma_n}{2}} d\varepsilon_0\,\gamma^{-}_{+-} + \bar{n}_r\int_{\frac{\omega}{2}-\frac{\Gamma_n}{2}}^{\frac{\omega}{2}+\frac{\Gamma_n}{2}} d\varepsilon_0\,\gamma^{+}_{+-} = \zeta(2\bar{n}_r+1)\,.\end{aligned} \tag{5.22}$$

with a coefficient ζ which is independent of emission or absorption processes. The phonon occupation n_l (n_r) are calculated around the absorption (emission) peak, since $\bar{n}$ is a smooth function of ε_0 close to these peaks (Fig. 5.5). Therefore we predict that

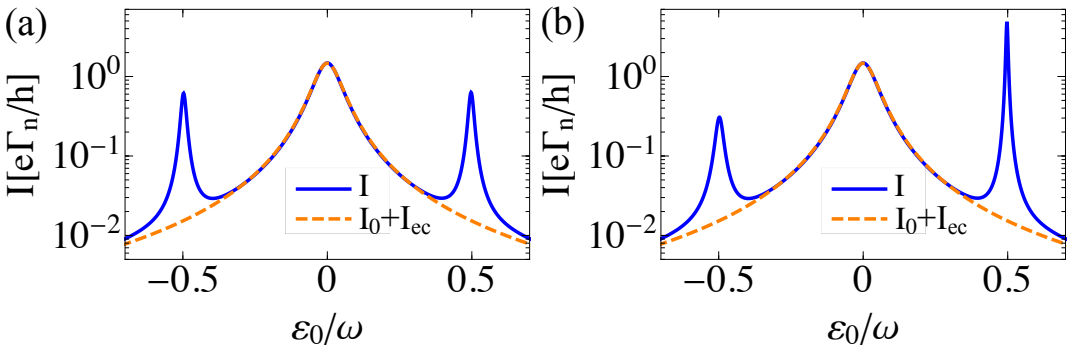

Figure 5.7: Total current I (solid blue line) and elastic current (dashed orange line) as function of ε_0 for $\Gamma_n = 0.01\omega$, $\Gamma_s = 0.05\omega$, $T = 10\omega$, $eV = 5\omega$, $\lambda = 0.02\omega$ for equilibrated (a) and unequilibrated vibration $\gamma_0/\omega = 10^{-4}$(b). The ratio between the areas underlying the two peaks is related to the phonon occupation.

then the experimental ratio between the areas underlying the two peaks, associated to the absorption and emission in the inelastic Andreev reflections corresponds to $\Delta I_\mathrm{l}/\Delta I_\mathrm{r} = (2\bar{n}_l + 1)/(2\bar{n}_r + 1)$. Eventually, other comparison with the theoretical predictions can be done whether one parameter of the systems as for instance Γ_s, can be varied.

5.3 Effects of quasiparticles

In the previous section, we focused on the subgap regime and discussed the damping and phonon occupation. In this section, we briefly consider the effects of a finite gap on the phonon occupation. The goal of this section is to show that ground-state cooling is achievable at finite Δ. To describe the effect of the quasiparticle we introduce the Hamiltonian of the normal-superconducting contact interacting with the resonator in Sec. 5.3.1. Compared to the previous section, we start with the BCS Hamiltonian of the right lead and will not use the hybridized Hamiltonian for the quantum dot and the superconductor of Eq. (5.4).

5.3.1 Model for quantum dot and leads

The quantum dot between a normal and a superconducting lead interacting with the resonator is described by

$$\hat{H} = \hat{H}_n + \hat{H}_t + \hat{H}_s + \hat{H}_d + \hat{H}_m\,. \tag{5.23}$$

The Hamiltonians $\hat{H}_n$ and $\hat{H}_t$ are given by Eq. (5.2) and (5.3) respectively. The superconducting lead is described by the BCS Hamiltonian [see Eq. (2.25)] $\hat{H}_s = \sum_{k\sigma}[\varepsilon_k \hat{a}^\dagger_{k\sigma}\hat{a}_{k\sigma} + \Delta \hat{a}^\dagger_{-k\downarrow}\hat{a}^\dagger_{k\uparrow} + \Delta^\dagger \hat{a}_{k\uparrow}\hat{a}_{-k\downarrow}]$ with the annihilation operators with spin σ and momentum k of the superconductor given by $\hat{a}_{k\sigma}$. The quantum dot is modeled by the Hamiltonian $\hat{H}_d = \varepsilon_0 \hat{n}_d$ with the bare energy level of the dot ε_0. The last

term in Eq. (5.23) is given by Eq. (5.5) and corresponds to the flexural mode and the coupling between the quantum dot and the flexural modes of the resonator.

5.3.2 Results for a single mode

The damping and phonon occupation are calculated in the same way as in Sec. 5.2.2 with Eqs. (5.15) and (5.16), respectively.

Before we give the expression for the damping, we briefly recall the results obtained in Sec. 2.3.1 for a normal-superconducting contact. An electron incoming below the superconducting gap can be either Andreev reflected or normal reflected. Above the gap, AR and NR is still possible but also quasiparticles contribute to transport. In the case of a normal-superconducting junction we can divide the quasiparticle contributions into direct tunneling (DT) and branch crossing (BC). Sketches of the corresponding processes of AR, NR, DT and BC are shown in Fig. 2.2.

Similar to the normal-superconducting contact, we can divide the total mechanical damping due to the electron-vibration interaction into a contribution from below and above the superconducting gap. Below the gap, inelastic Andreev reflection (γ_{AR}) and inelastic normal reflection (γ_{NR}) are possible. Above the gap inelastic direct quasiparticle tunneling (γ_{DT}), inelastic branch crossing (γ_{BC}) and inelastic tunneling via an intermediate state (γ_{IS}) start to contribute to transport [210]. In all these processes the electrons or holes interact with the resonator and absorb or emit a vibrational energy quantum. The total mechanical damping can then be written as

$$\gamma_{\mathrm{tot}} = \gamma_{\mathrm{AR}} + \gamma_{\mathrm{NR}} + \gamma_{\mathrm{DT}} + \gamma_{\mathrm{BC}} + \gamma_{\mathrm{IS}}. \tag{5.24}$$

We remark that for the discussion in this section, it is sufficient to separate between transport processes below and above the superconducting gap.

In the following, we give the exact result of the damping to infinite order in the tunneling t between the quantum dot and the leads. All damping coefficients in Eq. (5.24) can be expressed in terms of the transmission amplitudes

$$T^s_{\nu\bar{\nu}}(\varepsilon) = G_\nu(\varepsilon)F^*(\varepsilon + s\omega) - F(\varepsilon)G^*_{\bar{\nu}}(\varepsilon + s\omega)\,, \tag{5.25}$$
$$T^s_{\nu\nu}(\varepsilon) = G_\nu(\varepsilon)G^*_{\nu}(\varepsilon + s\omega) - F(\varepsilon)F^*(\varepsilon + s\omega)\,. \tag{5.26}$$

The elements $G_\nu(\varepsilon)$ and $F(\varepsilon)$ correspond to the exact Green's function of a dot coupled to a normal and a superconducting lead. A calculation of the retarded Green's function in Nambu space gives (see appendix C.1)

$$\begin{aligned}\hat{G}^R(\varepsilon) &= \begin{pmatrix} G_+(\varepsilon) & F(\varepsilon) \\ F(\varepsilon) & G_-(\varepsilon) \end{pmatrix} \\ &= \frac{1}{D}\begin{pmatrix} -(\varepsilon + \varepsilon_0 + i\Gamma_n + \varepsilon\Gamma_s/\Omega(\varepsilon)) & \Delta\Gamma_s/\Omega(\varepsilon) \\ \Delta\Gamma_s/\Omega(\varepsilon) & -(\varepsilon - \varepsilon_0 + i\Gamma_n + \varepsilon\Gamma_s/\Omega(\varepsilon)) \end{pmatrix}\end{aligned} \tag{5.27}$$

with $D = \Delta^2\Gamma_s^2/\Omega^2(\varepsilon) - (\varepsilon + \varepsilon_0 + i\Gamma_n + \varepsilon\Gamma_s/\Omega(\varepsilon))\,(\varepsilon - \varepsilon_0 + i\Gamma_n + \varepsilon\Gamma_s/\Omega(\varepsilon))$, $\Omega(\varepsilon) = \sqrt{\Delta^2 - (\varepsilon + i\eta)^2}$ and an infinitesimal small real part η.

The rates γ_{AR}, γ_{DT}, γ_{BC} and γ_{IS} are then given by

$$\gamma_{\mathrm{AR}} = \sum_{\nu,s} s\gamma^{s}_{\nu\bar{\nu}}\,, \tag{5.28}$$

$$\gamma_{\mathrm{DT}} = \sum_{s\nu} s(\gamma^{s\nu}_{\mathrm{DT},ns} + \gamma^{s\nu}_{\mathrm{DT},sn})\,, \tag{5.29}$$

$$\gamma_{\mathrm{BC}} = \sum_{s\nu} s(\gamma^{s\nu}_{\mathrm{BC},ns} + \gamma^{s\nu}_{\mathrm{BC},sn})\,, \tag{5.30}$$

$$\gamma_{\mathrm{IS}} = \sum_{s\nu} s(\gamma^{s\nu}_{\mathrm{IS},ns} + \gamma^{s\nu}_{\mathrm{IS},sn})\,, \tag{5.31}$$

with $\nu = (e,h) = \pm$, $\nu' = (e,h) = \pm$ and the notation $\bar{\nu} = -\nu$. The indexes n and s label a particle in the normal and superconducting lead, respectively. The first (second) index thereby refers to the incoming (outgoing) particle. Then, the first term in the Eqs. (5.29)-(5.31) describes an incoming particle in the normal lead and an outgoing particle in the superconducting lead. Similarly, the second term in the Eqs. (5.29)-(5.31) corresponds to an incoming particle in the superconducting lead and an outgoing particle in the normal metal.

The reflection inside the normal lead (NR) and the superconducting lead (SR) are

$$\gamma_{\mathrm{NR}} = \sum_{\nu,s} s\gamma^{s}_{\nu\nu}\,, \tag{5.32}$$

$$\gamma_{\mathrm{SR}} = \sum_{\nu,s} s(\gamma^{s\nu}_{\mathrm{DT,SR}} + \gamma^{s\nu}_{\mathrm{BC,SR}} + \gamma^{s\nu}_{\mathrm{IS,SR}})\,. \tag{5.33}$$

Reflection for an incoming particle inside the superconductor can be separated into DT, BC and IS.

The damping rates $\gamma^{s}_{\nu\nu'}$ in Eqs. (5.28) and (5.32) can be written as

$$\gamma^{s}_{\nu\nu'}(\omega) = \lambda^2 \frac{\Gamma_n^2}{2} \int \frac{d\varepsilon}{2\pi} f_\nu(\varepsilon)[1 - f_{\nu'}(\varepsilon + s\omega)]\,|T^{s}_{\nu\nu'}(\varepsilon)|^2\,, \tag{5.34}$$

in which we have defined the Fermi function $f_\nu(\varepsilon) = 1/[1 + \exp((\varepsilon - \nu\, eV))/T]$.

Introducing the density of states of the superconductor with

$$\rho(\varepsilon) = \theta(\varepsilon^2 - \Delta^2)\varepsilon/\sqrt{\varepsilon^2 - \Delta^2}\,, \tag{5.35}$$

we can write the rates as

$$\begin{aligned}
\gamma^{s\nu}_{\mathrm{DT},ns} &= 8\lambda^2\Gamma_n\Gamma_s \int \frac{d\varepsilon}{2\pi}\rho(\varepsilon+s\omega)|T^s_{\nu\nu}(\varepsilon)|^2 f_\nu(\varepsilon)[1-f_s(\varepsilon+s\omega)]\,,\\
\gamma^{s\nu}_{\mathrm{DT},sn} &= 8\lambda^2\Gamma_n\Gamma_s \int \frac{d\varepsilon}{2\pi}\rho(\varepsilon)|T^s_{\nu\nu}(\varepsilon)|^2 f_s(\varepsilon)[1-f_\nu(\varepsilon+s\omega)]\,,\\
\gamma^{s\nu}_{\mathrm{DT},ss} &= 8\lambda^2\Gamma_s^2 \int \frac{d\varepsilon}{2\pi}\rho(\varepsilon)\rho(\varepsilon+s\omega)|T^s_{\nu\nu}(\varepsilon)|^2 f_s(\varepsilon)[1-f_s(\varepsilon+s\omega)]\,,\\
\gamma^{s\nu}_{\mathrm{BC},ns} &= 8\lambda^2\Gamma_n\Gamma_s \int \frac{d\varepsilon}{2\pi}\rho(\varepsilon+s\omega)|T^s_{\nu\bar\nu}(\varepsilon)|^2 f_\nu(\varepsilon)[1-f_s(\varepsilon+s\omega)]\,,\\
\gamma^{s\nu}_{\mathrm{BC},sn} &= 8\lambda^2\Gamma_n\Gamma_s \int \frac{d\varepsilon}{2\pi}\rho(\varepsilon)|T^s_{\nu\bar\nu}(\varepsilon)|^2 f_s(\varepsilon)[1-f_\nu(\varepsilon+s\omega)]\,,\\
\gamma^{s\nu}_{\mathrm{BC},ss} &= 8\lambda^2\Gamma_s^2 \int \frac{d\varepsilon}{2\pi}\rho(\varepsilon)\rho(\varepsilon+s\omega)|T^s_{\nu\bar\nu}(\varepsilon)|^2 f_s(\varepsilon)[1-f_s(\varepsilon+s\omega)]\,,\\
\gamma^{s\nu}_{\mathrm{IS},ns} &= 16\lambda^2\Gamma_n\Gamma_s \int \frac{d\varepsilon}{2\pi}\rho(\varepsilon+s\omega)\mathrm{Re}[T_{\nu\bar\nu}(\varepsilon)T^*_{\nu\nu}(\varepsilon)]f_\nu(\varepsilon)[1-f_s(\varepsilon+s\omega)]\,,\\
\gamma^{s\nu}_{\mathrm{IS},sn} &= 16\lambda^2\Gamma_n\Gamma_s \int \frac{d\varepsilon}{2\pi}\rho(\varepsilon)\mathrm{Re}[T_{\nu\bar\nu}(\varepsilon)T^*_{\bar\nu\bar\nu}(\varepsilon)]f_s(\varepsilon)[1-f_\nu(\varepsilon+s\omega)]\,,\\
\gamma^{s\nu}_{\mathrm{IS},ss} &= 16\lambda^2\Gamma_s^2 \int \frac{d\varepsilon}{2\pi}\rho(\varepsilon)\rho(\varepsilon+s\omega)\mathrm{Re}[\frac{\Delta}{\varepsilon+s\omega}T_{\nu\bar\nu}(\varepsilon)T^*_{\nu\nu}(\varepsilon)+\frac{\Delta}{\varepsilon}T_{\nu\nu}(\varepsilon)T^*_{\bar\nu\nu}(\varepsilon)\\
&\quad+\frac{\Delta^2}{\varepsilon(\varepsilon+s\omega)}(T_{\nu\nu}(\varepsilon)T^*_{\bar\nu\bar\nu}(\varepsilon)+T_{\nu\bar\nu}(\varepsilon)T^*_{\bar\nu\nu}(\varepsilon))]f_s(\varepsilon)[1-f_s(\varepsilon+s\omega)]\,, \qquad (5.36)
\end{aligned}$$

with the Fermi function of the superconducting lead $f_s(\varepsilon) = [1+\exp(\varepsilon/T)]^{-1}$.

The processes of DT and BC can be understood in the following picture. We consider an incoming electron from the normal metal above the gap. The electron is transmitted to the quantum dot and then to the superconductor. In this way the charge of an electron is transfered form the normal to the superconductor. To the lowest order in the coupling ($\Gamma_n = \Gamma_s = \Gamma$), the process of DT is proportional to Γ^2. Instead of being transmitted, the electron can also be reflected at the superconductor and again at the quantum dot. In the process of a BC, the electron is then transmitted as a hole above the gap. Therefore, to the lowest order in the coupling, BC is proportional to Γ^4.

Similar to the inelastic Andreev reflection discussed in Sec. 5.2, the electron can interact with the resonator before or after an Andreev reflection which is described by the two amplitudes in the transmission.

A calculation of the phonon occupation as in Sec. 4.3.4, gives the result

$$\begin{aligned}
n = \frac{1}{\gamma_{\mathrm{tot}}}\Bigg(\sum_{\nu,s=\pm} s\Big[\gamma^s_{\nu\bar\nu} n_B\left(\omega+\nu s\, 2eV\right) + (\gamma^{s\nu}_{\mathrm{DT},ns}+\gamma^{s\nu}_{\mathrm{DT},sn}+\gamma^{s\nu}_{\mathrm{BC},ns}+\gamma^{s\nu}_{\mathrm{BC},sn}\\
+\gamma^{s\nu}_{\mathrm{IS},ns}+\gamma^{s\nu}_{\mathrm{IS},sn})n_B\left(\omega+\nu s\, eV\right)\Big] + (\gamma_{\mathrm{NR}}+\gamma_{\mathrm{SR}})n_B(\omega)\Bigg)\,. \qquad (5.37)
\end{aligned}$$

From Eq. (5.37), one expects that the processes above the gap can drive the resonator to a nonequilibrium state. A strong modification of the phonon occupation

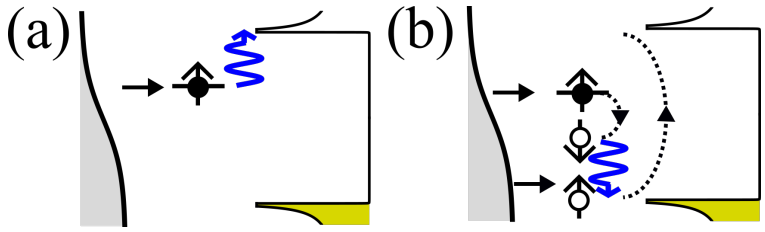

Figure 5.8: Sketch of processes with direct tunneling of an electron. The transmission amplitudes in a process of direct tunneling contain two path. In (a), the electron tunnels directly to the superconductor. In (b), the electron is first Andreev reflected, then the hole interact with the resonator and is again Andreev reflected. The two possible path can lead to cooling when the energy level ε is tuned below the superconducting gap edge about the frequency ω.

can occur close to the gap edge due to the divergence of the density of states of the superconducting gap edge. For instance, the sketches in Fig. 5.8(a) and (b) show the processes of direct tunneling of an incoming electron from the normal metal. The energy level of the quantum dot is tuned to $\varepsilon_0 = \Delta - \omega$. An electron tunneling to the dot can then tunnel to the superconductor only by absorbing a vibrational energy quantum. Fig. 5.8 shows the two possible path of the transmission given by Eq. (5.26). In Fig. 5.8(a), the electron tunnels directly to the superconductor without Andreev reflection. In Fig. 5.8(b), the electron is Andreev reflected, then the hole interacts with the resonator and the hole is again Andreev reflected as an electron and transmitted to the superconductor.

5.3.3 Phonon occupation

The phonon occupation at finite Δ is shown in Fig. 5.9 as a function of the voltage eV and the gate voltage ε_0. In the region $|\varepsilon_0| < \Delta$, the phonon occupation resembles the result of Sec. 5.2 in which the cooling and pumping of the resonator are related to the inelastic Andreev reflections. When the energy level approaches the gap edge, quasiparticle tunneling modify the phonon occupation.

When the gate voltage ε_0 is close to Δ, the quasiparticle tunneling drive the resonator the equilibrium and remove the instability. An example of the DT processes are shown in Fig. 5.8. In a similar way, when ε_0 is close to $-\Delta$, electron tunnel to the quantum dot and then to the superconducting by emission of a vibrational energy quantum. Thereby, the electron drive the resonator to equilibrium such that strong cooling is obtained for negative gate voltages with $|\varepsilon_0| < \Delta - \omega$.

5.4 Conclusion

We discussed the ground state cooling of a mechanical resonator coupled to a quantum dot in a normal-superconducting contact. The inelastic vibration-assisted Andreev

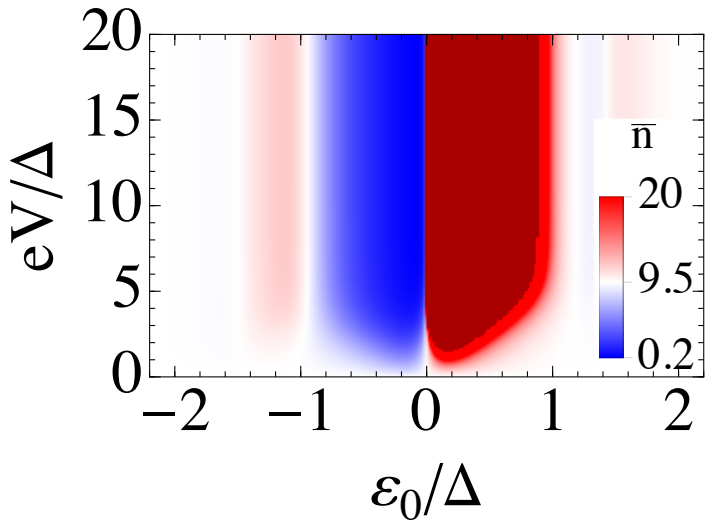

Figure 5.9: Phonon occupation as function of voltage eV and ε_0 for finite gap and a frequency of $\omega = 0.1\Delta$. The parameter are the same as in Fig. 5.5: $\Gamma_n = 0.1\omega$, $\Gamma_s = 0.35\omega$, $T = 10\omega$, $Q = 10^{-6}$, $\lambda = 0.1\omega$. When the energy level is shifted close to the gap $|\varepsilon_0| \lesssim \Delta - \omega$, quasiparticle tunneling drive the oscillator to equilibrium.

reflection allows to cool several mechanical modes. Although we focused on the subgap regime, the cooling is still possible at a finite superconducting gap. Finally we discussed the procedure to extract quantitative information about the phonon occupation by direct measurement of the dc current. Our proposal is well within the reach of the present state of art for carbon-based NEMS. The set-up with hybrid contacts in Fig. 5.1 can be experimentally implemented [209, 211]. Moreover, experiments of the last years achieved the coupling regime for flexural modes with electrostatic interaction [126, 127, 135, 212], such that the intrinsic mechanical damping γ_0 can be much smaller than the electromechanical one $\gamma \gg \gamma_0$.

6 Noise of a suspended carbon nanotube coupled to normal leads

The current noise can give information about the internal structure in a contact which is not accessible by current measurements. As we discussed in Sec. 2.4, the frequency-dependent noise reveals information about the excitation of the system. For this reason, we study in this chapter the zero-frequency and the frequency-dependent noise. The main goal of this chapter is to provide the derivation of the frequency-dependent noise in a quantum dot in contact with two normal leads and in the presence of electron-phonon interaction. We discuss a few exemplary cases to illustrate features of the electron-phonon interaction in the frequency-dependent noise. For sake of completeness, we also analyze the noise in a quantum dot without electron-phonon interaction which is coupled to two normal leads and to a normal and a superconducting lead. The latter represents a preliminary study for future works.

The results shown in this chapter could be useful to understand to which extent the occupation of the resonator can be extracted by measurements of the frequency-dependent noise. As we discussed in chapters 4 and 5, the measurement of the phonon occupation of the resonator by purely electronic transport is still an open question. The analysis of the noise is particularly interesting for a resonator coupled to a normal and a superconducting contact since, as we discuss in chapter 5, the resonator can be cooled to the ground-state in this kind of contact. However, in this chapter we focus on the frequency-dependent noise in a quantum dot coupled to two normal leads interacting with a resonator. In this case, we calculated the full expression of the noise to the leading order in the electron-phonon coupling. The generalization for the case of a normal and a superconducting lead with the electron-phonon coupling can been done straightforwardly and will be discussed in the future.

To gain insight into the problem, we focus in Sec. 6.1 on the noise in a quantum dot coupled to two normal leads and describe the derivation of the noise using the Keldysh Green's function technique in more detail. In Sec. 6.2, we consider the noise in a dot with a normal and superconducting contacts. Finally, in Sec. 6.3, we discuss the noise in a suspended CNTQD coupled to normal contacts and with the electron-phonon interaction. Throughout this chapter, we focus on the non-symmetrized noise defined as [12]

$$S(\omega) = 2\int_{-\infty}^{\infty} d(t-t')e^{i\omega(t-t')}\langle \hat{I}_l(t)\hat{I}_l(t')\rangle \,, \tag{6.1}$$

with the current operator on the left lead $\hat{I}_l(t)$.

6.1 Noise in a normal contact coupled to a quantum dot

We study the zero-frequency and the frequency-dependent noise in a quantum dot in contact with two normal leads. The results presented in this section are known and obtained in previous works (see Ref. [17]). Here, the goal is to apply the Keldysh Green's function technique to calculate the noise which is helpful to understand the derivation of the noise in the following sections.

We consider the Hamiltonian

$$\hat{H} = \hat{H}_l + \hat{H}_r + \hat{H}_t + \hat{H}_d \,, \tag{6.2}$$

with the Hamiltonians of the left and the right contact,

$$\hat{H}_l = \sum_k \xi_k \hat{c}_k^\dagger \hat{c}_k \,, \tag{6.3}$$

$$\hat{H}_r = \sum_k \xi_k \hat{a}_k^\dagger \hat{a}_k \,, \tag{6.4}$$

and the creation operators $\hat{c}_k^\dagger$ and $\hat{a}_k^\dagger$ on the left and right lead, respectively. The tunneling Hamiltonian is

$$\hat{H}_t = \sum_k \left[t_{ld} \hat{c}_k^\dagger \hat{d} + t_{rd} \hat{a}_k^\dagger \hat{d} + \text{H.c.} \right] \tag{6.5}$$

with the coupling energy $t_{\alpha d}$ with $\alpha = (l, r)$ and the dot's operator $\hat{d}^\dagger$. The dot is described by

$$\hat{H}_d = \varepsilon_0 \hat{d}^\dagger \hat{d} \ , \tag{6.6}$$

with the energy level of the dot ε_0. Using the Heisenberg equation of motion, the current operator of the Hamiltonian Eq. (6.2) can be written as ($e > 0$)

$$\hat{I}_l(t) = i \frac{e}{\hbar} \sum_k \left[\hat{d}^\dagger(t) t_{dl} \hat{c}_k(t) - \hat{c}_k(t) t_{ld} \hat{d}(t) \right] . \tag{6.7}$$

This current operator can now be used to calculate the noise of Eq. (6.1). When we employ the Keldysh Green's function formalism, the creation and annihilation operators with time arguments t and t' in Eq. (6.7) are replaced by operators with time arguments τ and τ' on the Keldysh contour. The times τ and τ' can be positioned on the upper and lower branch on the Keldysh contour which is shown in Fig. 2.1. The noise of Eq. (6.1) is then obtained by the greater element of the noise in Keldysh space where the time τ lies on the lower branch and the time τ' on the upper branch.

The average $\langle \hat{I}_l(\tau) \hat{I}_l(\tau') \rangle$ in Eq. (6.1) contains terms with four fermionic operators and we use the Wick's theorem to decompose this correlation function into Green's functions with two fermionic operators. In this way, only one pairing out of the three possible combinations of the four operators remains finite. The current-current correlation function can then be written as

$$\begin{aligned} \langle \hat{I}_l(\tau) \hat{I}_l(\tau') \rangle = \frac{e^2}{\hbar^2} \sum_{kk'} [& G_{kd}(\tau', \tau) t_{dk} G_{k'd}(\tau, \tau') t_{dk'} - G(\tau', \tau) t_{dk} G_{kk'}(\tau, \tau') t_{k'd} \\ & - t_{dk} G_{kk'}(\tau', \tau) t_{k'd} G(\tau, \tau') + t_{kd} G_{dk}(\tau', \tau) t_{k'd} G_{dk'}(\tau, \tau')] \,, \end{aligned} \tag{6.8}$$

with the momentum k and k' of the electrons in the left lead and the Green's function $G(\tau,\tau')$ of the dot. The Green's functions $G_{kd}(\tau,\tau')$ and $G_{kk'}(\tau,\tau')$ are obtained by the equation of motion and they are given by

$$G_{kd}(\tau,\tau') = \int d\tau_1\, g_k(\tau,\tau_1) t_{ld} G(\tau_1,\tau')\,, \tag{6.9}$$

$$G_{kk'}(\tau,\tau') = g_k(\tau,\tau') + \int d\tau_1 d\tau_2\, g_k(\tau,\tau_1) t_{kd} G(\tau_1,\tau_2) t_{dk'} g_{k'}(\tau_2,\tau')\,, \tag{6.10}$$

with the unperturbed Green's function $g_k(\tau,\tau')$ of the left lead. Inserting the latter equation into Eq. (6.8), the current-current correlation function is expressed as

$$\begin{aligned}\langle \hat{I}_l(\tau)\hat{I}_l(\tau')\rangle = \frac{2e^2}{\hbar^2}\int d\tau_1 d\tau_2 [&\Sigma_l(\tau',\tau_1)G(\tau_1,\tau)\Sigma_l(\tau,\tau_2)G(\tau_2,\tau') \\ &- G(\tau',\tau)\Sigma_l(\tau,\tau_1)G(\tau_1,\tau_2)\Sigma_l(\tau_2,\tau') \\ &- \Sigma_l(\tau',\tau_1)G(\tau_1,\tau_2)\Sigma_l(\tau_2,\tau)G(\tau,\tau') \\ &+ G(\tau',\tau_1)\Sigma_l(\tau_1,\tau)G(\tau,\tau_2)\Sigma_l(\tau_2,\tau') \\ &- \Sigma_l(\tau',\tau)G(\tau,\tau') - G(\tau',\tau)\Sigma_l(\tau,\tau')]\,,\end{aligned} \tag{6.11}$$

with the self-energy of the left lead defined as $\Sigma_l(\tau,\tau') = \sum_k t_{dk} g_k(\tau,\tau') t_{kd}$.

We then transform Eq. (6.11) from the contour time to the real time as described in Sec. 2.1.2 and perform a Fourier transformation. The greater element of the noise in Keldysh space can be simplified to

$$\begin{aligned}S(\omega) = \frac{4e^2}{h}\int d\varepsilon \{&T(\varepsilon)(1-T(\varepsilon-\omega))\left(f_l(\varepsilon)-f_r(\varepsilon)\right)\left(f_l(\varepsilon-\omega)-f_r(\varepsilon-\omega)\right) \\ &+ T(\varepsilon)\left(f_r(\varepsilon)(1-f_r(\varepsilon-\omega)) + f_l(\varepsilon+\omega)(1-f_l(\varepsilon))\right) \\ &+ 4\Gamma_l^2 |G^R(\varepsilon-\omega) - G^R(\varepsilon)|^2 f_l(\varepsilon)(1-f_l(\varepsilon-\omega))\}\,,\end{aligned} \tag{6.12}$$

with the transmission $T(\varepsilon) = 4\Gamma_l G^R(\varepsilon)\Gamma_r G^A(\varepsilon)$, the retarded and advanced Green's functions on the dot $G^R(\varepsilon) = 1/[\varepsilon - \varepsilon_0 + i(\Gamma_l+\Gamma_r)]$, $G^A(\varepsilon) = G^{R*}(\varepsilon)$, the Fermi function $f_\alpha(\varepsilon) = 1/[1+\exp((\varepsilon-\mu_\alpha)/k_BT)]$ and the chemical potentials of the leads μ_α with $\alpha = (l,r)$. If we make the assumption that the electronic structure in the leads slowly changes around the Fermi energy ε_F and approximate the Green's functions with their value at the Fermi energy, $G^R(\varepsilon) \simeq G^R(\varepsilon_F) = G^R$, the noise in Eq. (6.12) reduce to the expressions of Eq. (2.43).

In the next section, we calculate the Fano factor of Eq. (2.39) defined by

$$F = \frac{S(0)}{2e\langle I\rangle}\,, \tag{6.13}$$

with the noise $S(0)$ at zero frequency and the current $\langle I\rangle$. For a quantum dot coupled to two normal leads, the current is given by

$$\langle I\rangle = \frac{2e}{h}\int d\varepsilon\, T(\varepsilon)(f_l(\varepsilon)-f_r(\varepsilon))\,, \tag{6.14}$$

and reduces to

$$\langle I\rangle_{\max} = \frac{4e}{\hbar}\frac{\Gamma_l\Gamma_r}{\Gamma_l+\Gamma_r} \tag{6.15}$$

in the high-voltage limit $eV \gg (\varepsilon_0, \Gamma_l, \Gamma_r)$.

6.1.1 Current, shot noise and Fano factor

At zero-frequency, the noise is

$$S(0) = \frac{4e^2}{h} \int d\varepsilon \{T(\varepsilon)\left(f_r(\varepsilon)(1-f_r(\varepsilon)) + f_l(\varepsilon)(1-f_l(\varepsilon))\right)\} + T(\varepsilon)(1-T(\varepsilon))\left(f_l(\varepsilon)-f_r(\varepsilon)\right)^2 . \quad (6.16)$$

As we discussed in Sec. 2.4.1, thermal fluctuations are described by the terms like $f_\alpha(\varepsilon)(1-f_\alpha(\varepsilon))$ ($\alpha = (l,r)$) and the shot noise at zero temperature by the second line in Eq. (6.16). An analytic expression of the zero-frequency noise can be obtained at zero temperature and in the limit $eV \gg (\varepsilon_0, \Gamma_l, \Gamma_r)$. In this regime, the noise is

$$S(0) = 2e\langle I\rangle_{\max} \frac{\Gamma_l^2 + \Gamma_r^2}{(\Gamma_l + \Gamma_r)^2} . \quad (6.17)$$

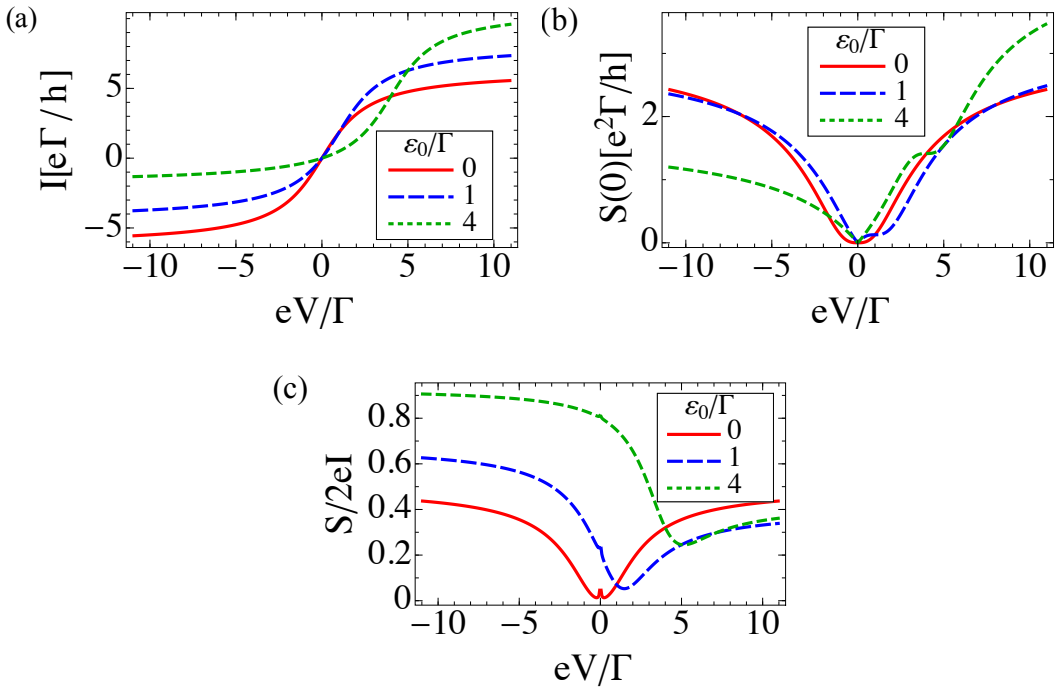

Figure 6.1: Transport properties of a quantum dot coupled to two normal leads. The voltage is applied asymmetrically with $\mu_l = eV$ and $\mu_r = 0$. Current (a), zero-frequency noise (b) and Fano factor (c) for different energies of the level on the dot. At negative voltages and ($|eV| \ll \Gamma$) and at $\varepsilon_0 = 4\Gamma$, current occurs out of resonance and the transmission is strongly suppressed such that the electrons tunnel uncorrelated through the quantum dot. The small transmissions give rise to a Fano factor of $F = 1$. At large positive voltages ($eV \gg \Gamma$), the Fano factor approaches $F = 0.5$ as given by Eq. (6.18).

With Eq. (6.15), the Fano factor then becomes

$$F = \frac{\Gamma_l^2 + \Gamma_r^2}{(\Gamma_l + \Gamma_r)^2} \tag{6.18}$$

and varies between $F = 0.5$ and $F = 1$ depending on the coupling to the leads. For symmetric coupling, $\Gamma_l = \Gamma_r$, the Fano factor becomes $F = 0.5$ and for strongly asymmetric coupling $\Gamma_l \gg \Gamma_r$ or $\Gamma_r \gg \Gamma_l$, the Fano factor is $F = 1$.

The current, the zero-frequency noise and the Fano factor are shown in Fig. 6.1 at zero temperature and for different energies of the quantum dot's level. The voltage is applied on the left lead with $\mu_l = eV$ and $\mu_r = 0$ and the energy of the quantum dot's level is measured with respect to the chemical potential of the right lead. We consider a symmetric coupling to the leads with $\Gamma_l = \Gamma_r = \Gamma$.

To understand the behavior of the Fano factor as a function of voltage, we consider as example an energy of the quantum dot's level of $\varepsilon_0 = 4\Gamma$ (green line in Fig. 6.1). For negative voltages and $|eV| \ll \Gamma$, the current is suppressed since the transport occurs out of resonance. In this case, the Fano factor approaches $F = 1$ indicating that the tunneling of individual electrons is uncorrelated. When the voltage is increased and approaches the energy level of the dot $\varepsilon_0 = 4\Gamma$ which is broadened by the coupling to the leads, the noise is suppressed. In this case, the transport occurs close to resonance, the transmission increases and hence the Fano factor decreases. For even larger positive voltages, we reach the high-voltage limit $eV \gg (\varepsilon_0, \Gamma)$, and the Fano factor approaches $F = 0.5$ pointing out resonant transport through the dot.

6.1.2 Frequency-dependent noise

Fig. 6.2 shows the frequency-dependent noise [Eq. (2.43)] at zero temperature and different voltages. Here, the voltage is applied symmetrically with $\mu_l = -\mu_r = eV/2$.

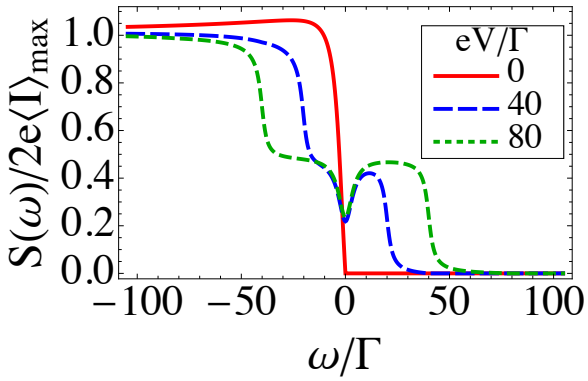

Figure 6.2: Frequency-dependent noise at zero temperature and $\varepsilon_0 = 0$. The voltage is applied symmetrically with $\mu_l = -\mu_r = eV/2$. The noise vanishes for $\omega > eV$. At negative frequencies, the noise shows a step-like increases when the frequency is larger than the voltage on the left lead, e.g. $|\omega| = -eV/2$.

Since the temperature is zero, thermal noise vanishes and the noise at $\omega = 0$ is solely due to the shot noise.

As discussed in Sec. 2.4.1 we can separate the frequency-dependent noise into a region of photon emission ($\omega > 0$) and photon absorption ($\omega < 0$). At zero voltage and zero temperature, the nanostructure can only absorb photons with frequency $|\omega|$ and hence the noise vanishes for positive noise frequencies (red line in Fig. 6.2). At finite voltage, emission of photons is also possible and the noise is different from zero for positive frequencies and $\omega < eV$ (blue and green line in Fig. 6.2).

At negative frequencies and at zero voltage, the noise first increases and approaches the value of $S_0 = (e^2/\hbar)4\Gamma_l = 2e\langle I\rangle_{\max}$ for $\omega \ll -|eV|$ corresponding to the Poisson value of the noise. S_0 corresponds to processes in which an electron tunnels to the quantum dot, is excited by a photon with frequency ω and then tunnels back to one of the leads. However, electrons with energy $-eV/2 < \varepsilon < eV/2 - \omega$ can tunnel only to the right lead. In the limit $\omega \ll -|eV|$ we also have $\omega \ll -\Gamma_n$ such that the time for an absorption of an electron by a photon is much smaller than the tunneling rate. In this case the tunneling of the electron is uncorrelated as indicated by the Poisson value of noise. Since the density of states on the quantum dot shows a Lorentzian dependence as a function of energy, the noise saturates for large negative frequencies. This behavior is different compared to noise in a quantum point contact as discussed in Sec. 2.4.1 in which the noise increases linearly with negative frequencies.

When a voltage is applied, the noise is reduced compared to the case of zero voltage since the states in the left lead are occupied up to the chemical potential and hence absorption from the quantum dot's level is suppressed for electrons tunneling to the left lead. At negative frequencies and $|\omega| = eV/2$, a second step occurs in the noise, since absorption of electrons above the chemical potential of the left lead is possible as indicated by the upward arrows in Fig. 6.3. In this case, the electrons can tunnel to the left and to the right lead. The downward arrows show the emission of photons at positive noise frequencies. The emission vanishes when $\omega > eV$.

Analytic expressions of the noise can be derived in two limits. The first limit corresponds to the high-voltage case in which the voltage is the larger than all other

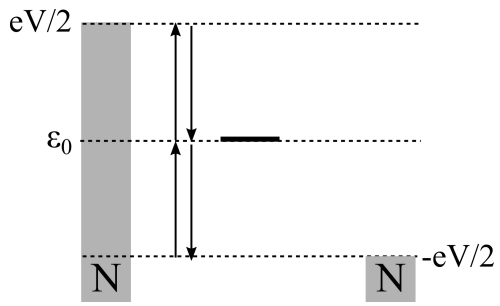

Figure 6.3: Sketch of absorption (upward arrow) and emission (downward arrow) processes corresponding to the second step in the frequency-dependent noise of Fig. 6.2 at finite voltage.

parameters, e.g. $eV \gg (\varepsilon_0, \Gamma_l, \Gamma_r, \omega)$. In Fig. 6.2, this limit corresponds to the plateau of the noise at finite frequency and is given by

$$S(\omega) = 2eI_{\max}\frac{4(\Gamma_l^2+\Gamma_r^2)+\omega^2}{4(\Gamma_l+\Gamma_r)^2+\omega^2}\,. \tag{6.19}$$

The second limit corresponds to the case when the frequency is larger than the other parameters, e.g. $\omega \gg (\varepsilon_0, \Gamma_l, \Gamma_r, eV)$. In this case the noise approaches the value S_0 for negative frequencies.

6.2 Noise in a normal-superconducting contact coupled to a quantum dot

We consider the noise in a quantum dot coupled to a normal and a superconducting contact. The proximity induced superconductivity on the quantum dot and the accompanied Andreev reflection have to be taken into account in this case. In this section, we are interested in the subgap regime in which the pairing Δ is the largest energy in the systems and hence contributions to the noise are solely due the Andreev reflection and we neglect the noise associated to the quasiparticles. Notice that we use the notation $\Gamma_l = \Gamma_n$ (left normal lead) and $\Gamma_r = \Gamma_s$ (right superconducting lead) for this system.

The Hamiltonian is given by Eq. (6.2) with the difference that the right lead is replaced by the BCS-Hamiltonian

$$\hat{H}_s = \sum_{k\sigma}\xi_k\hat{a}^\dagger_{k\sigma}\hat{a}_{k\sigma} + \Delta\hat{a}^\dagger_{-k\downarrow}\hat{a}^\dagger_{k\uparrow} + \Delta^\dagger\hat{a}_{k\uparrow}\hat{a}_{-k\downarrow} \tag{6.20}$$

with the operators $\hat{a}_k$ and $\hat{a}^\dagger_k$ of the superconducting lead and the superconducting gap Δ. The noise is calculated in the same way as in Sec. 6.1 but we have to introduce field operators in Nambu space to account for the correlation between the electron and holes. The current operator is finally given by

$$\hat{I}_l(t) = i\frac{e}{\hbar}\sum_k\left[\psi^\dagger_d(t)\tau_3 V_{dk}\psi_k(t) - \psi^\dagger_k(t)\tau_3 V_{kd}\psi_d(t)\right]\,, \tag{6.21}$$

with the Pauli matrix τ_3 in Nambu space and the field operators defined in Eq. (2.27). We then proceed to carry out the same steps from Eq. (6.8) to (6.11) to obtain the frequency-dependent noise. In the subgap regime ($\Delta \to \infty$), the result is

$$\begin{aligned}
S(\omega) = \frac{2e^2}{h}\int d\varepsilon\,[&2\left(T_{eh}(\varepsilon)(1-T_{eh}(\varepsilon-\omega)) + T_{eh}(\varepsilon-\omega)(1-T_{eh}(\varepsilon))\right)\\
&[(f_+(\varepsilon)-f_-(\varepsilon))(f_+(\varepsilon-\omega)-f_-(\varepsilon-\omega))]\\
&+2(T_{eh}(\varepsilon)+T_{eh}(\varepsilon-\omega))[f_+(\varepsilon)(1-f_+(\varepsilon-\omega)) + f_-(\varepsilon)(1-f_-(\varepsilon-\omega))]\\
&-4\,\Gamma_n^2|F(\varepsilon)-F(\varepsilon-\omega)|^2[f_+(\varepsilon)(1-f_-(\varepsilon-\omega)) + f_-(\varepsilon)(1-f_+(\varepsilon-\omega))]\\
&+4\,\Gamma_n^2|G_+(\varepsilon)-G_+(\varepsilon-\omega)|^2[f_+(\varepsilon)(1-f_+(\varepsilon-\omega))]\\
&+4\,\Gamma_n^2|G_-(\varepsilon)-G_-(\varepsilon-\omega)|^2[f_-(\varepsilon)(1-f_-(\varepsilon-\omega))]\Big]
\end{aligned} \tag{6.22}$$

with the transmission function for the Andreev reflections $T_{eh}(\varepsilon) = 4\Gamma_n^2|F(\varepsilon)|^2$, the Fermi function for electrons ($\nu = +$) and holes ($\nu = -$) $f_\nu(\varepsilon) = 1/[1 + \exp((\varepsilon - \nu\mu_l)/k_BT)]$ and the anomalous Green's function (see Appendix C.1)

$$F(\varepsilon) = -\frac{\Gamma_s}{(\varepsilon + \varepsilon_A + i\Gamma_n)(\varepsilon - \varepsilon_A + i\Gamma_n)}\,. \tag{6.23}$$

and the

$$G_\nu^R(\varepsilon) = \frac{-(\varepsilon + \nu\varepsilon_0 + i\Gamma_n)}{(\varepsilon + \varepsilon_A + i\Gamma_n)(\varepsilon - \varepsilon_A + i\Gamma_n)} \tag{6.24}$$

with the energies $\pm\varepsilon_A = \pm\sqrt{\varepsilon_0^2 + \Gamma_s^2}$ of the Andreev levels. In the limit $\Gamma_n \gg (eV, k_BT)$, the Green's functions can be approximated with their values at the Fermi energy $T_{eh}(\varepsilon) \simeq T_{eh}(\varepsilon_F) = T_{eh}$. Then, the last three terms in Eq. (6.22) vanish and the frequency-dependent noise reduces to the same expression of Refs. [17] and [213].

The current in the subgap regime for a quantum dot coupled to a normal lead and a superconductor is

$$\langle I\rangle = \frac{2e}{h}\int d\varepsilon\, T_{eh}(\varepsilon)(f_+(\varepsilon) - f_-(\varepsilon)) \tag{6.25}$$

and reduces to

$$\langle I\rangle_{\max} = \frac{4e}{\hbar}\frac{\Gamma_n\Gamma_s^2}{\Gamma_n^2 + \varepsilon_A^2}\,. \tag{6.26}$$

in the high-voltage limit $eV \gg (\Gamma_n, \varepsilon_A)$.

6.2.1 Zero-frequency noise

The zero-frequency noise is given by

$$S(0) = \frac{2e^2}{h}\int d\varepsilon \Big[4T_{eh}(\varepsilon)(1 - T_{eh}(\varepsilon))(f_+(\varepsilon) - f_-(\varepsilon))^2 + 4T_{eh}(\varepsilon)[f_+(\varepsilon)(1 - f_+(\varepsilon)) + f_-(\varepsilon)(1 - f_-(\varepsilon))]\Big]\,. \tag{6.27}$$

In the limit $k_BT \ll eV$, the second line in Eq. (6.27) can be neglected compared to the first line and the noise is solely given by shot noise. In the opposite limit $k_BT \gg eV$, the first line in Eq. (6.27) is negligible and the noise reduces to the thermal noise.

To gain insight into the zero-frequency noise, we first consider the limit of an energy-independent transmission. At zero temperature, the noise is $S(0) = 16eVT_{eh}(1 - T_{eh}) = 4\langle I\rangle e(1 - T_{eh})$ with the current $\langle I\rangle = 4T_{eh}eV$. The Fano factor then is $F = 2(1 - T_{eh})$. For small transmissions, $T_{eh} \ll 1$, the current is suppressed and the Fano factor reduces to $F = 2$, indicating that in a process of Andreev reflection a charge of $2e$ is transferred to the superconductor.

In general however, the transmissions depend on energy. The current, zero-frequency noise and the Fano factor are shown in Fig. 6.4. Note the symmetry of the noise with respect to the bias voltage which is applied on the normal lead. Figure 6.4(a) shows the current in the subgap regime as a function of the voltage. When the voltages

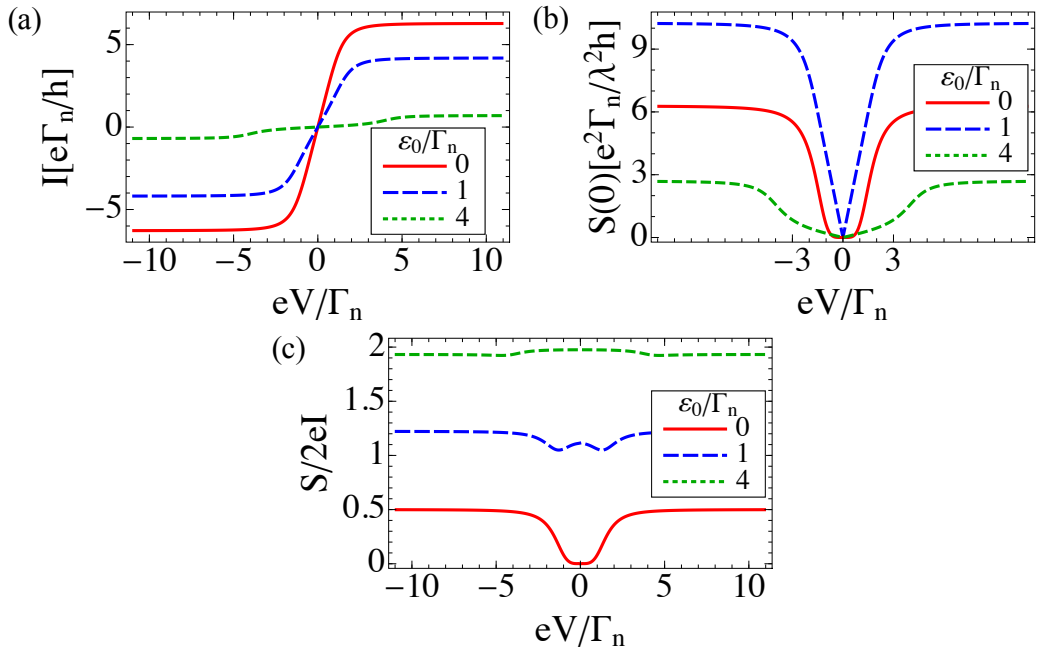

Figure 6.4: Transport properties of a quantum dot coupled to a normal and a superconducting contact at zero temperature. Current (a), zero-frequency noise (b) and Fano factor (c) for different energies of the level on the dot.

approaches the energy of the Andreev levels at $\pm\varepsilon_A$, the current increases (decreases) for positive (negative) voltages. The height of the step depends strongly on the energy of the quantum dot's level. Out of resonance, Andreev reflection is suppressed and the current increases less compared to the case on resonance.

The zero-frequency noise as a function of the voltage is shown in Fig. 6.4(b). In the high-voltage limit $eV \gg (\Gamma_n, \varepsilon_A)$, the noise reduces to

$$S(0) = 2e\langle I\rangle_{\max}\left(2 - \frac{\Gamma_s^2}{\Gamma_n^2+\varepsilon_A^2} - \frac{4\Gamma_n^2\Gamma_s^2}{(\Gamma_n^2+\varepsilon_A^2)^2}\right). \tag{6.28}$$

Equation (6.28) has a non-monotonic dependence on the ε_0. Moreover, a large gate voltage, $\varepsilon_0 \gg (\Gamma_n, \Gamma_s)$, suppresses the zero-frequency noise. In this regime, the last two terms in Eq. (6.28) vanish and the Fano factor becomes $F = 2$ indicating the uncorrelated transfer of one Cooper pairs at the time.

6.2.2 Frequency-dependent noise

We now study the frequency-dependent noise as a function of the noise frequency ω. The discussion is divided into two parts. We consider first the regime of zero and small voltages compared to the energy of the Andreev level ($|eV| < |\varepsilon_A|$). Second we discuss the opposite case with a voltage larger than the Andreev level ($|eV| > |\varepsilon_A|$). To reveal the features of the frequency-dependent noise in these two regimes, we focus

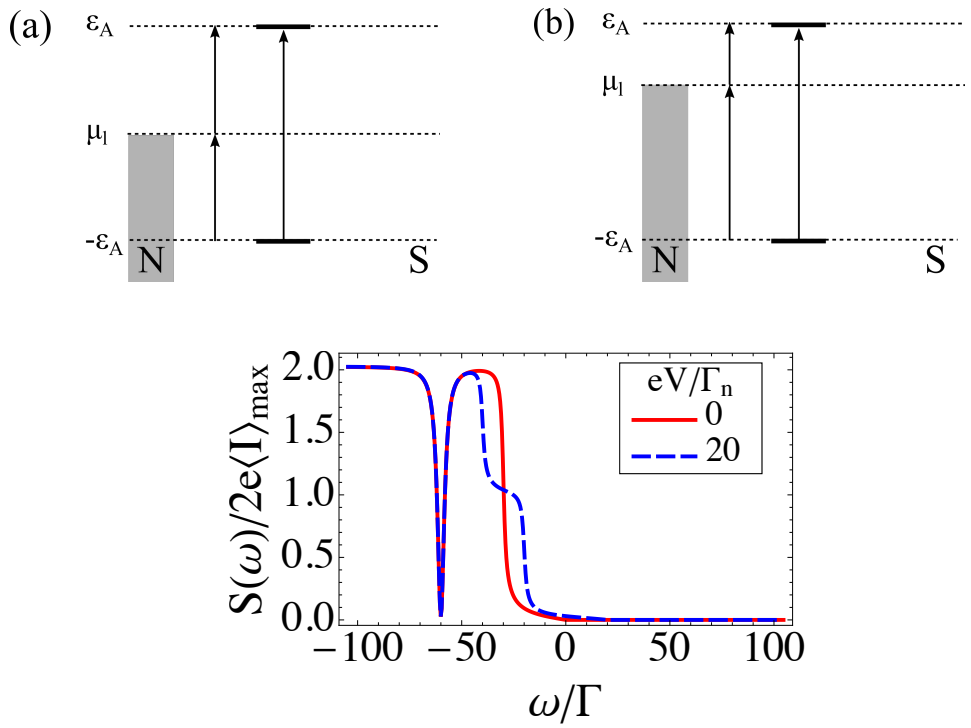

Figure 6.5: Sketch of absorption processes at zero voltage (a) and finite voltage (b) in the regime when the applied voltage is smaller than the Andreev level at ε_A. The frequency-dependent noise at zero temperature, $\Gamma_s = 30\Gamma_n$ and $\varepsilon_0 = 0$ is shown in (c). The noise vanishes when $\omega > 2eV$. The dip of the noise at $\omega = -60\Gamma_n = -2\varepsilon_A$ correspond to the absorption of an electron from the lower to the upper Andreev level. The step-like increase at $\omega = -30\Gamma_n = -\varepsilon_A$ at zero voltage corresponds to the transitions between the left chemical potential and the single Andreev levels. The degeneracy of these transitions is lifted at finite voltage where the step in the noise appear at $\omega = -20\Gamma_n$ and $\omega = -40\Gamma_n$ (blue dashed line).

on an asymmetric coupling to the leads with $\Gamma_s \gg \Gamma_n$ and restrict the discussion to the zero temperature limit.

Figure 6.5 shows the noise at $\Gamma_s = 30\Gamma_n$ and a quantum dot's level at $\varepsilon_0 = 0$. In this case the energies of the Andreev levels are at $\pm\varepsilon_A = \pm\Gamma_s$. At zero voltage the contact can only absorb photons with frequency ω and hence the noise vanishes for positive frequencies. The possible absorption processes at zero voltage are sketch in Fig. 6.5(a) and the noise is shown in Fig. 6.5(c) (red solid line). The noise shows a step when the frequency is close to the transition corresponding to the absorption from the left chemical potential to the upper Andreev level or an absorption from the lower Andreev level to the left chemical energy. In both cases we have $\omega = -\varepsilon_A = -\Gamma_s$. At a frequency of $\omega = -2\Gamma_s$ the noise is strongly suppressed. This process corresponds to the absorption of a photon with frequency $\omega = -2\varepsilon_A$ from the lower to the upper Andreev level. The strong suppression of the noise is related to the

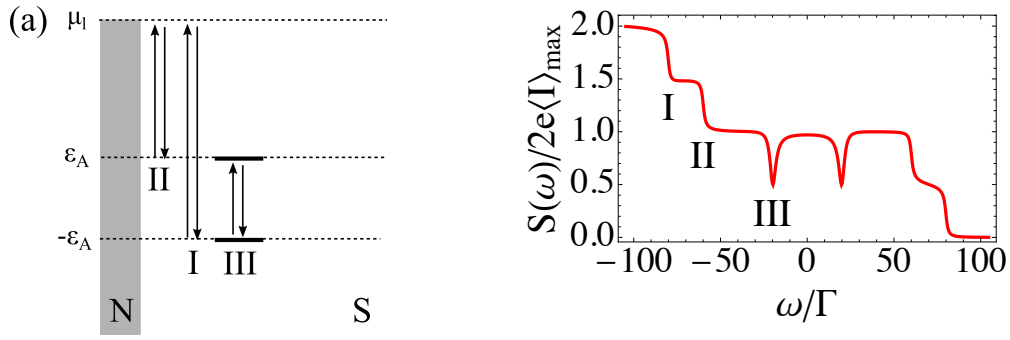

Figure 6.6: Sketch of absorption and emission processes (a) and frequency-dependent noise (b) at zero temperature in the regime $\varepsilon_A < eV$. The coupling to the superconducting lead is $\Gamma_s = 10\Gamma_n$, $\varepsilon_0 = 0$ and the voltage is $eV = 70\Gamma_n$. Since $eV > \varepsilon_A$, also emission of photons between the chemical potential of the left lead and the Andreev levels are allowed (downward arrows in (a)).

coherent destructive interference between the Andreev states [214].

The transition between the two Andreev levels is independent of voltage and hence the dip in the noise also appears with same frequency at finite voltage (dashed blue line). However, the degeneracy of the two processes involving the chemical potential of the normal lead to the upper and lower Andreev level is lifted and additional steps in the noise are visible at $\omega = \varepsilon_A - \mu_l$ and $\omega = \mu_l - \varepsilon_A$. These processes are sketched in Fig. 6.5(b) and the noise is shown in (c) (blue dashed line).

We also remark that compared to the threshold $\omega > eV$ of for photon emission at zero temperature for two normal contacts, here the noise vanishes for $\omega > 2eV$. Since the voltage is smaller than the splitting of the Andreev levels and the difference between the Andreev levels and the left chemical potential, the dips and the steps in the noise are not present at positive frequencies.

Figure 6.6 shows the frequency-dependent noise in the regime when the voltage is larger than the energy of the Andreev levels ($eV > |\varepsilon_A|$). Similar to the previous discussion, transitions appear between the Andreev levels and the chemical potential of the normal lead. However, since the voltage is larger than the Andreev level at ε_A, we also observe transition at positive noise frequencies. The emission of photons are indicated by the downward vertical arrows in Fig. 6.6(a).

As discussed in the introduction, the noise indeed reveals the structure of the internal excitations of the system.

6.3 Noise of a suspended carbon nanotube in a normal contact

In this section, we derive the frequency-dependent noise in a suspended carbon nanotube quantum dot coupled to two normal contacts. The interaction between the resonator and the quantum dot is taken into account to leading order in the coupling

λ between the dot and the resonator. The Hamiltonian is given by

$$\hat{H} = \hat{H}_l + \hat{H}_r + \hat{H}_t + \hat{H}_d + \hat{H}_m \,, \tag{6.29}$$

with the Hamiltonian of the left contact, $\hat{H}_l = \sum_k \xi_k \hat{c}_k^\dagger \hat{c}_k$, the right contact $\hat{H}_r = \sum_k \xi_k \hat{a}_k^\dagger \hat{a}_k$, and the creation operators $\hat{c}_k^\dagger$ and $\hat{a}_k^\dagger$ of the left and right lead, respectively. The tunneling Hamiltonian is $\hat{H}_t = \sum_k [t_{nd} \hat{c}_k^\dagger \hat{d} + t_{dn} \hat{d}^\dagger \hat{c}_k + t_{sd} \hat{a}_k^\dagger \hat{d} + t_{ds} \hat{d}^\dagger \hat{a}_k]$ with the coupling energy $t_{\alpha d}$ with $\alpha = (n, s)$ and the dot's operator $\hat{d}^\dagger$. The dot is described by $\hat{H}_d = \varepsilon_0 \hat{d}^\dagger \hat{d}$ with the energy level of the dot ε_0. We consider the Holstein model with an oscillator with frequency ω coupled linearly to the quantum dot

$$\hat{H}_m = \lambda \hat{n}_d (\hat{b}^\dagger + \hat{b}\ ) + \omega_0 \hat{b}^\dagger \hat{b} \,, \tag{6.30}$$

with the number operator $n_d = \hat{d}^\dagger \hat{d}$ of the dot. The annihilation and creation operators of the resonator are given by $\hat{b}$ and $\hat{b}^\dagger$ and the frequency is denoted by ω_0. The current operator is given by Eq. (6.7).

Similar to Sec. 6.1, we have to calculate the current-current correlation function $\langle \hat{I}_l(t) \hat{I}_l(t') \rangle$ which contains the expectation value of four operators. However, compared to the case without vibration, we are not able to decompose the average of the correlation function into Green's functions with two operators since the average is calculated with respect to a non-quadratic Hamiltonian due to the electron-phonon interaction in Eq. (6.30). To this end, we perform a perturbation expansion to the leading order in λ and write the expression in terms of Green's functions with two operators. The noise can then be written as

$$S(\omega) = S_0(\omega) + \lambda^2 S_1(\omega) \tag{6.31}$$

in which the second term contains the contribution from the electron-phonon interaction.

To calculate the frequency-dependent noise, we employ the Keldysh Green's function technique. Similar to Sec. 6.1, we first replace the time arguments t and t' of the operators in Eq. (6.7) with the times τ and τ' on the Keldysh contour shown in Fig. 2.1. Second, we perform an expansion of the noise to the leading order in λ and draw all irreducible Feynman diagrams. As a result we obtain the noise $S(\tau, \tau')$ in Keldysh space. The greater element of the latter quantity with the time τ on the lower branch and the time τ' on the upper branch then gives the non-symmetrized noise in Eq. (6.1). Third, we transform this greater element of the noise from the contour to the real time and make the Fourier transform of the expression.

6.3.1 Contour-time Feynman diagrams

A perturbative expansion gives that the noise can be divided into a mean-field contribution $S_{\mathrm{mf}}(\tau, \tau')$ and a term called vertex correction, $S_{\mathrm{vc}}(\tau, \tau')$, as

$$S_1(\tau, \tau') = S_{\mathrm{mf}}(\tau, \tau') + S_{\mathrm{vc}}(\tau, \tau') \,. \tag{6.32}$$

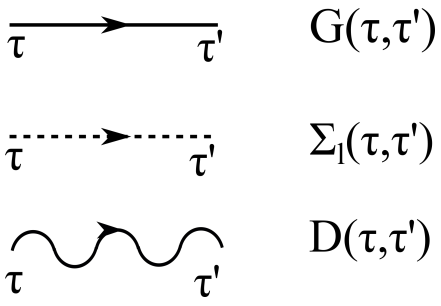

Figure 6.7: Elements of Feynman diagrams depending on the Keldysh contour times τ and τ'. The solid and dashed line represent the Green's function on the dot $G(\tau, \tau')$ and the self-energy of the left lead $\Sigma_l(\tau, \tau')$. The phonon propagator $D(\tau, \tau')$ is denoted by the wiggled line.

The separation of the correction to the noise into a mean field contribution and a vertex correction follows Ref. [170].

In the following, we discuss in detail the Feynman diagrams depending on the contour time. We will first discuss the mean-field noise and second focus on the vertex correction. The diagrammatic representation of the electron- and phonon Green's function is shown in Fig. 6.7.

We denote the contour-ordered Green's function of the dot $G(\tau, \tau')$ and the self-energy of the left lead $\Sigma_l(\tau, \tau')$ by a solid and dashed line, respectively. The contour-ordered phonon propagator $D(\tau, \tau')$ is depicted as a wiggled line.

Mean-field noise

The mean-field noise can be divided into a contribution due to rainbow (tb) and tapole (tp) diagrams. A diagrammatic representation of the diagrams constituting to the rainbow and tadole diagrams is shown in Fig. 6.8(a) and (b), respectively. These

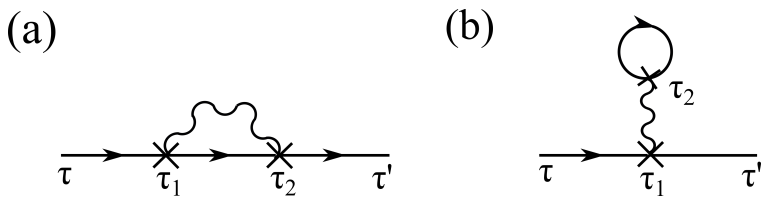

Figure 6.8: Diagrammatic representation of Eq. (6.33) and (6.34) containing the rainbow (a) and tadpole (b) diagrams. The solid line represents the Green's function $G(\tau, \tau')$ on the dot and the wiggled line the phonon propagator $D(\tau, \tau')$. The cross represents a vertex due to the electron-phonon interaction.

diagrams have the form

$$A^{\mathrm{mf}}_{\mathrm{rb}}(\tau,\tau') = \int d\tau_1 d\tau_2\, G(\tau,\tau_1)\Sigma^{\mathrm{mf}}_{\mathrm{rb}}(\tau_1,\tau_2)G(\tau_2,\tau')\,, \tag{6.33}$$

$$A^{\mathrm{mf}}_{\mathrm{tp}}(\tau,\tau') = \int d\tau_1 d\tau_2\, G(\tau,\tau_1)\Sigma^{\mathrm{mf}}_{\mathrm{tp}}(\tau_1,\tau_2)G(\tau_1,\tau')\,, \tag{6.34}$$

and differ in their time arguments of the Green's function. The self-energies due to the rainbow and tadpole diagrams are given by

$$\Sigma^{\mathrm{mf}}_{\mathrm{rb}}(\tau_1,\tau_2) = i\lambda^2 D(\tau_1,\tau_2)G(\tau_1,\tau_2)\,, \tag{6.35}$$

$$\Sigma^{\mathrm{mf}}_{\mathrm{tp}}(\tau_1,\tau_2) = -i\lambda^2 D(\tau_1,\tau_2)G(\tau_2,\tau_2)\,. \tag{6.36}$$

With the definition of the diagrams in Eq. (6.33) or (6.34), we can write down the contour-time Feynman diagrams contributing to the mean-field noise in Fig. 6.9. The rectangular box in Fig. 6.9 represents either the rainbow or the tadpole diagrams given by Eq. (6.33) or (6.34). The diagrams can be divided into two kinds. The first kind of diagrams, shown in Fig. 6.9(a), contain a single self-energy of the left

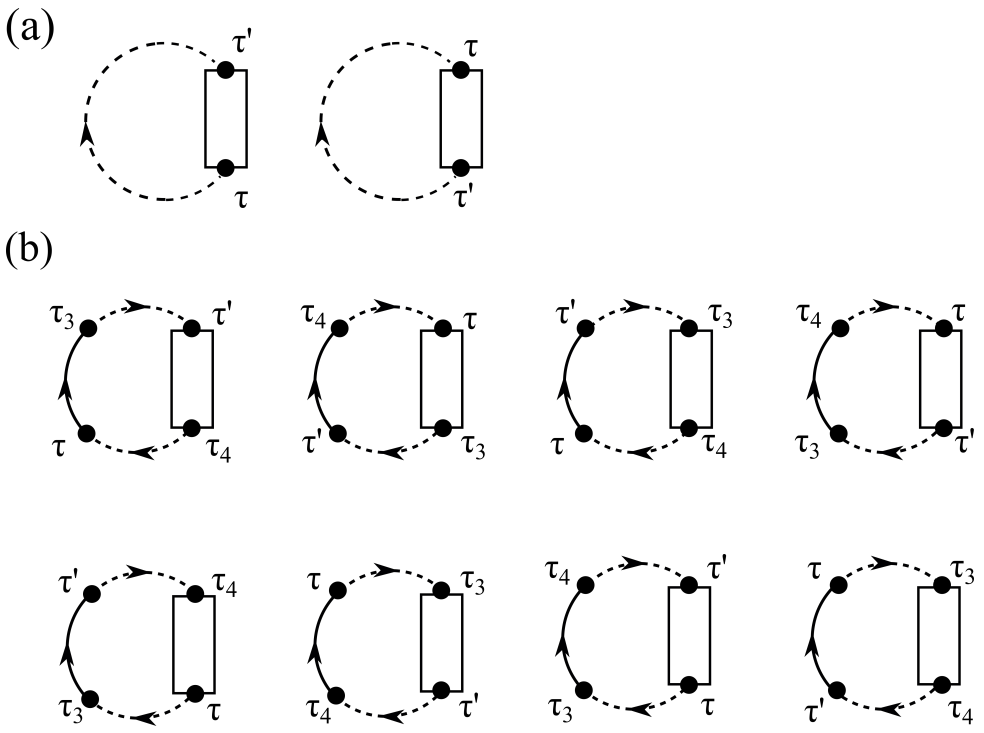

Figure 6.9: Diagrammatic representation of the noise. The solid line represent the electronic Green's function on the dot $G(\tau,\tau')$ and the dashed line the self-energy of the left lead, $\Sigma_l(\tau,\tau')$. The rectangular box represents either the diagram of Fig. 6.8(a) or Fig. 6.8(b). The time arguments τ_3 and τ_4 are internal indexes and the diagrams can be separated into contribution without (a) and with (b) internal indexes. The filled circle represents the tunneling between the left lead and the dot.

lead and the rectangular box. There are two different diagrams of the first kind. Since we want to calculate the frequency-dependent noise, the two diagrams shown in Fig. 6.9(a) will give different contributions to the noise. The second kind of diagrams contain two self-energies of the left lead and one electronic Green's functions. There are eight different diagrams of the second kind differing by the time labels.

Finally, we can write the mean-field noise as

$$\begin{aligned} S_{\mathrm{mf}}(\tau,\tau') = \frac{2e^2}{h}\sum_{\alpha=\mathrm{rb,tp}} \{\Sigma_l(\tau,\tau')A^{\mathrm{mf}}_\alpha(\tau',\tau) + A^{\mathrm{mf}}_\alpha(\tau,\tau')\Sigma_l(\tau',\tau) + \int d\tau_3 d\tau_4 \{ \\ G(\tau,\tau_3)\Sigma_l(\tau_3,\tau')A^{\mathrm{mf}}_\alpha(\tau',\tau_4)\Sigma_l(\tau_4,\tau) \\ + A^{\mathrm{mf}}_\alpha(\tau,\tau_3)\Sigma_l(\tau_3,\tau')G(\tau',\tau_4)\Sigma_l(\tau_4,\tau) \\ - G(\tau,\tau')\Sigma_l(\tau',\tau_3)A^{\mathrm{mf}}_\alpha(\tau_3,\tau_4)\Sigma_l(\tau_4,\tau) \\ - A^{\mathrm{mf}}_\alpha(\tau,\tau')\Sigma_l(\tau',\tau_3)G(\tau_3,\tau_4)\Sigma_l(\tau_4,\tau) \\ + \Sigma_l(\tau,\tau_3)G(\tau_3,\tau')\Sigma_l(\tau',\tau_4)A^{\mathrm{mf}}_\alpha(\tau_4,\tau) \\ + \Sigma_l(\tau,\tau_3)A^{\mathrm{mf}}_\alpha(\tau_3,\tau')\Sigma_l(\tau',\tau_4)G(\tau_4,\tau) \\ - \Sigma_l(\tau,\tau_3)A^{\mathrm{mf}}_\alpha(\tau_3,\tau_4)\Sigma_l(\tau_4,\tau')G(\tau',\tau) \\ - \Sigma_l(\tau,\tau_3)G(\tau_3,\tau_4)\Sigma_l(\tau_4,\tau')A^{\mathrm{mf}}_\alpha(\tau',\tau)\}\}\,. \end{aligned} \tag{6.37}$$

The first two terms in Eq. (6.37) corresponds to the diagrams shown in Fig. 6.9(a), and the following eight terms to the diagrams in Fig. 6.9(b).

Vertex correction

We now turn to the contribution to the noise due to the vertex correction $S_{\mathrm{vc}}(\tau,\tau')$. The vertex correction contains rainbow- and tadpole-like diagrams although the electronic Green's function connecting the phonon Green's function is replaced by the product of two electronic Green's function and a self-energy (see Fig. 6.10). The self-energies due to the vertex correction depend on the time τ' and can be divided into two kinds of diagrams depending on the position of τ'. The rainbow-like diagrams can be written as

$$\Sigma^{\mathrm{vc},I}_{\mathrm{rb}}(\tau_1,\tau_2) = i\lambda^2 \int d\tau_3\, G(\tau_1,\tau_3)\Sigma_l(\tau_3,\tau')G(\tau',\tau_2)D(\tau_1,\tau_2)\,, \tag{6.38}$$

$$\Sigma^{\mathrm{vc},II}_{\mathrm{rb}}(\tau_1,\tau_2) = i\lambda^2 \int d\tau_3\, G(\tau_1,\tau')\Sigma_l(\tau',\tau_3)G(\tau_3,\tau_2)D(\tau_1,\tau_2)\,, \tag{6.39}$$

and the tadpole-like diagrams are

$$\Sigma^{\mathrm{vc},I}_{\mathrm{tp}}(\tau_1,\tau_2) = -i\lambda^2 \int d\tau_3\, G(\tau',\tau_2)G(\tau_2,\tau_4)\Sigma_l(\tau_4,\tau')D(\tau_1,\tau_2)\,, \tag{6.40}$$

$$\Sigma^{\mathrm{vc},II}_{\mathrm{tp}}(\tau_1,\tau_2) = -i\lambda^2 \int d\tau_3\, \Sigma(\tau,\tau_4)G(\tau_4,\tau_2)\Sigma_l(\tau_2,\tau)D(\tau_1,\tau_2)\,. \tag{6.41}$$

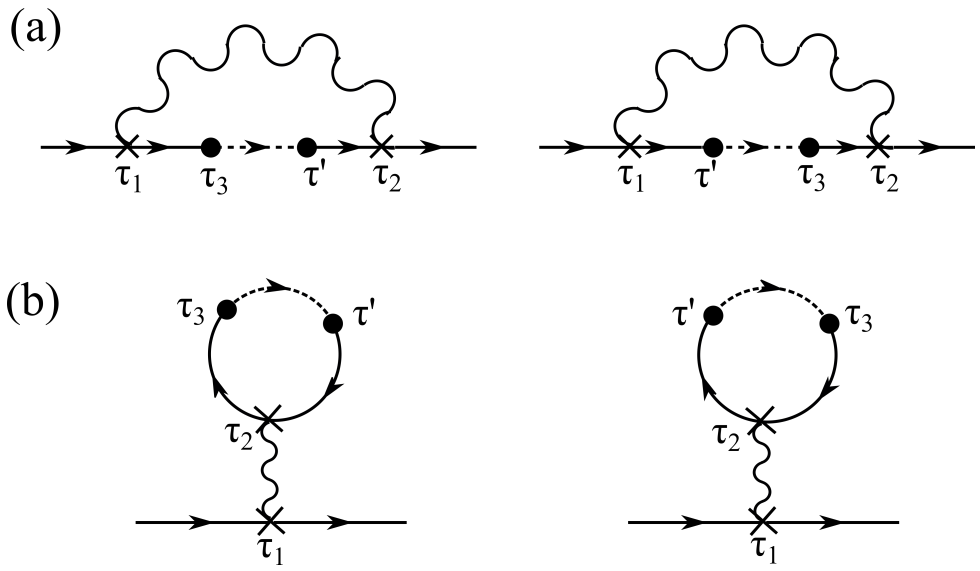

Figure 6.10: Real-time representation of the vertex correction. The diagrams in (a) and (b) show rainbow-and tadpole-like diagrams.

Similar to Eq. (6.34), we now define the expressions ($\beta = I, II$)

$$A_{\mathrm{rb}}^{\mathrm{vc},\beta}(\tau,\tau') = \int d\tau_1 d\tau_2\, G(\tau,\tau_1)\Sigma_{\mathrm{rb}}^{\mathrm{vc},\beta}(\tau_1,\tau_2)G(\tau_2,\tau')$$
$$A_{\mathrm{tp}}^{\mathrm{vc},\beta}(\tau,\tau') = \int d\tau_1 d\tau_2\, G(\tau,\tau_1)\Sigma_{\mathrm{tp}}^{\mathrm{vc},\beta}(\tau_1,\tau_2)G(\tau_1,\tau') \tag{6.42}$$

A diagrammatic representation of these diagrams is shown in Fig. 6.10. The difference between the two diagrams in Fig. 6.10 are the time label τ_3 and τ'. Finally, the contribution to the noise due to the vertex correction can be written as

$$S_{\mathrm{vc}}(\tau,\tau') = \frac{2e^2}{h}\int d\tau_4 \sum_{\alpha=\mathrm{tb,rb}} \left(A_\alpha^{\mathrm{vc},I}(\tau,\tau_4) - A_\alpha^{\mathrm{vc},II}(\tau,\tau_4)\right)\Sigma_l(\tau_4,\tau) + \Sigma_l(\tau,\tau_4)\left(A_\alpha^{\mathrm{vc},II}(\tau_4,\tau) - A_\alpha^{\mathrm{vc},I}(\tau_4,\tau)\right), \tag{6.43}$$

represented in Fig. 6.11. The triangle represents one of the two diagrams shown in Fig. 6.10(a) or (b), respectively. In total, we obtain eight diagrams due to the vertex correction.

6.3.2 Transformation from contour to real time

In a last step, we have to perform the transformation from the contour to the real time. The contour variables τ_3 and τ_4 are transformed by inserting a $\tau_3 = \tau_K$ matrix between the matrix Green's functions or self-energies in Keldysh space. The multiplication

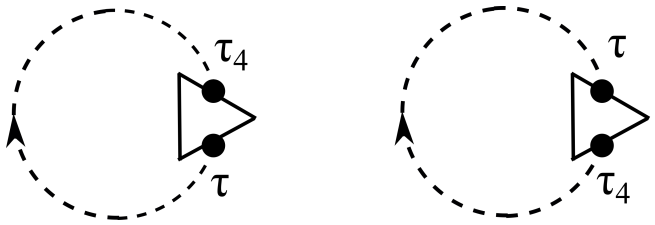

Figure 6.11: Real-time Feynman diagrams of the vertex correction. The triangle represents one of the two diagrams in Fig. 6.10(a) or (b), respectively.

with τ_K takes into account that the time arguments of the Green's function and self-energies can be on the upper or lower contour as discussed in Sec. 2.1.2. The transformation of the time variables τ_1 and τ_2 are more complicated since these time arguments appear in the Green's function, self-energies and the phonon propagators. In addition, one has to take care of time τ' appearing in the self-energies of the vertex correction. We denote matrices in Keldysh space with the symbol $\check{}$.

After a Fourier transformation and taking into account that the non-symmetrized noise corresponds to the greater element of the noise in Keldysh space, the mean-field contribution to the noise can be written as

$$\begin{aligned}
S_{\mathrm{mf}}(\omega) = \frac{2e^2}{h} \sum_{\alpha=\mathrm{rb,tp}} \int \frac{d\varepsilon}{2\pi} & \left(\check{\Sigma}_l(\varepsilon)\right)_{21} \left(\check{A}^{\mathrm{mf}}_\alpha(\varepsilon-\omega)\right)_{12} + \left(\check{A}^{\mathrm{mf}}_\alpha(\varepsilon)\right)_{21} \left(\check{\Sigma}_l(\varepsilon-\omega)\right)_{12} \\
&+ \left(\check{G}(\varepsilon-\omega)\check{\tau}_K\check{\Sigma}_l(\varepsilon-\omega)\right)_{21} \left(\check{A}^{\mathrm{mf}}_\alpha(\varepsilon)\check{\tau}_K\check{\Sigma}_l(\varepsilon)\right)_{12} \\
&+ \left(\check{A}^{\mathrm{mf}}_\alpha(\varepsilon-\omega)\check{\tau}_K\check{\Sigma}_l(\varepsilon-\omega)\right)_{21} \left(\check{G}(\varepsilon)\check{\tau}_K\check{\Sigma}_l(\varepsilon)\right)_{12} \\
&- \left(\check{G}(\varepsilon-\omega)\right)_{21} \left(\check{\Sigma}_l(\varepsilon)\check{\tau}_K\check{A}^{\mathrm{mf}}_\alpha(\varepsilon)\check{\tau}_K\check{\Sigma}_l(\varepsilon)\right)_{12} \\
&- \left(\check{A}^{\mathrm{mf}}_\alpha(\varepsilon-\omega)\right)_{21} \left(\check{\Sigma}_l(\varepsilon)\check{\tau}_K\check{G}(\varepsilon)\check{\tau}_K\check{\Sigma}_l(\varepsilon)\right)_{12} \\
&+ \left(\check{\Sigma}_l(\varepsilon-\omega)\check{\tau}_K\check{G}(\varepsilon-\omega)\right)_{21} \left(\check{\Sigma}_l(\varepsilon)\check{\tau}_K\check{A}^{\mathrm{mf}}_\alpha(\varepsilon)\right)_{12} \\
&+ \left(\check{\Sigma}_l(\varepsilon-\omega)\check{\tau}_K\check{A}^{\mathrm{mf}}_\alpha(\varepsilon-\omega)\right)_{21} \left(\check{\Sigma}_l(\varepsilon)\check{\tau}_K\check{G}(\varepsilon)\right)_{12} \\
&- \left(\check{\Sigma}_l(\varepsilon-\omega)\check{\tau}_K\check{A}^{\mathrm{mf}}_\alpha(\varepsilon-\omega)\check{\tau}_K\check{\Sigma}_l(\varepsilon-\omega)\right)_{21} \left(\check{G}(\varepsilon)\right)_{12} \\
&- \left(\check{\Sigma}_l(\varepsilon-\omega)\check{\tau}_K\check{G}(\varepsilon-\omega)\check{\tau}_K\check{\Sigma}_l(\varepsilon-\omega)\right)_{21} \left(\check{A}^{\mathrm{mf}}_\alpha(\varepsilon)\right)_{12}
\end{aligned} \tag{6.44}$$

with the rainbow- and tadpole diagrams

$$\begin{aligned}
\check{A}^{\mathrm{mf}}_{\mathrm{rb}}(\varepsilon) &= \check{G}(\varepsilon)\check{\Sigma}^{\mathrm{mf}}_{\mathrm{rb}}(\varepsilon)\check{G}(\varepsilon) \\
\check{A}^{\mathrm{mf}}_{\mathrm{tp}}(\varepsilon) &= \check{G}(\varepsilon)\check{\Sigma}^{\mathrm{mf}}_{\mathrm{tp}}(\varepsilon)\check{G}(\varepsilon)
\end{aligned} \tag{6.45}$$

and the self-energies

$$\check{\Sigma}^{\mathrm{mf}}_{\mathrm{rb}}(\varepsilon) = i\lambda^2 \int \frac{d\varepsilon'}{2\pi} \begin{pmatrix} G_{11}(\varepsilon-\varepsilon')D_{11}(\varepsilon) & -G_{12}(\varepsilon-\varepsilon')D_{12}(\varepsilon) \\ -G_{21}(\varepsilon-\varepsilon')D_{21}(\varepsilon) & G_{22}(\varepsilon-\varepsilon')D_{22}(\varepsilon) \end{pmatrix}, \tag{6.46}$$

$$\check{\Sigma}^{\mathrm{mf}}_{\mathrm{tp}}(\varepsilon) = -i\lambda^2 \begin{pmatrix} D^R(0) & 0 \\ 0 & -D^A(0) \end{pmatrix} \int \frac{d\varepsilon'}{2\pi} G_{12}(\varepsilon'). \tag{6.47}$$

The phonon Green's functions in Keldysh space are calculated in the similar way as in Sec. 4.3.2 with normal leads. The transformation of the vertex correction to the noise is

$$S_{\mathrm{vc}}(\omega) = \frac{2e^2}{h} \int \frac{d\varepsilon}{2\pi} \sum_\alpha \Big((\check{A}^{\mathrm{vc},I}_\alpha(\varepsilon) - \check{A}^{\mathrm{vc},II}_\alpha(\varepsilon))\check{\tau}_K \check{\Sigma}_l(\varepsilon-\omega) \Big)_{11} + \Big(\check{\Sigma}_l(\varepsilon)\check{\tau}_K (\check{A}^{\mathrm{vc},II}_\alpha(\varepsilon-\omega) - \check{A}^{\mathrm{vc},I}_\alpha(\varepsilon-\omega)) \Big)_{11}, \tag{6.48}$$

with the self-energies ($\beta = I, II$) due to rainbow-and tadpole-like diagrams

$$\check{\Sigma}^{\mathrm{vc},\beta}_{\mathrm{rb}}(\varepsilon) = i\lambda^2 \int \frac{d\varepsilon'}{2\pi} \begin{pmatrix} C^\beta_{11}(\varepsilon-\varepsilon')D_{11}(\varepsilon) & -C^\beta_{12}(\varepsilon-\varepsilon')D_{12}(\varepsilon) \\ -C^\beta_{21}(\varepsilon-\varepsilon')D_{21}(\varepsilon) & C^\beta_{22}(\varepsilon-\varepsilon')D_{22}(\varepsilon) \end{pmatrix}, \tag{6.49}$$

$$\check{\Sigma}^{\beta}_{\mathrm{tp}}(\varepsilon) = -i\lambda^2 \begin{pmatrix} D^R(0) & 0 \\ 0 & -D^A(0) \end{pmatrix} \int \frac{d\varepsilon'}{2\pi} \check{C}^\beta_{12}(\varepsilon') \tag{6.50}$$

and the functions

$$\check{C}^I(\varepsilon) = \begin{pmatrix} G_{11}(\varepsilon-\omega) & G_{12}(\varepsilon-\omega) \\ G_{21}(\varepsilon-\omega) & G_{22}(\varepsilon-\omega) \end{pmatrix} \check{\tau}_K \begin{pmatrix} \Sigma_{l,11}(\varepsilon-\omega) & 0 \\ \Sigma_{l,21}(\varepsilon-\omega) & 0 \end{pmatrix} \begin{pmatrix} G_{11}(\varepsilon) & G_{12}(\varepsilon) \\ 0 & 0 \end{pmatrix} \tag{6.51}$$

$$\check{C}^{II}(\varepsilon) = \begin{pmatrix} 0 & G_{12}(\varepsilon-\omega) \\ 0 & G_{22}(\varepsilon-\omega) \end{pmatrix} \begin{pmatrix} 0 & 0 \\ \Sigma_{l,21}(\varepsilon) & \Sigma_{l,22}(\varepsilon) \end{pmatrix} \check{\tau}_K \begin{pmatrix} G_{11}(\varepsilon) & G_{12}(\varepsilon) \\ G_{21}(\varepsilon) & G_{22}(\varepsilon) \end{pmatrix}. \tag{6.52}$$

Equations (6.44) -(6.51) are the main results of this chapter and allow for a detailed analysis of the frequency-dependent noise in the presence of electron-phonon interaction.

6.3.3 Examples of frequency-dependent noise at zero temperature

Before we start to discuss the correction to the frequency-dependent noise due to the electron-phonon coupling, we briefly recall the results of the current from Sec. 4.7. The correction to the current to the leading order in the electron-phonon coupling can be divided into an inelastic current and an elastic correction. At zero temperature, the inelastic current vanishes for $eV < \omega_0$ with the frequency ω_0 of the resonator. The elastic correction gives a contribution at all voltages and describes a virtual absorption of a phonon followed by a virtual emission of a phonon.

Similar to the current, we can divide the correction to the frequency-dependent noise into an inelastic part vanishing at negative frequencies with $|\omega| < \omega_0$ at $T = 0$ and an elastic correction.

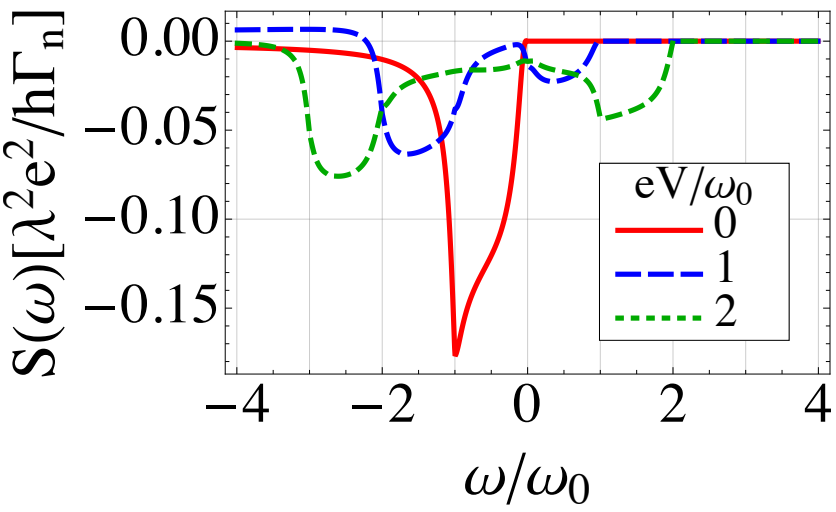

Figure 6.12: Correction to the frequency-dependent noise due to the electron-phonon interaction at zero temperature and $\varepsilon_0 = 0$, $\Gamma_l = \Gamma_r = 0.1\omega_0$ and $\mu_l = eV$ and $\mu_r = 0$.

Figure 6.12 shows the correction to the order λ^2 to the frequency-dependent noise at zero temperature and at $\varepsilon_0 = 0$. The coupling to the left and right leads are symmetric with $\Gamma_l = \Gamma_r = 0.1\omega_0$.

At zero voltage only absorption of photons with frequency ω are possible ($\omega < 0$).

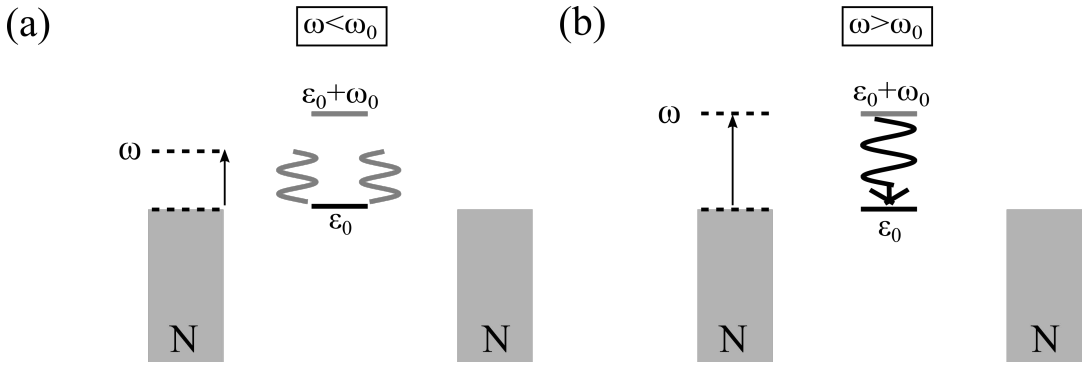

Figure 6.13: Sketch of elastic correction to the noise (a) and the inelastic contribution (b) at zero voltage and $\varepsilon_0 = 0$. The processes shown in (a) are possible for all negative frequencies whereas the processes in (b) give a contribution to the noise for $|\omega| > \omega_0$. The gray wiggled lines represent the virtual absorption and emission of a phonon. The vertical arrow shows the excitation of an electron from the left chemical potential μ_l by a photon with frequency ω. The wiggled solid line in (b) denotes the inelastic emission of a real phonon.

The frequency-dependent noise in Fig. 6.12 can then be understood in the following way. At zero voltage and negative frequencies with $|\omega| < \omega_0$, a photon is absorbed by the electron followed by a virtual emission and absorption of a phonon. This process is shown in Fig. 6.13(a) in which the virtual emission and absorption is represented by a gray wiggled line. After the interaction with the resonator, the electron can tunnel to the left or right lead since the states in the leads are unoccupied. At frequencies $|\omega| > \omega_0$ the resonator is excited by the photon as shown in Fig. 6.13(b) and then

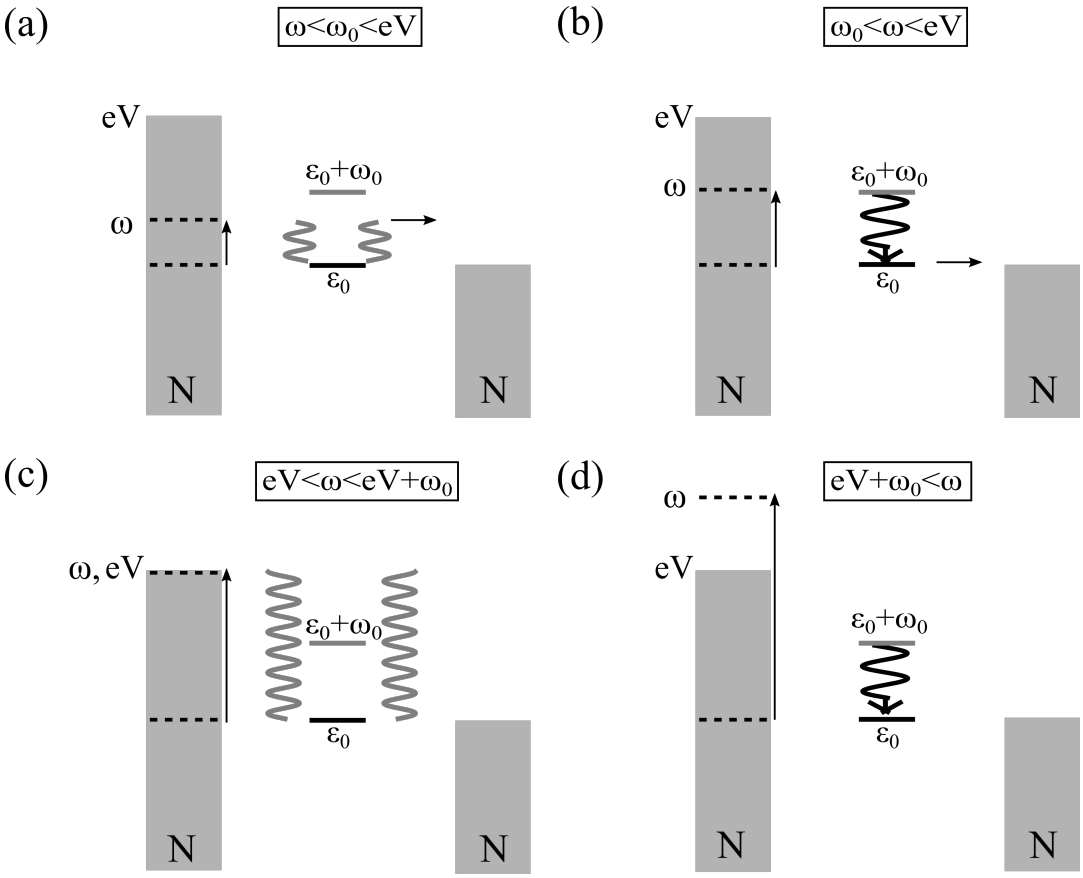

Figure 6.14: Sketches of the elastic correction to the noise and the inelastic contribution. In (a) and (b), the frequency ω is smaller than the voltage eV such that the electrons can only tunnel to the right lead after the interaction with the resonator. When additionally $\omega < \omega_0$, the electrons are excited by a photon and then interact elastically with the resonator by a virtual emission and absorption of a phonon. The virtual processes are drawn by a gray wiggled line. (b) shows the processes for $\omega_0 < \omega < eV$, in which the electrons is excited by a photon and then interacts inelastically with the resonator (black wiggled arrow). In (c) and (d), the frequency is larger than the voltage ($\omega > eV$) and the electron can be transmitted to the left or right lead after the interaction with the resonator. In this case the elastic correction to the noise (c) partially cancel with the inelastic contribution (d) as shown in Fig. 6.12.

can tunnel to the left or right lead. The correction to the noise due to the inelastic contribution has opposite sign compared with the elastic correction such that the contribution partially cancel.

The correction to the noise at finite voltage is shown by the blue and green dashed lines in Fig. 6.12. Here, we discuss as an example the case of $eV = 2\omega_0$.

We can separate the correction to the noise into four regions depending on the frequency ω, the frequency ω_0 of the resonator and the voltage eV. These processes successively start to contribute to the noise by increasing the frequency ω and are shown in Fig. 6.14(a)-(d).

The process in Fig. 6.14(a) corresponds to a frequency which is smaller than ω_0 and the voltage ($\omega < \omega_0 < eV$). In this case an electron is excited by the photon and then can only interact virtually with the resonator. After the interaction with the resonator the electron is transmitted to the right lead since the state in the left lead are occupied providing that electrons close to the dot's level represents the main contribution to the noise. This process is present for all negative frequencies ω. The regime in Fig. 6.14(b) is set by $\omega_0 < \omega < eV$. In this case, the electron can in addition to the process in (a) interact with the resonator by an inelastic emission of a phonon. Similar to regime in Fig. 6.14(a), the electron then tunnels to the right lead. When the frequency ω is larger than the voltage, $eV < \omega < eV + \omega_0$, the electron virtually excites the resonator, see Fig. 6.14(c). Compared to the regime (a), now the electron can tunnel to the left and the right lead. A large frequencies $eV + \omega_0 < \omega$, the inelastic excitation of the resonator are possible and the electron can again tunnel to the left and the right lead, see Fig. 6.14(d). Similar to the case at zero voltage, the elastic correction to the noise and the inelastic contribution partially cancel also at finite voltage for negative frequencies with $|\omega| > eV$.

6.4 Conclusion

In summary, we derived the frequency-dependent noise in a quantum dot coupled to normal leads and in the presence of the electron-phonon interaction. Similar to the current, the contribution to the noise to leading order in the electron-phonon coupling can be divided into an elastic correction and an inelastic contribution. The equations for the frequency-dependent noise opens the possibility to study the signature of the resonator in the noise for equilibrated and unequilibrated vibrations. One might expect features in the noise and its derivative at characteristic frequencies related ot the frequency of the resonator, the bias voltage and the energy level of the dot. Further analysis of these results is work in progress.

7 Conclusion and Outlook

In this work, we have investigated the quantum transport and the nonequilibrium phonon occupation in quantum dots with spin effects, electron-phonon interaction and superconductivity using the Keldysh Green's function technique.

In chapter 3, we discussed a hybrid junction that combines the properties of superconductivity and magnetism. We studied the transport through a quantum dot Josephson junction coupled to a molecular magnet via the exchange interaction. The interplay between Andreev bound levels on the dot and the molecular magnet allows to control the Josephson current and to drive the state of the junction from a 0 to a π state. This is achieved by varying external parameters like the magnetic field or the gate voltage. The proposed junction has not yet been realized experimentally. However, measurement of the current-phase relation or the critical current would in principle allow to extract internal parameters of the Josephson junction like for example the strength of the exchange coupling. Furthermore, the manipulation of Andreev states by a molecular magnet might be useful for possible applications in quantum computing.

The nonequilibrium phonon occupation and the quantum transport in suspended carbon nanotube quantum dots (CNTQDs) has been studied in chapters 4 and 5. Such systems are promising candidates to observe macroscopic quantum effects. These effects become only apparent if the mechanical motion is cooled to the quantum mechanical ground state. In chapters 4 and 5 we have considered two kinds of contacts and demonstrated that the flexural modes of a CNTQD can be cooled to the ground state by purely electronic transport.

In chapter 4 we have investigated the transport through a carbon nanotube quantum dot which is coupled to two ferromagnetic leads. Here, the spin-orbit coupling or an external magnetic gradient gives rise to a coupling between the spin of the electron and the vibration. Cooling to the ground state is optimal at the resonance when the vibrational frequency matches the magnetic field induced energy splitting of the quantum dot's energy levels. We demonstrated that the lowest phonon occupation is given by the square of the ratio between the coupling to the leads and the frequency of the flexural mode. Moreover, we showed that current measurements can reveal signatures of the nonequilibrium state of the resonator.

A hybrid junction consisting of a CNTQD coupled to a normal and a superconducting lead has been studied in chapter 5. We employed the capacitive coupling between the charges on the dot and the vibration to control the occupation of the flexural modes. The cooling of the resonator relies on the interference between two possible paths in a process of a vibration-assisted Andreev reflection. The two paths corresponds to the emission or absorption of an energy quantum before or after an Andreev reflection. The main results of chapter 5 are that (i) the ground-state cooling

occurs due to the interference between the two paths and (ii) ground-state cooling is possible for several modes simultaneously. The current to the leading order in the electron-phonon coupling strength reveals distinct features of the resonator in an out-of-equilibrium state.

The proposed junction in chapters 4 and 5 are difficult to fabricate experimentally. A major challenge in the system with ferromagnetic leads consists of manufacturing sufficiently strong coupling between the nanotube and the leads. Therefore, suspending a CNTQD between a normal and a superconducting lead seems more promising to be realized in the near future. An additional challenge in future experiments is to measure the phonon occupation by purely electronic current.

For the latter reason we derived in chapter 6 the frequency-dependent noise in a quantum dot coupled to two normal leads and in the presence of the electron-phonon interaction. The noise can be divided into an elastic correction and an inelastic contribution. The inelastic contribution vanishes for frequencies smaller than the frequency of the resonator. Chapter 6 contains very general results which have to be discussed in more detail in the future. The results for the frequency-dependent noise open the possibility to study to which extend the phonon occupation of the resonator can be detected by noise measurement. Chapter 6 also involves results which are preliminary for future works, namely the noise in a quantum dot coupled to a normal and a superconducting lead involving the electron-phonon interaction.

Appendix A

A.1 Electronic and Phonon Green's functions

The electronic Green's functions are defined as

$$G(\mathbf{x},t,\mathbf{x}',t') = G_{11}(\mathbf{x},t,\mathbf{x}',t') = -i\langle \mathcal{T}\psi(\mathbf{x},t)\psi^\dagger(\mathbf{x}',t')\rangle\,, \tag{A.1}$$

$$\tilde{G}(\mathbf{x},t,\mathbf{x}',t') = G_{22}(\mathbf{x},t,\mathbf{x}',t') = -i\langle \tilde{\mathcal{T}}\psi(\mathbf{x},t)\psi^\dagger(\mathbf{x}',t')\rangle\,, \tag{A.2}$$

$$G^<(\mathbf{x},t,\mathbf{x}',t') = G_{12}(\mathbf{x},t,\mathbf{x}',t') = i\langle \psi^\dagger(\mathbf{x}',t'),\psi(\mathbf{x},t)\rangle\,, \tag{A.3}$$

$$G^>(\mathbf{x},t,\mathbf{x}',t') = G_{21}(\mathbf{x},t,\mathbf{x}',t') = -i\langle \psi(\mathbf{x},t)\psi^\dagger(\mathbf{x}',t')\rangle\,, \tag{A.4}$$

$$G^R(\mathbf{x},t,\mathbf{x}',t') = -i\theta(t-t')\langle\{\psi(\mathbf{x},t),\psi^\dagger(\mathbf{x}',t')\}\rangle\,, \tag{A.5}$$

$$G^A(\mathbf{x},t,\mathbf{x}',t') = i\theta(t'-t)\langle\{\psi(\mathbf{x},t),\psi^\dagger(\mathbf{x}',t')\}\rangle\,, \tag{A.6}$$

$$G^K(\mathbf{x},t,\mathbf{x}',t') = -i\langle[\psi(\mathbf{x},t),\psi^\dagger(\mathbf{x}',t')]\rangle\,. \tag{A.7}$$

with the commutator (anti-commutator) denoted with $[\,,\,]$ ($\{\,,\,\}$) and the field operator $\psi(\mathbf{x},t)$ in the Heisenberg picture. In the case of bosonic field operators, the commutator is replaced by the anticommutator and a minus sign must be added in the lesser Green's function. In the dissertation, the time-ordered phonon Green's functions is denoted with $D_{11}(t,t') = -i\langle \mathcal{T}\hat{A}(t)\hat{A}^\dagger(t')\rangle$ with $\hat{A}(t) = \hat{b}^\dagger(t) + \hat{b}(t)$ with creation and annihilation operators of the phonons $b^\dagger(t)$ and $b(t)$.

A.2 Relation of Green's functions

The electronic Green's functions satisfy the following relations (we neglected the spacial dependence in the Green's functions)

$$G^R(t,t') - G^A(t,t') = G^>(t,t') - G^<(t,t') \tag{A.8}$$

$$G^R(t,t') = G_{11}(t,t') - G^<(t,t') = G^>(t,t') - G_{22}(t,t') \tag{A.9}$$

$$G^A(t,t') = -G_{22}(t,t') + G^<(t,t') = G_{11}(t,t') - G^>(t,t') \tag{A.10}$$

$$G_{11}(t,t') + G_{22}(t,t') = G^<(t,t') + G^>(t,t') = G^K(t,t') \tag{A.11}$$

$$G^<(t,t') = (G^K(t,t') - G^R(t,t') + G^A(t,t'))/2 \tag{A.12}$$

$$G^>(t,t') = (G^K(t,t') + G^R(t,t') - G^A(t,t'))/2\,. \tag{A.13}$$

The same relations are satisfied if the electronic field operators are replaced with bosonic field operators.

Appendix B

B.1 Phonon self-energy for the vibration environment coupling

We consider a mechanical oscillator coupled to the environment which is described as an ensemble of independent harmonic oscillators (the Caldeira-Leggett model). The Hamiltonian of the external environment reads

$$\hat{H}_{env} = (\hat{b}^\dagger + \hat{b}\ ) \sum_k \lambda_k (\hat{b}_k^\dagger + \hat{b}_k) + \sum_k \omega_k \hat{b}_k^\dagger \hat{b}_k \,. \tag{b.1}$$

As the Hamiltonian is bilinear, the model is exactly solvable. The phonon self-energy $\check{\Sigma}_0$ is composed by only one irreducible diagram. In the frequency space, the retarded and the Keldysh components of the self energy are given by

$$\Sigma_0^R(\varepsilon) = \sum_k \lambda_k^2 \left(\frac{1}{\varepsilon - \omega_k + i\eta} - \frac{1}{\varepsilon + \omega_k + i\eta} \right) , \tag{b.2}$$

$$\Sigma_0^K(\varepsilon) = 2i\mathrm{Im}\ \Sigma_0^R(\varepsilon)\coth(\varepsilon) \,. \tag{b.3}$$

To mimic the dissipation, the ensemble of oscillators form a bath with a continuous spectrum. Then, by replacing the sum with an integral over the frequencies, we introduce the spectral density function for ohmic dissipation

$$J(\varepsilon) = \sum_k \frac{\pi \lambda_k^2}{\omega_k} \left(\delta(\varepsilon - \omega_k) + \delta(\varepsilon + \omega_k)\right) = \frac{\varepsilon}{\omega} Q^{-1} \ . \tag{b.4}$$

with the coefficient Q corresponding to the quality factor of the oscillator. Finally, we can approximate $\Sigma_0^R(\varepsilon) \simeq \Sigma_0^R(\omega)$ for $Q \gg 1$ in the Dyson equation (4.24). We thus obtain

$$\gamma_0 = -\mathrm{Im}\ \Sigma_0^R(\omega) = \omega/Q \,, \tag{b.5}$$

$$\Sigma_0^K(\omega) = -2i\omega[1 + 2n_B(\omega)]/Q \,. \tag{b.6}$$

B.2 Retarded self-energy at zero temperature

The retarded self-energy in Eq. (4.38) can be calculated analytically at zero temperature. For completeness and comparison, we give here the expression for the real and imaginary parts. These expressions agree with the results of Ref. [165] albeit with

the generalized spin index for the spin-flip vertex interaction.

$$\text{Re } \Sigma^R_{\sigma\sigma}(\varepsilon) = \sum_{\alpha,s} \frac{\lambda^2 \Gamma^\sigma_\alpha}{(\varepsilon - \varepsilon_\sigma - s\omega)^2 + \Gamma^{\sigma\,2}} \left[\frac{\varepsilon - \varepsilon_\sigma - s\omega}{\Gamma^\sigma} \right.$$
$$\left. \left(\frac{1}{2} + \frac{s}{\pi} \tan^{-1} \frac{\varepsilon_\sigma - \mu_\alpha}{\Gamma^\sigma} \right) + \frac{s}{\pi} \ln \frac{|\varepsilon - s\omega - \mu_\alpha|}{\sqrt{(\varepsilon_\sigma - \mu_\alpha)^2 + \Gamma^{\sigma\,2}}} \right] , \quad \text{(b.7)}$$

and

$$\text{Im } \Sigma^R_{\sigma\sigma} = \sum_{\alpha,s} \frac{-\lambda^2 \Gamma^\sigma_\alpha \theta(s(\varepsilon - \mu_\alpha) - \omega)}{(\varepsilon - s\omega - \varepsilon_\sigma)^2 + \Gamma^{\sigma\,2}} , \quad \text{(b.8)}$$

with $\Gamma^\sigma = \Gamma^\sigma_l + \Gamma^\sigma_r$.

Appendix C

C.1 Electronic Green's functions for a quantum dot coupled to a normal and a superconducting lead

In this appendix, we give a detailed description of the Green's function on the dot without coupling to the resonator ($\lambda = 0$). The Hamiltonian is given by

$$\hat{H}_0 = \hat{H}_s + \hat{H}_n + \hat{H}_t + \hat{H}_d \tag{C.1}$$

with

$$\hat{H}_s = \sum_{k\sigma} \xi_k \hat{a}^\dagger_{k\sigma} \hat{a}_{k\sigma} + \Delta \hat{a}^\dagger_{-k\downarrow} \hat{a}^\dagger_{k\uparrow} + \Delta^\dagger \hat{a}_{k\uparrow} \hat{a}_{-k\downarrow} \,, \tag{C.2}$$

$$\hat{H}_n = \sum_{k\sigma} \xi_k \hat{c}^\dagger_{k\sigma} \hat{c}_{k\sigma} \,, \tag{C.3}$$

$$\hat{H}_t = \sum_{k\sigma} t_{l\sigma} \hat{c}^\dagger_{k\sigma} \hat{d}_\sigma + t_{r\sigma} \hat{a}^\dagger_{k\sigma} \hat{d}_\sigma + \text{H.c.} \,, \tag{C.4}$$

$$\hat{H}_d = \varepsilon_0 \hat{n}_d \,. \tag{C.5}$$

The annihilation operators with spin σ and momentum k are given by $\hat{a}_{k\sigma}$ for the superconductor, $\hat{c}_{k\sigma}$ for the normal metal and $\hat{d}_\sigma$ for the dot. The superconducting gap is denoted with Δ. The tunneling between the leads and the dot is described by $t_{l\sigma}$ and $t_{r\sigma}$, and the bare energy level of the dot is ε_0. $\hat{n}_d$ is the occupation of the quantum dot for a spin degenerate level $\hat{n}_d = \hat{d}^\dagger_\uparrow \hat{d}_\uparrow + \hat{d}^\dagger_\downarrow \hat{d}_\downarrow$. As we consider a spin-degenerate system, we omit the spin-index hereafter.

Using the Larkin-Ovchinnikov representation, the Green's function on the dot in Keldysh space (notation with $\check{}$) is given by

$$\check{G}(t,t') = \begin{pmatrix} \hat{G}^R(t,t') & \hat{G}^K(t,t') \\ 0 & \hat{G}^A(t,t') \end{pmatrix} , \tag{C.6}$$

with the retarded (R), advanced (A) and Keldysh (K) Green's functions in Nambu space (notation $\hat{}$) defined as

$$\hat{G}^R(t,t') = -i\theta(t-t')\langle\{\Psi_d(t), \Psi^\dagger_d(t')\}\rangle \,, \tag{C.7}$$

$$\hat{G}^A(t,t') = i\theta(t'-t)\langle\{\Psi_d(t), \Psi^\dagger_d(t')\}\rangle \,, \tag{C.8}$$

$$\hat{G}^K(t,t') = -i\langle[\Psi_d(t), \Psi^\dagger_d(t')]\rangle \,. \tag{C.9}$$

We use the spinor basis $\Psi^\dagger_d(t) = (d^\dagger_\uparrow(t)\, d_\downarrow(t))$. The Dyson equation for the Green's function on the dot is

$$\check{G}(\varepsilon) = \check{g}(\varepsilon) + \check{g}(\varepsilon)(\check{\Sigma}_n(\varepsilon) + \check{\Sigma}_s(\varepsilon))\check{G}(\varepsilon) \,, \tag{C.10}$$

with the unperturbed Green's function of the dot $\check{g}(\varepsilon)$ and the self-energies $\hat{\Sigma}_\alpha(\varepsilon)$ of the normal and superconducting lead ($\alpha = (n, s)$),

$$\check{g}(\varepsilon) = \begin{pmatrix} \hat{g}^R(\varepsilon) & \hat{g}^K(\varepsilon) \\ 0 & \hat{g}^A(\varepsilon) \end{pmatrix} \tag{C.11}$$

$$\check{\Sigma}_\alpha(\varepsilon) = \begin{pmatrix} \hat{\Sigma}^R_\alpha(\varepsilon) & \hat{\Sigma}^K_\alpha(\varepsilon) \\ 0 & \hat{\Sigma}^A_\alpha(\varepsilon) \end{pmatrix} . \tag{C.12}$$

In the following, we apply the voltage on the normal metal. In the wide-band approximation, the retarded, advanced and Keldysh self-energies of the normal metal are $\hat{\Sigma}^R_n = -i\Gamma_n$, $\hat{\Sigma}^A_n = i\Gamma_n$ and $\hat{\Sigma}^K_n(\varepsilon) = -2i\Gamma_n(1 - 2\hat{F}(\varepsilon))$ with the matrix function

$$\hat{F}(\varepsilon) = \begin{pmatrix} f_e(\varepsilon) & 0 \\ 0 & f_h(\varepsilon) \end{pmatrix} , \tag{C.13}$$

in which we have defined the Fermi functions for electron ($\nu = e = +$) and holes ($\nu = h = -$) $f_\nu(\varepsilon) = 1/[1 + \exp((\varepsilon - \nu\, eV))/T]$. The retarded and Keldysh self-energies of the superconductor are

$$\hat{\Sigma}^R_s(\varepsilon) = -\frac{\Gamma_s}{\Omega(\varepsilon)} \begin{pmatrix} \varepsilon + i\eta & \Delta \\ \Delta & \varepsilon + i\eta \end{pmatrix} \tag{C.14}$$

$$\hat{\Sigma}^K_s(\varepsilon) = (1 - 2f_0(\varepsilon)) \left(\hat{\Sigma}^R_s(\varepsilon) - \hat{\Sigma}^A_s(\varepsilon) \right) , \tag{C.15}$$

with $\Omega(\varepsilon) = \sqrt{\Delta^2 - (\varepsilon + i\eta)^2}$, an infinitesimal small real part η and the Fermi function of the superconductor $f_0(\varepsilon)$ ($\nu = 0$). The advanced self-energy is obtained by the adjoint retarded self energy, $\hat{\Sigma}^A_s(\varepsilon) = \hat{\Sigma}^{R\dagger}_s(\varepsilon)$.

With the Dyson equation, the retarded Green's function of the dot is given by

$$\hat{G}^R(\varepsilon) = \frac{1}{D} \begin{pmatrix} -(\varepsilon + \varepsilon_0 + i\Gamma_n + \varepsilon\Gamma_s/\Omega(\varepsilon)) & -\Delta\Gamma_s/\Omega(\varepsilon) \\ -\Delta\Gamma_s/\Omega(\varepsilon) & -(\varepsilon - \varepsilon_0 + i\Gamma_n + \varepsilon\Gamma_s/\Omega(\varepsilon)) \end{pmatrix} \tag{C.16}$$

$$= \begin{pmatrix} G_+(\varepsilon) & F(\varepsilon) \\ F(\varepsilon) & G_-(\varepsilon) \end{pmatrix} \tag{C.17}$$

with $D = \Delta^2\Gamma_s^2/\Omega^2(\varepsilon) - (\varepsilon + \varepsilon_0 + i\Gamma_n + \varepsilon\Gamma_s/\Omega(\varepsilon))\,(\varepsilon - \varepsilon_0 + i\Gamma_n + \varepsilon\Gamma_s/\Omega(\varepsilon))$. The Keldysh Green's function of the dot is obtained from Eq. (C.10) and is given by $\hat{G}^K(\varepsilon) = \hat{G}^R(\varepsilon)(\hat{\Sigma}^K_n(\varepsilon) + \hat{\Sigma}^K_s(\varepsilon))\hat{G}^A(\varepsilon)$.

In the limit $\Delta \to \infty$, the Green's function in Nambu space reduce to

$$\hat{G}^R(\varepsilon) = \frac{1}{\Gamma_s^2 - (\varepsilon - \varepsilon_0 + i\Gamma_n)(\varepsilon + \varepsilon_0 + i\Gamma_n)} \begin{pmatrix} -(\varepsilon + \varepsilon_0 + i\Gamma_n) & -\Gamma_s \\ -\Gamma_s & -(\varepsilon - \varepsilon_0 + i\Gamma_n) \end{pmatrix} , \tag{C.18}$$

which is the same result obtained with the hybridized Hamiltonian in Eq. (5.1).

In appendix C.2, we use the lesser and greater Green's function and self-energies to calculate the damping and the phonon occupation. These Green's function are

defined as

$$\hat{G}^{<}(t,t') = i\langle\psi_d^\dagger(t')\psi_d(t)\rangle \tag{C.19}$$
$$\hat{G}^{>}(t,t') = -i\langle\psi_d(t)\psi_d^\dagger(t')\rangle \tag{C.20}$$

and in Fourier space are given by

$$\hat{G}^{<,>}(\varepsilon) = \hat{G}^R(\varepsilon)(\Sigma_n^{<,>}(\varepsilon) + \Sigma_s^{<,>}(\varepsilon))\hat{G}^A(\varepsilon)\,. \tag{C.21}$$

with the self-energies

$$\hat{\Sigma}_s^{<}(\varepsilon) = -(\hat{\Sigma}_s^R(\varepsilon) - \hat{\Sigma}_s^A(\varepsilon))\hat{F}(\varepsilon)\,, \tag{C.22}$$
$$\hat{\Sigma}_n^{<}(\varepsilon) = 2i\Gamma_n f_0(\varepsilon)\,, \tag{C.23}$$
$$\hat{\Sigma}_s^{>}(\varepsilon) = (\hat{\Sigma}_s^R(\varepsilon) - \hat{\Sigma}_s^A(\varepsilon))(1-\hat{F}(\varepsilon))\,, \tag{C.24}$$
$$\hat{\Sigma}_n^{>}(\varepsilon) = -2i\Gamma_n(1-f_0(\varepsilon))\,. \tag{C.25}$$

C.2 Damping and phonon occupation

The mechanical damping γ and the steady nonequilibrium phonon occupation n are determined by the spectrum of the non-symmetrized noise of the electron occupation on the dot

$$S(\omega) = \int d(t_1-t_2)e^{i\omega(t_1-t_2)}\langle\hat{n}_d(t_1)\hat{n}_d(t_2)\rangle\,, \tag{C.26}$$

with the occupation on the dot $\hat{n}(t_1) = \hat{d}^\dagger(t_1)\hat{d}(t_2)$. The quantum statistical average in Eq. (C.26) is taken over the electron system. Introducing the Nambu space, the occupation on the dot can be written as $\hat{n}(t_1) = (\hat{d}^\dagger(t_1)\hat{d}(t_1) - \hat{d}(t_1)\hat{d}^\dagger(t_1))/2$. Then, calculation the average $\langle\hat{n}_d(t_1)\hat{n}_d(t_2)\rangle$ by using Wick's theorem, the charge correlation on the dot can be expressed as

$$\langle\hat{n}_d(t_1)\hat{n}_d(t_2)\rangle = \frac{1}{4}\mathrm{Tr}\left[\hat{\tau}_3\hat{G}^{<}(t_2,t_1)\hat{\tau}_3\hat{G}^{>}(t_1,t_2)\right]\,. \tag{C.27}$$

with the Pauli matrix τ_3. After a Fourier transformation, the non-symmetrized noise can be written as

$$S(\omega) = \frac{1}{4}\int\frac{d\varepsilon'}{2\pi}\mathrm{Tr}\left[\hat{\tau}_3\hat{G}^{<}(\varepsilon'-\omega)\hat{\tau}_3\hat{G}^{>}(\varepsilon')\right] \tag{C.28}$$

Then, using Eq. (C.21) we can write the noise as

$$S(\omega) = 2\sum_{s\nu\nu'} s(1+n(\omega+2s\nu))R^s_{\nu\nu'}(\omega) \tag{C.29}$$

with the coefficients

$$R^s_{\nu\nu'}(\omega) = \frac{\Gamma_n^2}{2}\int\frac{d\varepsilon}{2\pi}f_\nu(\varepsilon)[1-f_{\nu'}(\varepsilon+s\omega)]\left|T^s_{\nu\nu'}(\varepsilon)\right|^2\,, \tag{C.30}$$

and the transmission functions

$$T^s_{\nu\bar{\nu}}(\varepsilon) = G_\nu(\varepsilon)F^*(\varepsilon + s\omega) - F(\varepsilon)G^*_{\bar{\nu}}(\varepsilon + s\omega)\,, \tag{C.31}$$

$$T^s_{\nu\nu}(\varepsilon) = G_\nu(\varepsilon)G^*_{\nu}(\varepsilon + s\omega) - F(\varepsilon)F^*(\varepsilon + s\omega)\,. \tag{C.32}$$

The damping is calculated by [207]

$$\gamma = \frac{\lambda^2}{2}(S(\omega) - S(-\omega)) = \gamma_{\mathrm{AR}} + \gamma_{\mathrm{NR}}\,, \tag{C.33}$$

with the rates

$$\gamma_{\mathrm{AR}} = \sum_{\nu,s} s\gamma^s_{\nu\bar{\nu}}(\omega)\,, \tag{C.34}$$

$$\gamma_{\mathrm{NR}} = \sum_{\nu,s} s\gamma^s_{\nu\nu}(\omega)\,. \tag{C.35}$$

and $\gamma^s_{\nu\nu'}(\omega) = \lambda^2 R^s_{\nu\nu'}(\omega)$. The phonon occupation becomes

$$n = \frac{S(-\omega)}{S(\omega) - S(-\omega)} = \left(\sum_{\nu,s=\pm} s\gamma^s_{\nu\bar{\nu}}(\omega) n_B\left(\omega + \nu s\, 2eV\right) + \gamma_{\mathrm{NR}} n_B(\omega)\right)/\gamma\,. \tag{C.36}$$

C.3 Phonon Green's function for a resonator coupled to a normal and a superconducting lead

In this appendix, we calculate the phonon Green's function to the leading order in the electron-phonon interaction. The derivation follows Sec. 4.3.2 although the electronic Green's function are written in Nambu space.

We introduce the symmetrized bosonic operator $\hat{A}(t) = \hat{b}^\dagger(t) + \hat{b}(t)$, the contour ordering operator T_c on the Keldysh contour and define the phonon propagator on the Keldysh contour as $D(\tau, \tau') = -i\langle T_c \hat{A}(\tau)\hat{A}^\dagger(\tau')\rangle$ with the contour variable τ on the Keldysh contour. After a perturbation expansion to the leading order in the electron-vibration interaction, we transform the contour variable τ to the real time. The phonon Green's function in Keldysh space is given by

$$\breve{D}(t, t') = \begin{pmatrix} D_{11}(t, t') & D_{12}(t, t') \\ D_{21}(t, t') & D_{22}(t, t') \end{pmatrix} \tag{C.37}$$

and use the Larkin-Ovchinnikov rotation (see Sec. 2.1.2) to write the Dyson equation in the triangular form.

$$\breve{D}(t, t') = \begin{pmatrix} D^R(t, t') & D^K(t, t') \\ 0 & D^A(t, t') \end{pmatrix} \tag{C.38}$$

with

$$D^R(t, t') = -i\theta(t - t')\langle[\hat{A}(t), \hat{A}(t')]\rangle \tag{C.39}$$

$$D^A(t, t') = i\theta(t' - t)\langle[\hat{A}(t), \hat{A}(t')]\rangle \tag{C.40}$$

$$D^K(t, t') = -i\langle\{\hat{A}(t'), \hat{A}(t)\}\rangle\,. \tag{C.41}$$

Finally, we obtain the Dyson equation in Fourier space as

$$\check{D}(\varepsilon) = \check{D}_0(\varepsilon) + \check{D}_0(\varepsilon)\check{\Pi}(\varepsilon)\check{D}(\varepsilon)\,, \tag{C.42}$$

with

$$\check{d}_0(\varepsilon) = \begin{pmatrix} d_0^R(\varepsilon) & d_0^K(\varepsilon) \\ 0 & d_0^A(\varepsilon) \end{pmatrix} \text{ and } \check{\Pi}(\varepsilon) = \begin{pmatrix} \Pi^R(\varepsilon) & \Pi^K(\varepsilon) \\ 0 & \Pi^A(\varepsilon) \end{pmatrix}. \tag{C.43}$$

The bare phonon Green's functions in Eq. (4.10) are given by

$$d_0^{R,A}(\varepsilon) = 2\omega/[(\varepsilon \pm i\eta)^2 - \omega^2] \tag{C.44}$$

$$d_0^K(\varepsilon) = -2\pi i\,[\delta(\varepsilon-\omega)+\delta(\varepsilon+\omega)]\coth[\omega/(2T)] \tag{C.45}$$

In Eq. (4.10), $\check{\Pi}(\varepsilon)$ corresponds to the phonon self energy (polarization diagram) associated to the electron-vibration interaction between the resonator and the electrons. These self-energies are given by

$$\Pi^{R,A}(\varepsilon) = i\frac{\lambda^2}{2}\int\frac{d\varepsilon'}{2\pi}\mathrm{Tr}\left[\hat{\tau}_z\hat{G}^K(\varepsilon')\hat{\tau}_z\hat{G}^{A/R}(\varepsilon'-\varepsilon) + \hat{\tau}_z\hat{G}^{R/A}(\varepsilon')\hat{\tau}_z\hat{G}^K(\varepsilon'-\varepsilon)\right], \tag{C.46}$$

$$\Pi^K(\varepsilon) = i\frac{\lambda^2}{2}\int\frac{d\varepsilon'}{2\pi}\mathrm{Tr}\left[\hat{\tau}_z\hat{G}^K(\varepsilon')\hat{\tau}_z\hat{G}^K(\varepsilon'-\varepsilon) + \hat{\tau}_z\hat{G}^R(\varepsilon')\hat{\tau}_z\hat{G}^A(\varepsilon'-\varepsilon) + \hat{\tau}_z\hat{G}^A(\varepsilon')\hat{\tau}_z\hat{G}^R(\varepsilon'-\varepsilon)\right], \tag{C.47}$$

in which the trace Tr and the Pauli matrix τ_z acts on the Nambu space. From the Dyson equation Eq. (C.42), we obtain the retarded and Keldysh equations

$$D^{R,A}(\varepsilon) = \frac{2\omega}{\varepsilon^2-\omega^2-2\omega\Pi^{R,A}(\varepsilon)} \simeq \frac{1}{\varepsilon-\omega\pm i\gamma} - \frac{1}{\varepsilon+\omega\pm i\gamma}\,, \tag{C.48}$$

$$D^K(\varepsilon) = D^R(\varepsilon)\Pi^K(\varepsilon)D^A(\varepsilon) \simeq \Pi^K(\varepsilon)\sum_{s=\pm}\frac{1}{(\varepsilon+s\omega)^2+\gamma^2} \simeq i\pi\frac{\Pi^K(\varepsilon)}{\gamma(\varepsilon)}\left(\delta(\varepsilon-\omega)+\delta(\varepsilon+\omega)\right), \tag{C.49}$$

with the damping coefficient given by $\gamma = -\mathrm{Im}\,\Pi^R(\omega)$. In Eq. (4.24) we expanded the retarded and advanced phonon Green's function close to $\varepsilon \simeq \omega$ taking into account the frequency shift of the resonator $\Delta\omega = \mathrm{Re}\,\Pi^R(\omega)$. Equations (C.48) and (C.49) are valid in the limit of small damping $\gamma \ll \omega$.

C.4 Lowest order perturbation theory for the current

We use the spinor in Nambu space and the number operator in the normal lead as $\Psi_k^\dagger = (c_{k\uparrow}^\dagger\, c_{-k\downarrow})$ and $N_l = \frac{1}{2}\sum_k \Psi_k^\dagger\hat{\tau}_3\Psi_k$. The current through the left lead $I_l = -e\langle\frac{dN_l}{dt}\rangle$ $(e>0)$ can then be expressed as

$$I_l = \frac{e}{2\hbar}\int\frac{d\varepsilon}{2\pi}\,\mathrm{Re}\,\mathrm{Tr}[\tau_z(\hat{\mathcal{G}}^K(\varepsilon)\hat{\Sigma}_l^A + \hat{\mathcal{G}}^R(\varepsilon)\hat{\Sigma}_l^K(\varepsilon))]\,, \tag{C.50}$$

in which $\hat{\mathcal{G}}^K(\varepsilon)$ and $\hat{\mathcal{G}}^R(\varepsilon)$ refer to the dot Green's function. They correspond to the exact Green's function with coupling to the leads and including the electron-vibration interaction. To calculate the current in Eq. (C.50) we perform a perturbation expansion of these Green's functions to the leading order in the electron-vibration interaction. The current can then be decomposed into a elastic current, an elastic correction and an inelastic term as $I = I_0 + I_{\text{ec}} + I_{\text{in}}$ with

$$I_0 = \frac{e}{\hbar}\int \frac{d\varepsilon}{2\pi}\,\text{Re}\,\text{Tr}[\tau_z(\hat{G}_d^K\hat{\Sigma}_l^A + \hat{G}_d^R\hat{\Sigma}_l^K)]\,, \tag{C.51}$$

$$I_{\text{ec}} = \frac{e}{\hbar}\int \frac{d\varepsilon}{2\pi}\,\text{Re}\,\text{Tr}[\tau_z(\hat{G}^R\hat{\Sigma}^R_{\text{vib}}\hat{G}^K\Sigma_l^A + \hat{G}^K\hat{\Sigma}^A_{\text{vib}}\hat{G}^A\hat{\Sigma}_l^A \tag{C.52}$$

$$- \hat{G}^R\hat{\Sigma}^R_{\text{vib}}\hat{G}^R(\hat{\Sigma}_l^R - \hat{\Sigma}_l^A + \hat{\Sigma}_r^R - \hat{\Sigma}_r^A))\hat{G}^A\hat{\Sigma}_l^K]\,, \tag{C.53}$$

$$I_{\text{in}} = \frac{e}{2\hbar}\int \frac{d\varepsilon}{2\pi}\,\text{Re}\,\text{Tr}[\tau_z(\hat{G}^R\hat{\Sigma}^K_{\text{vib}}\hat{G}^A\hat{\Sigma}_l^A + \hat{G}^R\hat{\Sigma}^R_{\text{vib}}\hat{G}^A\hat{\Sigma}_l^K)]\,. \tag{C.54}$$

and the self-energies

$$\hat{\Sigma}^{R/A}_{\text{vib}}(\varepsilon) = i\frac{\lambda^2}{2}\int\frac{d\varepsilon'}{2\pi}D^{R/A}(\varepsilon')\tau_z\hat{G}^K(\varepsilon-\varepsilon')\tau_z + D^{R/A}(\varepsilon')\tau_z\hat{G}^K(\varepsilon-\varepsilon')\tau_z \tag{C.55}$$

$$- \tau_z\text{Tr}\left[\tau_z\hat{G}^K(\varepsilon')\right]D^{R,A}(0)\,, \tag{C.56}$$

$$\hat{\Sigma}^K_{\text{vib}}(\varepsilon) = i\frac{\lambda^2}{2}\int\frac{d\varepsilon'}{2\pi}\sum_{\xi=R,A,K}\left(D^{\xi}(\varepsilon')\tau_z\hat{G}^{\xi}(\varepsilon-\varepsilon')\tau_z\right) - \tau_z\text{Tr}\left[\tau_z\hat{G}^K(\varepsilon')\right]D^K(0)\,. \tag{C.57}$$

and the retarded and Kelysh Green's function given by Eq. (C.17) and Eq. (C.10), respectively. In the limit $\Delta \to \infty$, the inelastic current can be written as

$$I_{\text{in}} = \frac{e}{\hbar}\int\frac{d\varepsilon}{2\pi}\,\text{Re}\sum_s sn(s\omega)\text{Tr}[\tau_z(\hat{G}^R(\varepsilon)\hat{G}^>(\varepsilon+s\omega)\hat{G}^A(\varepsilon)\hat{\Sigma}_l^<(\varepsilon) \tag{C.58}$$

$$- \hat{G}^R(\varepsilon)\hat{G}^<(\varepsilon+s\omega)\hat{G}^A(\varepsilon)\hat{\Sigma}_l^>(\varepsilon))]\,.$$

with the Green's functions given by Eq. (C.21).

Bibliography

[1] R. P. Feynman, *Space-Time Approach to Quantum Electrodynamics*, Phys. Rev. **76**, 769 (1949).

[2] G. Rickayzen, *Green's Functions and Condensed Matter* (Academic Press, London, England, 1980).

[3] J. Rammer and H. Smith, *Quantum field-theoretical methods in transport theory of metals*, Rev. Mod. Phys. **58**, 323 (1986).

[4] J. Rammer, *Quantum Field Theory of Non-equilibrium States* (Cambridge University Press, Cambridge, England, 2007).

[5] L. V. Keldysh, *Diagram Technique for Nonequilibrium Processes*, Zh. Eksp. Teor. Fiz **47**, 1515 (1964).

[6] W. Belzig, F. K. Wilhelm, C. Bruder, G. Schön, and A. D. Zaikin, *Quasiclassical Green's function approach to mesoscopic superconductivity*, Superlattices and Microstructures **25**, 1251 (1999).

[7] G. C. Wick, *The Evaluation of the Collision Matrix*, Phys. Rev. **80**, 268 (1950).

[8] A. I. Larkin and Y. N. Ovchinnikov, *Nonlinear conductivity of superconductors in the mixed state*, Soviet Physics JETP **41**, 960 (1975).

[9] J. Bardeen, L. N. Cooper, and J. R. Schrieffer, *Theory of Superconductivity*, Phys. Rev. **108**, 1175 (1957).

[10] L. N. Cooper, *Bound Electron Pairs in a Degenerate Fermi Gas*, Phys. Rev. **104**, 1189 (1956).

[11] Y. Nambu, *Quasi-Particles and Gauge Invariance in the Theory of Superconductivity*, Phys. Rev. **117**, 648 (1960).

[12] Y. V. Nazarov and Y. M. Blanter, *Quantum Transport: Introduction to Nanoscience* (Cambridge University Press, Cambridge, England, 2009).

[13] A. F. Andreev, *The thermal conductivity of the intermediate state in superconductors*, Zh. Eksp. Teor. Fiz **46**, 1823 (1964).

[14] G. E. Blonder, M. Tinkham, and T. M. Klapwijk, *Transition from metallic to tunneling regimes in superconducting microconstrictions: Excess current, charge imbalance, and supercurrent conversion*, Phys. Rev. B **25**, 4515 (1982).

[15] B. D. Josephson, *Possible new effects in superconductive tunnelling*, Phys. Lett. **1**, 251 (1962).

[16] C. W. J. Beenakker, *Universal limit of critical-current fluctuations in mesoscopic Josephson junctions*, Phys. Rev. Lett. **67**, 3836 (1991).

[17] Y. M. Blanter and M. Büttiker, *Shot Noise in Mesoscopic Conductors*, Phys. Rep. **336**, 1 (2000).

[18] W. Schottky, *Über spontane Stromschwankungen in verschiedenen Elektrizitätsleitern*, Annalen der Physik **362**, 541 (1918).

[19] E. A. Laird, F. Kuemmeth, G. A. Steele, K. Grove-Rasmussen, J. Nygård, K. Flensberg, and L. P. Kouwenhoven, *Quantum transport in carbon nanotubes*, Rev. Mod. Phys. **87**, 703 (2015).

[20] J. Chaste, A. Eichler, J. Moser, G. Ceballos, R. Rurali, and A. Bachtold, *A nanomechanical mass sensor with yoctogram resolution*, Nat. Nanotechnol. **7**, 301 (2012).

[21] J. Moser, J. Güttinger, A. Eichler, M. J. Esplandiu, D. E. Liu, M. I. Dykman, and A. Bachtold, *Ultrasensitive force detection with a nanotube mechanical resonator*, Nat. Nanotechnol. **8**, 493 (2013).

[22] L. D. Landau and E. M. Lifshitz, *Theory of Elasticity* (Pergamon, Oxford, England, 1970).

[23] A. N. Cleland, *Foundations of Nanomechanics: from Solid-State Theory to Device Applications* (Springer, Berlin, 2003).

[24] A. K. Hüttel, M. Poot, B. Witkamp, and H. S. J. van der Zant, *Nanoelectromechanics of suspended carbon nanotubes*, New J. Phys. **10**, 095003 (2008).

[25] T. T. Heikkilä, *The Physics of Nanoelectronics: Transport and Fluctuation Phenomena at Low Temperatures* (Oxford University Press, Oxford, United Kingdom, 2013).

[26] T. Rocheleau, T. Ndukum, C. Macklin, J. B. Hertzberg, A. A. Clerk, and K. C. Schwab, *Preparation and detection of a mechanical resonator near the ground state of motion*, Nature **463**, 72 (2010).

[27] J. D. Teufel, T. Donner, D. Li, J. W. Harlow, M. S. Allman, K. Cicak, A. J. Sirois, J. D. Whittaker, K. W. Lehnert, and R. W. Simmonds, *Sideband cooling of micromechanical motion to the quantum ground state*, Nature **475**, 359 (2011).

[28] A. D. O'Connell, M. Hofheinz, M. Ansmann, R. C. Bialczak, M. Lenander, E. Lucero, M. Neeley, D. Sank, H. Wang, M. Weides, et al., *Quantum ground state and single-phonon control of a mechanical resonator*, Nature **464**, 697 (2010).

[29] A. A. Clerk, M. H. Devoret, S. M. Girvin, F. Marquardt, and R. J. Schoelkopf, *Introduction to quantum noise, measurement, and amplification*, Rev. Mod. Phys. **82**, 1155 (2010).

[30] M. Aspelmeyer, T. J. Kippenberg, and F. Marquardt, *Cavity optomechanics*, Rev. Mod. Phys. **86**, 1391 (2014).

[31] J. Moser, A. Eichler, J. Güttinger, M. I. Dykman, and A. Bachtold, *Nanotube mechanical resonators with quality factors of up to 5 million*, Nat. Nano. **9**, 1007 (2014).

[32] A. R. Rocha, V. M. García-Suárez, S. W. Bailey, C. J. Lambert, J. Ferrer, and S. Sanvito, *Towards molecular spintronics*, Nat. Mater. **4**, 335 (2005).

[33] S. A. Wolf, *Spintronics: A Spin-Based Electronics Vision for the Future*, Science **294**, 1488 (2001).

[34] L. Bogani and W. Wernsdorfer, *Molecular spintronics using single-molecule magnets*, Nat. Mater. **7**, 179 (2008).

[35] S. Sanvito and A. R. Rocha, *Molecular-spintronics: the art of driving spin through molecules*, J. Comput. Theor. Nanosci. **3**, 624 (2006).

[36] M. N. Leuenberger and D. Loss, *Quantum computing in molecular magnets*, Nature **410**, 789 (2001).

[37] C. Timm and M. Di Ventra, *Memristive properties of single-molecule magnets*, Phys. Rev. B **86**, 104427 (2012).

[38] A. Ardavan, O. Rival, J. Morton, S. Blundell, A. Tyryshkin, G. Timco, and R. Winpenny, *Will Spin-Relaxation Times in Molecular Magnets Permit Quantum Information Processing?*, Phys. Rev. Lett. **98**, 057201 (2007).

[39] W. Wernsdorfer, *Quantum Phase Interference and Parity Effects in Magnetic Molecular Clusters*, Science **284**, 133 (1999).

[40] W. Wernsdorfer, M. Soler, G. Christou, and D. N. Hendrickson, *Quantum phase interference (Berry phase) in single-molecule magnets of* $[Mn_{12}]^{2-}$, J. Appl. Phys. **91**, 7164 (2002).

[41] J. E. Grose, E. S. Tam, C. Timm, M. Scheloske, B. Ulgut, J. J. Parks, H. D. Abruña, W. Harneit, and D. C. Ralph, *Tunnelling spectra of individual magnetic endofullerene molecules*, Nat. Mater. **7**, 884 (2008).

[42] M.-H. Jo, J. E. Grose, K. Baheti, M. M. Deshmukh, J. J. Sokol, E. M. Rumberger, D. N. Hendrickson, J. R. Long, H. Park, and D. C. Ralph, *Signatures of Molecular Magnetism in Single-Molecule Transport Spectroscopy*, Nano Lett. **6**, 2014 (2006).

[43] H. Heersche, Z. de Groot, J. Folk, H. van der Zant, C. Romeike, M. Wegewijs, L. Zobbi, D. Barreca, E. Tondello, and A. Cornia, *Electron Transport through Single Mn_{12} Molecular Magnets*, Phys. Rev. Lett. **96**, 206801 (2006).

[44] J. J. Henderson, C. M. Ramsey, E. del Barco, A. Mishra, and G. Christou, *Fabrication of nanogapped single-electron transistors for transport studies of individual single-molecule magnets*, J. Appl. Phys. **101**, 09E102 (2007).

[45] F. Haque, M. Langhirt, E. del Barco, T. Taguchi, and G. Christou, *Magnetic field dependent transport through a Mn_4 single-molecule magnet*, J. Appl. Phys. **109**, 07B112 (2011).

[46] A. S. Zyazin, J. W. G. van den Berg, E. A. Osorio, H. S. J. van der Zant, N. P. Konstantinidis, M. Leijnse, M. R. Wegewijs, F. May, W. Hofstetter, C. Danieli, et al., *Electric Field Controlled Magnetic Anisotropy in a Single Molecule*, Nano Lett. **10**, 3307 (2010).

[47] E. Burzurí, A. S. Zyazin, A. Cornia, and H. S. J. van der Zant, *Direct Observation of Magnetic Anisotropy in an Individual Fe_4 Single-Molecule Magnet*, Phys. Rev. Lett. **109**, 147203 (2012).

[48] M. Urdampilleta, *Supramolecular spin valves*, Nat. Mater. **10**, 502 (2011).

[49] A. Candini, S. Klyatskaya, M. Ruben, W. Wernsdorfer, and M. Affronte, *Graphene Spintronic Devices with Molecular Nanomagnets*, Nano Lett. **11**, 2634 (2011).

[50] A. Y. Kasumov, K. Tsukagoshi, M. Kawamura, T. Kobayashi, Y. Aoyagi, K. Senba, T. Kodama, H. Nishikawa, I. Ikemoto, K. Kikuchi, et al., *Proximity effect in a superconductor-metallofullerene-superconductor molecular junction*, Phys. Rev. B **72**, 033414 (2005).

[51] C. B. Winkelmann, N. Roch, W. Wernsdorfer, V. Bouchiat, and F. Balestro, *Superconductivity in a single-C_{60} transistor*, Nat. Phys. **5**, 876 (2009).

[52] J. Clarke and F. K. Wilhelm, *Superconducting quantum bits*, Nature **453**, 1031 (2008).

[53] G. Wendin and V. S. Shumeiko, *Quantum bits with Josephson junctions*, Low Temp. Phys. **33**, 724 (2007).

[54] A. Zazunov, V. Shumeiko, E. Bratus, J. Lantz, and G. Wendin, *Andreev Level Qubit*, Phys. Rev. Lett. **90**, 087003 (2003).

[55] A. Zazunov, V. Shumeiko, G. Wendin, and E. Bratus, *Dynamics and phonon-induced decoherence of Andreev level qubit*, Phys. Rev. B **71**, 214505 (2005).

[56] N. Chtchelkatchev and Y. Nazarov, *Andreev Quantum Dots for Spin Manipulation*, Phys. Rev. Lett. **90**, 226806 (2003).

[57] M. Zgirski, L. Bretheau, Q. Le Masne, H. Pothier, D. Esteve, and C. Urbina, *Evidence for Long-Lived Quasiparticles Trapped in Superconducting Point Contacts*, Phys. Rev. Lett. **106**, 257003 (2011).

[58] J. Michelsen, V. Shumeiko, and G. Wendin, *Manipulation with Andreev states in spin active mesoscopic Josephson junctions*, Phys. Rev. B **77**, 184506 (2008).

[59] J.-D. Pillet, C. H. L. Quay, P. Morfin, C. Bena, A. L. Yeyati, and P. Joyez, *Andreev bound states in supercurrent-carrying carbon nanotubes revealed*, Nat. Phys. **6**, 965 (2010).

[60] J.-D. Pillet, P. Joyez, R. Žitko, and M. F. Goffman, *Tunneling spectroscopy of a single quantum dot coupled to a superconductor: From Kondo ridge to Andreev bound states*, Phys. Rev. B **88**, 045101 (2013).

[61] M. Della Rocca, M. Chauvin, B. Huard, H. Pothier, D. Esteve, and C. Urbina, *Measurement of the Current-Phase Relation of Superconducting Atomic Contacts*, Phys. Rev. Lett. **99**, 127005 (2007).

[62] L. N. Bulaevskii, V. V. Kuzii, and A. A. Sobyanin, *Superconducting system with weak coupling to the current in the ground state*, JETP Lett. **25**, 290 (1977).

[63] J. A. van Dam, Y. V. Nazarov, E. P. A. M. Bakkers, S. De Franceschi, and L. P. Kouwenhoven, *Supercurrent reversal in quantum dots*, Nature **442**, 667 (2006).

[64] V. Ryazanov, V. Oboznov, A. Rusanov, A. Veretennikov, A. Golubov, and J. Aarts, *Coupling of Two Superconductors through a Ferromagnet: Evidence for a π Junction*, Phys. Rev. Lett. **86**, 2427 (2001).

[65] T. Kontos, M. Aprili, J. Lesueur, F. Genêt, B. Stephanidis, and R. Boursier, *Josephson Junction through a Thin Ferromagnetic Layer: Negative Coupling*, Phys. Rev. Lett. **89**, 137007 (2002).

[66] C. Benjamin, T. Jonckheere, A. Zazunov, and T. Martin, *Controllable π junction in a Josephson quantum-dot device with molecular spin*, Eur. Phys. J. B **57**, 279 (2007).

[67] M. Lee, T. Jonckheere, and T. Martin, *Josephson Effect through an Isotropic Magnetic Molecule*, Phys. Rev. Lett. **101**, 146804 (2008).

[68] I. A. Sadovskyy, D. Chevallier, T. Jonckheere, M. Lee, S. Kawabata, and T. Martin, *Josephson effect through an anisotropic magnetic molecule*, Phys. Rev. B **84**, 184513 (2011).

[69] S. Teber, C. Holmqvist, and M. Fogelström, *Transport and magnetization dynamics in a superconductor/single-molecule magnet/superconductor junction*, Phys. Rev. B **81**, 174503 (2010).

[70] C. Holmqvist, S. Teber, and M. Fogelström, *Nonequilibrium effects in a Josephson junction coupled to a precessing spin*, Phys. Rev. B **83**, 104521 (2011).

[71] C. Holmqvist, W. Belzig, and M. Fogelström, *Spin-precession-assisted supercurrent in a superconducting quantum point contact coupled to a single-molecule magnet*, Phys. Rev. B **86**, 054519 (2012).

[72] C. Holmqvist, M. Fogelström, and W. Belzig, *Spin-polarized Shapiro steps and spin-precession-assisted multiple Andreev reflection*, Phys. Rev. B **90**, 014516 (2014).

[73] Z. Nussinov, A. Shnirman, D. Arovas, A. Balatsky, and J. Zhu, *Spin and spin-wave dynamics in Josephson junctions*, Phys. Rev. B **71**, 214520 (2005).

[74] J.-X. Zhu, Z. Nussinov, A. Shnirman, and A. Balatsky, *Novel Spin Dynamics in a Josephson Junction*, Phys. Rev. Lett. **92**, 107001 (2004).

[75] N. Roch, R. Vincent, F. Elste, W. Harneit, W. Wernsdorfer, C. Timm, and F. Balestro, *Cotunneling through a magnetic single-molecule transistor based on $N@C_{60}$*, Phys. Rev. B **83**, 081407 (2011).

[76] A. V. Rozhkov and D. P. Arovas, *Josephson coupling through a magnetic impurity*, Phys. Rev. Lett. **82**, 2788 (1999).

[77] E. Vecino, A. Martín-Rodero, and A. Yeyati, *Josephson current through a correlated quantum level: Andreev states and π junction behavior*, Phys. Rev. B **68**, 035105 (2003).

[78] F. Siano and R. Egger, *Josephson Current through a Nanoscale Magnetic Quantum Dot*, Phys. Rev. Lett. **93**, 047002 (2004).

[79] M.-S. Choi, M. Lee, K. Kang, and W. Belzig, *Kondo effect and Josephson current through a quantum dot between two superconductors*, Phys. Rev. B **70**, 020502 (2004).

[80] Y. Tanaka, A. Oguri, and A. C. Hewson, *Kondo effect in asymmetric Josephson couplings through a quantum dot*, New J. Phys. **9**, 115 (2007).

[81] C. Karrasch, A. Oguri, and V. Meden, *Josephson current through a single Anderson impurity coupled to BCS leads*, Phys. Rev. B **77**, 024517 (2008).

[82] J. S. Lim and M.-S. Choi, *Andreev bound states in the Kondo quantum dots coupled to superconducting leads*, J. Phys.: Condens. Matter **20**, 415225 (2008).

[83] H. Jørgensen, K. Grove-Rasmussen, T. Novotný, K. Flensberg, and P. Lindelof, *Electron Transport in Single-Wall Carbon Nanotube Weak Links in the Fabry-Perot Regime*, Phys. Rev. Lett. **96**, 207003 (2006).

[84] P. Jarillo-Herrero, J. A. van Dam, and L. P. Kouwenhoven, *Quantum supercurrent transistors in carbon nanotubes*, Nature **439**, 953 (2006).

[85] Y. Tserkovnyak, A. Brataas, G. Bauer, and B. I. Halperin, *Nonlocal magnetization dynamics in ferromagnetic heterostructures*, Rev. Mod. Phys. **77**, 1375 (2005).

[86] C. Kittel, *On the Theory of Ferromagnetic Resonance Absorption*, Phys. Rev. **73**, 155 (1948).

[87] C. Bell, S. Milikisyants, M. Huber, and J. Aarts, *Spin Dynamics in a Superconductor-Ferromagnet Proximity System*, Phys. Rev. Lett. **100**, 047002 (2008).

[88] G. Eilenberger, *Transformation of Gorkov's equation for type II superconductors into transport-like equations*, Zeitschrift für Physik **214**, 195 (1968).

[89] A. I. Larkin and Y. N. Ovchinnikov, *Quasiclassical method in the theory of superconductivity*, Sov. Phys. JETP **28**, 1200 (1969).

[90] J. W. Serene and D. Rainer, *The quasiclassical approach to superfluid 3He*, Phys. Rep. **101**, 221 (1983).

[91] J. Cuevas and M. Fogelström, *Quasiclassical description of transport through superconducting contacts*, Phys. Rev. B **64**, 104502 (2001).

[92] N. B. Kopnin, *Theory of Nonequilibrium Superconductivity* (Oxford University Press, Oxford, 2009).

[93] A.-P. Jauho, N. S. Wingreen, and Y. Meir, *Time-dependent transport in interacting and noninteracting resonant-tunneling systems*, Phys. Rev. B **50**, 5528 (1994).

[94] J. C. Cuevas and E. Scheer, *Molecular Electronics: An introduction to Theory and Experiment* (World Scientific Publishing Company, Singapore, 2010).

[95] C. W. J. Beenakker and H. van Houten, *Resonant Josephson Current Through a Quantum Dot*, in *Single-Electron Tunneling and Mesoscopic Devices* (Springer Berlin Heidelberg, Berlin, Heidelberg, 1992).

[96] A. A. Golubov, M. Y. Kupriyanov, and E. Il'ichev, *The current-phase relation in Josephson junctions*, Rev. Mod. Phys. **76**, 411 (2004).

[97] M. Roukes, *Nanoelectromechanical systems face the future*, Phys. World **14**, 25 (2001).

[98] K. L. Ekinci, *Electromechanical Transducers at the Nanoscale: Actuation and Sensing of Motion in Nanoelectromechanical Systems (NEMS)*, Small **1**, 786 (2005).

[99] K. L. Ekinci, X. M. H. Huang, and M. L. Roukes, *Ultrasensitive nanoelectromechanical mass detection*, Appl. Phys. Lett. **84**, 4469 (2004).

[100] R. G. Knobel and A. N. Cleland, *Nanometre-scale displacement sensing using a single electron transistor*, Nature **424**, 291 (2003).

[101] M. Li, H. X. Tang, and M. L. Roukes, *Ultra-sensitive NEMS-based cantilevers for sensing, scanned probe and very high-frequency applications*, Nat. Nanotechnol. **2**, 114 (2007).

[102] D. Rugar, R. Budakian, H. J. Mamin, and B. W. Chui, *Single spin detection by magnetic resonance force microscopy*, Nature **430**, 329 (2004).

[103] M. Blencowe, *Quantum electromechanical systems*, Phys. Rep. **395**, 159 (2004).

[104] K. C. Schwab and M. L. Roukes, *Putting mechanics into quantum mechanics*, Phys. Today **58**, 36 (2005).

[105] M. D. LaHaye, *Approaching the Quantum Limit of a Nanomechanical Resonator*, Science **304**, 74 (2004).

[106] A. H. Safavi-Naeini, J. Chan, J. T. Hill, T. P. M. Alegre, A. Krause, and O. Painter, *Observation of Quantum Motion of a Nanomechanical Resonator*, Phys. Rev. Lett. **108**, 033602 (2012).

[107] A. D. Armour, M. P. Blencowe, and K. C. Schwab, *Entanglement and Decoherence of a Micromechanical Resonator via Coupling to a Cooper-Pair Box*, Phys. Rev. Lett. **88**, 148301 (2002).

[108] J. Sköldberg, T. Löfwander, V. S. Shumeiko, and M. Fogelström, *Spectrum of Andreev Bound States in a Molecule Embedded Inside a Microwave-Excited Superconducting Junction*, Phys. Rev. Lett. **101**, 087002 (2008).

[109] G. Sonne, M. E. Peña-Aza, L. Y. Gorelik, R. I. Shekhter, and M. Jonson, *Cooling of a Suspended Nanowire by an ac Josephson Current Flow*, Phys. Rev. Lett. **104**, 226802 (2010).

[110] P. Rabl, P. Cappellaro, M. V. G. Dutt, L. Jiang, J. R. Maze, and M. D. Lukin, *Strong magnetic coupling between an electronic spin qubit and a mechanical resonator*, Phys. Rev. B **79**, 041302 (2009).

[111] S. D. Bennett, S. Kolkowitz, Q. P. Unterreithmeier, P. Rabl, A. C. Bleszynski Jayich, J. G. E. Harris, and M. D. Lukin, *Measuring mechanical motion with a single spin*, New J. Phys. **14**, 125004 (2012).

[112] P. Rabl, S. J. Kolkowitz, F. H. L. Koppens, J. G. E. Harris, P. Zoller, and M. D. Lukin, *A quantum spin transducer based on nanoelectromechanical resonator arrays*, Nat. Phys. **6**, 602 (2010).

[113] Z.-L. Xiang, S. Ashhab, J. You, and F. Nori, *Hybrid quantum circuits: Superconducting circuits interacting with other quantum systems*, Rev. Mod. Phys. **85**, 623 (2013).

[114] M. Poggio and C. L. Degen, *Force-detected nuclear magnetic resonance: recent advances and future challenges*, Nanotechnology **21**, 342001 (2010).

[115] H. J. Mamin, M. Poggio, C. L. Degen, and D. Rugar, *Nuclear magnetic resonance imaging with 90-nm resolution*, Nat. Nanotechnol. **2**, 301 (2007).

[116] F. Xue, P. Peddibhotla, M. Montinaro, D. P. Weber, and M. Poggio, *A geometry for optimizing nanoscale magnetic resonance force microscopy*, Appl. Phys. Lett. **98**, 163103 (2011).

[117] O. Arcizet, V. Jacques, A. Siria, P. Poncharal, P. Vincent, and S. Seidelin, *A single nitrogen-vacancy defect coupled to a nanomechanical oscillator*, Nat. Phys. **7**, 879 (2011).

[118] S. Kolkowitz, A. C. Bleszynski Jayich, Q. P. Unterreithmeier, S. D. Bennett, P. Rabl, J. G. E. Harris, and M. D. Lukin, *Coherent Sensing of a Mechanical Resonator with a Single-Spin Qubit*, Science **335**, 1603 (2012).

[119] P. Mohanty, G. Zolfagharkhani, S. Kettemann, and P. Fulde, *Spin-mechanical device for detection and control of spin current by nanomechanical torque*, Phys. Rev. B **70**, 195301 (2004).

[120] A. A. Kovalev, G. E. W. Bauer, and A. Brataas, *Current-driven ferromagnetic resonance, mechanical torques, and rotary motion in magnetic nanostructures*, Phys. Rev. B **75**, 014430 (2007).

[121] R. Jaafar, E. M. Chudnovsky, and D. A. Garanin, *Dynamics of the Einstein–de Haas effect: Application to a magnetic cantilever*, Phys. Rev. B **79**, 104410 (2009).

[122] G. Zolfagharkhani, A. Gaidarzhy, P. Degiovanni, S. Kettemann, P. Fulde, and P. Mohanty, *Nanomechanical detection of itinerant electron spin flip*, Nat. Nanotechnol. **3**, 720 (2008).

[123] M. Ganzhorn, S. Klyatskaya, M. Ruben, and W. Wernsdorfer, *Strong spin-phonon coupling between a single-molecule magnet and a carbon nanotube nanoelectromechanical system*, Nat. Nanotechnol. **8**, 165 (2013).

[124] V. Sazonova, Y. Yaish, H. Ustunel, D. Roundy, T. A. Arias, and P. L. McEuen, *A tunable carbon nanotube electromechanical oscillator*, Nature **431**, 284 (2004).

[125] A. K. Hüttel, G. A. Steele, B. Witkamp, M. Poot, L. P. Kouwenhoven, and H. S. J. van der Zant, *Carbon Nanotubes as Ultrahigh Quality Factor Mechanical Resonators*, Nano Lett. **9**, 2547 (2009).

[126] B. Lassagne, Y. Tarakanov, J. Kinaret, D. Garcia-Sanchez, and A. Bachtold, *Coupling Mechanics to Charge Transport in Carbon Nanotube Mechanical Resonators*, Science **325**, 1107 (2009).

[127] G. A. Steele, A. K. Huttel, B. Witkamp, M. Poot, H. B. Meerwaldt, L. P. Kouwenhoven, and H. S. J. van der Zant, *Strong Coupling Between Single-Electron Tunneling and Nanomechanical Motion*, Science **325**, 1103 (2009).

[128] S. Sapmaz, P. Jarillo-Herrero, Y. M. Blanter, C. Dekker, and H. S. J. van der Zant, *Tunneling in Suspended Carbon Nanotubes Assisted by Longitudinal Phonons*, Phys. Rev. Lett. **96**, 026801 (2006).

[129] R. Leturcq, C. Stampfer, K. Inderbitzin, L. Durrer, C. Hierold, E. Mariani, M. G. Schultz, F. von Oppen, and K. Ensslin, *Franck–Condon blockade in suspended carbon nanotube quantum dots*, Nat. Phys. **5**, 327 (2009).

[130] J. O. Island, V. Tayari, A. C. McRae, and A. R. Champagne, *Few-Hundred GHz Carbon Nanotube Nanoelectromechanical Systems (NEMS)*, Nano Lett. **12**, 4564 (2012).

[131] E. A. Laird, F. Pei, W. Tang, G. A. Steele, and L. P. Kouwenhoven, *A High Quality Factor Carbon Nanotube Mechanical Resonator at 39 GHz*, Nano Lett. **12**, 193 (2012).

[132] P. L. Stiller, S. Kugler, D. R. Schmid, C. Strunk, and A. K. Huttel, *Negative frequency tuning of a carbon nanotube nano-electromechanical resonator under tension*, Phys. Status Solidi B **250**, 2518 (2013).

[133] B. J. LeRoy, S. G. Lemay, J. Kong, and C. Dekker, *Scanning tunneling spectroscopy of suspended single-wall carbon nanotubes*, Appl. Phys. Lett. **84**, 4280 (2004).

[134] M. Poot and H. S. J. van der Zant, *Mechanical systems in the quantum regime*, Phys. Rep. **511**, 273 (2012).

[135] A. Benyamini, A. Hamo, S. V. Kusminskiy, F. von Oppen, and S. Ilani, *Real-space tailoring of the electron–phonon coupling in ultraclean nanotube mechanical resonators*, Nat. Phys. **9**, 1 (2014).

[136] K. M. Borysenko, Y. G. Semenov, K. W. Kim, and J. M. Zavada, *Electron spin relaxation via flexural phonon modes in semiconducting carbon nanotubes*, Phys. Rev. B **77**, 205402 (2008).

[137] F. Kuemmeth, S. Ilani, D. C. Ralph, and P. L. McEuen, *Coupling of spin and orbital motion of electrons in carbon nanotubes*, Nature **452**, 448 (2008).

[138] M. S. Rudner and E. I. Rashba, *Spin relaxation due to deflection coupling in nanotube quantum dots*, Phys. Rev. B **81**, 125426 (2010).

[139] K. Flensberg and C. M. Marcus, *Bends in nanotubes allow electric spin control and coupling*, Phys. Rev. B **81**, 195418 (2010).

[140] T. S. Jespersen, *Gate-dependent spin–orbit coupling in multielectron carbon nanotubes*, Nat. Phys. **7**, 348 (2011).

[141] A. Pályi, P. R. Struck, M. Rudner, K. Flensberg, and G. Burkard, *Spin-Orbit-Induced Strong Coupling of a Single Spin to a Nanomechanical Resonator*, Phys. Rev. Lett. **108**, 206811 (2012).

[142] C. Ohm, C. Stampfer, J. Splettstoesser, and M. R. Wegewijs, *Readout of carbon nanotube vibrations based on spin-phonon coupling*, Appl. Phys. Lett. **100**, 143103 (2012).

[143] J. Danon, *Spin-flip phonon-mediated charge relaxation in double quantum dots*, Phys. Rev. B **88**, 075306 (2013).

[144] K. Tsukagoshi, B. W. Alphenaar, and H. Ago, *Coherent transport of electron spin in a ferromagnetically contacted carbon nanotube*, Nature **401**, 572 (1999).

[145] A. Cottet, T. Kontos, S. Sahoo, H. T. Man, M.-S. Choi, W. Belzig, C. Bruder, A. F. Morpurgo, and C. Schönenberger, *Nanospintronics with carbon nanotubes*, Semicond. Sci. Technol. **21**, S78 (2006).

[146] A. Jensen, J. R. Hauptmann, J. Nygård, and P. E. Lindelof, *Magnetoresistance in ferromagnetically contacted single-wall carbon nanotubes*, Phys. Rev. B **72**, 035419 (2005).

[147] S. Sahoo, T. Kontos, J. Furer, C. Hoffmann, M. Gräber, A. Cottet, and C. Schönenberger, *Electric field control of spin transport*, Nat. Phys. **1**, 99 (2005).

[148] D. Radić, A. Nordenfelt, A. M. Kadigrobov, R. I. Shekhter, M. Jonson, and L. Y. Gorelik, *Spin-Controlled Nanomechanics Induced by Single-Electron Tunneling*, Phys. Rev. Lett. **107**, 236802 (2011).

[149] D. Fedorets, L. Y. Gorelik, R. I. Shekhter, and M. Jonson, *Spintronics of a Nanoelectromechanical Shuttle*, Phys. Rev. Lett. **95**, 057203 (2005).

[150] A. Khaetskii, V. N. Golovach, X. Hu, and I. Žutić, *Proposal for a Phonon Laser Utilizing Quantum-Dot Spin States*, Phys. Rev. Lett. **111**, 186601 (2013).

[151] P. Stadler, W. Belzig, and G. Rastelli, *Ground-State Cooling of a Carbon Nanomechanical Resonator by Spin-Polarized Current*, Phys. Rev. Lett. **113**, 047201 (2014).

[152] J. Brüggemann, S. Weiss, P. Nalbach, and M. Thorwart, *Cooling a Magnetic Nanoisland by Spin-Polarized Currents*, Phys. Rev. Lett. **113**, 076602 (2014).

[153] J. Atalaya and L. Y. Gorelik, *Spintronics-based mesoscopic heat engine*, Phys. Rev. B **85**, 245309 (2012).

[154] I. Bargatin and M. L. Roukes, *Nanomechanical Analog of a Laser: Amplification of Mechanical Oscillations by Stimulated Zeeman Transitions*, Phys. Rev. Lett. **91**, 138302 (2003).

[155] H. O. H. Churchill, F. Kuemmeth, J. W. Harlow, A. J. Bestwick, E. I. Rashba, K. Flensberg, C. H. Stwertka, T. Taychatanapat, S. K. Watson, and C. M. Marcus, *Relaxation and Dephasing in a Two-Electron ^{13}C Nanotube Double Quantum Dot*, Phys. Rev. Lett. **102**, 166802 (2009).

[156] M. Jonson, *Quantum-Mechanical Resonant Tunneling in the Presence of a Boson Field*, Phys. Rev. B **39**, 5924 (1989).

[157] N. S. Wingreen, K. W. Jacobsen, and J. W. Wilkins, *Inelastic scattering in resonant tunneling*, Phys. Rev. B **40**, 11834 (1989).

[158] K. Flensberg, *Tunneling broadening of vibrational sidebands in molecular transistors*, Phys. Rev. B **68**, 205323 (2003).

[159] S. Braig and K. Flensberg, *Vibrational sidebands and dissipative tunneling in molecular transistors*, Phys. Rev. B **68**, 205324 (2003).

[160] A. Mitra, I. Aleiner, and A. J. Millis, *Phonon effects in molecular transistors: Quantal and classical treatment*, Phys. Rev. B **69**, 245302 (2004).

[161] J. Koch, F. von Oppen, and A. V. Andreev, *Theory of the Franck-Condon blockade regime*, Phys. Rev. B **74**, 205438 (2006).

[162] M. Galperin, A. Nitzan, and M. A. Ratner, *Resonant inelastic tunneling in molecular junctions*, Phys. Rev. B **73**, 045314 (2006).

[163] A. Zazunov and T. Martin, *Transport through a molecular quantum dot in the polaron crossover regime*, Phys. Rev. B **76**, 033417 (2007).

[164] M. Galperin, M. A. Ratner, and A. Nitzan, *Molecular transport junctions: vibrational effects*, J. Phys.: Condens. Matter **19**, 103201 (2007).

[165] R. Egger and A. O. Gogolin, *Vibration-induced correction to the current through a single molecule*, Phys. Rev. B **77**, 113405 (2008).

[166] O. Entin-Wohlman, Y. Imry, and A. Aharony, *Voltage-induced singularities in transport through molecular junctions*, Phys. Rev. B **80**, 035417 (2009).

[167] S. Maier, T. L. Schmidt, and A. Komnik, *Charge transfer statistics of a molecular quantum dot with strong electron-phonon interaction*, Phys. Rev. B **83**, 085401 (2011).

[168] F. Pistolesi, *Cooling a Vibrational Mode Coupled to a Molecular Single-Electron Transistor*, J. Low Temp. Phys. **154**, 199 (2009).

[169] F. Cavaliere, E. Mariani, R. Leturcq, C. Stampfer, and M. Sassetti, *Asymmetric Franck-Condon factors in suspended carbon nanotube quantum dots*, Phys. Rev. B **81**, 201303 (2010).

[170] F. Haupt, T. Novotný, and W. Belzig, *Phonon-Assisted Current Noise in Molecular Junctions*, Phys. Rev. Lett. **103**, 136601 (2009).

[171] T. Novotný, F. Haupt, and W. Belzig, *Nonequilibrium phonon backaction on the current noise in atomic-sized junctions*, Phys. Rev. B **84**, 113107 (2011).

[172] M. Galperin, K. Saito, A. V. Balatsky, and A. Nitzan, *Cooling mechanisms in molecular conduction junctions*, Phys. Rev. B **80**, 115427 (2009).

[173] F. Haupt, T. Novotný, and W. Belzig, *Current noise in molecular junctions: Effects of the electron-phonon interaction*, Phys. Rev. B **82**, 165441 (2010).

[174] L. Arrachea, N. Bode, and F. von Oppen, *Vibrational cooling and thermoelectric response of nanoelectromechanical systems*, Phys. Rev. B **90**, 125450 (2014).

[175] K. Kaasbjerg, T. Novotný, and A. Nitzan, *Charge-carrier-induced frequency renormalization, damping, and heating of vibrational modes in nanoscale junctions*, Phys. Rev. B **88**, 201405 (2013).

[176] S. Walter and B. Trauzettel, *Momentum and position detection in nanoelectromechanical systems beyond the Born and Markov approximations*, Phys. Rev. B **83**, 155411 (2011).

[177] G. D. Mahan, *Many-Particle Physics* (Kluwer Academic/Plenum Publishers, New York, 2000).

[178] H. Bruus and K. Flensberg, *Many-Body Quantum Theory in Condensed Matter Physics: An Introduction* (Oxford University Press, New York, 2004).

[179] G. A. Steele, F. Pei, E. A. Laird, J. M. Jol, H. B. Meerwaldt, and L. P. Kouwenhoven, *Large spin-orbit coupling in carbon nanotubes*, Nat. Commun. **4**, 1573 (2013).

[180] A. Cottet, T. Kontos, S. Sahoo, H. T. Man, M. S. Choi, W. Belzig, C. Bruder, A. F. Morpurgo, and C. Schönenberger, *Nanospintronics with carbon nanotubes*, Semicond. Sci. Technol **21**, S78 (2006).

[181] A. Jensen, J. R. Hauptmann, J. Nygård, and P. E. Lindelof, *Magnetoresistance in ferromagnetically contacted single-wall carbon nanotubes*, Phys. Rev. B **72**, 035419 (2005).

[182] B. Kubala and J. König, *Aharonov-Bohm interferometry with quantum dots: scattering approach versus tunneling picture*, Phys. Rev. B **67**, 205303 (2003).

[183] B. Kubala and J. König, *Flux-dependent level attraction in double-dot Aharonov-Bohm interferometers*, Phys. Rev. B **65**, 245301 (2002).

[184] Y. S. Greenberg, Y. A. Pashkin, and E. Il'ichev, *Nanomechanical resonators*, Uspekhi Fizicheskikh Nauk **182**, 407 (2012).

[185] F. Marquardt, J. P. Chen, A. A. Clerk, and S. M. Girvin, *Quantum Theory of Cavity-Assisted Sideband Cooling of Mechanical Motion*, Phys. Rev. Lett. **99**, 093902 (2007).

[186] T. J. Kippenberg and K. J. Vahala, *Cavity optomechanics: back-action at the mesoscale.*, Science **321**, 1172 (2008).

[187] I. Martin, A. Shnirman, L. Tian, and P. Zoller, *Ground-state cooling of mechanical resonators*, Phys. Rev. B **69**, 125339 (2004).

[188] U. Lundin, *Localized heating or cooling in mesoscopic devices by electron transport*, Phys. Lett. A **332**, 127 (2004).

[189] D. A. Rodrigues, J. Imbers, and A. D. Armour, *Quantum Dynamics of a Resonator Driven by a Superconducting Single-Electron Transistor: A Solid-State Analogue of the Micromaser*, Phys. Rev. Lett. **98**, 067204 (2007).

[190] K. R. Brown, J. Britton, R. J. Epstein, J. Chiaverini, D. Leibfried, and D. J. Wineland, *Passive Cooling of a Micromechanical Oscillator with a Resonant Electric Circuit*, Phys. Rev. Lett. **99**, 137205 (2007).

[191] F. Xue, Y. D. Wang, Y.-x. Liu, and F. Nori, *Cooling a micromechanical beam by coupling it to a transmission line*, Phys. Rev. B **76**, 205302 (2007).

[192] S. Zippilli, G. Morigi, and A. Bachtold, *Cooling Carbon Nanotubes to the Phononic Ground State with a Constant Electron Current*, Phys. Rev. Lett. **102**, 096804 (2009).

[193] F. Santandrea, L. Y. Gorelik, R. I. Shekhter, and M. Jonson, *Cooling of Nanomechanical Resonators by Thermally Activated Single-Electron Transport*, Phys. Rev. Lett. **106**, 186803 (2011).

[194] Z.-Z. Li, S.-H. Ouyang, C.-H. Lam, and J. Q. You, *Cooling a nanomechanical resonator by a triple quantum dot*, Europhys. Lett. **95**, 40003 (2011).

[195] G. Sonne and L. Y. Gorelik, *Ground-State Cooling of a Suspended Nanowire through Inelastic Macroscopic Quantum Tunneling in a Current-Biased Josephson Junction*, Phys. Rev. Lett. **106**, 167205 (2011).

[196] P. Stadler, W. Belzig, and G. Rastelli, *Ground-State Cooling of a Carbon Nanomechanical Resonator by Spin-Polarized Current*, Phys. Rev. Lett. **113**, 047201 (2014).

[197] P. Stadler, W. Belzig, and G. Rastelli, *Control of vibrational states by spin-polarized transport in a carbon nanotube resonator*, Phys. Rev. B **91**, 085432 (2015).

[198] A. Naik, O. Buu, M. D. LaHaye, A. D. Armour, A. A. Clerk, M. P. Blencowe, and K. C. Schwab, *Cooling a nanomechanical resonator with quantum back-action*, Nature **443**, 193 (2006).

[199] M. P. Blencowe, J. Imbers, and A. D. Armour, *Dynamics of a nanomechanical resonator coupled to a superconducting single-electron transistor*, New J. Phys. **7**, 236 (2005).

[200] A. A. Clerk and S. Bennett, *Quantum nanoelectromechanics with electrons, quasi-particles and Cooper pairs: effective bath descriptions and strong feedback effects*, New J. Phys. **7**, 238 (2005).

[201] G. Rastelli, M. Houzet, L. Glazman, and F. Pistolesi, *Interplay of magneto-elastic and polaronic effects in electronic transport through suspended carbon-nanotube quantum dots*, Comptes Rendus Physique **13**, 410 (2012).

[202] F. Elste, S. M. Girvin, and A. A. Clerk, *Quantum Noise Interference and Back-action Cooling in Cavity Nanomechanics*, Phys. Rev. Lett. **102**, 207209 (2009).

[203] F. W. J. Hekking, A. O. Niskanen, and J. P. Pekola, *Electron-phonon coupling and longitudinal mechanical-mode cooling in a metallic nanowire*, Phys. Rev. B **77**, 033401 (2008).

[204] P. J. Koppinen and I. J. Maasilta, *Phonon Cooling of Nanomechanical Beams with Tunnel Junctions*, Phys. Rev. Lett. **102**, 165502 (2009).

[205] A. V. Feshchenko, L. Casparis, I. M. Khaymovich, D. Maradan, O. P. Saira, M. Palma, M. Meschke, J. P. Pekola, and D. M. Zumbühl, *Tunnel-Junction Thermometry Down to Millikelvin Temperatures*, Phys. Rev. Applied **4**, 034001 (2015).

[206] Q. Wang, H. Xie, H. Jiao, and Y.-H. Nie, *Electric-current–induced heat generation in a quantum dot coupled to a normal and a superconducting lead*, Euro. Phys. Lett. **101**, 47008 (2013).

[207] A. A. Clerk, *Quantum-limited position detection and amplification: A linear response perspective*, Phys. Rev. B **70**, 245306 (2004).

[208] B. J. LeRoy, S. G. Lemay, J. Kong, and C. Dekker, *Electrical generation and absorption of phonons in carbon nanotubes*, Nature **432**, 371 (2004).

[209] J. Gramich, A. Baumgartner, and C. Schönenberger, *Resonant and Inelastic Andreev Tunneling Observed on a Carbon Nanotube Quantum Dot*, Phys. Rev. Lett. **115**, 216801 (2015).

[210] J. C. Cuevas, A. Martín-Rodero, and A. L. Yeyati, *Hamiltonian approach to the transport properties of superconducting quantum point contacts*, Phys. Rev. B **54**, 7366 (1996).

[211] J. Schindele, A. Baumgartner, R. Maurand, M. Weiss, and C. Schönenberger, *Nonlocal spectroscopy of Andreev bound states*, Phys. Rev. B **89**, 045422 (2014).

[212] A. Eichler, M. del Álamo Ruiz, J. A. Plaza, and A. Bachtold, *Strong Coupling between Mechanical Modes in a Nanotube Resonator*, Phys. Rev. Lett. **109**, 025503 (2012).

[213] T. Martin, *Noise in mesoscopic physics*, Proceedings of the Les Houches Summer School, Session LXXXI, edited by H. Bouchiat et al. (Elsevier, New York, 2005).

[214] S. Droste, J. Splettstoesser, and M. Governale, *Finite-frequency noise in a quantum dot with normal and superconducting leads*, Phys. Rev. B **91**, 125401 (2015).

Publications

- P. Stadler, C. Holmqvist, and W. Belzig, *Josephson current through a quantum dot coupled to a molecular magnet*, Phys. Rev. B. **88**, 104512 (2013)
- P. Stadler, W. Belzig, and G. Rastelli, *Ground-State Cooling of a Carbon Nanomechanical Resonator by Spin-Polarized Current*, Phys. Rev. Lett. **113**, 047201 (2014)
- P. Stadler, W. Belzig, and G. Rastelli, *Control of vibrational states by spin-polarized transport in a carbon nanotube resonator*, Phys. Rev. B **91**, 085432 (2015)
- P. Stadler, W. Belzig, and G. Rastelli, *Ground-state cooling of a mechanical oscillator by interference in Andreev-reflection*, Phys. Rev. Lett. **117**, 197202 (2016)

Acknowledgments

This thesis would not have been possible without the help of many people

First of all, I would like to express my gratitude to my supervisor Prof. Wolfgang Belzig, who gave me the opportunity to realize my PhD thesis in the Quantum transport group and supported my project in every possible way during my time as a PhD student. I benefited much from his expertise and guidance.

I also would like to thank Dr. Gianluca Rastelli for many discussion and his great interest on the topics I was working on. In many cases, Gianluca guided me through the dissertation and gave the directions on which problem to focus on. I always found working with him rewarding.

At the beginning of my dissertation, I benefited much from discussion with Dr. Cecilia Holmqvist.

Finally, I would like to thank the members of the Quantum Transport Group at the University Konstanz for their support whenever I had questions or problems.